

**Plasma Spray and Pack Cementation Process Optimization and  
Oxidation Behaviour of Novel Multilayered Coatings**

By

Feng Gao

B. Eng., M.A.Sc. Materials

A thesis submitted to the Faculty of Graduate and Postdoctoral Affairs

in partial fulfilment of

the degree requirements of

Doctor of Philosophy

Ottawa-Carleton Institute for

Mechanical and Aerospace Engineering

Department of Mechanical and Aerospace Engineering

Carleton University

Ottawa, Ontario, Canada

December, 2012

Copyright ©

2012 Feng Gao



Library and Archives  
Canada

Published Heritage  
Branch

395 Wellington Street  
Ottawa ON K1A 0N4  
Canada

Bibliothèque et  
Archives Canada

Direction du  
Patrimoine de l'édition

395, rue Wellington  
Ottawa ON K1A 0N4  
Canada

*Your file Votre référence*

*ISBN: 978-0-494-94216-1*

*Our file Notre référence*

*ISBN: 978-0-494-94216-1*

#### NOTICE:

The author has granted a non-exclusive license allowing Library and Archives Canada to reproduce, publish, archive, preserve, conserve, communicate to the public by telecommunication or on the Internet, loan, distribute and sell theses worldwide, for commercial or non-commercial purposes, in microform, paper, electronic and/or any other formats.

The author retains copyright ownership and moral rights in this thesis. Neither the thesis nor substantial extracts from it may be printed or otherwise reproduced without the author's permission.

#### AVIS:

L'auteur a accordé une licence non exclusive permettant à la Bibliothèque et Archives Canada de reproduire, publier, archiver, sauvegarder, conserver, transmettre au public par télécommunication ou par l'Internet, prêter, distribuer et vendre des thèses partout dans le monde, à des fins commerciales ou autres, sur support microforme, papier, électronique et/ou autres formats.

L'auteur conserve la propriété du droit d'auteur et des droits moraux qui protègent cette thèse. Ni la thèse ni des extraits substantiels de celle-ci ne doivent être imprimés ou autrement reproduits sans son autorisation.

---

In compliance with the Canadian Privacy Act some supporting forms may have been removed from this thesis.

While these forms may be included in the document page count, their removal does not represent any loss of content from the thesis.

Conformément à la loi canadienne sur la protection de la vie privée, quelques formulaires secondaires ont été enlevés de cette thèse.

Bien que ces formulaires aient inclus dans la pagination, il n'y aura aucun contenu manquant.

Canada

## **ABSTRACT**

The hot section components in gas turbines are subjected to a harsh environment with the temperature being increased continuously. The higher temperature has directly resulted in severe oxidation of these components. Monolithic coatings such as MCrAlY and aluminide have been traditionally used to protect the components from oxidation; however, increased operating temperature quickly deteriorates the coatings due to accelerated diffusion of aluminum in the coatings. To improve the oxidation resistance a group of multilayered coatings are developed in this study. The multilayered coatings consist of a Cr-Si co-deposited layer as the diffusion barrier, a plasma sprayed NiCrAlY coating as the middle layer and an aluminized top layer. The Cr-Si and aluminized layers are fabricated using pack cementation processes and the NiCrAlY coatings are produced using the Mettech Axial III™ System. All of the coating processes are optimized using the methodology of Design of Experiments (DOE) and the results are analyzed using statistical method. The optimal processes are adopted to fabricate the multilayered coatings for oxidation tests. The coatings are exposed in air at 1050°C and 1150°C for 1000 hr. The results indicate that a Cr layer and a silicon-rich barrier layer have formed on the interface between the Cr-Si coating and the NiCrAlY coating. This barrier layer not only prevents aluminum and chromium from diffusing into the substrate, but also impedes the diffusion of other elements from the substrate into the coating. The results also reveal that, for optimal oxidation resistance at 1050°C, the top layer in a multilayered coating should have at least Al/Ni ratio of one; whereas the multilayered coating with the Al/ Ni ratio of two in the top layer exhibits the best oxidation resistance at 1150°C. The DOE methodology provides an excellent means for process optimization

and the selection of oxidation test matrix, and also offers a more thorough understanding of the effects of process parameters on the coating microstructure, and the effects of layers and their interactions on the oxidation behavior of the multilayered coatings.

## **ACKNOWLEDGEMENTS**

I owe my sincere gratitude to my supervisors, Prof. Xiao Huang, Prof. Rong Liu (Carleton University, Canada), and Dr. Qi Yang (National Research Council, Canada), for their constant support and valuable suggestions. Thank you for being there for me when I needed your advice or recommendations.

I would like to express my great appreciation to my family for their continuous support and patience.

I am grateful to Mr. Fred Barrett (Carleton University, Canada) for spraying all specimens and to Mr. Yunfen Qian for his help in the preparation of the metallographic specimens.

I thank the staff of the Mechanical and Aerospace Engineering at Carleton University and Institute of Aerospace Research at National Research Council Canada (NRC) for all the help that they have provided me with throughout my studies at Carleton University.

## TABLE OF CONTENTS

ABSTRACT.....	ii
ACKNOWLEDGEMENTS.....	iv
TABLE OF CONTENTS.....	v
LIST OF TABLES.....	x
LIST OF FIGURES.....	xiv
NOMENCLATURE.....	xx
LIST OF ACRONYMS.....	xxiii
Chapter 1: Introduction.....	1
1.1    Background and Significance.....	1
1.1.1    Temperature Environments of Hot Section in Gas Turbines.....	1
1.1.2    Oxidation of Coatings.....	2
1.1.3    Development of Coatings with Oxidation Resistance.....	2
1.2    Research Objectives and Methodologies.....	3
1.2.1    Designing Multilayered Coatings.....	4
1.2.2    Optimizing Coating Processes.....	4
1.2.3    Fabricating Multilayered Coatings.....	5
1.2.4    Investigating the Oxidation Behavior of Multilayered Coatings.....	5
1.3    Thesis Structure.....	5
Chapter 2: Literature Review.....	8
2.1    Operating Conditions of the Hot Section Components in Gas Turbines.....	8

2.2	Coating Degradation Mechanisms.....	9
2.2.1	Oxidation of Metals .....	10
2.2.2	Oxidation of Coatings.....	12
2.2.3	Requirements for Oxidation Resistant Coatings.....	15
2.3	Coating Processes .....	16
2.3.1	Diffusion Coatings.....	17
2.3.2	Overlay Coatings .....	29
2.3.3	Diffusion between Coating and Substrate .....	36
2.3.4	Duplex Layer and Multilayered Coatings.....	40
2.4	Design of Experiments Methodology .....	42
2.4.1	Two-Level Full Factorial Design.....	43
2.4.2	Two-level Fractional Factorial Design .....	44
2.4.3	Response Surface Methodology (RSM) .....	45
2.4.4	Taguchi Method.....	47
2.4.5	Analysis of Variance (ANOVA) Table .....	52
2.5	Summary of Literature Review.....	56
<b>Chapter 3: Coating and Process Design.....</b>		<b>58</b>
3.1	Design of Multilayered Coatings.....	58
3.2	Coating Process Optimization .....	62
3.2.1	Plasma Spray Process Optimization .....	62
3.2.2	Pack Cementation Process Optimization.....	62
3.3	Coating Characterization .....	63
3.4	Summary of Coating and Process Design.....	64

Chapter 4: Process Optimization for NiCrAlY Coatings.....	65
4.1    Experimental Procedure.....	65
4.1.1    Coating Materials and Substrate .....	65
4.1.2    Plasma Spraying Process .....	66
4.1.3    Coating Characterization .....	67
4.2    Regression Analysis.....	72
4.3    Results and Discussion for Process Optimization .....	73
4.3.1    Microstructures of NiCrAlY Coatings.....	73
4.3.2    Results from First Set of Experiments.....	76
4.3.3    Discussion on Results from First Set of Experiments .....	84
4.3.4    Results from Second Set of Experiments .....	93
4.3.5    Concept of Process Index .....	94
4.3.6    Regression Analysis and Validity of Process Index .....	97
4.3.7 <i>PI</i> Development Guidelines for Other Thermal Spray Processes.....	106
4.4    Summary of Process Optimization for NiCrAlY Coatings .....	108
Chapter 5: Process Optimization for Diffusion Coatings .....	110
5.1    Process Optimization for the Aluminide Coatings .....	110
5.1.1    Experimental Procedure.....	111
5.1.2    Elemental Distribution and Microstructure .....	114
5.1.3    Coating Thickness and Al/Ni Ratio .....	118
5.1.4    Analysis of Variance for Coating Thickness and Al/Ni Ratio.....	119
5.1.5    Regression Equation for Coating Thickness and Al/Ni Ratio .....	120
5.2    Process Development for Cr-Si Coatings .....	128

5.2.1	Experimental Procedure.....	128
5.3	Cr-Si Coating Thickness.....	130
5.3.1	Optimization of Cr-Si Coating Process .....	130
5.3.2	Microstructures of Cr-Si Coatings.....	135
5.4	Summary of Process Optimization for Diffusion Coatings.....	138
Chapter 6: Fabrication of Coatings.....		139
6.1	Coatings for Oxidation Tests.....	139
6.2	Fabrication of Multilayered Coatings.....	141
6.2.1	Fabrication Procedures .....	141
6.2.2	Elemental Distributions in Multilayered Coatings .....	142
6.2.3	Microstructures of Multilayered Coatings.....	144
6.3	Fabrication of Baseline Coatings.....	148
6.4	Summary of Coating Fabrication.....	159
Chapter 7: Oxidation Tests and Results Discussion.....		160
7.1	Procedure of Oxidation Tests .....	160
7.2	Mass Change of Coatings.....	160
7.3	Microstructure and Morphology of Oxidized Coating Surfaces .....	168
7.4	Effects of Coating Layer on Area of Oxide Scales.....	178
7.5	Characterization of Cr-Si Barrier Layer .....	185
7.5.1	Structure of Barrier Layer.....	185
7.5.2	Elemental Distributions in Coatings without NiCrAlY Layer.....	186
7.5.3	Formation of Barrier Layer.....	193
7.5.4	Function of Barrier Layer .....	199

7.5.5	Effectiveness of Barrier Layer.....	202
7.5.6	Effects of Barrier Layer on the Formation of Interdiffusion Zone.....	204
7.5.7	Effects of Barrier Layer at Different Exposure Temperatures.....	205
7.6	Summary of Oxidation Tests.....	214
Chapter 8: Conclusions and Future Work.....		216
8.1	Conclusions.....	216
8.2	Future Work.....	218
REFERENCES.....		220
APPENDIX.....		236

## LIST OF TABLES

Table 1.1 Rotor inlet temperatures for typical gas turbine engines .....	1
Table 2.1 Oxides formed at various temperatures .....	12
Table 2.2 Optimal aluminum and chromium contents for high-temperature oxidation resistance .....	15
Table 2.3 Reactions for aluminizing, chromizing and siliconizing process .....	18
Table 2.4 Pack components, process parameters, pack cementation processes, and phases in coatings .....	21
Table 2.5 Pack compositions and process parameters for co-deposition processes .....	26
Table 2.6 Oxides formed with temperature for MCrAlY coatings.....	35
Table 2.7 Diffusion barriers and their performance .....	39
Table 2.8 2 <sup>2</sup> design with 4 treatment combinations and two main effects and one interaction .....	45
Table 2.9 ANOVA table of the yield for the example in section 2.4.5 .....	54
Table 3.1 Processes for the multilayered coating .....	61
Table 3.2 Compositions of key elements for various layers of multilayered coatings .....	61
Table 4.1 Powder parameters and powder feed rate.....	65
Table 4.2 Taguchi matrix and process parameters .....	67
Table 4.3 Percentages of crack, pore, unmelted particle and oxide in coatings .....	76
Table 4.4 Optimal parameters for minimizing coating features according SNRs .....	80
Table 4.5 Values of $x_1$ , $x_2$ , $x_3$ and $x_4$ used in regression equation .....	81
Table 4.6 Procedure of stepwise regression analysis for porosity .....	82
Table 4.7 Regression equations for four coating microstructure features .....	83

Figure 2.18 Overlay plot for the three responses .....	52
Figure 2.19 Normal probability plot of residuals . .....	56
Figure 3.1 Strategy to improve oxidation resistance of a coating. ....	58
Figure 3.2 Phase diagram of a Si-Cr-Ni ternary system .....	60
Figure 4.1 Image of a coating specimen in the group of coating 1-1. ....	68
Figure 4.2 Microstructure of coatings for first set of experiments. ....	70
Figure 4.3 EDS mapping images of coating 1-2 and coating 1-7.....	71
Figure 4.4 XRD spectra for NiCrAlY coatings. ....	75
Figure 4.5 Results of the experiments for the first Taguchi matrix.....	80
Figure 4.6 Normality and independence test of the regression equation for crack. ....	84
Figure 4.7 Pareto diagrams showing the effects of process parameters on coating features. .....	90
Figure 4.8 Plot of the $\Omega$ value vs. exponents $a$ , $b$ , and $c$ , respectively, in the range of 0.5 to 3.0. ....	99
Figure 4.9 Plot of the $\Omega$ value vs. exponent $b$ and $c$ , respectively, in the range of 0.25 to 0.50. ....	101
Figure 4.10 $\Omega$ value vs. exponent $b$ and $c$ , respectively, in the range of 0 to 0.25. ....	101
Figure 4.11 Comparison of predicated and measured values of the four microstructure features for the three sets of experiment.....	104
Figure 5.1 Pictorial representation of a three-level Box-Behnken response surface design for the aluminizing process.....	113
Figure 5.2 Image of coating 4-1 and 4-7. ....	114
Figure 5.3 Cross section images of the coating 4-1 and 4-7.....	115

Table 4.8 Comparison of the experimental results with the values calculated from the regression equations.....	85
Table 4.9 Effects of process parameters on coating features.....	86
Table 4.10 Sequential sums of squares of process parameters on coating features.....	87
Table.4.11 Parameters of the experiments used to assess the validity of the regression equations .....	93
Table 4.12 Results of the second set of the Taguchi matrix.....	94
Table 4.13 Summary of associated process parameters, normalized parameters.....	95
Table 4.14 Results of the regression analysis of the enthalpy .....	97
Table 4.15 Half of two-level factorial design for determining <i>PI</i> values.....	98
Table 4.16 Summary of <i>PIs</i> ' values for the two-level factorial matrix .....	98
Table 4.17 Coefficients of determination of regression equations for coating features with respect to all <i>PI</i> values.....	99
Table 4.18 Coefficients of determination for the microstructural features of NiCrAlY coatings with respect to the <i>PI</i> values for <i>b</i> from 0.50 to 3.00.....	100
Table 4.19 Coefficients of determination with respect to <i>PI</i> values from the two-level full factorial design.....	100
Table 4.20 Regression equations for coating features with respect to <i>PI</i> .....	102
Table 4.21 Relation of coating features to <i>PI</i> values.....	105
Table 4.22 Comparison between the predicted and experimental results for the second set of experiments.....	106
Table 5.1 Conditions of the specimens for the aluminizing process .....	111
Table 5.2 Compositions of SS304L and IN738.....	111

Table 5.3 Box–Behnken design for the aluminizing process .....	112
Table 5.4 Parameters for aluminizing process.....	113
Table 5.5 Coating thickness and the maximum ratio of aluminum to nickel content .....	118
Table 5.6 ANOVA table for coating thickness.....	119
Table 5.7 ANOVA table for ratio of Al to Ni.....	120
Table 5.8 Values or formulas of the partial derivatives.....	121
Table 5.9 Process parameters of additional tests for model verification .....	128
Table 5.10 Comparison between the predicted and experimental results.....	128
Table 5.11 Taguchi L4 array for the process development of Cr-Si coating.....	129
Table 5.12 Parameters for the L4 array .....	129
Table 5.13 Coating thickness for Cr-Si coating.....	130
Table 5.14 Concentrations of Si and Cr and the differences between measured data and ideal values in Cr-Si coatings .....	132
Table 5.15 Parameters for optimizing both silicon and chromium contents .....	132
Table 5.16 EDS results for the phases in the coating .....	138
Table 6.1 Two-level full factorial design for determining coating layers for oxidation tests .....	140
Table 6.2 Design matrix for oxidation test coatings.....	140
Table 6.3 Pack cementation parameters for multilayered coatings .....	141
Table 6.4 Plasma spray parameters for multilayered coatings .....	142
Table 6.5 Parameters of diffusion processes .....	149
Table 6.6 Summary of coating processes .....	149
Table 7.1 Mass change for individual coating specimen.....	162

Table 7.2 ANOVA table for mass change .....	163
Table 7.3 Effect, sequential SS, and percent contribution of factors and interactions for mass change .....	165
Table 7.4 Maximum and surface aluminum contents after the oxidation tests .....	168
Table 7.5 EDS results of various phases on the surface of coatings .....	169
Table 7.6 Average areas of oxide scales for the seven micrographs in each group .....	180
Table 7.7 Area calculation of oxide scale in a coating specimen .....	181
Table 7.8 ANOVA results for oxide scales .....	182
Table 7.9 Effect, sequential SS, and percent contribution of factors and interactions for the total areas of oxide scales .....	183
Table 7.10 EDS results of various phases in the coatings .....	189
Table 7.11 Phases in the coatings after exposure at 1050°C and 1150°C .....	213

## LIST OF FIGURES

Figure 2.1 Gas turbine inlet temperature trends . . . . .	9
Figure 2.2 Effects of major cycle parameters on micro-turbine performance . . . . .	10
Figure 2.3 Schematic representation of the oxidation stages of NiCrAlY coatings . . . . .	14
Figure 2.4 Cross-sectional morphology of an Amdry 962 coating after oxidized at 1200°C for 50 hr . . . . .	14
Figure 2.5 Contact pack and out-of-pack process schematic diagrams . . . . .	19
Figure 2.6 Schematic diagram of an above-the-pack device . . . . .	20
Figure 2.7 Al–Ni–Cr phase diagram at 1000°C. . . . .	26
Figure 2.8 Comparison of the temperature and velocity of particles in plasma spray and HVOF processes. . . . .	31
Figure 2.9 Configurations of traditional radial plasma gun and axial III gun . . . . .	32
Figure 2.10 Comparison of temperature and velocity of particles in thermal spray systems . . . . .	32
Figure 2.11 Relative oxidation and corrosion resistance of high-temperature systems . . .	33
Figure 2.12 Diffusion directions of elements in a Ni-based coating and substrate system. . . . . .	37
Figure 2.13 Micrograph of a smart coat showing the three-layer microstructure . . . . .	42
Figure 2.14 An example of the response surface and contour plot . . . . .	44
Figure 2.15 Graphical representations of the Box–Behnken and central composite design. . . . . .	47
Figure 2.16 Response surface and contour plots for the viscosity . . . . .	51
Figure 2.17 Response surface and contour plots for molecular weight . . . . .	52

Figure 5.4 Concentration distribution and XRD spectra for coating 4-1 and 4-7. ....	117
Figure 5.5 Ratio of Al at.% to Ni at.% versus the distance from coating surface for coating 4-1 and 4-7. ....	117
Figure 5.6 Contour plots of the coating thickness. ....	123
Figure 5.7 Response surface and contour plots of the Al/Ni ratio. ....	125
Figure 5.8 Overlapped contour plots for response surface models at 1000°C. ....	127
Figure 5.9 Image of coating 5-4. ....	129
Figure 5.10 Coating thickness versus process parameters. ....	131
Figure 5.11 Effects of process parameters on Si content and SNRs. ....	133
Figure 5.12 Effects of process parameters on Cr content and SNRs. ....	134
Figure 5.13 Microstructural analyses of coating 5-4. ....	137
Figure 6.1 Pictorial representation of a two-level full factorial design for the aluminizing process. ....	140
Figure 6.2 Two multilayered coatings ....	142
Figure 6.3 Concentration profiles of major elements in multilayer coatings. ....	144
Figure 6.4 Structure and phase analyses of the multilayered coating with aluminide I top coat. ....	146
Figure 6.5 Structure and phase analyses of the multilayered coating with aluminide II top coat. ....	148
Figure 6.6 SEM image and concentration profiles of major elements for coating O1 (Cr-Si coating/aluminide I) before oxidation tests. ....	151
Figure 6.7 SEM image and concentration profiles of major elements for coating O8 (Cr-Si coating/aluminide II) before oxidation tests. ....	152

Figure 6.8 Al/Ni ratio in coating O1, O3, O7 and O8. ....	152
Figure 6.9 XRD spectra of coating O1 and O8.....	153
Figure 6.10 SEM image and concentration profiles of major elements for coating O3 (aluminide I) before oxidation tests.....	155
Figure 6.11 SEM image and concentration profiles of major elements for coating O7 (aluminide II) before oxidation tests.....	156
Figure 6.12 SEM image and concentration profiles of major elements for coating O4 (NiCrAlY/aluminide II) before oxidation tests.....	157
Figure 6.13 SEM image and concentration profiles of major elements for coating O6 (NiCrAlY/aluminide I) before oxidation tests.....	158
Figure 7.1 Specimens for the oxidation test at 1050°C. ....	161
Figure 7.2 Contour plots of mass changes for multilayered coatings.....	167
Figure 7.3 Surface morphologies of and XRD spectra of coating O2.....	171
Figure 7.4 Surface morphologies and XRD spectra of coating O5. ....	173
Figure 7.5 Morphology on the top surface of the coating O1.....	175
Figure 7.6 Morphology of coating O3 surface. ....	175
Figure 7.7 Morphology the coating O4 surface.....	176
Figure 7.8 Morphology of coating O6 surface. ....	176
Figure 7.9 Morphology of coating O7 surface. ....	177
Figure 7.10 Morphology of coating O8 surface. ....	177
Figure 7.11 Morphology specimen O9 surface. ....	178
Figure 7.12 Morphology of coating O10 surface. ....	178
Figure 7.13 Binarized cross sectional image for coating O1.....	179

Figure 7.14 Contour plots of the oxide scale area. ....	185
Figure 7.15 Al and Cr concentration analyses in coating O1 (Cr-Si coating/aluminide I) after 1000 hr exposure at 1050°C. ....	188
Figure 7.16 Concentration analyses in coating O3 (aluminide I) after 1000 hr exposure at 1050°C. ....	190
Figure 7.17 Concentration analyses in coating O8 (Cr-Si coating/aluminide II) after 1000 hr exposure at 1050°C. ....	191
Figure 7.18 Concentration analyses in coating O7 (aluminide II) after 1000 hr exposure at 1050°C. ....	192
Figure 7.19 Concentration analyses in coating O2 (aluminide II) after 1000 hr exposure at 1050°C. ....	196
Figure 7.20 Concentration analyses of coating O5 (Cr-Si coating/NiCrAlY/aluminide I) after 1000 hr exposure at 1050°C. ....	198
Figure 7.21 SEM image of coating O6 (NiCrAlY/aluminide I) after 1000 hr exposure at 1050°C. ....	199
Figure 7.22 Concentration analyses in coating O4 (aluminide II) after 1000 hr exposure at 1050°C. ....	202
Figure 7.23 Concentration analyses in coating O2 (Cr-Si coating/ NiCrAlY/aluminide II) after 1000 hr exposure at 1150°C. ....	208
Figure 7.24 Concentration analyses in coating O5 (Cr-Si coating/NiCrAlY/aluminide I) after 1000 hr exposure at 1150°C. ....	210
Figure 7.25 SEM image of coating O4 (NiCrAlY/aluminide II) after 1000 hr exposure at 1150°C. ....	210

Figure 7.26 Concentration analyses in coating O6 (NiCrAlY/aluminide I) after 1000 hr exposure at 1150°C.....211

Figure 7.27 Concentration analyses in coating O7 (aluminide II) after 1000 hr exposure at 1150°C.....212

## NOMENCLATURE

- a* exponent for the equation of process index
- A* aluminum content in the powder mixture for the aluminizing process
- b* exponent for the equation of process index
- c* exponent for the equation of process index
- C* ratio of  $H_2 + N_2$  over total gas flow
- $C_H$  hydrogen proportion for working gas of ASP
- $C_N$  nitrogen proportion for working gas of ASP
- D* diameter of nozzle
- $D_o$  normalized diameter of nozzle in inch
- E* NiCrAlY in regression equation of mass loss
- F* Fisher value
- $\bar{F}$  mean value of response functions
- G* total flow rate
- $G_o$  normalized total flow rate
- H* enthalpy per liter of working gas
- I* current
- $I_o$  normalized current
- L* spray distance
- $L_o$  normalized spray distance
- m* regression freedom
- n* residual freedom
- N* nickel content in the powder mixture for the aluminizing process

$p$	$p$ -value
PI	process index
$r$	exponent the polynomial equation for coating features
$R$	coefficient of determination
$S$	powder size
$S_0$	normalized powder size
$T$	temperature for the aluminizing process
$U$	barrier coating in the regression equation of mass loss
$V$	NiCrAlY in the regression equation of mass loss
$W$	aluminized coating in the regression equation of mass loss
$Y$	regression equation for $PI$
$Y_M$	regression equation of mass loss
$Y_O$	regression equation of the total areas of oxide scales
$Y_R$	regression equation of Al/Ni ratio for the aluminizing process
$Y_T$	regression equation of coating thickness for the aluminizing process
$x_1$	particle size in the regression equations of NiCrAlY coatings
$x_2$	nozzle size in the regression equations of NiCrAlY coatings
$x_3$	total gas rate in the regression equations of NiCrAlY coatings
$x_4$	ratio of $H_2 + N_2$ over gas flow in the regression equations
$\alpha$	critical value for an $F$ distribution
$\beta$	NiAl phase
$\beta_0$	constant in the regression equation for $PI$
$\beta_1$	variable in the regression equation for $PI$

- $\beta_2$  variable in the regression equation for *PI*
- $\beta_3$  variable in the regression equation for *PI*
- $\gamma$  Ni solution
- $\gamma'$  Ni<sub>3</sub>Al phase
- $\Omega$  geometrical mean of the coefficients of determination

## **LIST OF ACRONYMS**

APS	atmospheric plasma spraying
CTE	coefficient of thermal expansion
CVD	chemical vapor deposition
DOE	design of experiment
DOF	degree of freedom
EB-PVD	electron beam physical vapor deposition
EDS	energy dispersive spectroscopy
HTHC	high-temperature hot corrosion
HTHA	high-temperature high-activity (CVD process)
HTLA	high-temperature low-activity (CVD process)
HVOF	high-velocity-oxy-fuel thermal spray
IGT	industrial gas turbines
LPPS	low pressure plasma spraying
LTHC	low-temperature hot- corrosion
LTHA	low-temperature high-activity (CVD process)
MWM	meandering winding magnetometer
PI	process index
PVD	physical vapor deposition
RIT	rotor-inlet temperatures
RSM	response of surface methodology
SEM	scanning electron microscopy

SNR	signal-noise ratio
SPS	shrouded plasma spraying
TBC	thermal barrier coating
TCP	topologically closed packed
TGO	thermally grown oxide
VPS	vacuum plasma spraying
XRD	X-ray diffraction
YSZ	yttria stabilized zirconia

## **Chapter 1: Introduction**

### **1.1 Background and Significance**

#### **1.1.1 Temperature Environments of the Hot Section in Gas Turbines**

Over the last decade, intensive research has been carried out on the coatings for the hot section components in gas turbine engines in order to enable a further increase in turbine rotor-inlet temperatures [ 1 ]. Higher rotor-inlet temperatures (RITs) are imperative for gas turbine engines to operate more efficiently. Currently, the temperatures at the entrance to the turbine for modern gas turbine engines can be as high as 1650°C [2] and RITs can be over 1400°C, as shown in Table 1.1[3]. Moreover the temperatures at the leading edges of rotor airfoils can exceed 1100°C, which is close to the incipient melting point of most superalloys.

**Table 1.1 Rotor inlet temperatures for typical gas turbine engines [3]**

Engine	Rotor inlet temp. , °C	Power output, MW	Efficiency, %
Westinghouse 501G	1426	240	58
Siemens V84/3a	1310	170	57
Alstom GT26	1240	281	57
GE 7FA	1290	150	55

Owing to the limited chromium and aluminum contents in superalloys, which result in their relatively low intrinsic resistance to high temperature oxidation, most superalloys cannot survive at temperatures over 1100°C. Therefore, various coatings are extensively implemented on the hot section components in gas turbines.

### **1.1.2 Oxidation of Coatings**

The mechanism of the oxidation depends on the exposure temperature and the composition of coatings. At a temperature below 800°C, coatings suffer low-temperature oxidation and some of the most active elements, such as Al, Cr, Si, are selectively oxidized to form a dense oxide scale, which protects the coatings from further oxidation. At a temperature above 800°C, nickel, along with aluminum and chromium, is also oxidized. Porous Ni(Al, Cr)<sub>2</sub>O<sub>4</sub> scales form when the aluminum content in the coatings is depleted, leading to the spallation of the scales during cooling [4].

The aluminum depletion in the coatings results from aluminum diffusing into the substrate and the continuous spallation of the aluminum-rich oxide scales. Furthermore, extensive internal oxidation of both the substrate and the surface scale takes place due to inward diffusion of oxygen [5]. When aluminum is depleted, the protective oxide layer on the coatings breaks down and the growth of the porous nickel-rich oxides is increased. Therefore various coatings have been developed with the objective to overcome aluminum depletion.

### **1.1.3 Development of Coatings with Oxidation Resistance**

Since the early 1960s, continuing research efforts have been made to develop coatings to protect the hot section components from oxidation. However, failures of coated components still occur from time to time as a result of severe oxidation at high temperatures. One of the noticeable reasons for the failure of the coatings under oxidation environments is the diffusion of the coating elements into the substrate and also the alloying elements from the substrate into the coating. Previous research has

proved that diffusion occurs between the coating and the substrate. For example, the work by Gao *et al.* [6] on Sermaloy 1515 (a Si modified aluminide coating) coating showed that aluminum depletion occurred and Kirkendall pores appeared along the interface of the coating and the substrate.

Although research has been carried out to study the phenomenon of the elemental diffusion between the coating and the substrate [7, 8], a solution is urgently needed for gas turbine industry to prevent this diffusion as much as possible. The formation of an effective diffusion barrier between a coating and a substrate has the potential to prevent aluminum from diffusing into the substrate and to offer the better protection against oxidation. This concept has been utilized in the present research to develop multilayered coatings.

In more details, multilayered coatings, composed of an aluminum-rich top layer, a NiCrAlY intermediate layer and a barrier layer, are proposed. The aluminum-rich top layer acting as an aluminum reservoir is imperative for the formation of protective scales and for the replenishment of aluminum in the top layer where aluminum is depleted due to the continuous spallation of oxide scales. The chromium enriched NiCrAlY layer works as a chromium reservoir for inward chromium diffusion to form a Cr-rich layer at the interface between the NiCrAlY, and the barrier layer impedes aluminum diffusion into the substrate.

## **1.2 Research Objectives and Methodologies**

This research is aimed at developing multilayered coatings with improved oxidation resistance for the hot section components in gas turbines. The major tasks towards the completion of the objective include designing multilayered coatings, optimizing coating

processes, fabricating the multilayered coatings, and investigating the oxidation behavior of the multilayered coatings at two temperatures.

### **1.2.1 Designing Multilayered Coatings**

To resist oxidation at high temperatures, a multilayered coating is expected to possess the functions of an aluminum reservoir, a chromium reservoir, and a diffusion barrier. Aluminized and chromized coatings applied via CVD or pack cementation are ideal for providing the aluminum and chromium reservoir. Another option for the chromium reservoir is the overlay MCrAlY coatings. The advantage of the MCrAlY coatings is the flexibility in adjusting the composition of the coatings [9]. The goal for the three layer structure is to form a Cr-rich layer between the chromium reservoir layer and the diffusion barrier layer [10]. As this Cr-rich layer contains less than 0.3 at.% aluminum [11], this layer is thought to be able to impede aluminum diffusion. To maintain this Cr-rich barrier layer stable at high temperatures without chromium diffusion into the substrate, the diffusion barrier layer must contain stable chromium intermetallics. Most Cr-Si intermetallics are very stable at high temperatures; for example, the melting temperatures for  $C_3Si$  and  $CrSi_2$  are 1770°C and 1490°C, respectively [12]. Therefore a Cr and Si-rich diffusion barrier layer deposited directly onto the substrate is necessary. Consequently a multilayered coating consists of an aluminized top layer, a NiCrAlY middle layer, and a chromizing and siliconizing barrier layer.

### **1.2.2 Optimizing Coating Processes**

For each coating process development, DOE methodology is employed. The Mettech Axial III™ system is used to produce the NiCrAlY coating and the target of

the process optimization is to achieve a coating with minimum pores, unmelted particles and oxides, and also free of cracks. A pack cementation process is employed for the aluminizing, chromizing and siliconizing coatings. The target of the process optimization is to produce coatings with expected compositions and microstructure integrity.

### **1.2.3 Fabricating Multilayered Coatings**

The optimized processes are used to fabricate two types of multilayered coatings. The difference between the two multilayered coatings is that the aluminum content in the top layer of one coating is as twice as that in the top layer of another. The multilayered coatings are examined on the basis of the elemental distributions in the coatings, and the multilayered coatings satisfy the design requirements if the elemental distributions are within the desired design ranges.

### **1.2.4 Investigating the Oxidation Behavior of Multilayered Coatings**

Multilayered coatings with baseline coatings are exposed at 1050°C and 1150°C for 1000 hr. Mass change and the area of oxide scales are measured after the tests. Models relating the mass change and the area of oxide scales are then developed and used to evaluate the effects of each layer and the interactions between each layer on the oxidation behavior of all coatings.

## **1.3 Thesis Structure**

Chapter 1 is the introduction to this research, covering the background, significance, objectives of this research, and the methodologies used to accomplish the research objectives.

Chapter 2 is the literature review, containing a survey of the existing coatings and the coating processes for the gas turbine hot section components with a focus on the performance of the existing multilayer coatings. The literature review has revealed that the existing coatings in the market have limited oxidation resistance and therefore there is a strong demand from the gas turbine industry for developing multilayered coatings with a diffusion barrier.

Chapter 3 provides the details of coating design and process selection. The requirements for the multilayered coatings and their individual layers are proposed, and the structure and composition of the multilayered coatings are then designed.

Chapter 4 describes the methods and procedures of optimizing the plasma spray process for NiCrAlY coatings using Mettech Axial III™ system. Two Taguchi arrays are used to optimize the plasma spray process so that the effects of the spray process parameters on coating features can be characterized. The results from the arrays are used to create regression equations to predict the required coating features. Further to the regression analysis, a process index (*PI*) is proposed as a complex variable incorporating a number of process parameters. The regression equations employing *PI* as the only variable are then correlated with additional experimental data.

Chapter 5 presents the details of the optimization procedure of the pack cementation process for the aluminized top layer on the NiCrAlY coating and a Cr-Si coating on the IN738 substrate. The optimization of the aluminizing process is based on the experiment that is designed using a response surface methodology, in which three parameters, the aluminum content, nickel content in the pack powder and the temperature of the process, are investigated. The effects of three parameters on the

thickness and Al/Ni ratio of the coatings are analyzed and subsequently modeled. The process to produce the Cr-Si coating with 25-30 at.% Si and 25-30 at.% Cr on the IN738 substrate is optimized by a Taguchi L4 array with two-levels and three factors.

Chapter 6 outlines the steps of the fabrication process for multilayered coatings. The multilayered coatings are fabricated through a combination of plasma spray process and pack cementation process. The fabrication process for the multilayered coatings is divided into three steps. The first step is to co-diffuse chromium and silicon on the IN738 substrate using pack cementation process. The second step is to deposit a NiCrAlY coating onto the Cr-Si coating using plasma spray process. The final step is an aluminizing treatment on the NiCrAlY coating, in order to develop an aluminum-rich layer. To characterize the oxidation behavior of the multilayered coatings, other traditional coatings are also produced for comparison. A two-level full factorial design will be employed to select other coatings.

Chapter 7 describes the details of the oxidation tests and presents the test results. The models developed for the mass change and the total area of oxide scales are explained.

Chapter 8 summarizes experimental and analytical results and highlights the conclusions drawn from this research. It also elaborates on the contributions of this work with regard to the oxidation resistance improvement provided by the developed coatings. The future work of this research is also recommended.

## **Chapter 2: Literature Review**

### **2.1 Operating Conditions of the Hot Section Components in Gas Turbines**

The demand for fossil fuel power generation is expected to grow to almost 1600 GW capacity by 2015 and to about 2000 GW by 2020 globally [13]. The market for industrial gas turbines (IGT) continues to increase due to the attractive price of electricity generated by IGTs. In the meantime, recent efforts to use less expensive fuels in industrial gas turbines significantly impact the performance of the hot section components in gas turbines. Since these components are expensive and have finite life; their durability plays an important role in controlling the maintenance intervals, life span and the life cycle costs of a gas turbine unit. Therefore a thorough understanding of the operating conditions of the hot section components in gas turbines and exploring effective protection is very important.

For gas turbines, one of the most important operating conditions is the rotor inlet temperature (RIT). Currently, RITs can be over 1400°C and eventually reach 1600-1700°C in the future (Figure 2.1) [14] since increasing rotor inlet temperatures can promote higher efficiency and power generation capability of gas turbine engines (Figure 2.2) [15]. A considerable increase in RIT can be achieved by a combination of the applications of cooling processes and thermal barrier coatings (TBCs) so that the maximum metal temperatures can be maintained below 1000°C. Given the soaring RITs, however, the coatings on the hot section components, metallic bond coatings for TBC and coatings in internal passages must withstand more severe oxidation attack due to the higher temperatures.

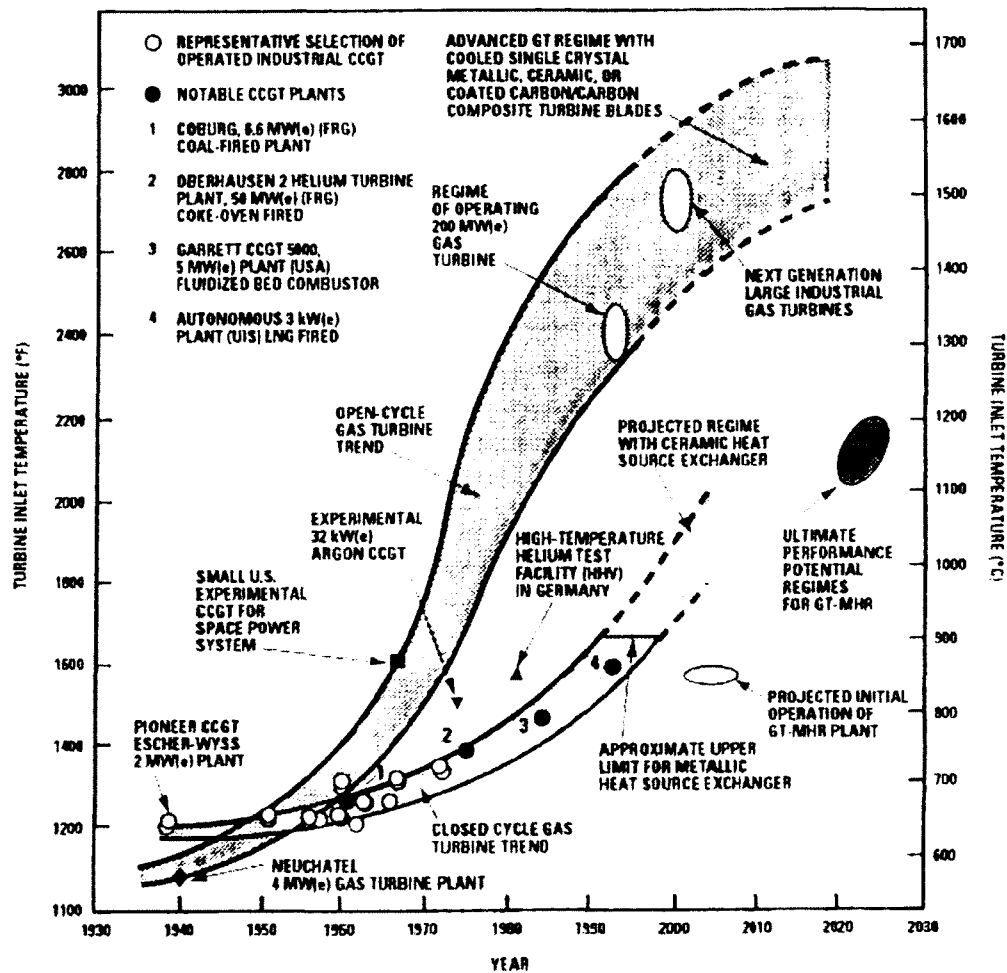
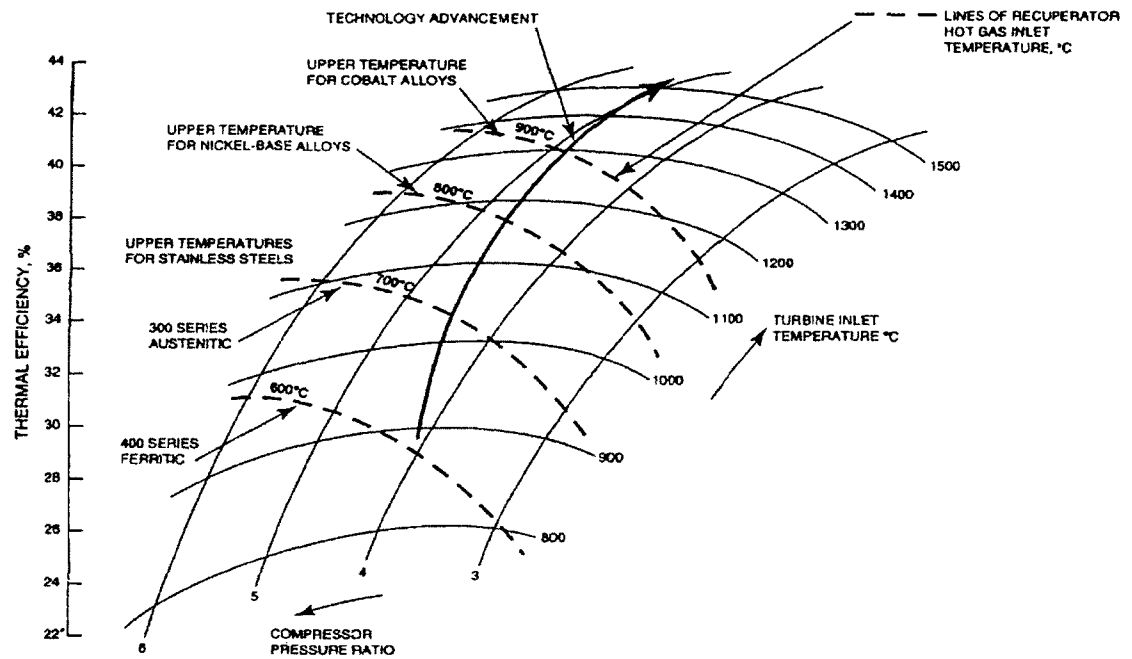


Figure 2.1 Gas turbine inlet temperature trends [14].

## 2.2 Coating Degradation Mechanisms

The degradation mechanisms of coatings are complex and affected by various factors such as coating microstructure, alloy composition, surface condition, oxygen and sulfur partial pressures, service atmosphere, and temperature. In general, most coatings fail due to high temperature oxidation and hot corrosion. Three accelerated degradation processes can be defined in the order of increasing temperature as: Type II hot corrosion, Type I hot corrosion and high temperature oxidation [16]. Hot corrosion occurs due to the reactions of chemicals that are associated with impurities in fuels, such as vanadium compounds and sulfates. During combustion these impurities can

form compounds with a low melting point. These melted salts are highly corrosive for coatings. This research, however, focuses on the oxidation behavior of coatings under high temperatures.



**Figure 2.2 Effects of major cycle parameters on micro-turbine performance [15].**

### 2.2.1 Oxidation of Metals

Most coatings for hot section components are metal-based, and the oxidation of the coatings literally is the oxidation of metallic elements. Oxidation of a metal falls into a five-step sequence [17]:

- (1) adsorption of molecular oxygen onto the metal surface from the environment
- (2) dissociation of molecular oxygen into atomic oxygen
- (3) combination of oxygen atoms and metal atoms
- (4) formation of islands of oxide and growth of the islands
- (5) formation of a continuous oxide film

The rate of oxidation depends on the rate of oxygen access to the metal atoms. There are three equations to describe the rate of metal oxidation [18]. Some metals, such as aluminum and chromium, exhibit oxide growth behavior described by the logarithmic-type rate equation at low temperature ( $< 500^{\circ}\text{C}$ ). This equation is valid only for very thin oxide scales, which form rapidly upon exposure to an oxidizing environment and then grow slowly with time. At high temperatures ( $> 500^{\circ}\text{C}$ ), the growth of oxide scales is usually limited by diffusion. The growth rate is then proportional to the thickness of the oxide scales, and parabolic-type rate equations apply. Moreover the growth rate of the oxide scales is proportional to the flux of ionic species through the oxide scales. This flux is proportional to the diffusion coefficient and the oxygen gradient. The metals that exhibit the parabolic-type oxide growth behaviour include iron, cobalt and nickel. A linear rate is observed when oxide scales undergo extensive cracking, spalling, or the oxide scales are porous.

The formation of a dense, continuous, and adherent oxide scale that allows slow diffusion represents the best means of protection for metals. At high temperatures,  $\text{Al}_2\text{O}_3$ ,  $\text{Cr}_2\text{O}_3$  and  $\text{SiO}_2$ , are almost exclusively employed. Aluminum oxide scales, formed by selective oxidation of aluminum in alloys or in coatings, are the primary means of protection for nickel-based superalloys in gas turbines. Chromium oxide scales are used in heat-resistant alloys where sulfidation is a major concern. Silicide-based coatings are used to protect some alloys which are unable to form protective  $\text{Al}_2\text{O}_3$  scales [19]. Consequently the coatings for hot section components usually consist of these active elements.

## 2.2.2 Oxidation of Coatings

The formation of oxide scales of an alloy or a coating under high temperatures usually depends on the composition of the alloy or the coating, temperature and exposure time. The oxides formed at various temperatures for different elements and coatings are listed in Table 2.1.

In the temperature range of 700-850°C,  $\gamma$ -Al<sub>2</sub>O<sub>3</sub> and Cr<sub>2</sub>O<sub>3</sub> grow at a relatively high rate and form protective oxide scales [20]. In the temperature range of 850-1050°C,  $\theta$ -Al<sub>2</sub>O<sub>3</sub> and CrO<sub>3</sub> are formed. CrO<sub>3</sub> is volatile and becomes gas at temperatures above 1100°C [21]. SiO<sub>2</sub> is very stable even when the temperature exceeds 1100°C [19].

The temperature for a coating to form a protective oxide scale can be as high as 800°C because of high aluminum and chromium contents in the coating. At temperatures above 800°C, the formation of porous Ni(Al,Cr)<sub>2</sub>O<sub>4</sub> scales leads to the spallation of the scales during cooling [22]. Therefore, a coating with high chromium content could fail due to the formation of porous Ni(Al,Cr)<sub>2</sub>O<sub>4</sub> scales or CrO<sub>3</sub>. Both diffusion coatings and overlay coatings are limited to 1100°C because further oxidation promotes the formation of porous Ni(Al,Cr)<sub>2</sub>O<sub>4</sub> scales, which leads to spallation of the scale during cooling.

**Table 2.1 Oxides formed at various temperatures**

Temp, °C	Al [20]	Cr [21]	Si [19]	Aluminide [23]	NiCrAlY [22]
700-850	$\gamma$ -Al <sub>2</sub> O <sub>3</sub>	Cr <sub>2</sub> O <sub>3</sub>		$\gamma$ -Al <sub>2</sub> O <sub>3</sub>	$\gamma$ -Al <sub>2</sub> O <sub>3</sub> , Cr <sub>2</sub> O <sub>3</sub>
850-1100	$\theta$ -Al <sub>2</sub> O <sub>3</sub>	CrO <sub>3</sub> , Cr <sub>2</sub> O <sub>3</sub>	SiO <sub>2</sub>	$\theta$ -Al <sub>2</sub> O <sub>3</sub> , NiO	$\theta$ -Al <sub>2</sub> O <sub>3</sub> , Cr <sub>2</sub> O <sub>3</sub> , NiO
> 1100	$\alpha$ -Al <sub>2</sub> O <sub>3</sub>	CrO <sub>3</sub> (gas)		$\alpha$ -Al <sub>2</sub> O <sub>3</sub> , NiAl <sub>2</sub> O <sub>4</sub>	$\alpha$ -Al <sub>2</sub> O <sub>3</sub> , NiAl <sub>2</sub> O <sub>4</sub> , Cr <sub>2</sub> O <sub>3</sub> , CrO <sub>3</sub> (gas)

In general, when exposure temperatures exceed 800°C, the oxidation behavior of diffusion coatings and MCrAlY coatings follows a four stage process [22]:

(1) Transient oxidation. At this oxidation stage, NiO, Cr<sub>2</sub>O<sub>3</sub> and α-Al<sub>2</sub>O<sub>3</sub> form on the coating surface simultaneously. The α-Al<sub>2</sub>O<sub>3</sub> grains are small and equiaxed in the outer region.

(2) Steady-state oxidation. At this oxidation stage, a continuous α-Al<sub>2</sub>O<sub>3</sub> scale forms and reduces the diffusion rate of oxygen. Coarse and columnar α-Al<sub>2</sub>O<sub>3</sub> is formed in the inner region.

(3) Aluminum depletion and nickel outward diffusion. As the oxidation time is increased, aluminum depletion causes the formation of Ni(Al,Cr)<sub>2</sub>O<sub>4</sub> layer and porous Ni(Al,Cr)<sub>2</sub>O<sub>4</sub> scales spall off during cooling.

(4) Internal Cr<sub>2</sub>O<sub>3</sub> oxide formation. Further depletion of aluminum causes the formation of internal Cr<sub>2</sub>O<sub>3</sub>, and the Cr<sub>2</sub>O<sub>3</sub> evaporate (when transformed to CrO<sub>3</sub>) and exhausts the chromium in the coatings.

A schematic diagram presenting the four stages is illustrated in Figure 2.3, and Figure 2.4 shows the cross-sectional morphology of the corresponding oxide scales formed on the surface of Amdry 962 coating (Ni-22Cr-10Al-1Y) after oxidation testing at 1200°C for 50 hr [24].

Kirkendall pores (interfacial cavity) are observed in the coating, as shown in Figure 2.4. When the supply of aluminum is exhausted as a result of both further oxidation at the coating surface and diffusion into the substrate, extensive internal oxidation of both the substrate and surface scale occurs due to inward diffusion of oxygen and outward diffusion of metallic elements such as Ni and Ti. The alumina scales break down and

growth of nickel-rich oxides is enhanced. The cracks initiate within the nickel-rich oxide nodular region at the coating surface, eventually propagate through the coating into the substrate and cause the spallation of the oxide scales [24].

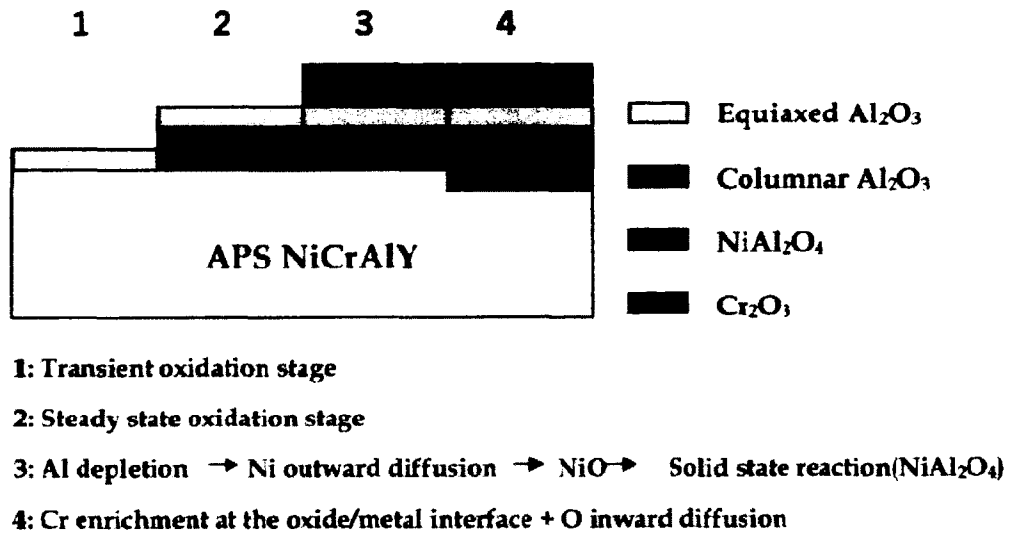


**Figure 2.3 Schematic representation of the oxidation stages of NiCrAlY coatings [24].**

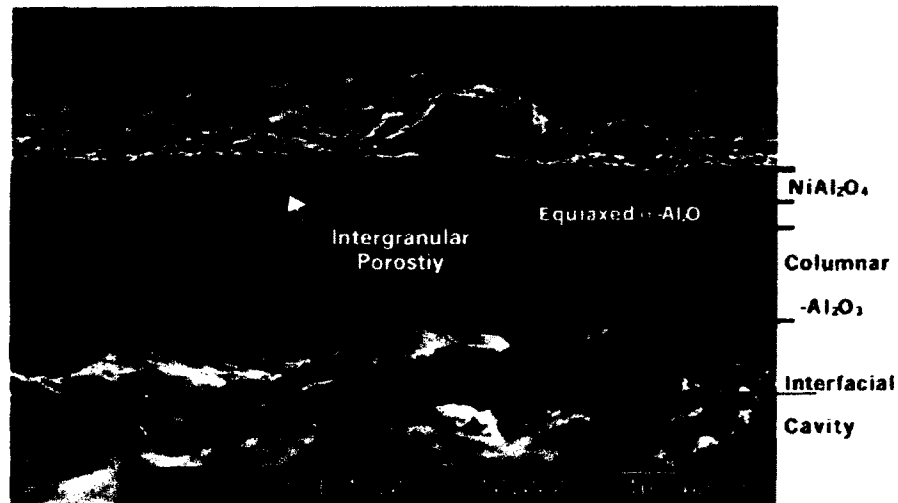


**Figure 2.4 Cross-sectional morphology of an Amdry 962 coating after oxidized at 1200°C for 50 hr [24].**

### 2.2.3 Requirements for Oxidation Resistant Coatings

To prevent the oxide scales on coatings from spalling, some basic requirements for coating composition must be taken into consideration [25]:

(1) The coating should form thermodynamically stable protective phases on its surface by reacting with the operating environment.

(2) These protective phases should grow slowly in order to keep coating reservoir depletion rates at a low level.

(3) Diffusion between the coating and the substrate should not occur or proceed as slowly as possible.

(4) The coating should contain elements Al, Cr, and Si, or maybe Ti. For Al and Cr, the optimal contents to achieve the best oxidation resistance at corresponding temperatures are given in Table 2.2 [26].

**Table 2.2 Optimal aluminum and chromium contents for high-temperature oxidation resistance [26]**

Temp., °C	Cr, wt.%	Al, wt.%
950	16-24	13-18
1100	25-30	14-16

(5) Highly pure alumina scale offers the best protection under high temperature oxidation. Sustainable aluminum content in the coating should be a major driving force for the development of coating technology [10].

(6) There should be a diffusion barrier between the coating and the substrate to block inward diffusion of aluminum into the substrate. The diffusion barrier consists of slow diffusion elements such as Cr, Si and Re [10].

(7) The coefficients of thermal expansion of the coating and the substrate should be as close as possible so that thermal cyclic stresses can be minimized in the system during the temperature changes [26].

### **2.3 Coating Processes**

In the development of superalloys for the hot section components in gas turbines, optimization of their high-temperature mechanical properties has been progressed toward reducing chromium content (to avoid TCP phase formation) with the increased refractory element additions, such as Mo, Re and W. Therefore most of the superalloy compositions contain a lower chromium content (and limited Al) with respect to providing adequate oxidation resistance through the formation of a slow growing and stable oxide scale. To compensate for this limited oxidation resistance, coatings enriched with aluminum, and perhaps chromium, are applied to the alloys. The types of coatings currently used on the hot section components of turbine engines fall into three basic groups [27, 28]:

- diffusion coatings
- overlay coatings
- thermal barrier coatings

Diffusion coatings and overlay coatings are of major concern in this study and are discussed in the following sections since these two processes are used to produce coatings in this research.

### **2.3.1 Diffusion Coatings**

#### **2.3.1.1 Fundamentals of Diffusion Coating Process**

The techniques for forming diffusion coatings can be true chemical vapor deposition, slurry or pack cementation process [27]:

(1) Chemical vapor deposition (CVD). The reactions to produce chemical vapors occur in a gas generator placed remotely from the deposition zone; the reactive species are then transported in a gaseous form into the process chamber and diffuse into the substrate.

(2) Slurry process. Slurry process is comprised of dipping the substrate into a slurry onto and drying the coated substrate followed by heating (sintering) the coating/substrate component in a furnace. The slurry consists of pure aluminum, silicon, magnesium, inert filler and resin. Usually Si-modified aluminide coatings are fabricated by a slurry process.

(3) Pack cementation process. Pack cementation process is also essentially a chemical vapor deposition process. The components to be coated are placed in a sealed or semi-sealed container (retort) together with a powder mixture that consists of metal elements to be deposited, halide activators and inert fillers. The halide activators are usually added in small quantities (1-6 wt.%) [29]. The sealed container is then heated under a protective atmosphere of argon to a temperature between 700°C and 1150°C, and held for a specified duration. At the elevated temperatures, the halide activators (such as  $\text{NH}_4\text{Cl}$  or  $\text{NH}_4\text{F}$ ) react with the metal elements in the powder mixture and form a series of metal halide vapor species such as  $\text{AlCl}$ ,  $\text{AlCl}_2$ ,  $\text{AlCl}_3$ ,  $\text{Al}_2\text{Cl}_6$ , and  $\text{CrAl}_2$  with a characteristic partial pressure distribution that is determined by their

thermodynamic stability in a particular powder pack and atmosphere [29]. The coating is formed via reactions of metal halide vapors on the substrate surface and subsequent solid state diffusion between the diffusing elements and the substrate. Pack cementation process will be discussed in more detail in section 2.3.1.2.

In all these processes, coatings are formed at elevated temperatures via diffusion transport of one or more elements from the gas phase to the substrate surface, and then the element(s) are deposited and consequently interact with the substrate to form a coating. Diffusion coatings have better adherence to the substrate than that by other coating processes such as thermal spray and PVD, because diffusion coatings are usually regarded as a part of the substrate. Therefore diffusion coatings can be implemented as single coatings as well as base or bond coats in multilayered coating systems.

### 2.3.1.2 Chemical Reactions in Pack Cementation Processes

A pack cementation process, based on the metallic species in the powder mixture, is also called aluminizing process, chromizing process and siliconizing process. The reactions for these processes are quite similar and summarized in Table 2.3 [17].

**Table 2.3 Reactions for aluminizing, chromizing and siliconizing process**

Process	Reactions
Aluminizing	$\text{NH}_4\text{Cl} = \text{NH}_3 + \text{HCl}$
	$2\text{Al} + 6\text{HCl} = 2\text{AlCl}_3 + 3\text{H}_2$
	$\text{AlCl}_3 + 2\text{Al} = 3\text{AlCl}$
	$3\text{AlCl} + 2\text{Ni} = 2\text{NiAl} + \text{AlCl}_3$
Chromizing	$\text{NH}_4\text{Cl} = \text{NH}_3 + \text{HCl}$
	$\text{Cr} + 2\text{HCl} = \text{CrCl}_2 + \text{H}_2$
	$2\text{CrCl}_2 + \text{H}_2 = 2\text{HCl} + 2\text{Cr}$
Siliconizing	$\text{NH}_4\text{Cl} = \text{NH}_3 + \text{HCl}$
	$\text{Si} + 2\text{HCl} = \text{SiCl}_2 + \text{H}_2$
	$\text{SiCl}_2 + \text{H}_2 = 2\text{HCl} + \text{Si}$

### 2.3.1.3 Pack Cementation Processes

Pack cementation processes can be classified into contact pack, out-of-pack, and above-the-pack process. For the contact pack process, components are loaded into an alumina crucible and directly embedded in the powder mixture for the contact arrangement (Figure 2.5a) [30]. For the out-of-pack process, components are separated from the pack powder by either porous alumina paper or foam disks (Figure 2.5b). For the above-the-pack process, components are placed or hung above a powder tray that contains the powder mixture (Figure 2.6) [31]. The advantages of the out-of-pack and the above-the-pack process are achieving uniform coating thickness and the ability to coat the internal passages. The disadvantage of the above-the-pack process is that the partial pressure of some metal halide vapor species is so low that the metal contents in resulted coating are insufficient to protect the components. Of these processes, the contact pack process is the most versatile and cost effective process and is thus used in this research.

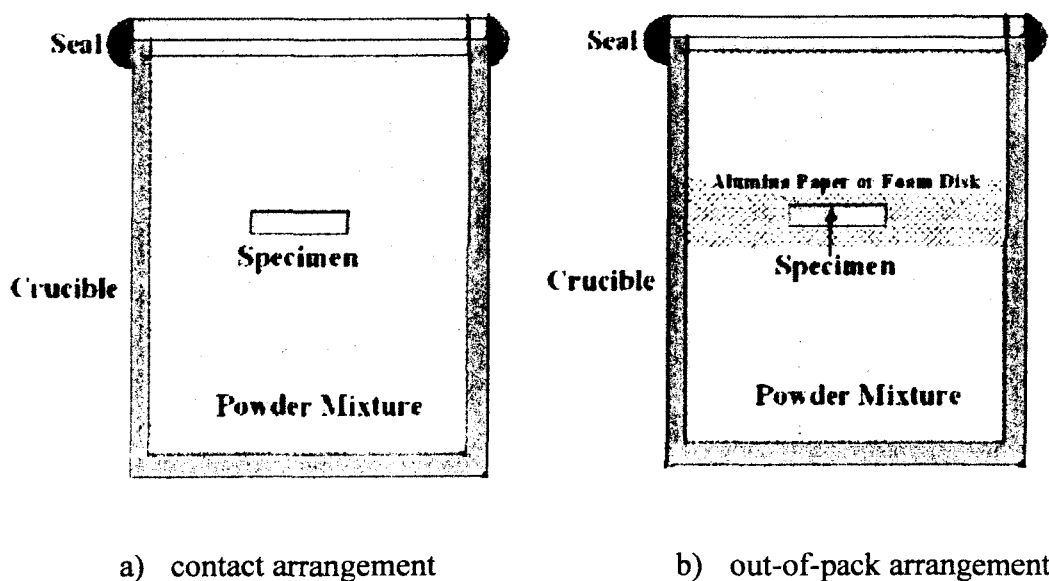


**Figure 2.5 Contact pack and out-of-pack process schematic diagrams [30].**

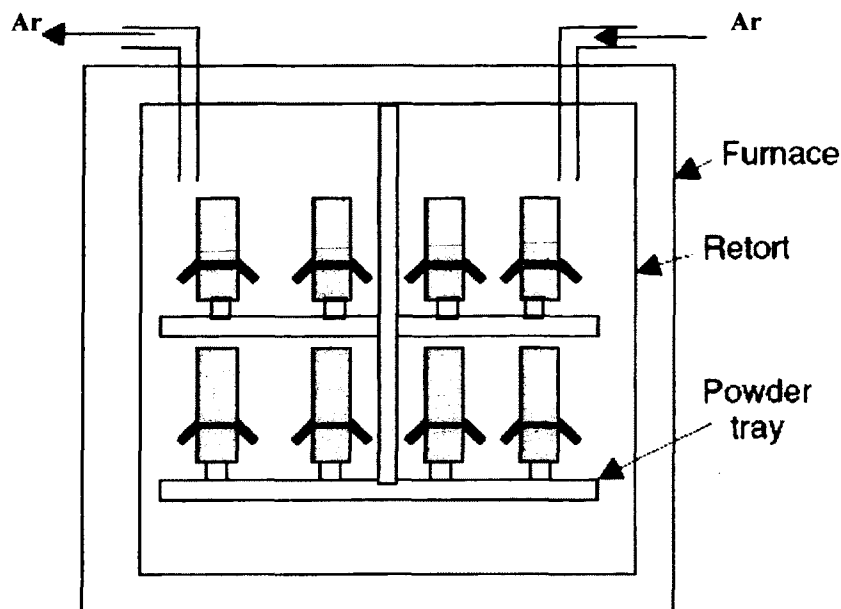


**Figure 2.6 Schematic diagram of an above-the-pack device [17].**

#### **2.3.1.4 Parameters of Pack Cementation Processes**

Atmosphere in retort, the composition of the pack, and process temperature and duration are of major concern for developing a successful pack cementation process. The examples of the parameters for aluminizing chrominizing and siliconizing processes are given in Table 2.4 [32, 33, 34]. The constituents of a pack cementation mixture include metallic powder (Al, Cr, Si, and Ni), halide activator ( $\text{NH}_4\text{Cl}$  or  $\text{MgF}_2$ ) and inert filler ( $\text{Al}_2\text{O}_3$  or  $\text{SiO}_2$ ).

##### **(1) Aluminizing process**

The most important parameters for aluminizing processes are the aluminum activity in the aluminum source (metallic powder or master alloy) and the temperature of the process. In a high-activity pack aluminizing process, the aluminum concentration is often greater than 60 at.% in the aluminum source and the process results in aluminum

inward-diffusion into the substrate surface where the formed aluminide layer contains several other alloying elements from the substrate. On the other hand, when the aluminum concentration is less than 60 at.% in the source, it is classified as a low-activity pack aluminizing process, where a nickel outward-diffusion occurs predominantly and the aluminide layer formed contains less amounts of alloying elements from the substrate [33].

**Table 2.4 Pack components, process parameters, pack cementation processes, and phases in coatings [32, 33, 34]**

Process	Pack components (wt.%)	Temperature and time	Phases in coating
Low-temperature high-activity (LTHA)	NiAl (15%), NH <sub>4</sub> Cl (2%), Al <sub>2</sub> O <sub>3</sub> (83%)	800°C, 2 hr 1100°C, 4 hr	Ni <sub>2</sub> Al <sub>3</sub> and NiAl NiAl
High-temperature low-activity (HTLA)	NiAl (15%), NH <sub>4</sub> Cl (2%), Al <sub>2</sub> O <sub>3</sub> (83%)	1100°C, 3-4 hr	NiAl
High-temperature high-activity (HTHA)	NiAl (15%), NH <sub>4</sub> Cl (2%), Al <sub>2</sub> O <sub>3</sub> (83%)	1034°C, 4 hr	Ni <sub>2</sub> Al <sub>3</sub> and NiAl with precipitates
Aluminizing	Al (20%), Ni (10%), NH <sub>4</sub> Cl (1.5%), Al <sub>2</sub> O <sub>3</sub> (68.5%)	900°C, 4 hr	Ni <sub>2</sub> Al <sub>3</sub> and NiAl
Chromizing	Cr (25%), NH <sub>4</sub> Cl (4%), Al <sub>2</sub> O <sub>3</sub> (71%)	1150°C, 1 hr	Cr-Ni enrichment solid solution
Siliconizing	Si (10%), Ni (6%), MgF <sub>2</sub> (1%), Al <sub>2</sub> O <sub>3</sub> (80%)	1000°C, 1 hr	Ni <sub>2</sub> Si and Ni <sub>3</sub> Si
	Si (35%), NH <sub>4</sub> Cl (5%) Al <sub>2</sub> O <sub>3</sub> (60%)	1100°C, 10 hr	Ni <sub>2</sub> Si and Ni <sub>3</sub> Si

In addition to the aluminum activity, the process temperature plays a significant role in the formation of the aluminide coating. An aluminizing process can be carried out at either a low temperature (700 to 850°C) or a high temperature (900 to 1100°C). The temperature determines the diffusion rates of aluminum, nickel and other elements, and has strong influence on the composition and thickness of the alumina layer. Different

combination of the aluminum activity and the process temperature leads to three common aluminizing processes: low-temperature high-activity (LTHA), high-temperature low-activity (HTLA), and high-temperature high-activity (HTHA).

1) Low-temperature high-activity (LTHA)

Typically, the low-temperature high-activity process is a two-step process, which is carried out at temperatures in a range of 700°C to 850°C, followed by a diffusion treatment above 1000°C to achieve a NiAl structure. In the low-temperature high-activity (LTHA) process, aluminum inward-diffusion dominates the growth of the aluminide coating and a Ni<sub>2</sub>Al<sub>3</sub> phase is formed in the coating (the ratio of the diffusion coefficients for aluminum and nickel ( $D_{Al}/D_{Ni}$ ) is about 10 in an aluminum-rich Ni<sub>2</sub>Al<sub>3</sub>/NiAl phase structure). In the LTHA process, aluminum is the leading diffusing species [9] and a subsequent heat treatment is applied to convert the aluminum-rich Ni<sub>2</sub>Al<sub>3</sub> phase to a NiAl phase. Accordingly the coating formed using the LTHA process is composed of an outer layer of an aluminum-rich phase, which is typically NiAl or a mixture of Ni<sub>2</sub>Al<sub>3</sub> and NiAl, and an inner diffusion layer formed on the substrate side.

2) High-temperature high-activity (HTHA)

The high-temperature high-activity (HTHA) process is a one step process carried out at a temperature above 1000°C for a predetermined duration to produce a NiAl coating layer [33]. In the high-temperature high-activity (HTHA) process, the coating growth takes place by aluminum inward-diffusion initially, followed by an intermediate stage where the growth involves both aluminum inward-diffusion and nickel outward-diffusion. In the final stage, nickel outward-diffusion dominates the coating formation process. Thus, a typical coating produced by the HTHA process consists of three layers:

an outer layer of  $\text{Ni}_2\text{Al}_3$  or a mixture of  $\text{Ni}_2\text{Al}_3$  and  $\text{NiAl}$ , an intermediate  $\text{NiAl}$  layer, and a diffusion layer adjacent to the substrate [33]. A subsequent diffusion heat treatment can convert the  $\text{Ni}_2\text{Al}_3$  phase to a  $\text{NiAl}$  phase if  $\text{Ni}_2\text{Al}_3$  phase dominates the coating.

### 3) High-temperature low-activity (HTLA)

Similarly the high-temperature low-activity (HTLA) process is also a one step carried out at a temperature above  $1000^\circ\text{C}$ . In HTLA process, nickel outward-diffusion dominates the growth of the coating due to the higher ratio (3 to 3.5) of the diffusion coefficients for nickel and aluminum ( $D_{\text{Ni}}/D_{\text{Al}}$ ) at temperatures above  $1000^\circ\text{C}$  [35]. A nickel-rich  $\beta$ - $\text{NiAl}$  phase is formed in this process. Therefore a typical coating produced by the HTLA process consists of two layers: an outer  $\text{NiAl}$  layer and an inner diffusion layer.

An important difference between the outward growth and the inward growth of coatings is that there will be less of the slowly diffusing elements (W, Mo and Ta) in the coating in the former case. Therefore the outward growing coating provides better resistance to the spallation of the oxide scales due to a high purity of the alumina scale formed.

The aluminum pickup by the substrate is very fast during early stages of aluminizing and diminishes with time. Most of the aluminum is picked up by the specimen during the first hour of aluminizing [33].

### (2) Chromizing process

Simple chromizing process can be identified as chromium inward-diffusion. For nickel based superalloys, chromizing is used to produce Ni-Cr solid solution layers,

usually containing 20-25 wt.% Cr. However in some instances the concentration of chromium at the surface can reach up to 35 wt % for a detrimental  $\alpha$ -Cr to form. This problem can be avoided by utilizing the above-the-pack process, in which the chromium is transported to the substrate as a vapor phase from non-contact source. The pack mixture usually contains 30-60 wt.% of Cr powder, 40-60 wt.% of refractory powder (kaolin, alumina, or magnesia), and 1-3 wt.% ammonium chloride as activator [36]. The temperature for chromizing ranges from 1000 to 1200°C and the duration is typically 1 to 4 hr. Increasing temperature will enhance chromium diffusion and the temperature should be controlled to avoid the formation of detrimental  $\alpha$ -Cr phase. As reported in literature [37], both the total chromium uptake and the chromium supplied by the reduction reaction were almost linear with time for a short period but became parabolic as the treatment continued, similar to the aluminizing process.

### (3) Siliconizing process

Simple siliconizing process can be identified as silicon inward-diffusion or nickel outward-diffusion [38]. When silicon is deposited on nickel,  $\text{Ni}_2\text{Si}$  is the first phase to form, followed by  $\text{Ni}_5\text{Si}_2$  and  $\text{Ni}_3\text{Si}$  [32, 34]. It is also known that nickel is distributed uniformly in the substrate and the coating layer, while a sharp change in silicon concentration is observed from the coating to substrate interface. Siliconized coatings contain voids in the interface, which deteriorate the bonding between the substrate and the coating. The process temperature will influence the nickel and silicon concentrations and microstructure. The pack mixture usually contains 10-40 wt.% Si powder, 50–80 wt.% alumina, and 3-10 wt.% ammonium chloride. The temperature for

siliconizing process ranges from 1000°C to 1200°C [32] and duration is between 1 to 4 hr.

The temperature range and the process duration for both chromizing process and siliconizing process are similar (1000°C to 1200°C and 1 to 4 hr). Therefore a Cr-Si co-deposition process is possible to produce a coating with high chromium and silicon contents at the same time.

### **2.3.1.5 Co-Depositions Processes**

Applications of monolithic aluminized, chromized or siliconized coatings are often limited in their mechanical property and oxidation resistance. Therefore co-deposition processes have been developed in order to obtain combined performance of coatings. Comparisons of the co-diffused coating with a standard commercial aluminized coating reveal many beneficial effects of the two element or multiple element co-diffusion coatings [39]. Typical co-deposition processes are to form chromium or silicon modified aluminide, where the diffusion of aluminum is combined with chromium or silicon by incorporating appropriate amount of metal halides into the aluminizing atmosphere or Cr/Si powder into the pack. Several pack compositions and process parameters for co-deposition are provided Table 2.5.

#### **(1) Al-Cr co-deposition process**

The Al-Cr co-deposition process can be either high-temperature low-activity (HTLA) or low-temperature high-activity (LTHA) or single step high-temperature high-activity (HTHA) [40]. The primary phases in the coating produced by a co-deposition process are similar to phases produced by the corresponding aluminizing

process except that there are other precipitates in the coating or elements in the solid solution of the coating.

**Table 2.5 Pack compositions and process parameters for co-deposition processes**

Process	Pack components (wt.%)	Temp. and time	Phase
Al-Cr co-deposition [39]	Al/Cr master alloys NH <sub>4</sub> Cl, CrCl <sub>3</sub> , AlCl <sub>3</sub> , Al <sub>2</sub> O <sub>3</sub>	1000-1150°C, 4-6 hr	Ni <sub>2</sub> Al <sub>3</sub> and NiAl
Al-Cr-Hf co-deposition [40]	Al/Cr master alloys, Hf/HfO <sub>2</sub> , NH <sub>4</sub> Cl, CrCl <sub>3</sub> , AlCl <sub>3</sub> , Al <sub>2</sub> O <sub>3</sub>	1000-1150°C, 4-6 hr	Ni <sub>2</sub> Al <sub>3</sub> , NiAl, Al <sub>3</sub> Hf, Al <sub>3</sub> Hf and AlHf
Al-Si co-deposition [41]	Al, Si powder, NH <sub>4</sub> Cl, Al <sub>2</sub> O <sub>3</sub>	1000°C, 4hr	Ni <sub>2</sub> Al <sub>3</sub> , NiAl, Ni <sub>2</sub> Si, Ni <sub>3</sub> Si,
Cr-Si co-deposition [42]	Cr/Si master alloys, NH <sub>4</sub> Cl, CrCl <sub>2</sub> , Al <sub>2</sub> O <sub>3</sub>	1050°C, 6 hr	Cr <sub>2</sub> Si, Cr <sub>3</sub> Ni <sub>2</sub> Si

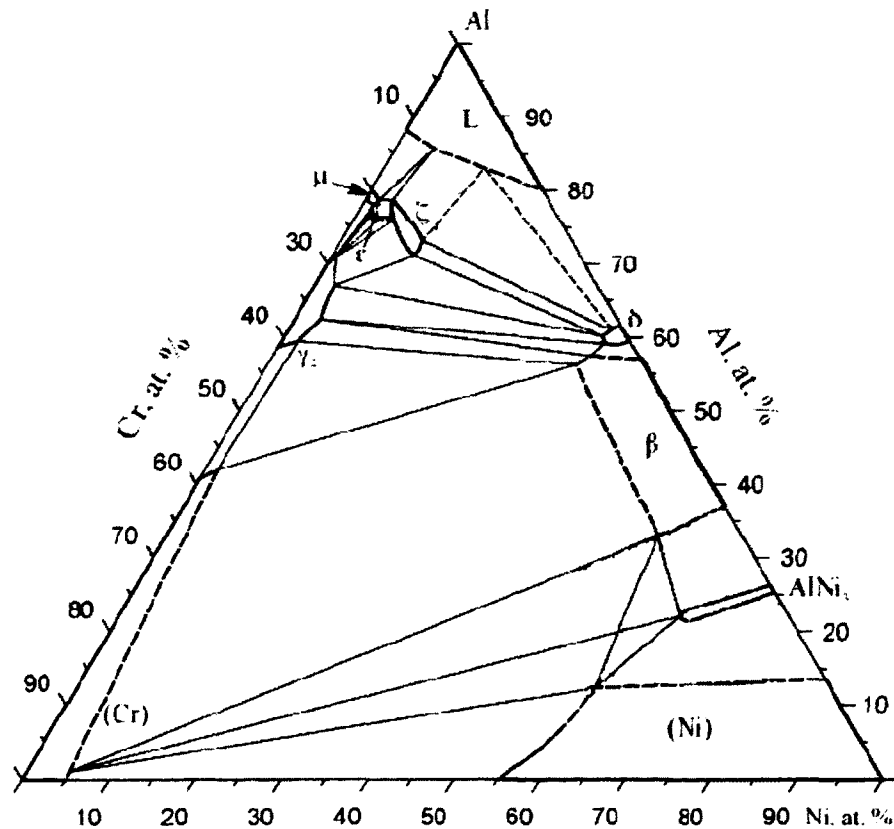


**Figure 2.7 Al-Ni-Cr phase diagram at 1000°C [43].**

The chromium modified aluminide can also be produced by stepwise aluminizing and chromizing. However the second step chromizing may significantly reduce aluminum content in the outer layer due to the formation of volatile aluminum chloride during chromizing. Consequently chromium content in the outer layer can reach as high as 70 at.%, leading to  $\alpha$ -Cr formation [32].

A two-step process with first chromizing and then aluminizing has been employed to create a chromium diffusion barrier to prevent aluminum from diffusing into the substrate [44]. When aluminum is deposited on chromium, chromium solid solution is the first phase to form, followed by  $\eta$  ( $\text{Cr}_2\text{Al}$ ) and  $\zeta$  ( $\text{Cr}_5\text{Al}_8$ ) [45]. The  $\eta$  phase is stable at a temperature below  $910^\circ\text{C}$  and the  $\zeta$  phase below  $1350^\circ\text{C}$ . Both of them can retard further aluminum diffusion when the aluminum content reaches the point where  $\eta$  ( $\text{Cr}_2\text{Al}$ ) and  $\zeta$  ( $\text{Cr}_5\text{Al}_8$ ) phases form.

## (2) Al-Si co-deposition process

Al-Si co-deposition process generally yields low silicon contents due to high activity of aluminum present in the pack mixture. One example given in literature [46] showed that the maximum silicon content of about 1 at.% was obtained with a pack mixture of 90 wt.% Si and 10 wt.% Al. Employing 95 wt.% Si in the pack could lead to a much higher concentration of about 50 wt.% silicon in the top layer [46]. The silicon modified aluminide coatings are comprised of nickel aluminide phases in the coating and fine nickel silicide precipitates in the outer zone.

A two-step process with first aluminizing and then siliconizing was also adopted to produce silicon-containing coatings. However this process may reduce the aluminum content of the outer layer significantly since the formation of volatile aluminum

chloride during siliconizing leads to the replacement of nickel aluminides by nickel silicides. Nickel silicides are generally not considered effective as protective coatings for the intended application due to their brittleness. Therefore single-step co-deposition process with a well-adjusted pack mixture is a more practical and cost-effective process [46].

Of the several diffusion coatings, silicon-containing diffusion aluminides such as Sermaloy J and Sermaloy 1515 [47] performed well under either type I or type II hot corrosion conditions. This is attributed to the formation of a continuous oxide layer with a low defect concentration on the coating surface. However, the silicon content must be greater than 10 wt.% in order to enhance the hot corrosion resistance of nickel based alloys [36, 48].

### (3) Cr-Si co-deposition process

A number of studies of the Cr-Si co-deposition process on Fe-based alloys were reported [42] and the process parameters are summarized in Table 2.5 [49]. It seems that the chromium content can easily reach around 50 at.% [50], whereas silicon content cannot reach beyond 10 at.% [49]. No report was found for Cr-Si co-deposition process on Ni-based alloys.

#### **2.3.1.6 Heat Treatments of Diffusion Coatings**

Heat treatments can increase the coating thickness for all diffusion coatings. The concentrations of elements become uniform after certain heat treatments. The temperature for heat treatment of diffusion coatings ranges from 950-1150°C and the duration is 2-8 hr. For certain coatings, heat treatments are imperative in order to obtain optimal coating performance. Of the various diffusion coatings, heat treatments are

most important for aluminide coatings or modified aluminide coatings because heat treatments can promote the transformation of  $\text{Ni}_2\text{Al}_3$  into NiAl phase which offers superior oxidation resistance [51].

Heat treatment media can also be a factor that influences coating properties. It has been demonstrated that the coatings treated in an argon atmosphere are less susceptible to cracking than the coatings treated in air [51].

### **2.3.2 Overlay Coatings**

Overlay coatings for the hot section components in gas turbine engines are usually referred to MCrAlY coatings, which can be fabricated using thermal spray processes, including air plasma spray (APS), high-velocity-oxy-fuel (HVOF) thermal spray, vacuum plasma spraying, low-pressure plasma spraying (LPPS), and cold spray (CP). These processes offer a significant advantage of flexibility in the composition of the coatings that can be deposited. However the disadvantage of these overlay processes is that they are impractical to coat internal diameter or deep groove.

Generally speaking, all these thermal spray processes can be used to produce overlay coatings; but only air plasma spray process (APS) is pertinent to this research and will be further discussed in detail.

#### **2.3.2.1 Air Plasma Spray Process**

Air plasma spray process is a coating deposition process in which molten, semi-molten or solid particles are deposited onto a substrate in air, with or without the protection of Ar. This process uses ionized gas to accelerate the particles and to heat them up at the same time. The temperature and velocity of the particles influence several key coating properties such as coating roughness, coating thickness, porosity

and the formation of cracks. Plasma spray process has the advantage of being able to deposit any material in the form of powder at a rate of 20-50  $\mu\text{m}/\text{min}$  [17].

A comparison between the air plasma spray process and the High Velocity Oxygen Fuel (HVOF) spray process can highlight an advantage of the plasma spray process (Figure 2.8). For HVOF spray process, the fuel (mainly acetylene) is burnt with oxygen under a high pressure and generates a high-velocity exhaust jet; and the particles reach the surface of the component through the exhaust jet. The main advantages of this process are a shorter residence time for the particles in flame and a higher kinetic energy of the particles; hence a denser coating can be created with fewer oxides [52]. However, as the temperature of the HVOF flame is much lower than that of the plasmas spray flame, HVOF process is limited to fabricate metallic coatings. Recently a novel air plasma spray device, the Mettech Axial III™ System, combines the advantages of regular APS and HVOF process and can produce much better metallic coatings as well as ceramic coatings.

#### **2.3.2.2 Mettech Axial III™ System**

A Mettech Axial III™ System employed in this research is a type of the air plasma spray apparatus. This system has a novel axial powder injection system, in which powder is carried through the center powder port and ejects co-axially with the plasma gases, while the conventional plasma spray system injects powder through the radial powder port (Figure 2.9).

A comparison of temperature and kinetic energy for conventional plasma spray, HVOF and Mettech Axial III™ System is illustrated in Figure 2.10. The advantages of

the Mettech Axial III™ system over conventional plasma spray system (radial powder injection) can be summarized as:

- full entrainment of powder in the plasma jet, which increases deposition efficiency [53]
- more thermal and kinetic energy, which enhances the density and adhesion between the coating and substrate, and reduces oxidation

The increased kinetic energy, however, shortens the dwelling time for particles in plasma gas and unmelted particles increase. Therefore the size of metallic powders should not exceed 100  $\mu\text{m}$ .

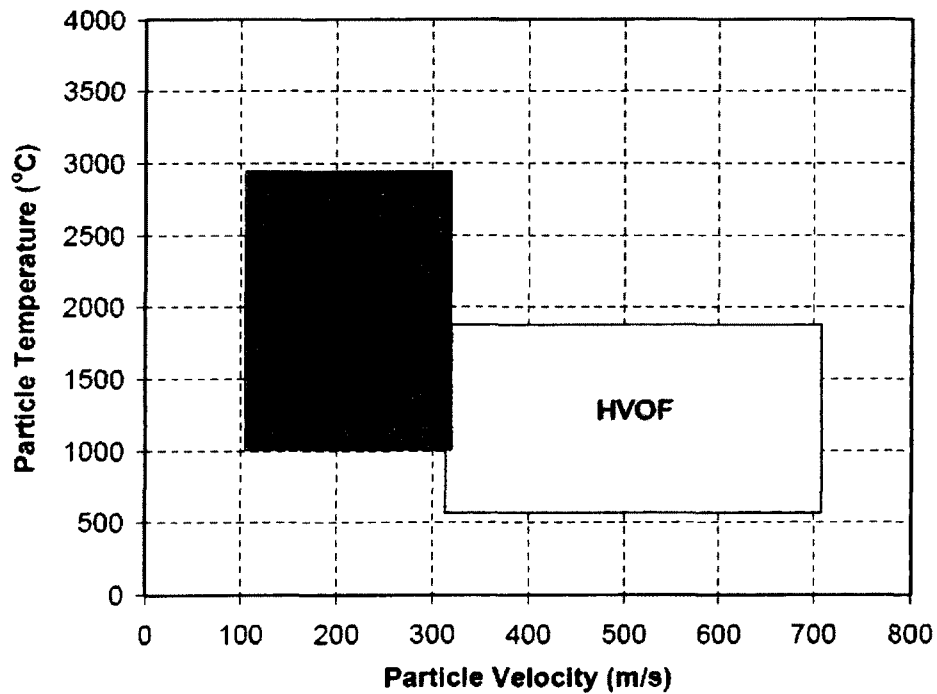
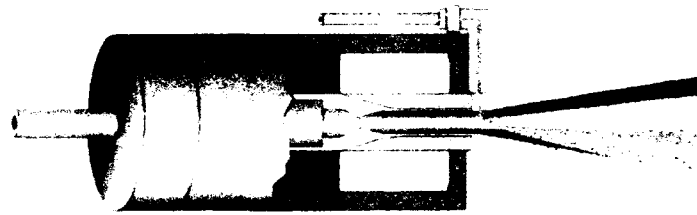
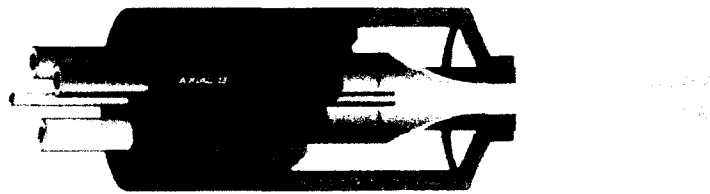


**Figure 2.8 Comparison of the temperature and velocity of particles in plasma spray and HVOF processes [54].**



Traditional Radial Plasma Gun



Axial III Plasma Gun

Figure 2.9 Configurations of traditional radial plasma gun and axial III gun [54].

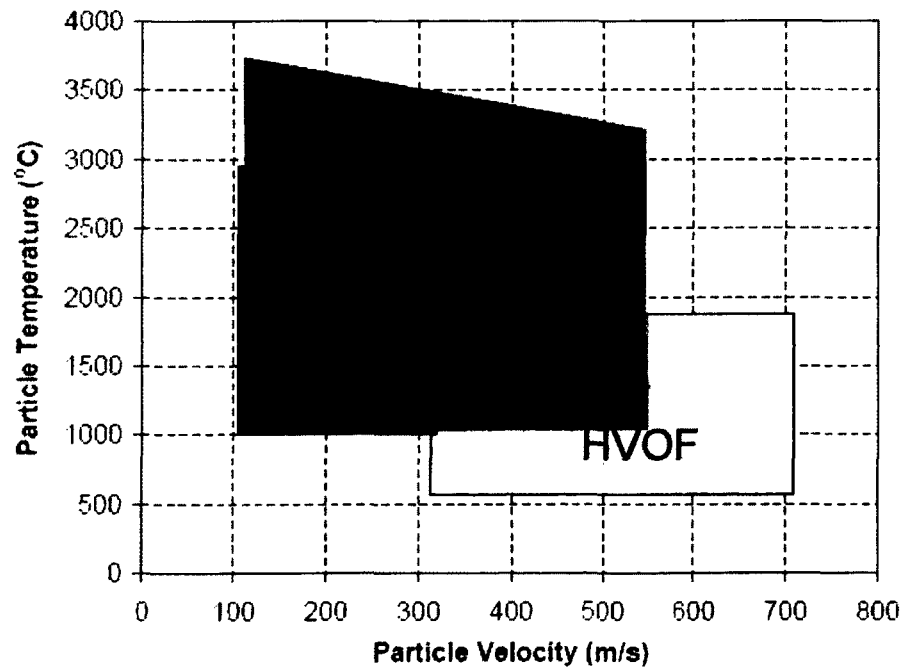
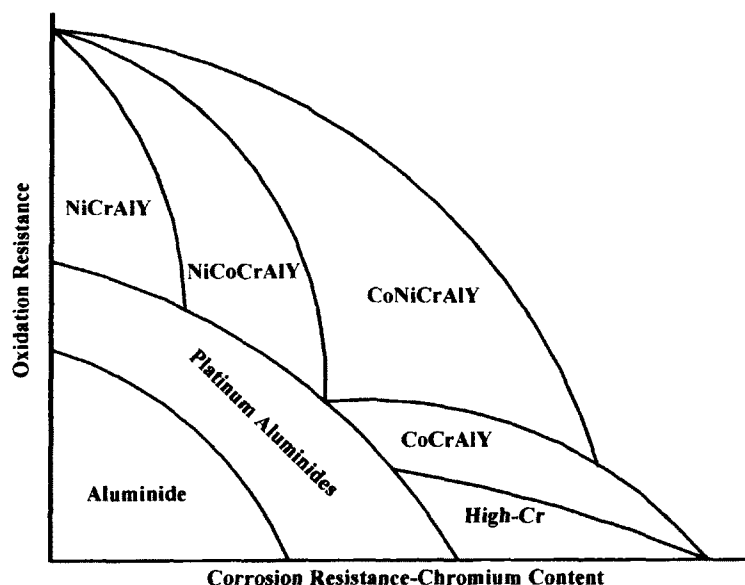


Figure 2.10 Comparison of temperature and velocity of particles in thermal spray systems [54].

### 2.3.2.3 Overlay Coating Compositions

Overlay coatings have the composition configuration of MCrAlX, where M = Ni, Co, Fe or a combination of these, and X = Y, Hf, Zr. The elements in the coatings are selected based on the requirements for the ductility and oxidation of the coatings. The composition ranges of common overlay coatings are typically 15-28 wt.% Cr, 4-18 wt.% Al, 0.5-0.8 wt.% Y with balance of Ni or Co [9].

The coatings with 18-22 wt.% Cr and 8-12 wt.% Al generally perform better at higher temperatures where oxidation is the dominant failure mode (above 900°C) [22]. Under high-temperature oxidizing conditions, NiCrAlYs and NiCoCrAlYs perform better than cobalt-based CoCrAlYs or CoNiCrAlYs, as illustrated schematically in Figure 2.11 [55].



**Figure 2.11 Relative oxidation and corrosion resistance of high-temperature systems [55].**

However, at relatively low temperatures (650-800°C) where hot corrosion predominates, CoNiCrAlYs and CoCrAlYs systems with high Cr (15-20%) usually outperform NiCrAlY-based systems [56, 57]. Therefore nickel-based systems should be used when oxidation is the major concern, whereas cobalt-based systems should be considered when hot corrosion must be coped with. For NiCrAlY coatings, aluminum and chromium are main elements contributing to the formation of protective oxide scales. Aluminum content is to balance the need for forming a continuous and adherent thermal growth oxide (TGO) with an adequate reservoir of aluminum and to prevent embrittlement with excessive aluminum [22]. To improve the adherence of the alumina scales, active elements such as Y are incorporated in these coatings in a small amount (less than 1 wt.%). NiCrAlY coatings with 18-22 wt.% Cr and 8-12 wt.% Al typically consist of a cubic  $\beta$  (NiAl) phase, a brittle  $\sigma$ -Cr phase and the  $\gamma'/\gamma$  matrix. Although yttrium is often observed in the oxides, it is also present at grain boundaries in the form of Ni<sub>5</sub>Y yttride [58].

The oxidation behavior of NiCrAlY coatings depends on various factors: alloy composition, temperature and exposure time. Higher chromium content significantly reduces the oxidation resistance of NiCrAlY, especially when the temperature exceeds 1100°C. Comparing the first coating and the third coating in Table 2.6, spallation occurs after 10 hr exposure at 1100°C for Amdry 962 coating (Ni-31Cr-11Al-0.6Y) [32], whereas spallation does not occur even after 100 hr at 1200°C for Amdry 964 coating (Ni-23Cr-11Al-1Y). Apparently higher chromium content at high temperatures leads to the formation of CrO<sub>3</sub> (gas), which is formed due to the oxidation of Cr<sub>2</sub>O<sub>3</sub> [59], and causes the spallation of the scales. More oxide protrusions, which results from the

formation of  $\text{Cr}_2\text{O}_3$ , are observed on the surface of Amdry 964 coating than on the Amdry 962 coating.

Also shown in Table 2.6 low aluminum content causes rapid coating failure at high temperatures (comparing the second coating and third coating in Table 2.6). At  $1200^\circ\text{C}$ , Ni-23Cr-6Al-0.4Y coating with 6 wt.% Al fails after 30 hr, whereas no spallation is found for Ni-22Cr-10Al-1Y with 10 wt.% Al after 100 hr. Some studies have indicated that increasing aluminum from 8% to 12 wt.% in MCrAlY coatings could significantly reduce the dissolution of NiAl in the substrate and diffusion zone since the high aluminum content in MCrAlY coatings acted an aluminum reservoir to replenish aluminum depletion in the subsurface and in the diffusion zone [60].

The effects of other alloying elements on the oxidation resistance of MCrAlY coatings have been reported as well. Yttrium, cerium, lanthanum, zirconium, and scandium significantly increase the oxidation resistance by improving the adhesion between the coating and the protective oxide [61]. Also, elements Re and Hf have been found to impede the diffusion between the coating and the substrate [62].

**Table 2.6 Oxides formed with temperature for MCrAlY coatings**

Coating	Process	Oxidation condition	Oxides	Time of scale spallation, hr
Ni-31Cr-11Al-0.6Y [32]	APS	1100°C, 5 hr	$\alpha\text{-Al}_2\text{O}_3$	No spallation
		1100°C, 50 hr	$\alpha\text{-Al}_2\text{O}_3, \text{Cr}_2\text{O}_3, \text{NiAl}_2\text{O}_4$	Spallation at 10
		1100°C, 100 hr	$\alpha\text{-Al}_2\text{O}_3, \text{Cr}_2\text{O}_3, \text{NiAl}_2\text{O}_4$	Spallation at 10
Ni-23Cr-6Al-0.4Y [63]	APS	1200°C, 10 hr	$\alpha\text{-Al}_2\text{O}_3$	No spallation
		1200°C, 100 hr	$\alpha\text{-Al}_2\text{O}_3, \text{Cr}_2\text{O}_3, \text{NiAl}_2\text{O}_4$	Spallation at 30
Ni-22Cr-10Al-1 [32]	APS	1200°C, 5 hr	$\alpha\text{-Al}_2\text{O}_3$	No spallation
		1200°C, 50 hr	$\alpha\text{-Al}_2\text{O}_3, \text{Cr}_2\text{O}_3, \text{NiAl}_2\text{O}_4$	No spallation
		1200°C, 100 hr	$\alpha\text{-Al}_2\text{O}_3, \text{Cr}_2\text{O}_3, \text{NiAl}_2\text{O}_4$	No spallation

#### **2.3.2.4 Heat Treatments of NiCrAlY Coatings**

The purpose of post-coating heat treatment on NiCrAlY coatings is to promote the formation of  $\gamma'/\gamma$  two-phase structure in NiCrAlYs since only meta-stable  $\gamma$  phase can be obtained in NiCrAlYs due to high cooling rate that is required for cooling melting particles during spraying [64]. Heat treatments can also help seal pores in the coatings [65, 66, 67] and release the residual stresses within the coatings. Consequently heat treatments can improve the adhesion between the coating and the substrate, and alter the behavior of oxide formation, which in turn improve the coating oxidation resistance. The NiCrAlY coatings without any heat treatment are prone to the formation of spinel-type oxides instead of pure  $\text{Al}_2\text{O}_3$  [68]. Heat treatments for NiCrAlY coatings are usually carried out at 1100°C for 3-5 hr in vacuum or in air followed by furnace cooling.

#### **2.3.3 Diffusion between Coating and Substrate**

##### **2.3.3.1 Synopsis**

In both MCrAlY and diffusion coatings, aluminum-rich phase serves as an aluminum reservoir for the formation of continuous, stable, and protective  $\text{Al}_2\text{O}_3$  scales. During high temperature exposure, aluminum content decreases with time due to the diffusion of aluminum toward the substrate, and meanwhile the elements from the substrate diffuse into the coating. Such a phenomenon is called interdiffusion. Previous studies have shown that interdiffusion may contribute more to the overall aluminum depletion [69, 70] than to oxidation and spallation. When aluminum concentration in the coating falls below 10 at.%, the coating can no longer maintain the continuity of alumina scale and thus lose its effectiveness. Furthermore, the diffusion of alloying elements from the substrate into the coating can be detrimental to the coating

performance. Figure 2.12 illustrates the diffusion directions of various elements [71]. Cr, Al and Co diffuse into the nickel based substrate, whereas Ni, Ti, W and Ta diffuse into the coating. In addition to aluminum depletion, Kirkendall voids also form in the diffusion zone, which is responsible for a substantial reduction in the coating strength and subsequent coating spalling. Large brittle precipitates are also found in the diffusion zone, increasing the tendency for crack formation and the rate of crack growth.

Considering the significance of diffusion in determining the lifetime of coatings, diffusion barrier layers have gained particular interest lately and will be further discussed in the next section.

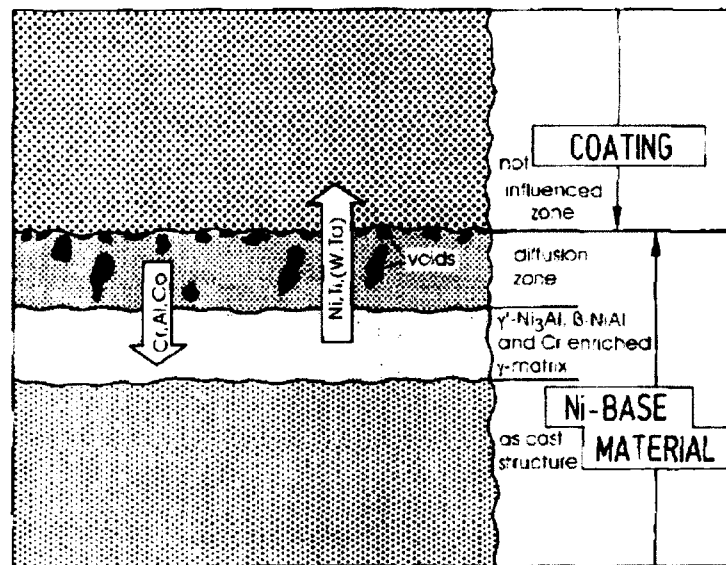


**Figure 2.12 Diffusion directions of elements in a Ni-based coating and substrate system [71].**

### 2.3.2.2 Diffusion Barrier

Applying a diffusion barrier actually is not a new concept since platinum in aluminide coatings has been regarded as a barrier to prevent aluminum diffusion. This

barrier greatly reduces aluminum depletion and accordingly improves oxidation resistance of the coatings. Basic requirements for the diffusion barriers are [71]:

- low diffusivity for elements in both coating and substrate and no change of properties to the coating and substrate
- low aluminum solubility in the diffusion barrier layers
- long durability at high temperatures with constant thickness
- capability of good adhesion between coating and substrate

Several diffusion barriers are described in Table 2.7. The assessment method for the effectiveness of a diffusion barrier usually is to examine the profiles of the elements in the coating and the substrate before and after oxidation testing. The weight gain/loss measurements help to characterize coating performance.

Current diffusion barriers fall into two groups: oxides (Al-O-N, Al<sub>2</sub>O<sub>3</sub>, Cr-O-N, ZrO<sub>2</sub>) [71, 72, 73, 74] and intermetallics [72, 73]. Ion-plated Al-O-N films exhibit excellent inhibition for diffusion of alloying elements between the coating and the substrate. The diffusion of aluminum and chromium into the substrate and cobalt, titanium and nickel into the coating is effectively retarded by these barrier coatings [71, 74]. However oxide barriers are reported to deteriorate the cohesion between the coating and the substrate due to the difference of thermal expansion coefficient between coatings and superalloys substrate, and to induce considerable residual stresses at the interface [75].

Most metallic diffusion barriers are M-Ni-(Cr) based alloys. M represents Re [76, 77], W [82], or Hf [78]. The barrier mechanism of these elements is that these elements form a layer that consists of phases with these elements such as  $\sigma$  phase (Re-Cr-Ni),

NW phase, and Ni<sub>3</sub>Hf phase; the layer containing one or more of these phases is reported to be an effective barrier for aluminum.

**Table 2.7 Diffusion barriers and their performance**

Coating	Process	Structure	Oxidation conditions	Diffusion or reaction
Al-O-N + MCrAlY [71]	RF sputtering	amorphous Al <sub>2</sub> O <sub>3</sub>	1100°C at 400 hr	No diffusion
			30 s at 1115°C at ambient up to 2500 cycles	No diffusion cycles
Al-O-N + NiCoCrAlY [62]	Arc ion plating	$\alpha$ -Al <sub>2</sub> O <sub>3</sub> + hexagonal - AlN	1050°C at 100 hr	Ti diffusion
			900°C at 1400 hr	Ti diffusion
Al-O-N + MCrAlY [79]	Magnetron sputtering ion plating	amorphous Al <sub>2</sub> O <sub>3</sub> or hexagonal AlN	1200°C at 4 hr	Reacted with Ti
			1100°C at 4 hr	No diffusion
$\gamma$ -Al <sub>2</sub> O <sub>3</sub> + MCrAlY [79]	Magnetron sputtering ion plating, annealing at 1100°C for 4h	$\alpha$ -Al <sub>2</sub> O <sub>3</sub>	1100°C at 4 hr	Ti diffusion
Cr-O-N + NiCoCrAlY [80]	Arc ion plating	Cr <sub>2</sub> O <sub>3</sub> + CrN	1050°C at 100 hr	No diffusion
			900°C at 1400 hr	No diffusion
$\sigma$ -Re-Cr-Ni + aluminide [81]	Electroplating Re, Cr-pack cementation, electroplating Ni, Al-pack cementation	Re-Cr-Ni	1200°C at 100 hr	No diffusion
			1100°C at 100 hr	No diffusion
Ni-W [82]	Electroplating W, electroless plating MCrAlY, Electroplating Pt, Al-pack cementation	W-Cr-Ni	850°C, Na <sub>2</sub> SO <sub>4</sub> At 2000 hr	No Al and Cr diffusion into substrate, W diffusion into MCrAlY, Cr diffusion into NiW

However, there are several drawbacks in these barriers. Chromium can easily penetrate through  $\sigma$  phase to the substrate and form a needle-like precipitation zone [77]; and this zone deteriorates the properties of the substrate. Although the barrier layer with NiW phase can act as a diffusion barrier for both aluminum and chromium, the presence of W-rich phase can result in a low adherence of the  $\text{Al}_2\text{O}_3$  scale [82]. The barrier layer with  $\text{Ni}_3\text{Hf}$  phase has limited high-temperature stability [78].

Recent studies have found the occurrence of self-formed Cr-rich layers when coatings contained aluminum and chromium underwent isothermal oxidation cycles [10]; and this layer almost did not dissolve any aluminum [11], which made this layer very promising being a barrier layer. However, the Cr-rich layer could not preserve required thickness and composition without careful control of the process parameters. Therefore one of the main objectives of this study is to obtain any self-formed Cr-rich layer with certain thickness and composition and to stabilize it during high temperature exposure.

### **2.3.4 Duplex Layer and Multilayered Coatings**

#### **2.3.4.1 Aluminized MCrAlY Overlay Coatings**

The stringent requirements for gas turbine coatings can seldom be met by using a single-layered coating. Therefore multilayered coatings have been developed for decades to accomplish the required roles. In a simpler form, duplex coatings are usually aluminized MCrAlY coatings [83]. The advantage of duplex coatings is that they provide better oxidation resistance due to extra aluminum reservoir from aluminide coating; and improved bonding strength of the coating and enhanced resistance to thermal fatigue from a more compliant inner layer. It has been demonstrated that the

service lives of duplex coatings are increased by a factor of 1.4 to 2 under high temperature oxidation condition, compared with single ones [84]. MCrAlYs in duplex coatings are usually produced by a plasma spray process, and an aluminizing process can be achieved by pack cementation or CVD [85]. CVD usually produces cleaner aluminized layer and longer cyclic lives.

Other duplex coating structures are also reported to offer better oxidation resistance [86]. An over-siliconizing MCrAlY with an outer layer of silicides exhibits improved oxidation resistance due to the formation of continuous SiO<sub>2</sub>.

#### **2.3.4.2 Multilayered Coatings**

One of well-known multilayered coatings is the smart coating that was designed to maintain a stable protective oxide and self-healing [26,87]. Both aluminum and chromium reservoirs were incorporated into the smart coating to compensate any active element depletion. This smart coating was produced using a combination of plasma spray and diffusion process. As illustrated in Figure 2.13, there are three coating layers in a smart coating, including an overlayer of a  $\beta$ -NiAl rich zone (A zone: outer aluminide diffusion layer) to provide high-temperature oxidation resistance and resistance to high-temperature hot corrosion, a chromium enriched region (B zone: chromium-rich layer by HVOF) midway through the coating, which limits low temperature hot corrosion attack, and a standard NiCrAlY overlay coating (C zone: Co-32Ni-21Cr-8Al-0.5Y layer by argon-shrouded plasma spraying).

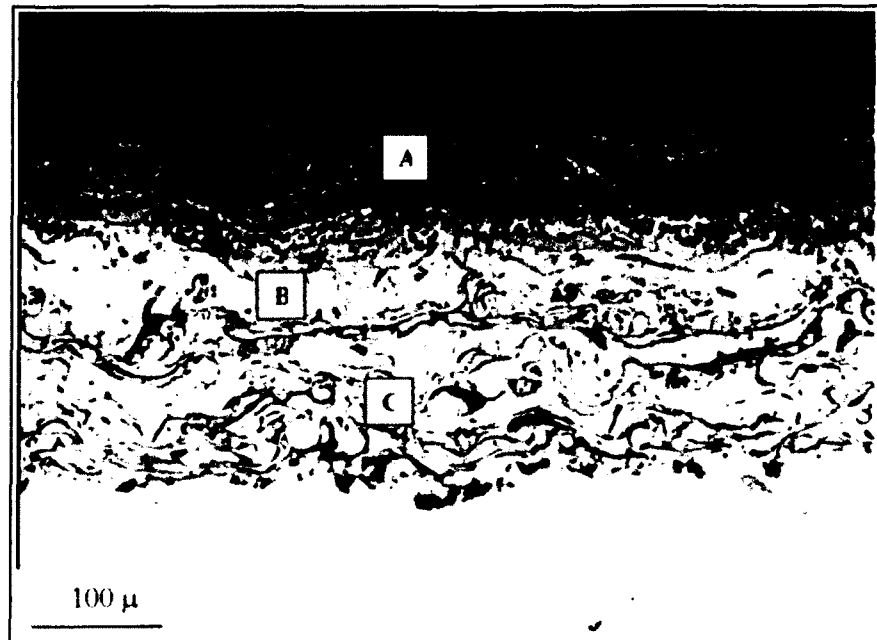


**Figure 2.13 Micrograph of a smart coat showing the three-layer microstructure [26].**

#### **2.4 Design of Experiments Methodology**

As the optimization of a coating microstructure requires a full control of the numerous operating parameters, design of experiments (DOE) may provide a useful tool for the process development and later on the interpretation of the results. DOE methodologies used in the past to optimize the air plasma coating process can be categorized into the following groups [88, 89,90]:

- two-level full factorial designs
- two-level fractional factorial designs
- response of surface methodology (RSM) designs
- Taguchi method

### 2.4.1 Two-Level Full Factorial Design

A two-level full factorial design is the design in which two settings of every factor appear with every setting of every other factor. Two-level factorial designs are used when interactions between factors are considered [91]. The performance characteristic or the properties of products (responses) can be represented as a polynomial equation (regression equation) of following form [88]:

$$Y = b_0 + \sum b_i X_i + \sum b_{ij} X_i X_j + \sum b_{ijk} X_i X_j X_k \quad (2-1)$$

where  $i, j, k$  vary from 1 to the number of variables; coefficient  $b_0$  is the mean of responses of all the experiment;  $b_i$  coefficient represents the effect of the variable  $X_i$ , and  $b_{ij}, b_{ijk}$  are the coefficients of regression which represent the effects of interactions of variables  $X_i X_j, X_i X_j X_k$  respectively. The regression coefficient is half of the effect estimate [91]. The magnitude and direction of the factor effects on the performance characteristic are based on the sign and magnitude of the regression coefficient of the factor. Another way to examine the factor effects on the performance characteristic is to evaluate the response surface and contour plot obtained from the regression equation. If the interaction terms are in the regression equation the response surface is a curve plane and the contour lines of constant value are curved as well (Figure 2.14) [91]. Full factorial designs are not recommended when 5 or more factors are involved because of large numbers of the combinations of the setting for all factors.

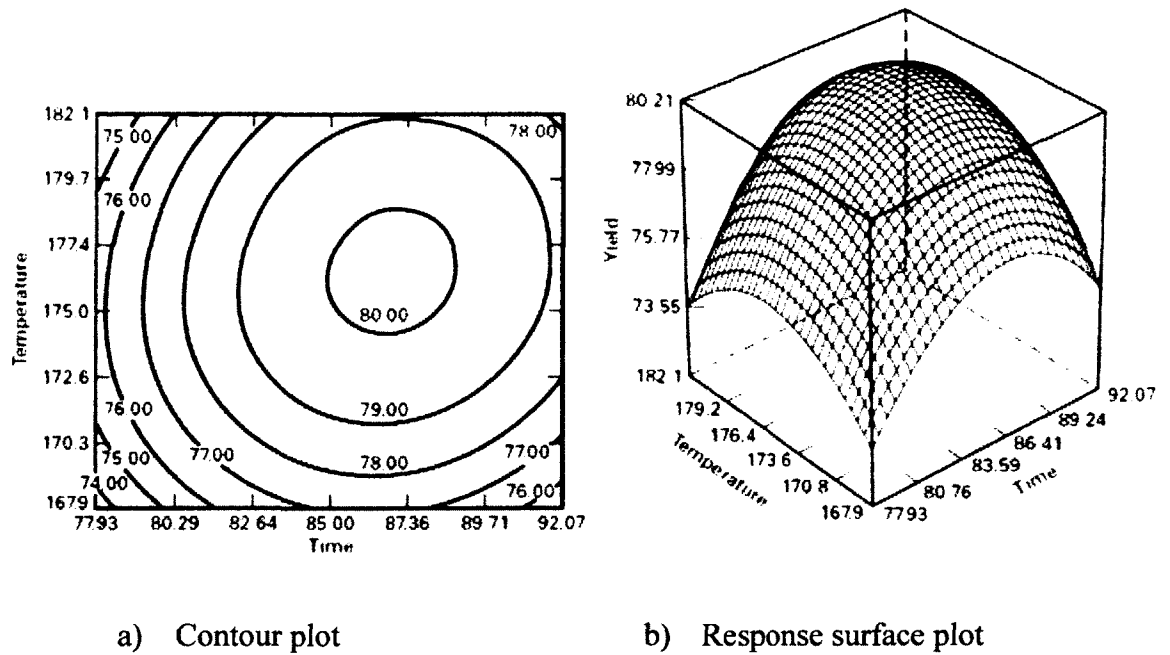


**Figure 2.14 An example of the response surface and contour plot [91].**

### 2.4.2 Two-level Fractional Factorial Design

The purpose of the fractional factorial design is to extract part of experiments from the full factorial design, which enables the realization of main effects of variables. For example, a complete  $2^5$  design requires 32 runs, and only 5 of the 31 degrees of freedom correspond to the main effects, and only 7 degrees correspond to two-factor interactions; therefore, there are only 12 degrees of freedom associated with the effects that are likely to be of major interest. The remaining 19 degrees of freedom are associated with three-factor and higher interactions, which are sometime reasonably assumed to be negligible. Therefore these interactions have to be confounded with blocks and only the blocks with the factors of major interest are investigated. For example, a  $2^2$  design with 4 treatment combinations and two main effects and an interaction is given in Table 2.8, and 4 treatment combinations, (1),  $a$ ,  $b$ , and  $ab$ , are confounded into two blocks. There is an identity column  $I$ , which is always plus. In the

design, the defining relation for confounding is  $I = AB$ , which means the combinations with the plus sign [ $ab$  and  $(1)$ ] are in block 1 and the combination with the minus sign ( $a$  and  $b$ ) are in block 2.  $AB$  is called the generator of this fraction. Only block 2 is investigated if the high order interaction ( $AB$ ) is negligible. The generators should be carefully chosen so that the estimates of main and interaction effects cannot be neglected [91].

**Table 2.8  $2^2$  design with 4 treatment combinations and two main effects and one interaction**

Treatment combination	Factorial effect				Block
	$I$	$A$	$B$	$AB$	
$(1)$	+	-	-	+	1
$a$	+	+	-	-	2
$b$	+	-	+	-	2
$ab$	+	+	+	+	1

The effects of each factor on the performance characteristic are analyzed based on the regression equation from the design and the response surface and contour plot obtained from the regression equation. However, some terms in the regression equation are eliminated due to confounding.

### 2.4.3 Response Surface Methodology (RSM)

Response surface designs are applied when the relationship between the response and factors is not linear and a RSM design must be used to determine quadratic or cubic terms. Therefore a regression equation for RSM includes quadratic or cubic terms beside linear and interaction terms [92]:

$$Y = b_0 + \sum b_i X_i + \sum b_{ii} X_i^2 + \sum b_{iii} X_i^3 + \sum b_{ij} X_i X_j + \sum b_{ijk} X_i X_j X_k \quad (2-2)$$

The regression coefficients in the regression equation are estimated using the method of least squares. If the response is well modeled by a linear function of the independent variables, then the function will be considered to be the first-order model. If there is a curvature in the system, then a polynomial of higher order, such as the second-order model and the third-order model, must be used.

The response surface analysis is then performed using the fitted surface (fitted model). If the fitted surface is an adequate approximation of the true response function, the analysis of the fitted surface will be approximately equivalent to the analysis of the actual system. Designs for fitting response surfaces are called response surface designs. The most common methods for response surface designs are the Box–Behnken design and the central composite design [88]. A Box–Behnken design is formed by combining  $2^k$  factorials with incomplete block designs, which includes all middle points of the edges of the  $k$  factors cube and no points at the vertices of the cubic (Figure 2.15a). The Box–Behnken design is also called a spherical design since all points lie on a sphere. A central composite design (CCD) consists of a  $2^k$  factorial with  $2k$  axial runs, and some center runs (Figure 2.15b).

The analysis of a fitted model to find the optimum set of operating conditions for the factors includes [92]:

- 1) Finding some special points such as the maximum point, the minimum point, or the saddle point
- 2) Constructing and evaluating response surface and contour plots
- 3) Optimizing multiple responses by overlaying the contour plots

#### 2.4.4 Taguchi Method

Taguchi method is a statistical technique developed by Genichi Taguchi to improve the quality of manufactured goods, and more recently found wide applications in process design and optimization [93]. One of the advantages of using Taguchi method in process optimization is to minimize experimental runs using saturated fractional factorials for two-level screening designs or three-level designs. Another advantage is that Taguchi method has proposed the Signal-to-Noise ratio (SNR) to optimize a process. The process is optimized by controlling the factors that maximize the Signal-to-Noise ratios.

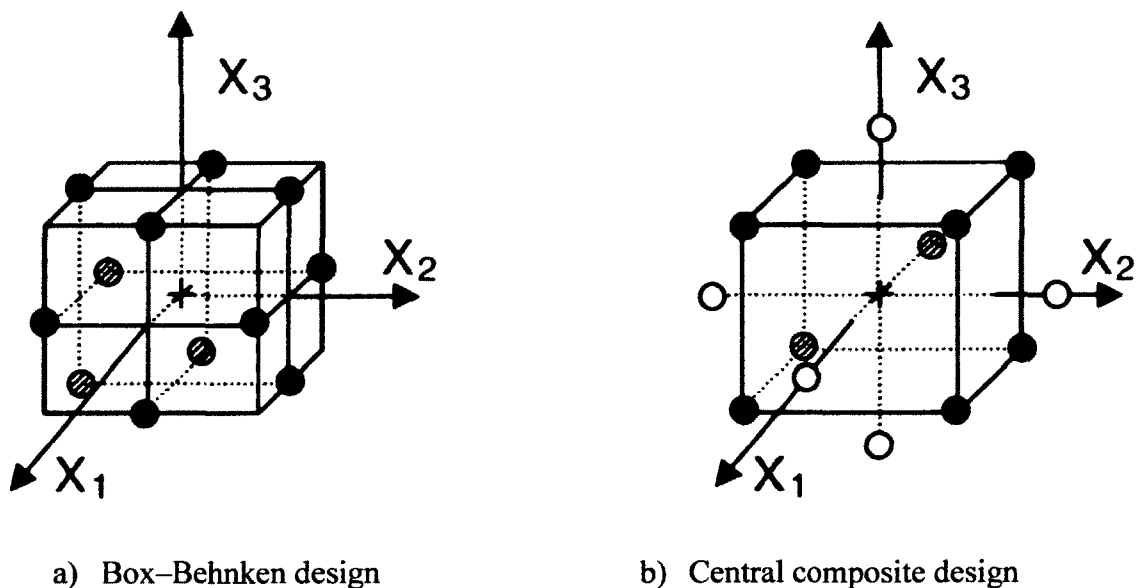


**Figure 2.15 Graphical representations of the Box-Behnken and central composite design [88].**

##### 2.4.4.1 Taguchi Arrays

All Taguchi arrays are orthogonal and most of Taguchi arrays are saturated. An orthogonal array is a matrix in which its transpose is equal to its inverse; a fractional factorial design is saturated if the number of treatment combinations is equal to that of

parameters in the model to be estimated. All two-level designs, such as L4, L8, L12, L16 and L32, are saturated [93]. The advantage of using saturated fractional factorials is to that this method can minimize experimental runs. For example, a process with 7 variables, each with 2 levels, would require 128 ( $2^7$ ) experiments to test all variables in a full factorial design. However using Taguchi's saturated fractional factorials, only 8 experiments are necessary. This allows for the identification of key parameters that have the most effect on the performance characteristic value so that further experimentation on these parameters can be performed while the parameters which have little effect can be ignored.

#### 2.4.4.2 Signal-to-Noise Ratio

The Signal-to-Noise ratio is defined as: [94]

$$SN = 10 \log \frac{\bar{y}_i^2}{s_i^2} \quad (2-3)$$

where  $\bar{y} = \frac{1}{N} \sum_{u=1}^{N_i} y_{i,u}$ ;  $s_i^2 = \frac{1}{N_i-1} \sum_{u=1}^{N_i} (y_{i,u} - \bar{y}_i)^2$ ;  $\bar{y}$  is the mean of measured results;  $y_{i,u}$  is a measured result;  $s_i$  is the variance;  $i$  is experiment number;  $u$  is trial number;  $N_i$  is the number of trials for experiment  $i$ . There are three Signal-to-Noise ratios of common interest for process optimization: normal-the-best, smaller-the-better, and larger-the-better.

##### (1) Normal-the-best

This case arises when an ideal response varies around a setting target level, meaning that neither a smaller nor a larger value is desirable. The equation for this case is equation (2-3).

##### (2) Smaller-the-better

This applies to cases where an ideal response is zero, meaning that this is usually the SNR for all undesirable characteristics such as pores, cracks etc. In the case of minimizing the undesirable characteristics, the following definition of the SN ratio should be calculated [94]:

$$SN = -10 \log \left( \sum_{u=1}^{N_i} \frac{y_u^2}{N_i} \right) \quad (2-4)$$

where  $y_u$  is a measured result. Also, when an ideal value is finite and its maximum or minimum value is defined, then the difference between measured data and ideal value is expected to be as small as possible. The equation of SNR then becomes [94]:

$$SN = -10 \log \left( \sum_{u=1}^{N_i} \frac{(y_u - y_l)^2}{N_i} \right) \quad (2-5)$$

where  $y_l$  is the ideal value.

### (3) Larger-the-better

In this scenario, an ideal response is required to reach the maximum, meaning that this is usually the SNR for all desirable characteristics such as oxidation resistance, corrosion and wear resistance. To maximize the desirable characteristics, the following equation of the SN ratio should be applied [94]:

$$SN = -10 \log \left( \frac{1}{N_i} \sum_{u=1}^{N_i} \frac{1}{y_u^2} \right) \quad (2-6)$$

#### 2.4.4.3 Disadvantage of Taguchi

One disadvantage of the Taguchi method is that the SNRs are only relative and cannot exactly determine the highest effect on the performance characteristic value by parameters [95]. Also, as orthogonal arrays do not test all variable combinations, Taguchi method has no scope for estimation of interactions between parameters; therefore this method should not be used to examine the relationships between all

variables [95], and the performance characteristic is represented by a simple first order polynomial.

#### **2.4.4.4 Procedure of Taguchi Method**

Taguchi proposed a standard 8-step procedure for applying his method for optimizing any process [94]:

- (1) Identification of the main function, side effects, and failure mode
- (2) Identification of the noise factors, testing conditions, and quality characteristics
- (3) Identification of the objective function to be optimized
- (4) Identification of the control factors and their levels
- (5) Selections of the orthogonal array
- (6) Conduct of the experiment
- (7) Analysis of the data and prediction of the optimal levels
- (8) Verification of the experiment

In summary, the process optimization follows 8-steps of planning, conducting and evaluating results of array experiments to determine the best levels of control factors. Orthogonal arrays are used to determine the best levels of control factors. The best levels of control factors are those that maximize the Signal-to-Noise ratios. Three Signal-to-Noise ratios are used to optimize a process. The optimized process is the process with the maxim Signal-to-Noise ratio.

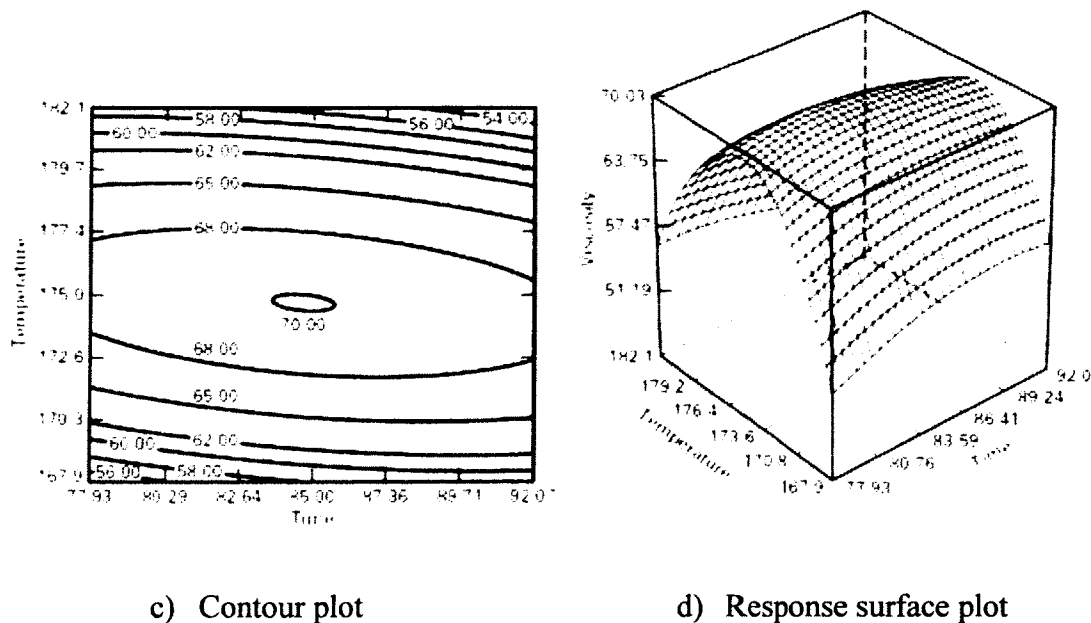
#### **2.4.4.5 Optimization of Several Responses**

An approach to optimizing several responses is to overlay the contour plots for each response and to figure out the regions that are of common interest for all response. For example, in a chemical process optimization, the operating conditions that maximize

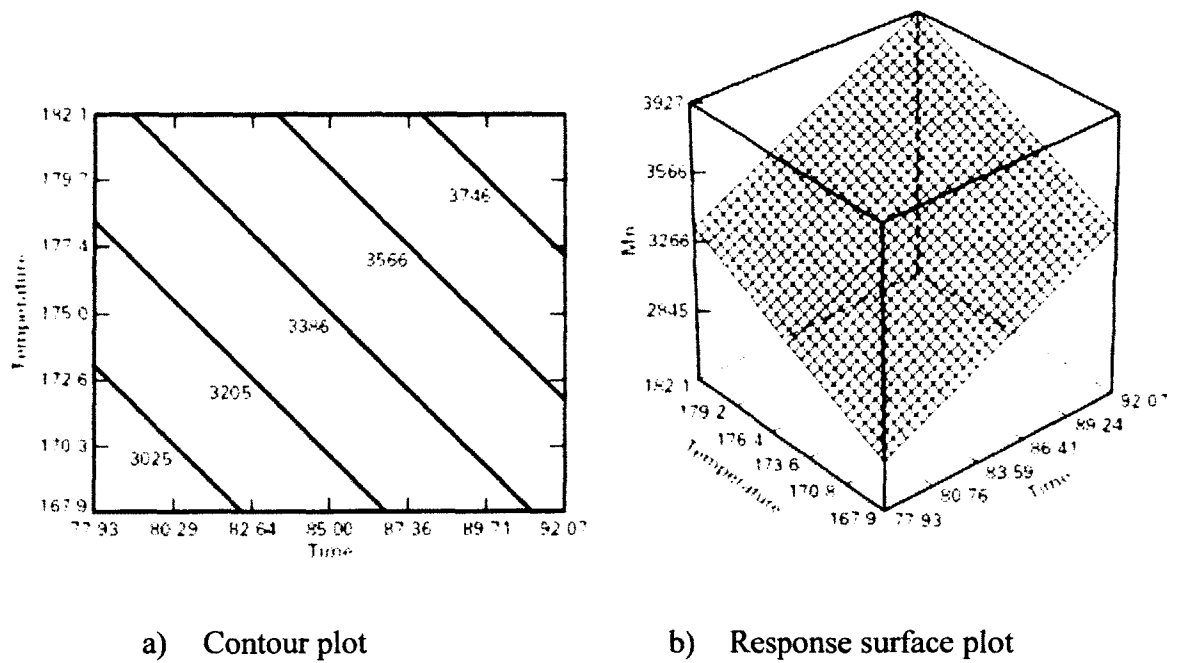
the yield of a process are of interest. Other responses in this case are the viscosity and the molecular weight (Mn) of the product. Two controllable variables are reaction time and reaction temperature. The response surface and contour plots for the yield, viscosity, and molecular weight are illustrated in Figure 2.14, Figure 2.16 and Figure 2.17, respectively.

Figure 2.18 shows an overlay plot for the three responses with contours for the conditions:  $78.5 < \text{yield}$ ,  $62 < \text{viscosity} < 68$ , and  $\text{molecular weight} < 3400$ . The unshaded portion of Figure 2.18 shows the combinations of time and temperature that result in a satisfactory outcome.

Another approach to optimizing several responses is to use a global desirability to incorporate the desirability factor of all responses; the global desirability is geometrical mean value of the desirability factors. Determination of the maximum point of the global desirability is a way to optimize several responses simultaneously [88].



**Figure 2.16 Response surface and contour plots for the viscosity [91].**



**Figure 2.17 Response surface and contour plots for molecular weight [91].**

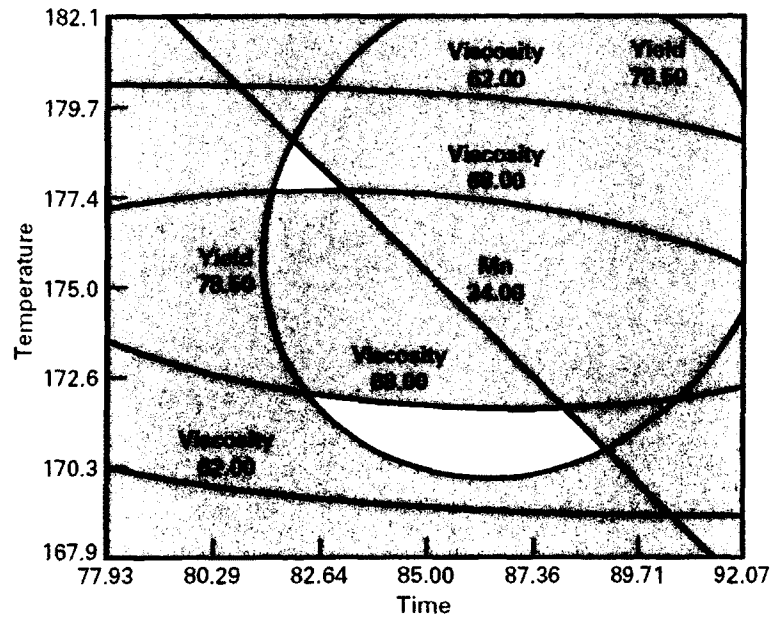


**Figure 2.18 Overlay plot for the three responses [91].**

#### 2.4.5 Analysis of Variance (ANOVA) Table

An effective regression equation should meet the following requirements [96]: a high confidence level, the effectiveness of the regression equation, and error prediction.

The confidence level could be determined from the Fisher value of the regression equation. Fisher value of the regression equation can be calculated using the following equation [97]:

$$F_0 = \frac{MS_T}{MSE} \quad (2-7)$$

where  $MS_T$  is the treatment mean square, and  $MSE$  is the residual mean square. If the Fisher value ( $F_0$ ) of the regression equation is larger than the threshold  $F$  value,  $F(m, n, 1 - \alpha)$ , its confidence level would be higher than  $1 - \alpha$ , where  $m$  is the freedom of the regression equation,  $n$  is residual degrees, and  $\alpha$  is the critical value for an  $F$  distribution, which is usually set 0.05. The threshold value,  $F(m, n, 1 - \alpha)$ , can be found in most statistics computational resources when the numerator ( $m$ ), denominator ( $n$ ) and  $\alpha$  values are given [98]. The  $p$ -value of the regression equation can be calculated if  $F_0$ ,  $m$ , and  $n$  are known. If  $p$ -value of the regression equation is less than 0.05 ( $\alpha$ ), the regression equation is significant. The  $p$ -value of factors and their interactions can also be calculated if the  $F_0$  values of the factors and their interactions are known. Similarly if  $p$ -value of a factor is less than 0.05 ( $\alpha$ ), the factor is considered significant.

The effectiveness of a regression equation can also be determined by the coefficient of determination,  $R^2$ , of the regression equation [93,99]. This coefficient describes the percentage of the response variation that the equation can account for, i.e., it is a statistical measure of how well the regression line approximates the real data points. The general acceptable value of  $R^2$  is 75% [93].

A proper prediction of error should be consistent with the reliability of the experimental data, i.e., the error should be within certain confidence interval of the experimental data. It can be measured by the residual mean square value. If the process

parameters are  $X_1$ ,  $X_2$ ,  $X_3$  and  $X_4$ , there would be a probability of  $1 - \alpha$  that the predicted response function is among  $F(X_1, X_2, X_3, X_4) \pm 2 \times (\text{residual mean square})^{1/2}$  [96]. The confidence intervals of the measured data at  $1 - \alpha$  confidence level are calculated by the following formula:

$$F(X_1, X_2, X_3, X_4) = \bar{F} \pm t(1 - \alpha/2, n) \times \sqrt{MSE} \quad (2-8)$$

where  $\bar{F}$  is mean value of response functions,  $t(1 - \alpha/2, n)$  is 100  $(1 - \alpha/2, n)$  percentile of the  $t$  distribution with  $n$  degrees of freedom, and  $MSE$  is residual mean square.

An analysis of variance (ANOVA) table provides all values that are needed to determine the effectiveness of a regression equation for a response. Table 2.9 is an example of the ANOVA table of the chemical process described in section 2.4.5 [91]. The  $p$ -values for the regression equation (model) and all terms except the interaction term  $AB$  are much less than 0.05, therefore the regression equation and all terms except  $AB$  are significant. The  $AB$  term should be eliminated from the regression equation based on its  $p$ -value.

**Table 2.9 ANOVA table of the yield for the example in section 2.4.5 [91]**

Source	DOF	Sum of squares	Mean square	$F$ value	$Prob > F$
Model	5	28.25	5.68	79.85	<0.0001
<i>A, Time</i>	1	7.92	7.92	111.93	<0.0001
<i>B, Temperature</i>	1	2.12	2.12	30.01	0.0009
$A^2$	1	13.18	13.18	186.22	<0.0001
$B^2$	1	6.97	6.97	98.56	<0.0001
$AB$	1	0.25	0.25	3.53	0.1022
Residual	7	0.50	0.071		
Lack of fit	3	0.28	0.094	1.78	0.2897
Pure error	4	0.21	0.053		
Total	12	28.47			
$R^2$		98.28%			

A lack of fit output appears in the variance table. If the  $p$ -value is greater than 0.05 ( $\alpha$ ), it is concluded that there is not enough evidence at given  $\alpha$  level to support that there is a lack of fit. In this example case, the  $p$ -value of the lack of fit is 0.2897, which suggests that the regression equation fits results well. The  $R^2$  at 98.28% confirms the fitness of the regression equation.

As with most of the statistical analysis methods, analysis of variance is based on several assumptions, including that the errors are normally and independently distributed with zero mean; therefore examination of the residuals, which represent errors in a regression equation, should be an imperative part of analysis of variance. A verification of the normality assumption can be made by plotting the normal probability of the residuals. If the residual distribution is normal, this plot will resemble a straight line (Figure 2.19) [92].

Unfortunately, with the small amount of samples, a considerable fluctuation around the straight line often occurs; therefore, a moderate departure from the straight line does not necessarily mean a serious violation of the normality assumption. Substantial deviations from the straight line are a cause for concern [92]. A check of the independence assumption can be made by plotting the residuals versus the fitted (predicted) values. If the model is correct and the independence assumption will be satisfied, the plot of the residuals versus the fitted (predicted) values should not reveal any obvious pattern.

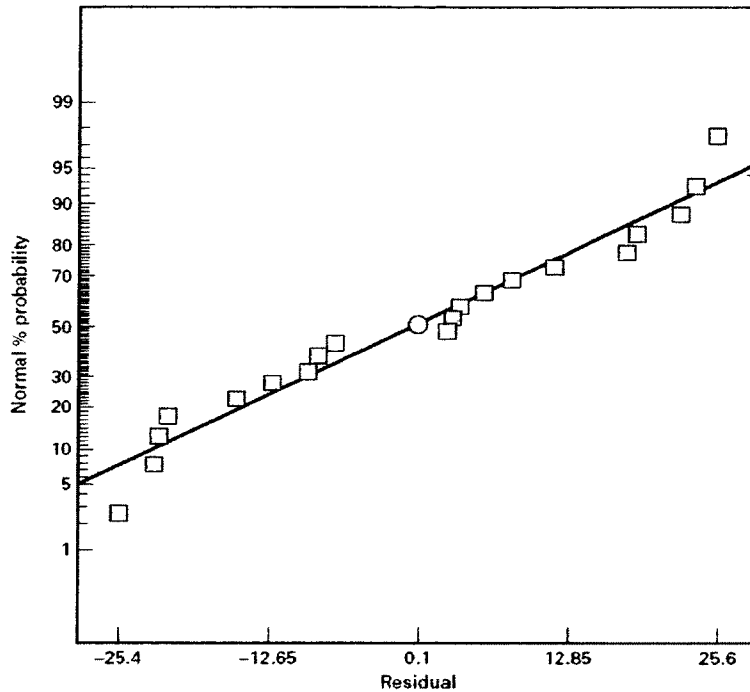


**Figure 2.19 Normal probability plot of residuals [91].**

## 2.5 Summary of Literature Review

Despite the progress in coating development, the necessity of advanced coating systems for hot section gas turbine components continues to be the top priority in various high-temperature material projects due to the ever increasing RITs [100]. The higher RITs accelerate the oxidation of coatings [101]. The advanced coating systems with increased resistance to high-temperature oxidation will rely on the microstructure stability of the coating and the superalloy substrate, especially in terms of reducing the effects of diffusion on the stability of the alloy microstructure and the life of the coating. These requirements call for significantly different composition and microstructure designs from modern gas turbines.

In this research, multilayered coatings will be developed to achieve better high-temperature oxidation resistance compared to the existing coatings, and the outcomes

of this research are expected to provide a new coating system and associated coating processes.

## Chapter 3: Coating and Process Design

### 3.1 Design of Multilayered Coatings

Aluminum forms a protective scale on coating surface upon reacting with oxygen, which protects the coating and substrate from further oxidation. However, aluminum eventually exhausts because of two reasons: diffusion of aluminum into the substrate and the formation of new alumina scale due to the spallation of existing oxide scale. Therefore the strategy used to improve oxidation resistance is to prevent aluminum from diffusing into the substrate and to increase aluminum content in the coating (Figure 3.1).

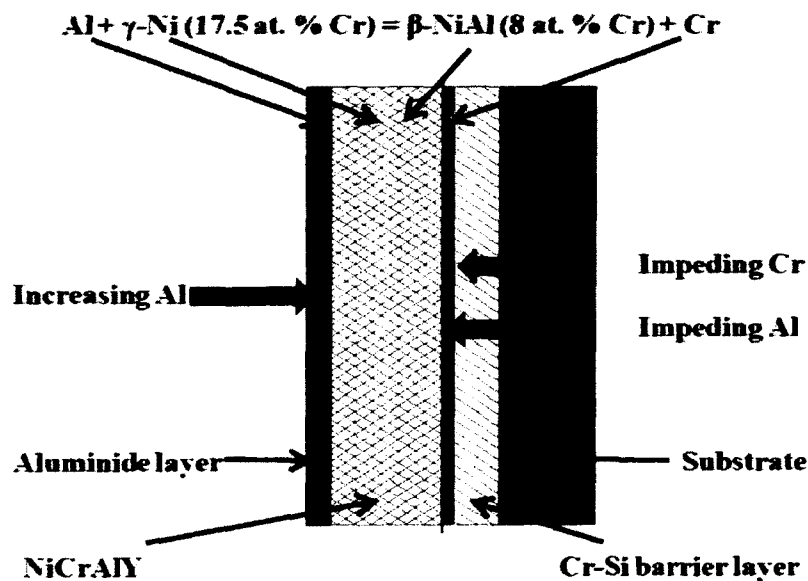


**Figure 3.1 Strategy to improve oxidation resistance of a coating.**

The common approach to impede aluminum diffusion in a coating is to apply a diffusion barrier between the coating and the substrate. The diffusion barriers could be aluminum and chromium oxides or Ni based intermetallics. The top coatings are usually aluminide and MCrAlY. Previous research indicates that when the top layer is

the Al-rich phase, a Cr layer can form because of the oxidation of the Al-rich phase and the transition of the  $\beta$  phase; this Cr layer hardly contains aluminum [11]. This phenomenon suggests that a Cr layer can be artificially made to impede aluminum diffusion.

Therefore this research is to develop a coating system that can self-form a Cr layer during coating process or exposure at high temperatures. There are two approaches to obtain a Cr-layer. One is to oxidize a Cr contained coating that consists of the Al-rich phase to form the Cr layer. Another approach is to aluminize a Cr contained coating to promote  $\beta$  phase transition and Cr atom release. No matter which approach is employed, a Cr contained coating and an aluminized layer on the coating are required. When the Cr contained coating is aluminized, the Cr-layer forms in the coating to impede aluminum diffusion, and another layer is needed to prevent Cr from diffusing into the substrate. Therefore a three-layer structure is necessary to achieve these goals: an Al-rich top layer to provide sufficient aluminum and to promote chromium release; a  $\gamma$  phase middle layer with high chromium content to provide chromium atoms, and a bottom layer to prevent chromium from diffusing into the substrate.

Apparently an aluminized layer is the best candidate for the top layer; the NiCrAlY coating was selected since the chromium content in NiCrAlYs is easily manipulated. The bottom layer should consist of a chromium containing intermetallics and be very stable at high temperature. The isothermal phase diagram of the Si-Cr-Ni ternary system at 1050°C [102], shown in Figure 3.2, indicates that a  $\psi$ -phase ( $\text{Cr}_2\text{Ni}_3\text{Si}$ ) exists within the composition range of 20-30 at.% Si and 50-60 at.% Cr at 1050°C. At 900°C, the composition ranges of the  $\psi$ -phase ( $\text{Cr}_2\text{Ni}_3\text{Si}$ ) hardly substantially diminish, which

suggests that the  $\psi$ -phase has good stability between 900 °C and 1050°C. As such, a chromium and silicon-rich barrier layer was considered in this study as a diffusion barrier.

A Cr-Si co-deposition using the pack cementation process was selected based on its simplicity and the popularity in industry. The NiCrAlY coating was produced by atmospheric plasma spray with a Mettech Axial III™ System. Following plasma spraying, the aluminum-rich top coat was deposited using the pack cementation process. A summary of the processes for the multilayered coatings is shown in Table 3.1.

A diffusion coating could also be produced using slurry. The disadvantage of using slurry is a need for application of the slurry by hand. It causes uneven coatings on a specimen surface. The variation in thickness between the specimens of one batch is usually 20 to 50  $\mu\text{m}$  [103]. Such variation is too large for the most diffusion coatings that are usually around 100  $\mu\text{m}$  thick in this study. Therefore all diffusion coatings in this study are produced using pack cementation process.

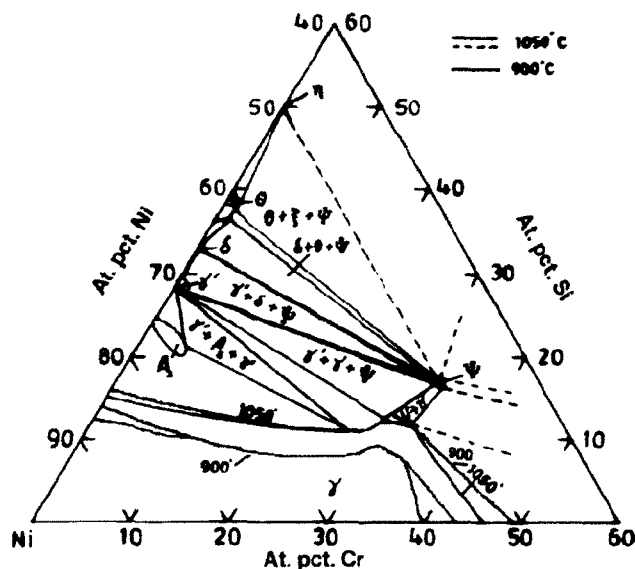


Figure 3.2 Phase diagram of a Si-Cr-Ni ternary system [102].

**Table 3.1 Processes for the multilayered coating**

Layer	Diffusion barrier	NiCrAlY	Top layer
Composition	Cr-Si	Ni-22Cr-10Al-1Y	Aluminizing
Process	Pack cementation	Atmospheric plasma spray	Pack cementation

The composition ranges of each layer in the multilayered coatings are summarized in Table 3.2. For multilayered coating I and II, 20-30 at.% Cr and 20-30 at.% Si in the diffusion barrier were targeted; 20-30 at.% Cr plus the chromium released from the NiCrAlY layer ensured sufficient chromium to form a chromium and silicon-rich  $\psi$  phase layer. The NiCrAlY coating with about 10 wt. % Al and 20 wt. % Cr was used as the intermediate layer. For the top aluminized coating, the concept of the Al/Ni ratio was proposed for control the aluminum content in the aluminized layer. The Al/Ni ratios for multilayered coating I and multilayered coating II are 1 and 2 respectively. The Al/Ni ratio at 1 promotes  $\beta$  phase transition to form a Cr layer in multilayered coating I during aluminizing process. The Al/Ni ratio at 2 promotes the formation of the Al-rich phase in multilayered coating II during aluminizing process, and the Al-rich phase is oxidized during oxidation tests to form a Cr layer. The substrate for all multilayered coatings is IN738.

**Table 3.2 Compositions of key elements for various layers of multilayered coatings**

Layer	Diffusion barrier	NiCrAlY	Al/Ni ratio in top layer	Substrate
Multilayered coating I	20-30 at.% Cr, 20 - 30 at.% Si, bal. Ni	Ni-22Cr-10Al-1Y (17.5 at.% Cr, 15.4 at.% Al)	1	IN738
Multilayered coating II			2	

## **3.2 Coating Process Optimization**

### **3.2.1 Plasma Spray Process Optimization**

The Taguchi method was used to optimize plasma spray process, and the target of the optimization of the plasma spray process was to obtain NiCrAlY coatings with the fewest number of pores, unmelted particles and oxides, and with no cracks. The typical parameters of a plasma spray process are as follows:

- powder size
- current
- flow rate and composition of working gas
- spray distance
- nozzle size

Two Taguchi arrays were introduced and two sets of experiments for NiCrAlY coatings were conducted to determine the influence of these parameters on the coating microstructural features. Regression equations for predicting the microstructural features of NiCrAlY coatings were developed based on the experimental results.

### **3.2.2 Pack Cementation Process Optimization**

The response surface methodology was employed to optimize the aluminum content and nickel content in the pack powder mixture, and process temperature so that the coatings with the expected Al/Ni ratios were obtained. The typical parameters for a pack cementation process are as follows:

- the composition of a pack powder mixture
- process temperature
- process duration

- atmosphere

The optimization of the aluminizing process was implemented by controlling the aluminum activity during diffusion process, and the aluminum activity was associated with the aluminum content and nickel content in the pack powder mixture, and process temperature. The target of the optimizations of the aluminizing processes was to obtain aluminized coatings with Al/Ni ratios at 1 and 2.

A Taguchi array was used for Cr-Si co-deposition process to optimize the chromium content and silicon content in the pack powder mixture, and process temperature so that the coatings with the expected compositions were obtained. The target of the optimizations of the Cr-Si co-deposition process was to obtain Cr-Si coatings with 20-30 at.% Cr, 20 -30 at.% Si. Argon purging was used for all process settings.

### **3.3 Coating Characterization**

All coating specimens were characterized to investigate the effects of deposition processes on the coating microstructural features and properties. For diffusion coatings, the thicknesses, compositions, phases, and elemental distributions are essential for the coating characterization. For NiCrAlY coatings, coating thickness, formation of oxide, pores, and occurrence of cracks and unmelted particles were examined. The methods that were used to characterize the coatings include:

- measurements of coating thickness, the percentage of pores, cracks, oxides, and unmelted particles using an optical microscope with image analysis software
- mapping of elemental distributions in various layers of the coating structures using energy dispersive spectroscopy (EDS)
- identification of phases in the coatings using XRD

Coating characterization after oxidation tests includes:

- weight change
- examination of the oxide scales after oxidation tests
- elemental (particularly Al, Si and Cr) redistribution after testing

A comparison of coating microstructural features before and after oxidation tests provided insight in oxidation mechanisms.

### **3.4 Summary of Coating and Process Design**

Multilayered coatings consist of three layers, which include an aluminized layer, a NiCrAlY layer and a Cr-Si layer. The aluminized layer provides sufficient aluminum in the top layer and promotes chromium release; the NiCrAlY layer with high chromium content provide chromium atoms to release and to form a Cr layer that is the barrier layer for Al diffusion; and the Cr-Si layer prevents chromium from diffusing into the substrate. The targets of the optimizations of the coating processes for the three layers are to obtain:

- aluminized coatings with Al/Ni ratios at 1 and 2
- NiCrAlY coatings with the fewest number of pores, unmelted particles and oxides, and with no cracks
- Cr-Si coatings with 20-30 at.% Cr, 20 -30 at.% Si

## Chapter 4: Process Optimization for NiCrAlY Coatings

### 4.1 Experimental Procedure

#### 4.1.1 Coating Materials and Substrate

Three different commercially available spherical, gas atomized powders were used in this study and the nominal composition and size for each powder are listed in Table . The powder feed rates were measured for each powder at four settings, which were defined as the numbers at 4, 5, 6, and 7, respectively. 304 stainless steel plates were used as the substrate based on the reasons below:

- (1) The microstructure of SS304 is  $\gamma$  phase, which is similar to IN738. Therefore the coefficients of thermal expansion for SS304 and IN738 are close.
- (2) There is no diffusion between a plasma spray coating and the substrate, thus the microstructure of the substrate hardly affects the microstructural features of the coating.
- (3) SS304 is much cheaper than IN738.

**Table 4.1 Powder parameters and powder feed rate**

Trade name of Praxair	Powder size, $\mu\text{m}$	Composition, wt.%	Carrier gas flow rate, sl/min	Powder feed rate, g/min			
				7	6	5	4
NI-246-4	-90+38	Ni-31Cr-11Al-0.1Y	12	102	82	57	43
NI-164-2	-75 +45	Ni-22Cr-10Al-1Y	12	102	84	72	48
NI-343	-45+10	Ni-22Cr-10Al-1Y	12	110	96	80	52

The 304 stainless steel plates were cut to a size of  $25 \times 80$  mm; then the cut plates were blasted using 46 grit alumina abrasive with a nozzle pressure at 80psi. The plate surface was blasted around one minute until there was no sign of non-blasted areas and a uniform grit blasted and rough surface was to achieve for 2 hr before plasma

spraying. The surface roughness  $R_a$ , for all specimens used in this study, ranges from 2.5 to 3.0  $\mu\text{m}$ .

#### **4.1.2 Plasma Spraying Process**

The coatings were produced using the Mettech Axial III™ system with different powder feed rates as listed in Table 4.2. The specimens were clamped onto a turn table with a rotational speed of 220 rpm and a vertical motion speed of 17 mm/s. The vertical motion distance was 120 mm, which allowed specimens to be heated and coated evenly. An up-down motion of the table during spraying is defined as a heating cycle, while the heating cycle before spraying is defined as a preheating cycle. The purpose of preheating was to eliminate any moisture in the substrate and to increase the temperature of the substrate because the heated substrate enabled better adhesion between the coating and substrate. Immediately before the spraying, the substrates were moved up and down five times to be pre-heated. Argon gas was used as the primary and powder carrier gas. Hydrogen ( $\text{H}_2$ ) and nitrogen ( $\text{N}_2$ ) were employed as the secondary gases for spraying.

The first Taguchi matrix was designed to systematically vary the settings of the following four parameters: powder size, the internal diameter of the nozzle, the total flow rate of secondary gas, and the ratio of  $\text{H}_2 + \text{N}_2$  flow rate over the total secondary gas flow rate. Based on the results from the first set of experiments, the second set of Taguchi matrix was designed to examine the effects of total flow rate of secondary gas, the ratio of  $\text{H}_2 + \text{N}_2$  flow rate over the total secondary gas flow rate, the current, and the spray distance. Finally an extra set of tests were conducted to verify the validity of the regression equations derived from the first and second set of experiments and to

examine the process repeatability. All parameters for the three sets of experiments are summarized in Table 4.2. The following parameters were kept constant for this study: primary gas (Ar: 225 sl/min), powder carrier gas flow rate (Ar:12 sl/min), total spraying time (2 min), and preheating cycle (5 cycles).

**Table 4.2 Taguchi matrix and process parameters**

Test	Coating	Powder size , μm	Nozzle size , mm.	Total flow rate, sl/min	H <sub>2</sub> , %	N <sub>2</sub> , %	Current, (A)	Dist-ance, mm	Powder feed rate, g/min
1st	1-1		12.7	300	30				
	1-2	-90/+38	11.1	265	23				48
	1-3		9.5	230	16				
	1-4	-75/+45	12.7	265	16				
	1-5		11.1	230	30	10	250	150	43
	1-6		9.5	300	23				
	1-7		12.7	230	23				
	1-8	-45/+10	11.1	300	16				52
	1-9		9.5	265	30				
2nd	2-1				30		250	200	
	2-2			300	20		200	150	
	2-3				10		150	100	
	2-4				30		200	100	
	2-5	-75/+45	11.1	265	20	10	150	200	102
	2-6				10		250	150	
	2-7				30		150	150	
	2-8			230	20		250	100	
	2-9				10		200	200	
3rd	3-1				16				
	3-2	-45/+10	9.5	230	23	10	250	150	96
	3-3				25				

#### 4.1.3 Coating Characterization

The groups for the specimens of the first set of experiments were designated from coating 1-1 to coating 1-9 according to the spraying parameters assigned. There were 8 specimens in each group. One of the specimens in the group of coating 1-1 is presented in Figure 4.1 The coated specimens were cross-sectioned, mounted, ground and

polished. The microstructure analyses were performed using a Philips XL30 SEM to obtain images of the coatings. The SEM images of the coatings generated in the first set of the experiments are presented in Figure 4.2. The microstructural features of the coatings, such as pores, cracks, unmelted particles, and oxides can be identified. Energy dispersive X-ray (EDS) mappings (of elements Al and O) were used to distinguish pores and oxides, as shown in Figure 4.3. In particular, three levels of contrast were identified. The darkest regions in the Al map represent pores (some small size pores were accompanied by oxides), while bright contrasted regions are oxides, and the intermediate contrasted regions correspond to the bulk of the NiCrAlY coatings. The oxide is assumed to be alumina ( $\text{Al}_2\text{O}_3$ ) since the distributions of Al and O on EDS elemental maps are identical, as shown in Figure 4.3.

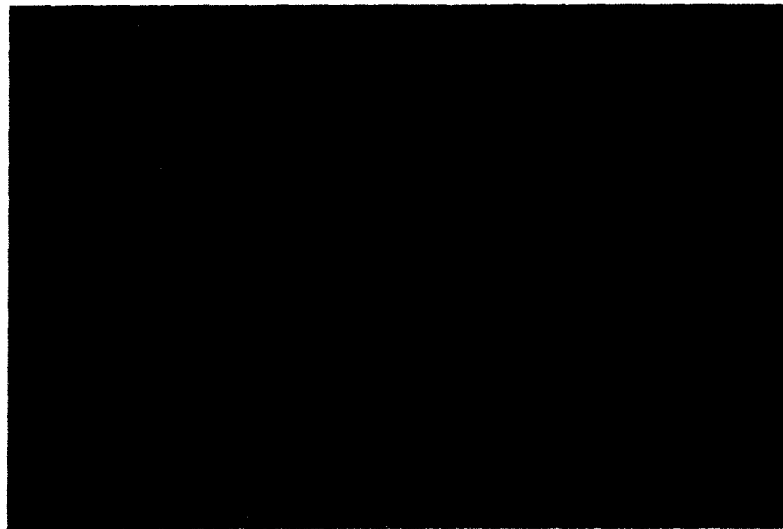
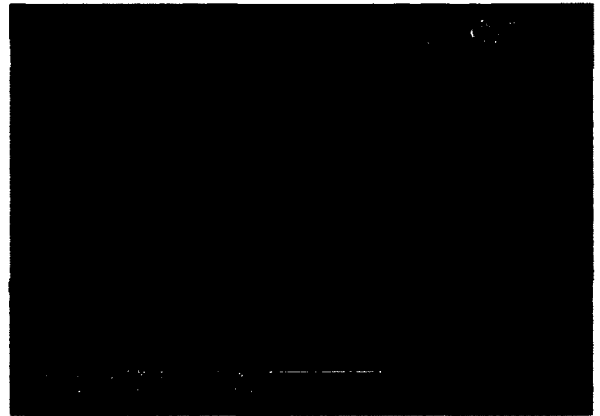


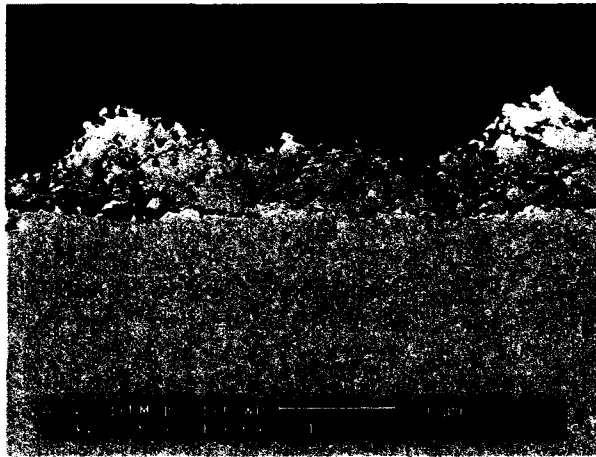
**Figure 4.1 Image of a coating specimen in the group of coating 1-1.**



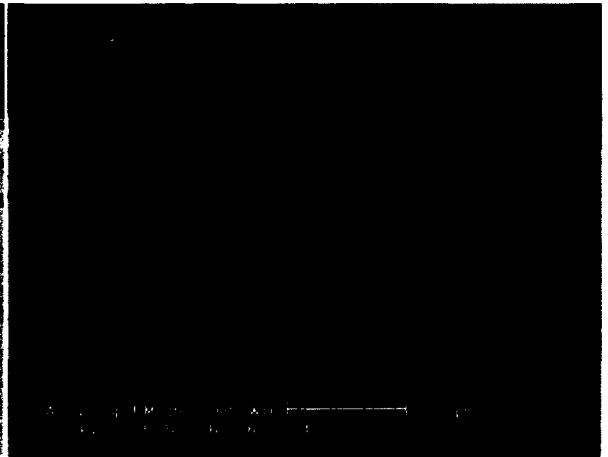
a) Microstructure of specimen 1-1



b) Microstructure of specimen 1-2



c) Microstructure of specimen 1-3



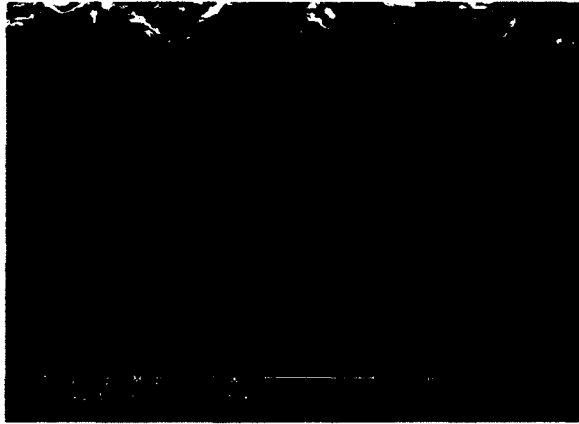
d) Microstructure of specimen 1-4



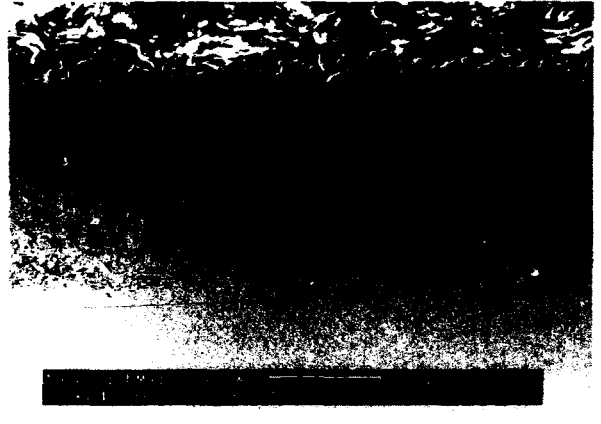
e) Microstructure of specimen 1-5



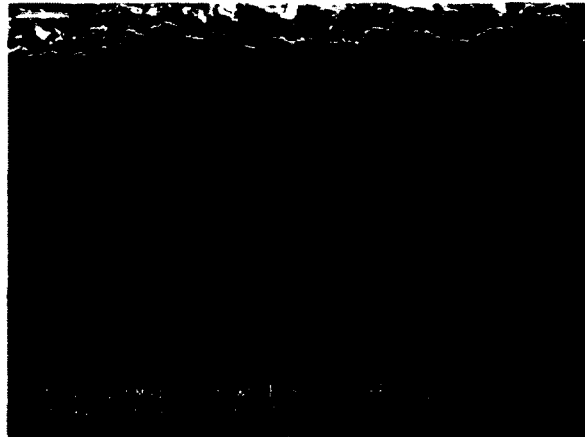
f) Microstructure of specimen 1-6



g) Microstructure of specimen 1-7



h) Microstructure of specimen 1-8



i) Microstructure of specimen 1-9

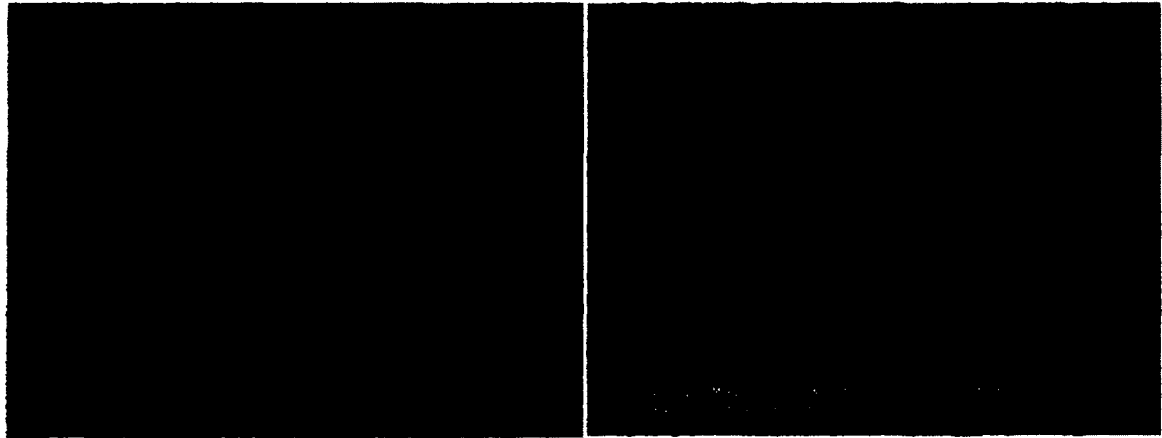
**Figure 4.2 Microstructure of coatings for first set of experiments.**



a) SEM image of specimen 1-2

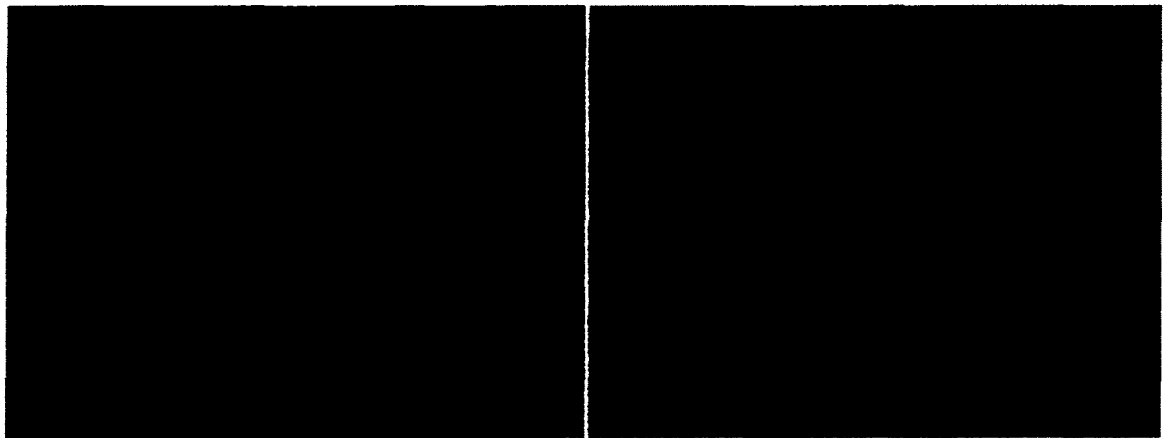


b) EDS mapping image for O



c) EDS mapping image for Al

d) SEM image of specimen 1-7



e) EDS mapping image for O

f) EDS mapping image for Al

**Figure 4.3 EDS mapping images of coating 1-2 and coating 1-7.**

Image analysis software (Clemex Technologies Inc. Canada) was used to determine the percentage of pores, unmelted particles and oxide phases in the coatings. The image processing started with a routine that consists of four steps:

- Image acquisition: importing a stored image of a coating
- Binarization: creating a bitplane of the microstructural features of the coating to

be measured

- Binary operations: modifying the bitplane to ensure that it accurately represents one of the microstructural features of the coating

- Measurements: measuring the size and area percentage of the bitplane for the particular microstructural feature of the coating over the whole field

For measuring unmelted particles, the following microstructural characteristics were used: spherical or semispherical shaped particles, and clear boundaries with surrounding regions as shown in Figure 4.2.

The percentage for cracks was based on the length of the crack over the length of the interface between the coating and the substrate for each image, and the percentage of other microstructural features of the coating was taken from the area of the coating feature over the whole area of the field (image) analyzed.

Twenty SEM images at a magnification of 500X taken along the coating layer were imported to the image analysis program for measuring the percentages of the microstructural features of the coating. The final data are the average of the results from the twenty images. The final data were used for regression analysis.

#### 4.2 Regression Analysis

Theoretically, the measured percentages of crack, porosity, unmelted particle and oxide can be considered as the response functions of the four process parameters investigated in this study. Polynomial equations of the four process parameters can be expressed as [98]:

$$F(x_1, x_2, x_3, x_4) = A + \sum_{i=1}^4 x_i + \sum_{i=1}^4 \sum_{i < j}^4 x_i x_j + \dots + \sum_{i=1}^4 \sum_{i < j}^4 x_i^{r-1} x_j^{r-1} + \sum_{i=1}^4 x_i^r \quad (4-1)$$

where  $A$  is a constant,  $F(x_1, x_2, x_3, x_4)$  stands for the percentage of crack, porosity, unmelted particle and oxides,  $x_1, x_2, x_3, x_4$  are powder size, nozzle size, total gas flow rate, the ratio of  $H_2$  plus  $N_2$  over total gas flow rate, respectively, and  $r$  is the order of the polynomial equation. The larger the exponent  $r$ , the more accurate the polynomial equation is. However, a value of  $r$  equivalent to one is generally used to simplify the calculations and analysis. In the present analysis,  $r$  values from one to two were used to generate the equations and the results were compared.

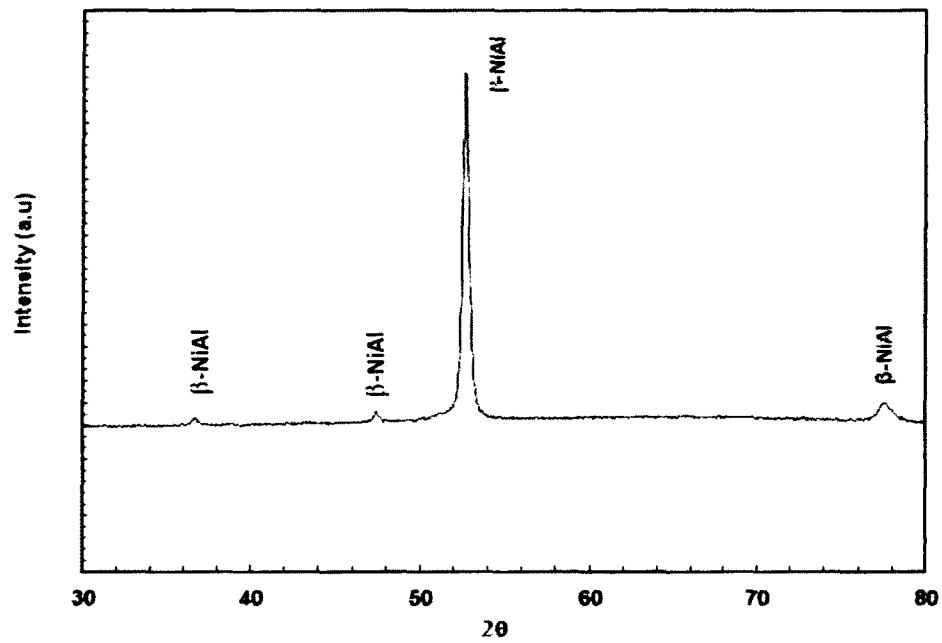
After the crack, porosity, unmelted particle and oxide data of the experimental trials were obtained, the polynomial equations related to the investigated process parameters were generated by regression analysis. However, nine trials, shown in Table 4.2, were insufficient to conduct a regression of the experimental results with an order of more than one in a regression equation. Therefore the variables in the regression equation must be shifted using statistical testing to eliminate the terms that influence the response functions negligibly, and retain only those statistically significant to the response function. In the present analysis, a stepwise regression method was used. It started with a simple model and gradually more parameters, higher orders of parameters and their interactions were incorporated until the model became significant.

### **4.3 Results and Discussion for Process Optimization**

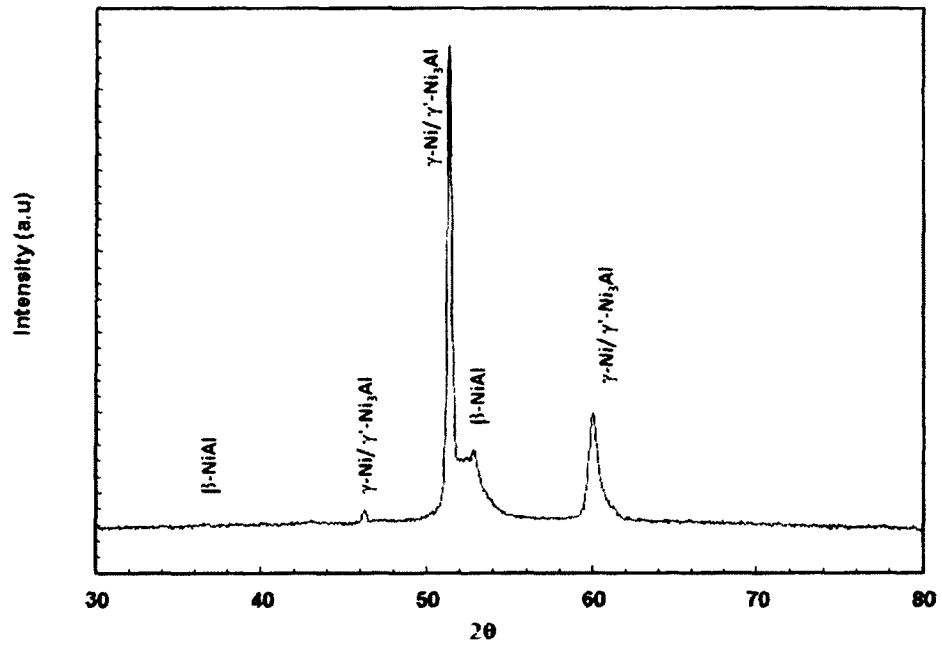
#### **4.3.1 Microstructures of NiCrAlY Coatings**

As observed in Figure 4.2, NiCrAlY coatings have a typical splat microstructure with pores, oxides and unmelted particles. Cracks are observed in some coating specimens (Figure 4.2c and Figure 4.2d) at the coating/substrate interface. The amounts of cracks, pores and unmelted particles vary significantly with the powder size and

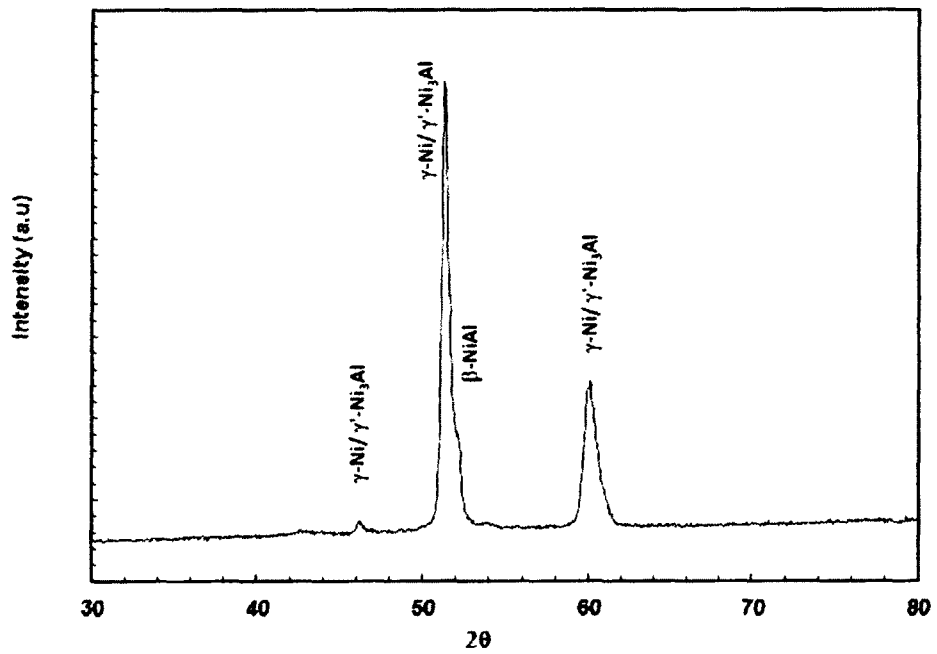
other process parameters. On basis of the analysis of the XRD spectra in Figure 4.4, The microstructure of the as-sprayed NiCrAlY coating contains single  $\beta$ -NiAl phase (with a fraction of dissolved chromium) when chromium content is 32% in Ni 246, whereas the NiCrAlY coating is composed of  $\beta$  (NiAl) +  $\gamma$ (Ni) /  $\gamma'$ (Ni<sub>3</sub>Al) when Cr content is 22% in Ni 164 and 343. Instead of Cu  $k_{\alpha}$  radiation, in this research the Co  $k_{\alpha}$  radiation was used for XRD.



a) XRD spectrum for coating 1-1



b) XRD spectrum for coating 1-5



c) XRD spectrum for coating 1-9

**Figure 4.4 XRD spectra for NiCrAlY coatings.**

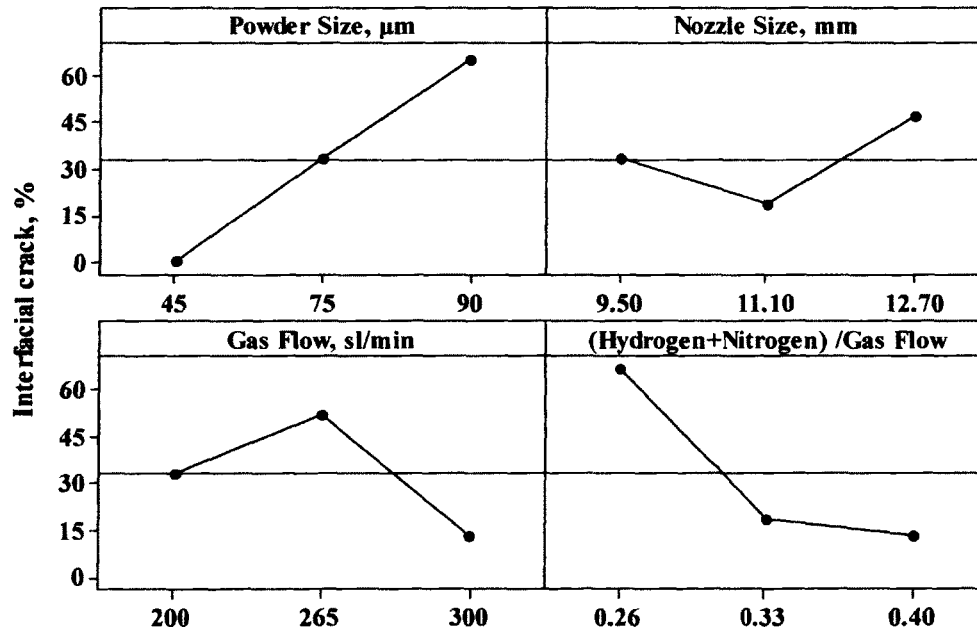
### 4.3.2 Results from the First Set of Experiments

The quantitative results for four coating features are summarized in Table 4.3. Based on the results, the influences of each spraying process parameter on these coating features are illustrated in Figure 4.5.

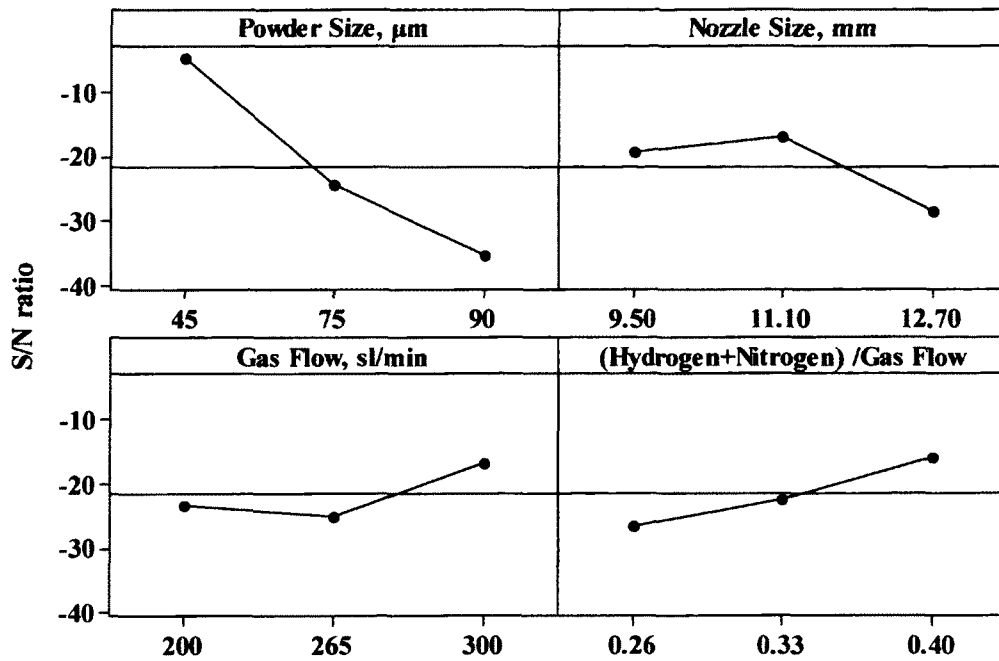
**Table 4.3 Percentages of crack, pore, unmelted particle and oxide in coatings**

Coating	Crack at interface, %	Porosity*, %	Unmelted particles, %	Oxide, %
1-1	40.2	8.17	6.10	2.87
1-2	56.3	10.83	10.30	1.10
1-3	100.0	20.84	45.00	0.00
1-4	100.0	18.06	15.35	0.00
1-5	0.0	7.70	4.40	6.77
1-6	0.0	5.20	12.13	4.50
1-7	0.0	5.10	0.00	12.67
1-8	0.0	4.80	2.93	8.73
1-9	0.0	4.00	0.00	14.20

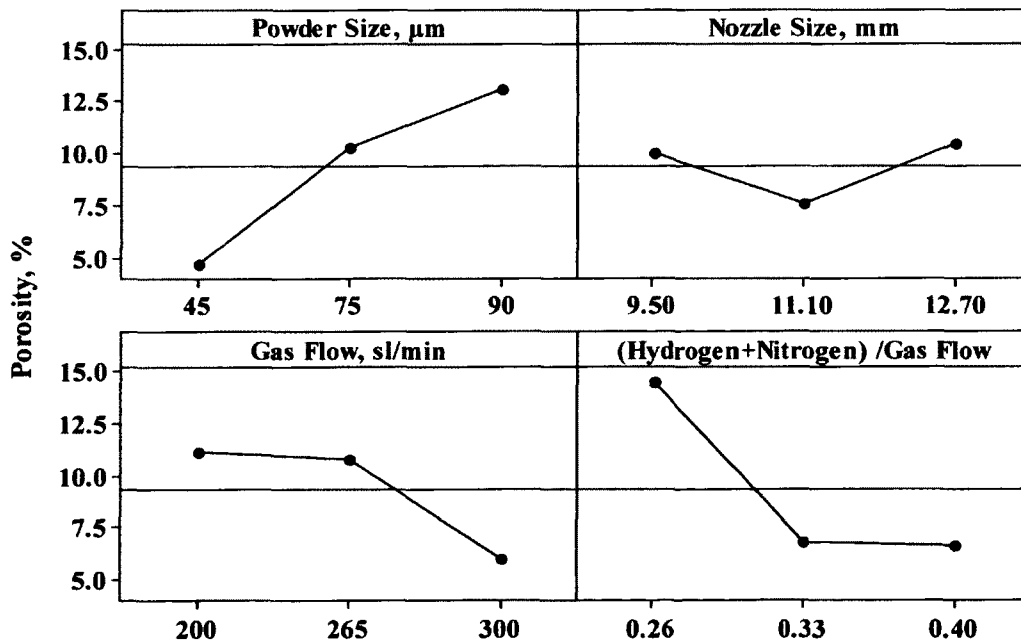
\* Measured based on area percentage of pores over total area analyzed.



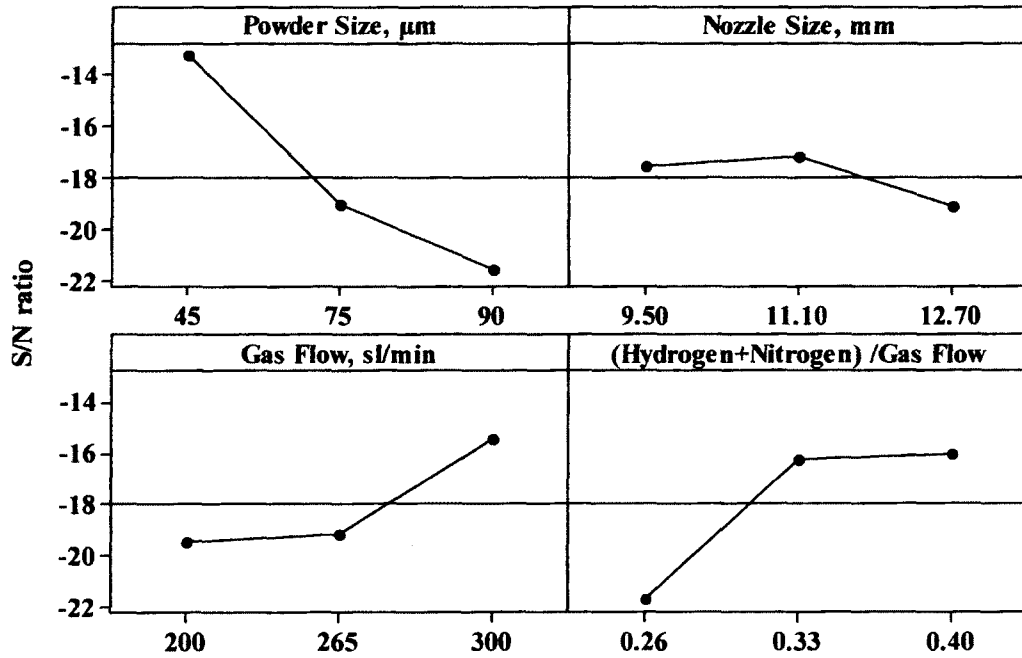
a) Influences of spraying process parameters on cracking



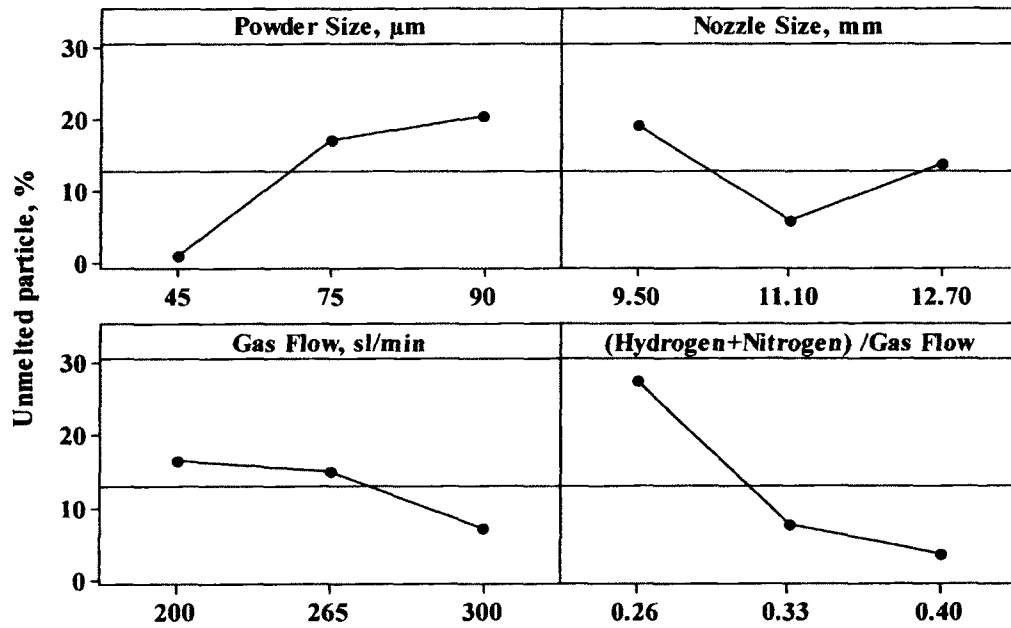
b) Signal-to-Noise ratio of the parameters on cracking



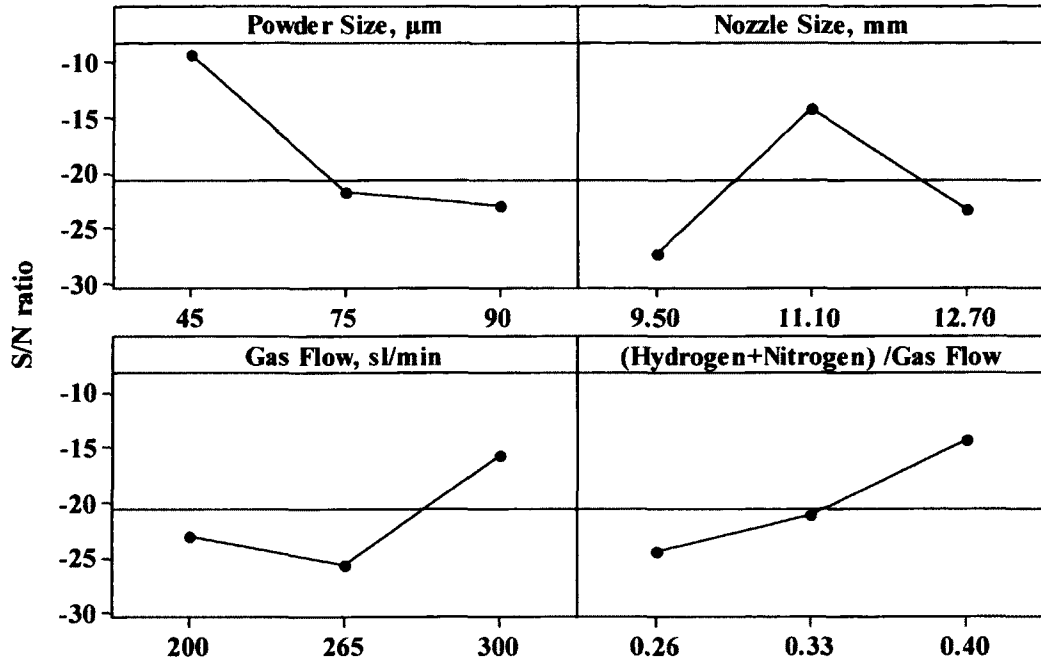
c) Influence of spraying process parameters on porosity



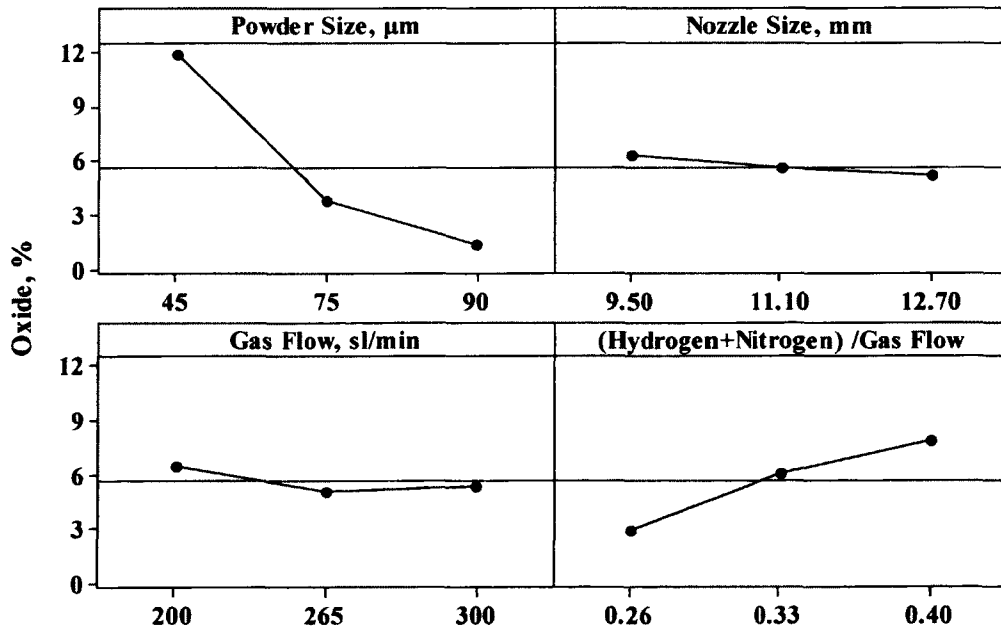
d) Signal-to-Noise ratio of the parameters on porosity



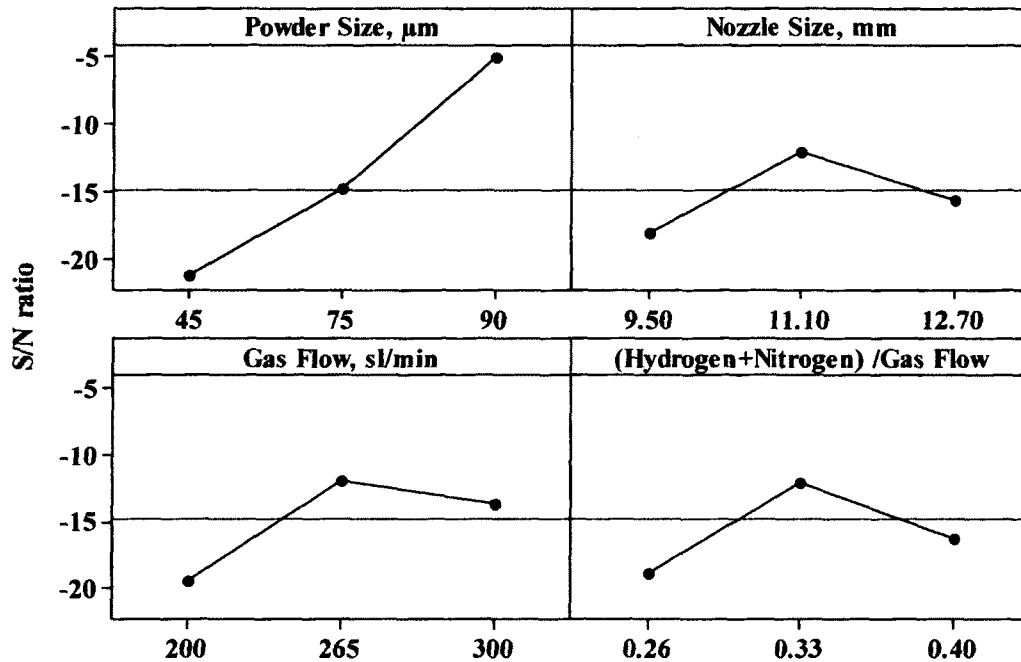
e) Influence of spraying process parameters on unmelted particles



f) Signal-to-Noise ratio of the parameters on unmelted particles



g) Influence of spraying process parameters on percentage of oxide



h) Signal-to-Noise ratio of the parameters on unmelted particles

**Figure 4.5 Results of the experiments for the first Taguchi matrix.**

All coating features are defects that should be minimized using the smaller-the-better SNRs for each spraying process parameter. The optimal parameters for minimizing coating features are summarized in Table 4.4 based in the plot of the SNRs versus process parameters (Figure 4.5). The optimal parameters for minimizing all coating features are almost identical except that the optimal powder size for minimizing oxides is 90  $\mu\text{m}$  instead of 45  $\mu\text{m}$ .

**Table 4.4 Optimal parameters for minimizing coating features according SNRs**

Coating feature	Powder size, $\mu\text{m}$	Nozzle size, mm	Total gas flow rate, sl/min	$\text{H}_2 + \text{N}_2$ over total gas flow rate
Cracking	45	11.10	300	0.40
Porosity	45	11.10	300	0.40
Unmelted particles	45	11.10	300	0.40
Oxide	90	11.10	265	0.33

The four process parameters used in regression equations are given in Table 4.5. The influences of parameters on coating features cannot be accurately predicated using simple linear regressions based on the curves in Figure 4.5. Therefore the combination of process parameters (such as  $x_1x_2$ ,  $x_1x_3$ ,  $x_3x_4$ ) and higher orders of these process variables (such as  $x_1^2$ ) need to be incorporated into the regression equation in order to correlate the parameters with the coating features more accurately.

**Table 4.5 Values of  $x_1$ ,  $x_2$ ,  $x_3$  and  $x_4$  used in regression equation**

$x_1$ , powder size, $\mu\text{m}$	maximum $x_2$ , nozzle size in mm	$x_3$ , total flow rate at sl/min	$x_4$ , ratio of $\text{H}_2 + \text{N}_2$ over total gas
90	12.7	300	0.40
75	11.1	265	0.33
45	9.5	230	0.26

A stepwise regression analysis started with a simple linear regression model for the powder size, which is illustrated in Table 4.6. A set criterion,  $p = 0.65$ , was applied for removing and adding parameters. Some parameters were eliminated if  $p$ -value was too low. In each step the parameters were added in the equation when the  $p$ -values of the parameters were greater than 0.65, and the parameters were removed from the equation when the  $p$ -values of the parameters were less than 0.65. In the meanwhile the standard deviation ( $S$ ) and coefficient of determination ( $R^2$ ) were also calculated and included in Table 4.6. These parameters remained in the last step created the regression equations for all four coating features summarized in Table 4.6. Also included in this table are other statistic values such as  $S$ ,  $R^2$ ,  $F$ ,  $m$ ,  $n$ , and  $p$ -value as well as  $RSS$  and  $MSE$ .  $RSS$  represents residual sum of squares. All regression equations have five degree of freedom ( $m$ ) and residuals have three degrees of freedom ( $n$ ).

**Table 4.6 Procedure of stepwise regression analysis for porosity**

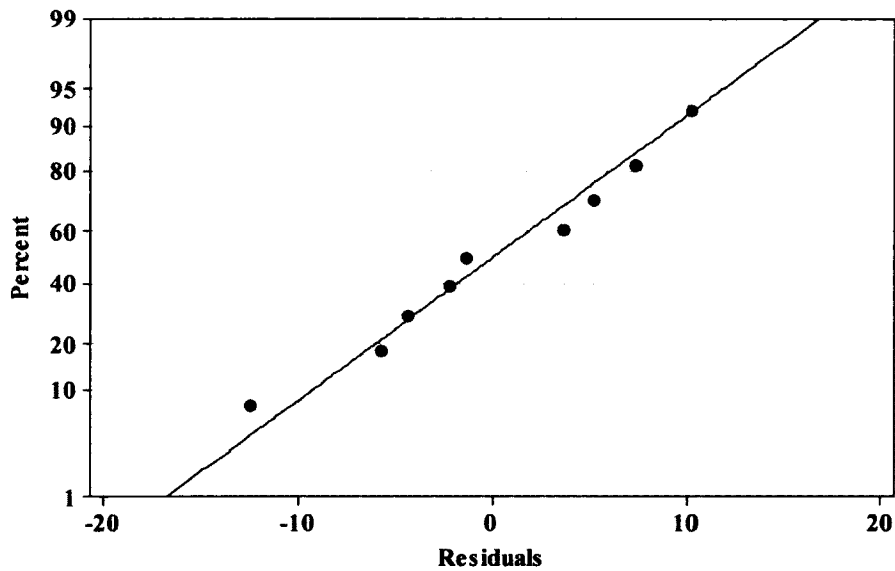
Parameter and statistical values	Step				
	1	2	3	4	5
Constant	-3.84	-3.84	-21.10	-50.31	13.53
$x_1$	$1.88 \times 10^5$	$4.81 \times 10^5$	$9.28 \times 10^5$	$1.24 \times 10^6$	$1.14 \times 10^6$
$p(x_1)$	0.11	0.072	0.036	0.134	0.769
$x_1x_4$		$-8.86 \times 10^5$	$-2.24 \times 10^6$	$-3.19 \times 10^6$	$-2.84 \times 10^6$
$p(x_1x_4)$		0.015	0.054	0.012	0.006
$x_4^2$			154.00	254.00	$7.61 \times 10^2$
$p(x_4^2)$			0.177	0.033	0.018
$x_2$				1.53	1.38
$p(x_2)$				0.068	0.026
$x_4$					$-3.60 \times 10^2$
$p(x_4)$					0.047
$S$	4.57	4.10	3.01	2.62	1.11
$R^2$	72.24	72.15	87.98	93.19	98.75

In the polynomial equations containing the process parameters concerned in this study, all  $F$  values in Table 4.7 are greater than the threshold  $F(5, 3, 0.95) = 9.01$ . In all cases  $R^2$  values are over 96%, which indicate that less than 4% of the total variations are not explained by the regression relationships. Thus, it can be concluded that the regression equations are all significant. It should be noted that  $x_3$  (total gas flow rate) has not been included in the regression equations because of its insignificant influence.

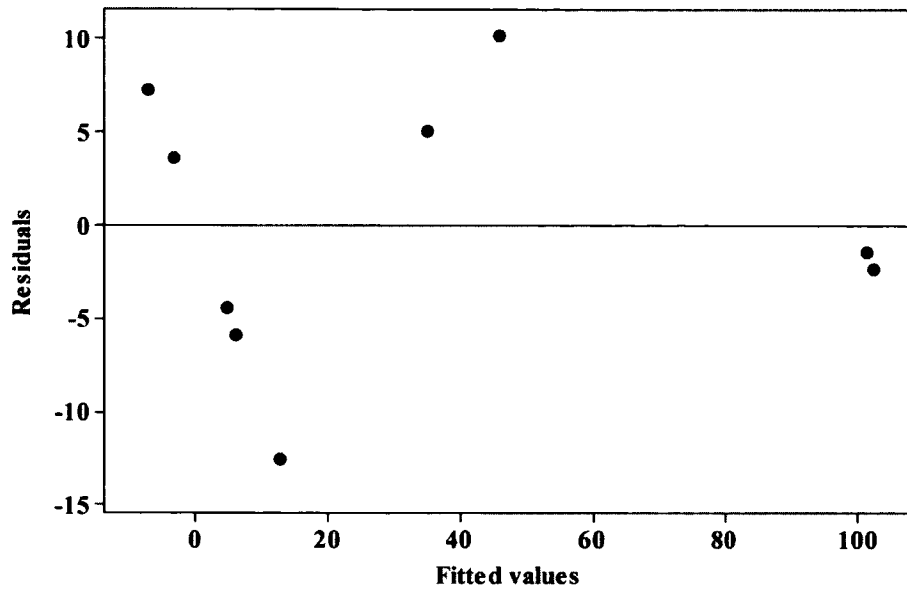
Normality test and independence test of the regression equations for the coating features verified the validity of the equations. An example of the test is illustrated on Figure 4.5, and the residuals are correlated with the line of normality test and the distribution of the residuals is random and independent.

**Table 4.7 Regression equations for four coating microstructure features**

Feature	Regression equations	<i>S</i>	<i>R</i> <sup>2</sup>	<i>F</i>	<i>p</i> -value	<i>RSS</i>	<i>MSE</i>
Crack	$C(x_1, x_2, x_3, x_4) = -3.00 + 7.78 \times 10^6 \times x_1 - 1.88 \times 10^3 \times x_4 - 1.96 \times 10^7 \times x_1 \times x_4 + 0.57 \times x_2^2 + 4.35 \times 10^3 \times x_4^2$	11.8	97.2	21.0	0.015	14584.7	138.7
Porosity	$P(x_1, x_2, x_3, x_4) = 13.53 + 1.14 \times 10^6 \times x_1 + 1.38 \times x_2 - 3.60 \times 10^2 \times x_4 - 2.84 \times 10^6 \times x_1 \times x_4 + 7.61 \times 10^2 \times x_4^2$	1.1	98.7	47.4	0.005	293.8	1.2
Un-melted particle	$U(x_1, x_2, x_3, x_4) = 49.00 + 3.32 \times 10^6 \times x_1 - 8.53 \times 10^2 \times x_4 - 5.84 \times 10^7 \times x_1 \times x_4 - 7.13 \times 10^9 \times x_1^2 + 1.65 \times 10^3 \times x_4^2$	4.7	96.7	22.0	0.005	1989.5	22.7
Oxide	$O(x_1, x_2, x_3, x_4) = -5.50 + 1.42 \times 10^5 \times x_1 + 0.44 \times x_2 + 43.4 \times x_4 - 0.87 \times x_1 \times x_2 - 6.80 \times 10^{-2} \times x_2^2$	0.9	99.0	59.6	0.003	224.4	0.8



a) Normal probability plot of the residuals



b) Independence test

**Figure 4.6 Normality and independence test of the regression equation for crack.**

Table 4.8 compares the measured results of the coating features from the experiment with the values calculated from the regression equations. The calculated values agree well with the experimental results and the predicted errors fall into the confidence interval of the measured data at 95% confidence level ( $\alpha = 0.05$ ).

### 4.3.3 Discussion on the Results from the First Set of Experiments

Table 4.9 summarizes the effects of the process parameters on the microstructural features of NiCrAlY coatings based on the regression equations. It is generally accepted that the spray parameters could be ranked based on their  $p$ -values on coating features [104] and accordingly the ranking has been made as shown in Table 4.9. All parameters are categorized into three levels: the most significant, medium significant and least significant. The most significant process parameters found in this study are the particle size ( $x_1$ ), the ratio of  $H_2 + N_2$  over total gas ( $x_4$ ), their interaction ( $x_1x_4$ ) and their

squared values ( $x_1^2$  and  $x_4^2$ ). The next important parameters are nozzle size ( $x_2$ ) and parameters related to the nozzle size.

**Table 4.8 Comparison of the experimental results with the values calculated from the regression equations**

Coating	Crack at interface, %			
	E-value*	C- value^	Predicted error	Confidence interval at 95%
1-1	39.15	34.80	16.44-63.56	2.55-77.45
1-2	56.36	45.80	32.44-79.56	18.55-93.45
1-3	100.00	100.00	76.44-100.00	62.55-100.00
1-4	100.00	100.00	76.44-100.00	62.55-100.00
1-5	0	12.57	0.00-23.56	0.00-37.45
1-6	0	5.78	0.00-23.56	0.00-37.45
1-7	0	4.42	0.00-23.56	0.00-37.45
1-8	0	0.00	0.00-23.56	0.00-37.45
1-9	0	0.00	0.00-23.56	0.00-37.45
Coating	Porosity, %			
	E-value	C-value	Predicted error	Confidence interval at 95%
1-1	8.17	8.62	5.94-10.4	4.63-11.71
1-2	10.30	10.64	8.07-12.53	6.76-13.84
1-3	20.84	20.11	18.61-23.07	17.30-24.38
1-4	18.06	18.70	15.83-20.29	14.52-21.60
1-5	7.70	8.57	5.47-9.93	4.16-11.24
1-6	5.20	5.61	2.97-7.43	1.66-8.74
1-7	5.10	4.36	2.87-7.33	1.56-8.64
1-8	4.80	4.89	2.57-7.03	1.26-8.34
1-9	4.00	4.68	1.77-6.23	0.46-7.54
Coating	Unmelted particles, %			
	E-value	C- value	Predicted error	Confidence interval at 95%
1-1	6.10	4.30	0.00-15.63	0.00-21.26
1-2	10.30	15.07	0.77-19.83	0.00-25.46
1-3	45.00	44.78	35.47-54.53	29.84-60.16
1-4	15.35	31.92	5.82-24.88	0.19-30.51
1-5	4.40	3.70	0.00-13.93	0.00-19.56
1-6	12.13	9.72	2.60-21.66	0.00-27.29
1-7	0.00	0.00	0.00-9.53	0.00-15.16
1-8	2.93	6.20	0.00-12.46	0.00-18.09
1-9	0.00	2.50	0.00-9.53	0.00-15.16

Table 4.8 continued

Coating	Oxide,%			
	E-value	C- value	Predicted error	Confidence interval at 95%
1-1	2.87	2.39	1.13-4.61	0.10-5.64
1-2	1.10	0.74	0.00-2.84	0.00-3.87
1-3	0.00	0.00	0.00-1.74	0.00-2.77
1-4	0.00	0.69	0.00-1.74	0.00-2.77
1-5	6.77	7.37	5.03-8.51	4.00-9.54
1-6	4.50	5.30	2.76-6.24	1.73-7.27
1-7	12.67	12.47	10.93-14.41	9.90-15.44
1-8	8.73	8.48	6.99-10.47	5.96-11.50
1-9	14.20	13.96	12.46-15.94	11.43-16.97

\*E-value: Experimentally measured value

^C-value: Calculated value from regression equation

Table 4.9 Effects of process parameters on coating features

Para- meter	<i>p</i> -value and rank							
	Crack at interface	Rank	Porosity	Rank	Unmelted powder	Rank	Oxide	Rank
$x_1$	0.012	1	0.004	1	0.060	2	0.465	3
$x_2$	0.000		0.026	4	0.000	-	0.955	5
$x_4$	0.204	5	0.042	5	0.165	4	0.006	1
$x_1x_2$	0.000	-	0.000	-	0.000	-	0.105	2
$x_1x_4$	0.020	2	0.006	2	0.029	1	0.000	-
$x_1^2$	0.000	-	0.000	-	0.419	5	0.000	-
$x_2^2$	0.036	3	0.000	-	0.000	-	0.797	4
$x_4^2$	0.083	4	0.018	3	0.096	3	0.000	-

The sequential sums of squares (*SS*) for parameters included in the regression equations (Table 4.10) can be quantitatively calculated to provide comparison of the significance of various parameters on coating microstructural features. The sequential *SS* measures the reduction in the residual sums of squares (*RSS*) provided by each additional parameter in the regression equation. If the sequential *SS* of a parameter substantially reduces the residual sums of squares in a regression equation, this parameter becomes significant in the equation. Based on the percentage of the

sequential sums of squares over total sums of squares for each parameter (Table 4.10), Pareto diagrams can be generated to analyze the impact of various process parameters, as shown in Figure 4.7. Pareto diagrams are simple bar charts that rank related process parameters in decreasing order of significance. The principle of Pareto diagram is based on the unequal distribution of things in the universe. It is the law of the "more important few versus the trivial many" [105]. By graphing each coating feature with respect of the sequential SS for all process parameters, the most significantly parameter could be identified.

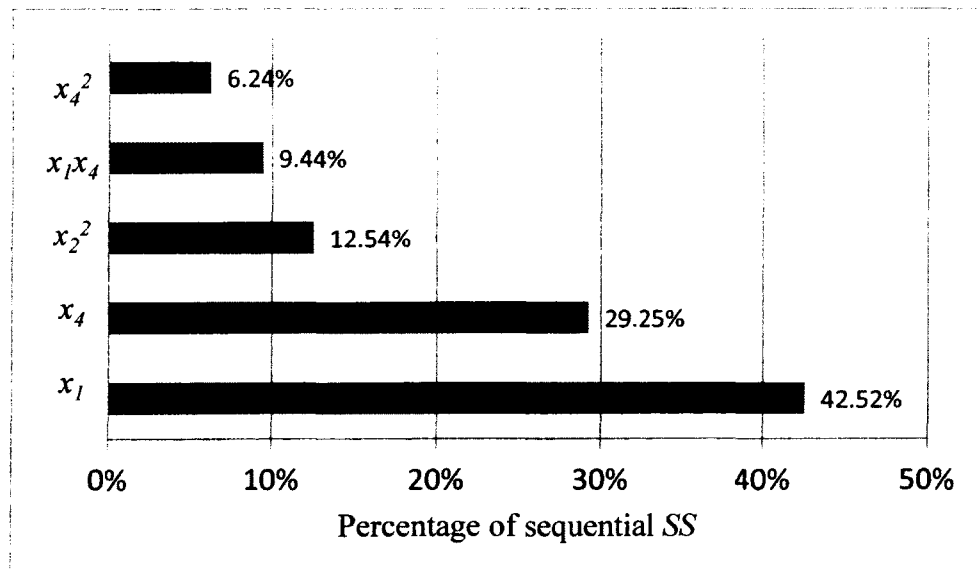
**Table 4.10 Sequential sums of squares of process parameters on coating features**

Process parameter	Crack at interface		Porosity	
	Sequential SS	Percent, %	Sequential SS	Percent, %
$x_1$	6202.02	42.50	111.82	38.06
$x_2$	0.00	0.00	0.28	0.10
$x_4$	4266.70	29.50	94.65	32.22
$x_1x_2$	0.00	9.44	0.00	0.00
$x_1x_4$	1376.20	0.00	59.24	20.16
$x_1^2$	0.00	6.24	0.00	0.00
$x_2^2$	1829.60	12.50	0.00	0.00
$x_4^2$	10.20	0.00	27.80	9.46
Total SS	14584.70		293.79	
Process parameter	Unmelted powder		Oxide	
	Sequential SS	Percent, %	Sequential SS	Percent, %
$x_1$	633.97	31.55	180.60	80.47
$x_2$	0.00	0.00	1.66	0.74
$x_4$	873.63	43.48	38.05	16.95
$x_1x_2$	0.00	0.00	4.05	1.80
$x_1x_4$	350.96	17.47	0.00	0.00
$x_1^2$	19.87	0.99	0.00	0.00
$x_2^2$	0.00	0.00	0.06	0.03
$x_4^2$	130.90	6.51	0.00	0.00
Total SS	2009.23		224.43	

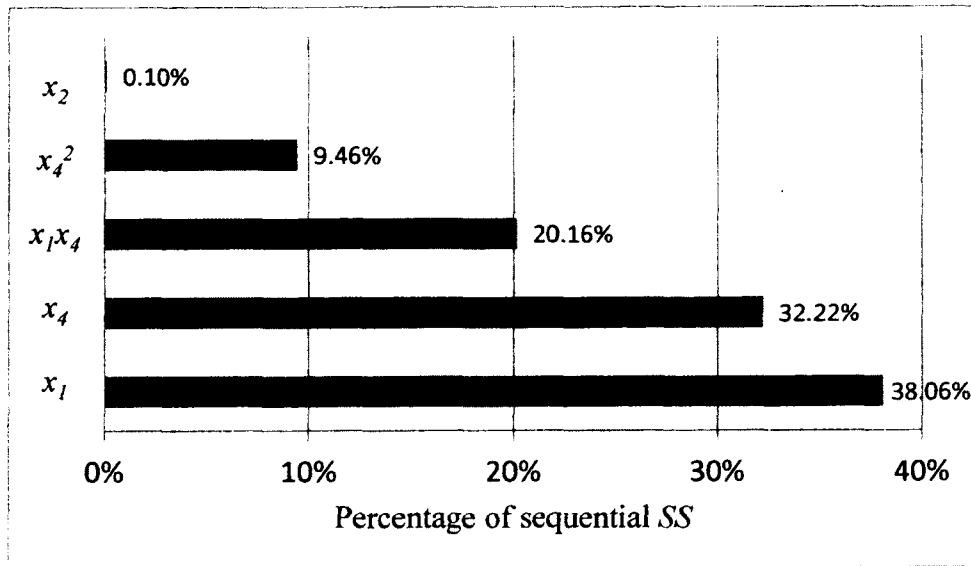
Examining Table 4.10, it is found that over 80% of sequential SS is accumulated from the sequential SS of particle size ( $x_1$ ), the ratio of H<sub>2</sub> + N<sub>2</sub> over total gas ( $x_4$ ), and

parameters related to them. This suggests that powder particle size and the ratio of  $H_2 + N_2$  over total gas are the most dominating factors for all coating microstructural features. Within the range of the experimental parameters used in this study, smaller powder particle size and higher ratio of  $H_2 + N_2$  over total gas reduce the percentages of cracks, pores, unmelted particles but increase the percentage of oxides. Nozzle size has certain influence on oxides. The trend observed from the percentage of SS also coincides with that found from the graphic illustrations of Figure 4.5g.

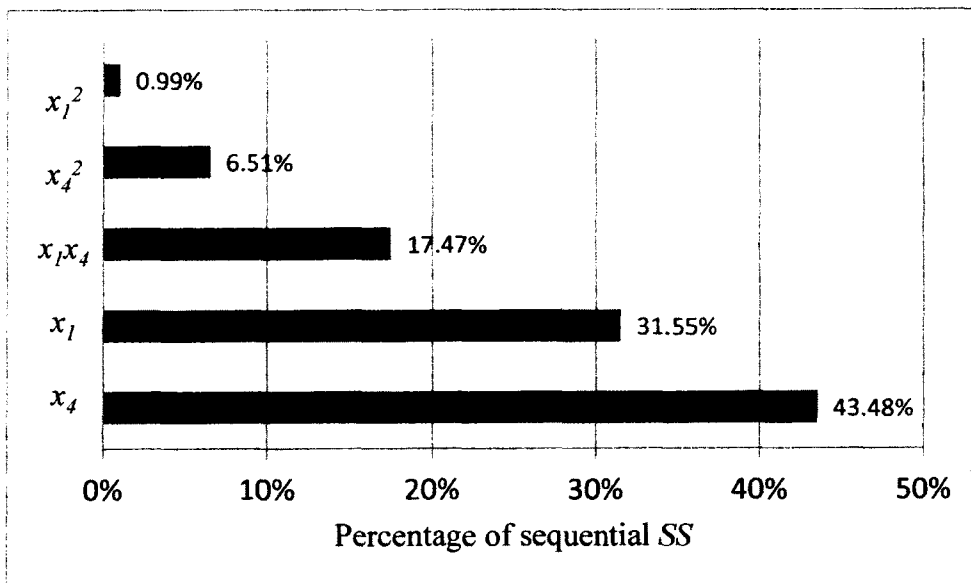
The effects of the process parameters on the coating features are reflected through investigating their influences on the powder particle velocity and temperature. In order to understand the particle melting process, the influences of the parameters on the particle flight time, flame temperature and heat transfer coefficient have been taken into consideration.



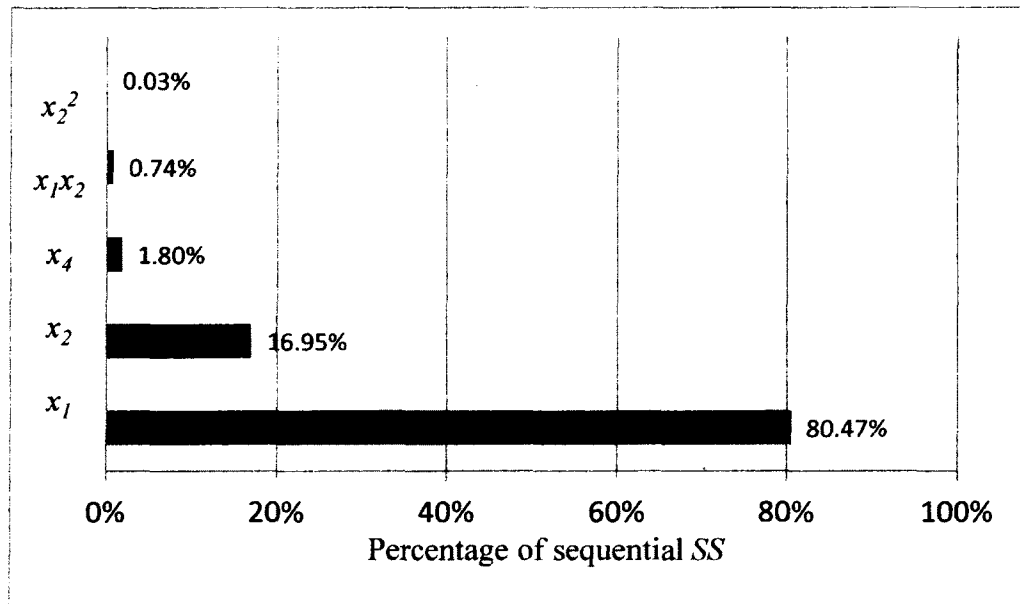
a) Effects of various process parameters on cracking



b) Effects of various process parameters on porosity



c) Effects of various process parameters on unmelted particle



d) Effects of various process parameters on percentage of oxides

**Figure 4.7 Pareto diagrams showing the effects of process parameters on coating features.**

In general, a better melting process is expected if more heat is convectively transferred to the particles, which suggests that the particles are easier to be melted in the plasma gas with the higher flame temperature and the larger heat transfer coefficient in addition to longer residence time. Previous study attempted to characterize the behavior of the particle flow in an axial injection plasma torch [53]. Based on the results of this study, the reasons that powder size has the most significant influence on melting status of particle can be described as follows:

(1) Temperature is uniform across the particle stream and the particle velocity can reach 380-550 m/s near the torch axis. Therefore at the beginning most particles penetrate the flame center easily and the temperature of the particles increases during spraying. The particle trajectory and velocity within the plasma flame are then

determined by the mass and the size of the particles. Small particles may be vaporized prior to reaching the substrate, whereas large particles may not be completely melted upon impacting or missing the target entirely. Accordingly only a fraction of the particles can reach the substrate to form the coating and the ranges of the size of the particles that form the coating are very narrow [106].

(2) Heat transfer coefficient increases with decreasing powder size.

(3) The enthalpy for melting a large particle, which depends on volume of the particle (assuming constant heat capacity and density), is much more than that for melting a small particle.

Small particles are more likely to melt than large particles; using small particles apparently decreases the tendency of forming unmelted particles and pores. However small particles are easier oxidized due to the large surface-to-volume ratio. The dependence of particle size on coating cracking may be likely due to the fact that the residual stress between the coating and the substrate varies with particle size. In plasma spraying, residual stress arises from the quenching stress during solidification of molten particles and thermal stress because of the difference in coefficient of thermal expansion (CTE) between the coating and the substrate [107]. Other parameters may also affect the residual stress level such as preheat temperature, sand blasting before spraying [108], and phase transformation (for ferrous and precipitation-hardenable alloys). In this research, the thermal mismatch between the coating and the substrate is very small because they are both nickel-based, therefore the residual stress mainly resulted from the quenching stress, which was related to the solid shrinkage of splats during solidification and the restraint between splats. The large splats, produced by

large particles, create more solid shrinkage than small splats, and the restraint between large splats is stronger than that between small splats. Consequently the coating produced by large particles has tendency to micro-cracking and micro-crack-induced delamination.

The ratio of  $H_2 + N_2$  over total gas flow affects powder particle temperature via plasma enthalpy and heat transport. Higher plasma enthalpy is associated with higher ratio of  $H_2 + N_2$  over total gas flow as both of these diatomic gases transfer heat to the particles more efficiently than argon. As a result the particles in the plasma stream with a higher ratio of  $H_2 + N_2$  experienced a higher in-flight temperature [109].

Nozzle size has certain effects on particle velocity and the shape of the plasma flame [53]. The particle velocity decreases and the shape of the plasma flame gets broader when nozzle size increases, and thus the residence time of the particle in the plasma stream increases. The longer residence time, consequently high particle temperature, helps to eliminate cracks, pores and unmelted particles; however, lower particle velocity promotes the formation of cracks and pores due to low kinetic energy of the particle and the formation of unmelted particles since some particles move away from the hot core of the plasma jet. The combination of these two factors results in the parabolic shaped curves for the percentages of cracks, pores and unmelted particles as a function of nozzle size, which is shown in Figure 4.5a, Figure 4.5c, and Figure 4.5e. Whereas the curve for the percentage of oxides is almost a straight line (Figure 4.5g) because both low particle velocity and broaden plasma flame promote oxidation. Such nozzle size has been found to have more influence on the formation of oxides than on the other coating features, which is further illustrated in Figure 4.6d.

Gas flow rate, to certain extent, should have influence on the particle velocity and coating features related to particle velocity, particularly porosity. However the influence of total gas flow rate was not observed within the range of variation in this study, and this could in part because of the near sonic velocity of the plasma stream generated in Mettech Axial III™ System. Therefore the total gas flow rate and its related parameters were not included in any regression equation.

The regression equations obtained from section 4.2.2 were validated with another experiment using the process parameters listed in Table.4.11. The experimental results of four key microstructure features were compared to the values calculated from the regression equations. The differences between the experimental results and the calculated values are trivial, confirming the validity of the regression equations.

**Table.4.11 Parameters of the experiments used to assess the validity of the regression equations**

Process parameter	Code	Value	Coating feature	*E-value, %	^C-value, %	Relative error,%
Powder size, μm	$x_1$	45	Crack,%	0.00	0.00	0.00
Nozzle size, mm	$x_2$	9.38	Porosity,%	4.10	3.60	12.19
Gas flow rate, Sl/min	$x_3$	230	Unmelted particles,%	5.23	5.46	-4.40
Ratio of H <sub>2</sub> + N <sub>2</sub> over total gas, %	$x_4$	26	Oxide,%	7.80	7.12	8.72

\*E-value: Experimentally measured value

^C-value: Calculated value from regression equation

#### 4.3.4 Results from the Second Set of Experiments

The purpose of the second set of experiments was to relate multiple process parameters with coating properties and develop a concept: process index (*PI*).

Therefore another L9 Taguchi matrix, shown in Table 4.2, was designed to include current and spray distance so that the relationships between enthalpy and process parameters could be examined. The coating specimens obtained from the second set of experiments were designated as specimen 2-1 to specimen 2-9. The powder used for the second set of experiments was NI-164-2 and nozzle size was fixed at 11.1 mm, which favored coating quality based on the results of the first set of experiments. The results of the second set of experiments are presented in Table 4.12.

**Table 4.12 Results of the second set of the Taguchi matrix**

Specimen	Crack at interface, %	Porosity, %	Unmelted particles, %	Oxide, %	Enthalpy, J/sl
2-1	0.00	4.21	2.27	7.03	12.5
2-2	12.00	5.24	3.13	2.83	10.6
2-3	100.00	21.23	35.00	0.00	7.2
2-4	0.00	4.64	2.60	7.60	11.2
2-5	89.00	4.07	8.73	2.67	8.8
2-6	64.00	2.16	8.97	1.67	11.6
2-7	20.00	2.55	4.87	6.17	10.0
2-8	0.00	4.12	8.90	3.43	11.5
2-9	100.00	22.86	45.00	0.00	8.5

#### 4.3.5 Concept of the Process Index

In order to relate multiple process parameters with coating properties, a process index ( $PI$ ) is introduced in the following equation:

$$PI = f(C, D, G, I, L, S) \quad (4-2)$$

where  $C$  is the ratio of  $H_2 + N_2$  over total gas flow;  $D$ ,  $G$ ,  $I$ ,  $L$ , and  $S$  stand for the normalized diameter of the nozzle, total gas flow rate, current, spray distance, and powder size, respectively. These dimensionless values, as shown in Table 4.13, are the

normalized parameters by the median values of the parameters used in two Taguchi matrices.

**Table 4.13 Summary of associated process parameters, normalized parameters**

Coating	<i>S</i>	<i>D</i>	<i>G</i>	<i>C</i>	<i>I</i>	<i>L</i>
1-1	1.20	1.33	1.13	0.40	1.25	1.00
1-2	1.20	1.00	1.00	0.33	1.25	1.00
1-3	1.20	0.87	0.87	0.26	1.25	1.00
1-4	1.00	1.33	1.00	0.26	1.25	1.00
1-5	1.00	1.00	0.87	0.40	1.25	1.00
1-6	1.00	0.87	1.13	0.33	1.25	1.00
1-7	0.45	1.33	0.87	0.33	1.25	1.00
1-8	0.45	1.00	1.13	0.26	1.25	1.00
1-9	0.45	0.87	1.00	0.40	1.25	1.00
2-1	1.00	1.00	1.13	0.40	1.25	1.33
2-2	1.00	1.00	1.13	0.30	1.00	1.00
2-3	1.00	1.00	1.13	0.20	0.75	0.67
2-4	1.00	1.00	1.00	0.40	1.00	0.67
2-5	1.00	1.00	1.00	0.30	0.75	1.33
2-6	1.00	1.00	1.00	0.20	1.25	1.00
2-7	1.00	1.00	0.87	0.40	0.75	1.00
2-8	1.00	1.00	0.87	0.30	1.25	0.67
2-9	1.00	1.00	0.87	0.20	1.00	1.33
3-1	0.60	0.87	0.87	0.26	1.25	1.00
3-2	0.60	0.87	0.87	0.33	1.25	1.00
3-3	0.60	0.87	0.87	0.35	1.25	1.00
Parameter relation	$\frac{x_1}{75\mu\text{m}}$	$\frac{x_2}{11.1\text{mm}}$	$\frac{x_3}{265}$	$x_4$	$\frac{I_o}{200\text{A}}$	$\frac{L_o}{150\text{mm}}$

$I_o$  = current (A),  $L_o$  = working distance (mm)

The purpose of developing the *PI* was to design a method to combine various process parameters into one index number. It is recognized that *PI* could be described in a complex polynomial with respect to the process parameters. From engineering point of view, however, the tedious polynomial is impractical and a simpler fractional equation will be developed.

The influence of the process parameters on coating features can be reflected from the changes in particle velocity and temperature. The process parameters that control particle velocity and temperature will have impact on coating's microstructural features. Based on the analysis in previous section, the total gas flow rate was not considered in the equation of the *PI* because the total gas flow rate had minimal effect on coating features. Parameters such as powder size *S*, nozzle size *D* and spray distance *L* were considered as denominators due to the inverse effect on the particle velocity and temperature while the ratio of H<sub>2</sub> + N<sub>2</sub> over total gas flow and power input were included in *PI* as numerators. Instead of using the electric power (*I·V*, where *V* cannot be controlled in the process directly), enthalpy *H* was used to reflect the change in internal energy of plasma gas or, in other words, enthalpy *H* was the energy transferred to plasma as a result of arc heating. Enthalpy, in current content, was normalized to a standard liter of gas used in the process and equals to electric energy (a function of current *I* and *C*) minus energy loss due to cooling.

The effects of the powder size on the coating features can be understood in terms of its influence on particle velocity and temperature, which depend on the volume of particles (assuming constant heat capacity and density). Therefore the power of the particle size *S* was designated as 3. Considering that the velocity of plasma stream for the Mettech Axial III™ System is close to the sonic speed, the effect of spray distance *L* on the particle velocity was limited. As such an exponent of 0.5 was arbitrarily designated to *L*. The exponents for other parameter are from 0.5 to 3.0 and designated as *a*, *b* and *c*. The equation for *PI* is:

$$PI = \frac{C^a \times H^b}{S^3 \times D^c \times \sqrt{L}} \quad (4-3)$$

The relation between enthalpy and the process parameters was obtained on the basis of the regression analysis of the results from the second set of experiments (Table 4.12). The enthalpy is the response and four normalized process parameters are defined as variables. The results for the regression analysis of the enthalpy are given in Table 4.14.

**Table 4.14 Results of the regression analysis of the enthalpy**

Terms	Coefficient	<i>p</i> -value
Constant	0.28	0.922
Normalized total flow rate ( <i>F</i> )	0.39	0.863
Ratio of $H_2 + N_2$ over total gas flow ( <i>C</i> )	10.67	0.017
Normalized current ( <i>I</i> )	6.40	0.004
Normalized spray distance ( <i>L</i> )	-0.051	0.954

The variables with *p*-values greater than 0.05 were not significant and were eliminated from the regression equation and the equation was therefore simplified as:

$$H = 0.28 + 10.67 \times C + 6.40 \times I \quad (4-4)$$

where *I* is the normalized current. Equation (4-5) was obtained by substituting equation (4-4) into equation (4-3):

$$PI = \frac{C^a \times (0.28 + 10.67 \times C + 6.40 \times I)^b}{S^3 \times D^c \times \sqrt{L}} \quad (4-5)$$

#### 4.3.6 Regression Analysis and Validity of the Process Index

For each set of process parameters, a *PI* value was calculated using equation (4-5). The *PI* value was then used as the only variable to derive a series of regression equations for the coating microstructural features. These regression equations must be effective and significant. A general regression model is defined as:

$$Y, \% = \beta_0 + \beta_1 \log_{10}(PI) + \beta_2 [\log_{10}(PI)]^2 + \beta_3 [\log_{10}(PI)]^3 \quad (4-6)$$

where  $Y$  represents one of the coating microstructural features in percentage, and  $\beta_0, \beta_1, \beta_2$  and  $\beta_3$  are constant determined based on experimental results. In order to determine the exponents  $a, b$ , and  $c$  in equation (4-5), a one-half two-level factorial design was introduced to screen  $a, b$ , and  $c$ , each given a value from 0.5-3.0 (Table 4.15). The corresponding  $PI$  values are given in Table 4.16.

**Table 4.15 Half of two-level factorial design for determining  $PI$  values**

$PI$	$a$	$b$	$c$
$PI_1$	0.5	3.0	0.5
$PI_2$	0.5	0.5	3.0
$PI_3$	3.0	0.5	0.5
$PI_4$	3.0	3.0	3.0

**Table 4.16 Summary of  $PIs'$  values for the two-level factorial matrix**

Coating	$PI_1$	$PI_2$	$PI_3$	$PI_4$
1-1	2169.95	0.68	0.14	107.64
1-2	2273.01	1.45	0.09	142.20
1-3	2163.08	1.95	0.05	105.61
1-4	3023.08	0.94	0.07	51.08
1-5	4324.33	2.76	0.28	437.59
1-6	4211.01	3.80	0.17	373.14
1-7	15767.62	4.92	0.63	483.53
1-8	16140.67	10.28	0.35	556.36
1-9	21463.73	19.37	1.38	3076.50

Based on the  $PI$  values obtained according to Table 4.15 for the first set of experiments, the coefficients of determination,  $R^2$ , for each coating feature with respect to all  $PIs$  (with different exponents of  $a, b$  and  $c$ ) were calculated and summarized in Table 4.17.

To optimize all coefficients of determination simultaneously, an  $\Omega$  factor was introduced to combine the coefficients of determination of all microstructural features for each  $PI$ .  $\Omega$  is the geometrical mean of the coefficients of determination for all the

microstructural features of coatings. The optimization process was based on the determination of the maximum of  $\Omega$  values for all  $PI$ s using Minitab. The results from the optimization process are presented in Figure 4.8. The optimal points are located at the intersection of the blue dash line and the red lines. The blue dash line represents the maximum  $\Omega$  value, and the red line represents the value of  $a$ ,  $b$ , or  $c$  corresponding to the maximum  $\Omega$  value. Based on this figure,  $\Omega$  reaches the peak value when  $a = 3$ , and  $c \leq 0.5$ .

**Table 4.17 Coefficients of determination of regression equations for coating features with respect to all  $PI$  values**

$PI$	Coefficient of determination, $R^2$				
	Crack	Porosity	Unmelted particle	Oxides	$\Omega$
$PI_1$	60.32	49.90	40.81	88.10	57.32
$PI_2$	64.51	59.43	38.77	77.44	58.22
$PI_3$	92.50	95.01	87.10	99.61	93.44
$PI_4$	87.52	71.02	40.81	86.61	68.44

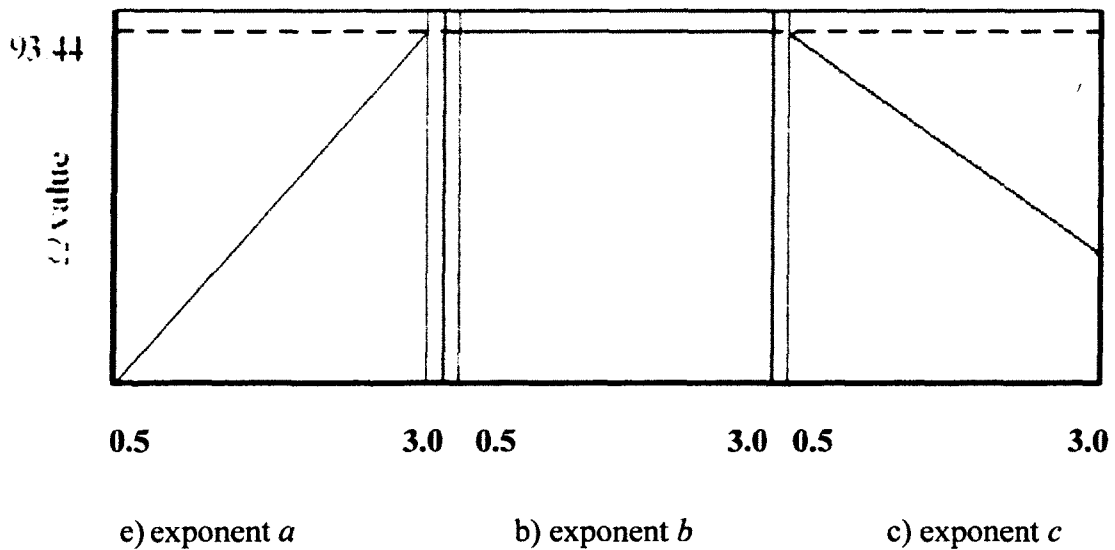


**Figure 4.8 Plot of the  $\Omega$  value vs. exponents  $a$ ,  $b$ , and  $c$ , respectively, in the range of 0.5 to 3.0.**

Four points for  $b$  from 0.5 to 3.0 (Table 4.18) were further tested and all  $\Omega$  values are identical, which indicates the optimal  $b$  value is between 0 and 0.5. Additional tests for  $b$  and  $c$  were carried out to verify whether there would be optimal points within the range of 0 to 0.5. Two one half two-level factorial designs after deleting identical terms were tested by fixing  $a$  as 3 and  $b$  and  $c$  at the ranges of 0.50 to 0.25 and 0.25 to 0, respectively, and the optimization graphs are shown in Figure 4.9 and Figure 4.10. The maximum  $\Omega$  values for all  $PI$ s, which are 93.44%, are those with  $c = 0.5$  and  $b = 0.50$ . Therefore the equation for  $PI$  is optimized as:

$$PI = \left(\frac{c}{5}\right)^3 \times \sqrt{\frac{(0.28+10.7 \times c+6.4 \times I)}{D \times L}} \quad (4-7)$$

**Table 4.18 Coefficients of determination for the microstructural features of NiCrAlY coatings with respect to the  $PI$  values for  $b$  from 0.50 to 3.00**

$PI$	$a$	$b$	$c$	Coefficient of determination, $R^2$				
				Crack	Porosity	Unmelted particle	Oxide	$\Omega$
$PI_5$	3.00	1.00	0.50	92.50	95.01	87.10	99.61	93.44
$PI_6$		1.50						
$PI_7$		2.00						
$PI_8$		2.50						

**Table 4.19 Coefficients of determination with respect to  $PI$  values from the two-level full factorial design**

$PI$	$a$	$b$	$c$	Coefficient of determination, $R^2$				
				Crack	Porosity	Unmelted particle	Oxides	$\Omega$
$PI_9$	3.00	0.25	0.25	89.51	92.33.	91.11	99.50	93.07
$PI_{10}$		0.50	0.50	92.50	95.01	87.10	99.61	93.44
$PI_{11}$		0.00	0.00	86.42	89.40	91.11	99.11	92.05

Substituting equation (4-7) into equation (4-6), a series of regression equations for the microstructural features of NiCrAlY coatings with respect to  $PI$  were derived and

are summarized in Table 4.20. An effective regressed equation should be at high confidence level so that the equation reflects the influences of the variables on the response function. All  $F$  values (Fisher value) in Table 4.20 are greater than the threshold  $F(3, 5, 0.95) = 5.41$ . Therefore the regression equations in Table 4.20 are all considered significant.

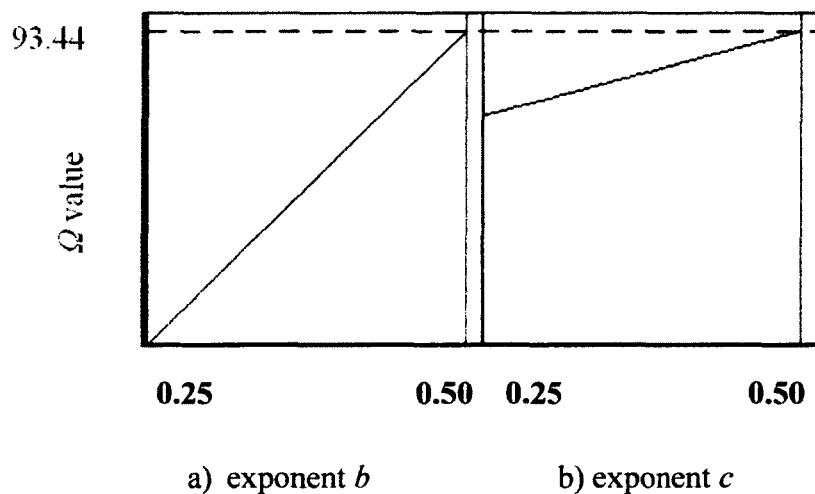


**Figure 4.9 Plot of the  $\Omega$  value vs. exponent  $b$  and  $c$ , respectively, in the range of 0.25 to 0.50.**

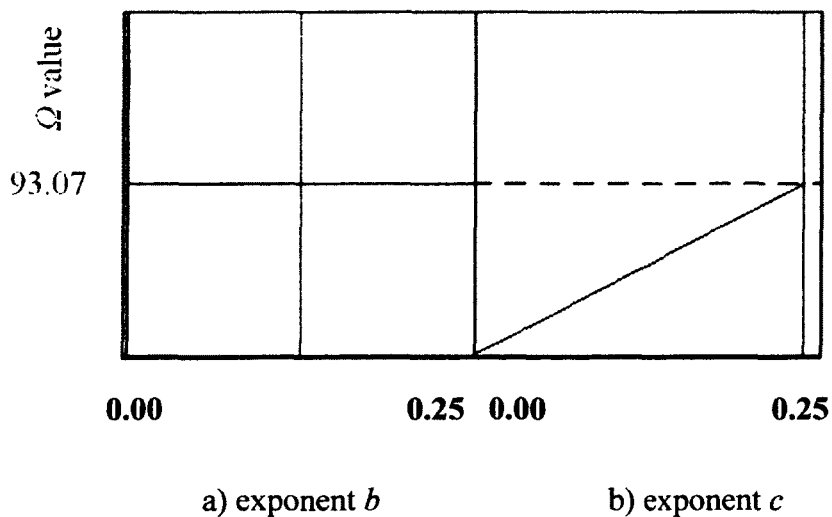
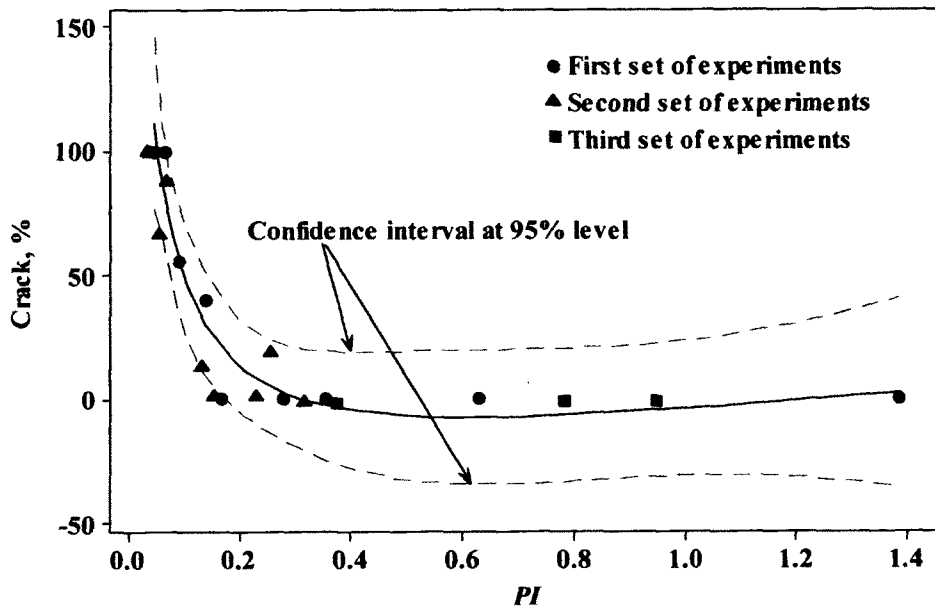


**Figure 4.10  $\Omega$  value vs. exponent  $b$  and  $c$ , respectively, in the range of 0 to 0.25.**

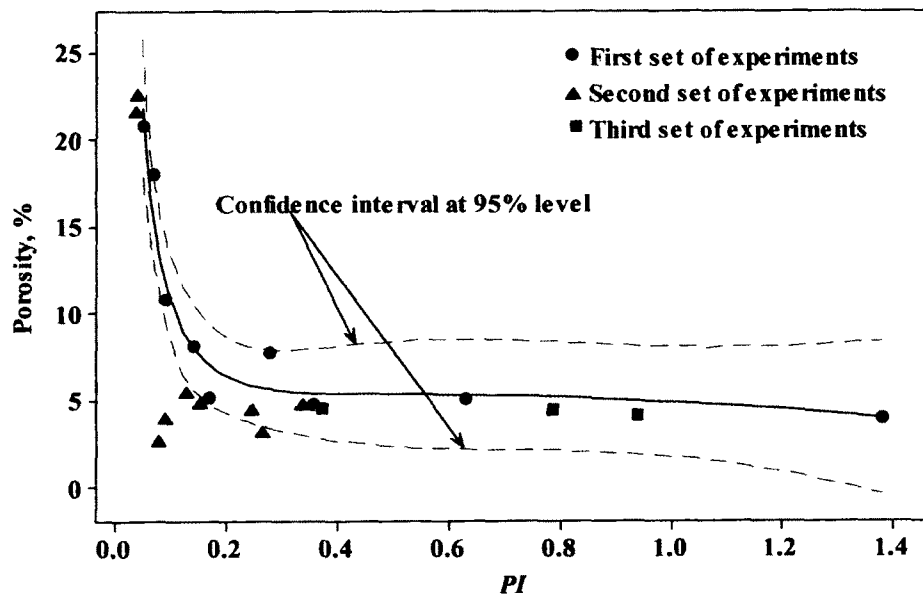
**Table 4.20 Regression equations for coating features with respect to  $PI$**

Coating feature	Regression Equation	$R^2$	$F$	Threshold $F$ value
Crack at interface	Crack, % = $-3.75 + 34.99 \times \log_{10}(PI) + 78.90 \times [\log_{10}(PI)]^2 - 10.01 \times [\log_{10}(PI)]^3$	92.50	20.67	
Porosity	Porosity, % = $4.38 - 4.02 \times \log_{10}(PI) - 13.04 \times [\log_{10}(PI)]^2 - 15.03 \times [\log_{10}(PI)]^3$	95.00	31.44	
Unmelted particle	Unmelted particle, % = $2.96 - 19.93 \times \log_{10}(PI) - 60.79 \times [\log_{10}(PI)]^2 - 52.60 \times [\log_{10}(PI)]^3$	87.10	11.27	5.41
Oxide	Oxide, % = $13.24 + 5.99 \times \log_{10}(PI) - 17.95 \times [\log_{10}(PI)]^2 - 10.42 \times [\log_{10}(PI)]^3$	99.60	466.94	

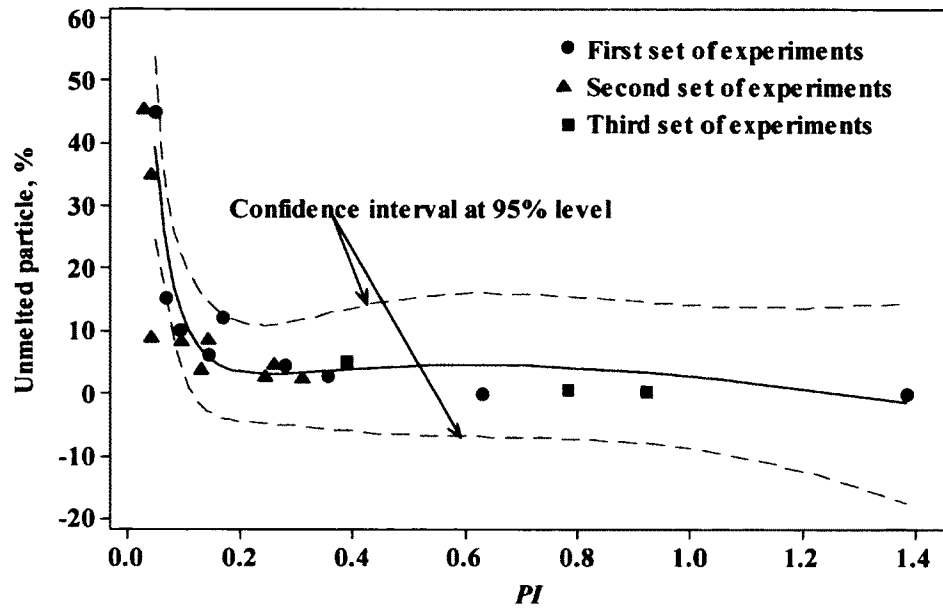
The four microstructural features of the coatings versus the  $PI$  values are illustrated in Figure 4.11. Also included in this figure are the results from the second and third sets of experiments. As seen in Figure 4.11, most data from the second and third set of experiments fall within 95% confident level of the data from the first set of experiments, and the values of coating features predicted by the regression equations all fall within 95% confidence level of the experimental data. Therefore, it can be concluded that the regression equations given in Table 4.20 fit well with the experimental results.



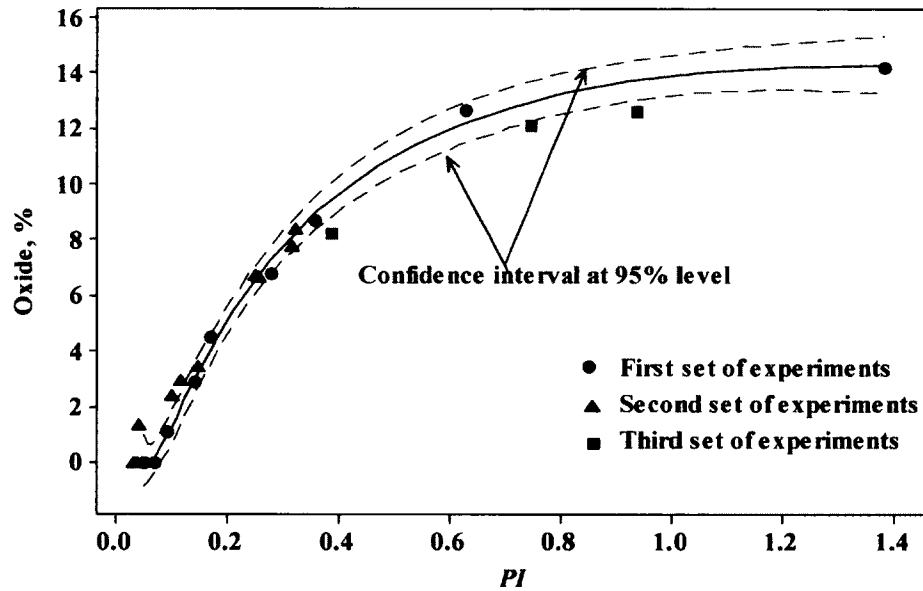
a) Measured and predicted crack percentage as a function of  $PI$



b) Measured and predicted porosity as a function of  $PI$



c) Measured and predicted unmelted particle percentage as a function of  $PI$



d) Measured and predicted oxide percentage as a function of  $PI$

**Figure 4.11 Comparison of predicted and measured values of the four microstructure features for the three sets of experiments.**

According to the comparison in Figure 4.11, the coating features can be categorized into three levels based on the *PI* values, as summarized in Table 4.21. When the *PI* value is less than 0.2, the coating has inferior quality, which represents the condition under which cracks go through the coating/substrate interface and large pores and unmelted particles are numerous within the coating. However, very limited oxides are found in the coating when the *PI* value is less than 0.2. When the *PI* values are greater than 0.2 but less than 0.4; there are moderate amounts of cracks, pores and unmelted particles and increased percentage of oxide. Whereas when  $0.6 > PI > 0.4$ , there are minimum cracks in the coating, and much less pores and unmelted particles within the coating but the amount of oxides exceeds 6%. There are no unmelted particles and cracks in the coatings when the *PI* values exceed 0.6 but the amount of oxides surpasses 10%.

**Table 4.21 Relation of coating features to *PI* values**

Conditions	Crack at interface, %	Porosity, %	Unmelted particle,%	Oxide, %
$0.2 > PI$	100	> 10	> 20	0
$0.4 > PI > 0.2$	20-100	5-10	10-20	0-6
$0.6 > PI > 0.4$	0	< 5	< 10	> 6
$PI > 0.6$	0	< 5	0	> 6

The purpose of another set of experiments was to verify the *PI* based the regression equations, which were derived from the first and second set of experiments. Table 4.22 provides comparison between the predicted and experimental results for the third set of experiments. The discrepancies between the predicted (using *PI* based empirical regression equations) and experimental results are trivial, which verifies the validity of

these *PI*-based regression equations (These regression equations are valid only within the designed scopes investigated in this study).

**Table 4.22 Comparison between the predicted and experimental results for the second set of experiments**

Coating	Crack at interface, %			Porosity, %		
	Experiment value	Predicted value	Relative error	Experiment value	Predicted value	Relative error
3-1	0.00	0.00	0.00	4.40	4.88	-10.90
3-2	0.00	0.00	0.00	4.30	4.68	-8.84
3-3	0.00	0.00	0.00	3.73	4.49	-20.37
Coating	Unmelted particles, %			Oxide, %		
	Experiment value	Predicted value	Relative error	Experiment value	Predicted value	Relative error
3-1	5.23	4.59	12.37	7.88	8.33	-5.71
3-2	0.00	4.47	-	11.10	12.40	-11.71
3-3	0.00	3.53	-	11.50	13.03	-13.30

#### 4.3.7 *PI* Development Guidelines for Other Thermal Spray Processes

The motivation for developing a *PI* is to estimate the microstructural features of coatings when defining initial spraying parameters. The method developed in this study can be applied to other thermal spray processes although coefficients for the regression equations will change from system to system. Based on the results of this study with Mettech Axial III™ system, the qualitative trends relating process parameters to coating microstructural features are applicable to other equipment based on the same operating principles, i.e., plasma based spray system systems. For other coating processes such as HVOF, VPS or cold spray, the following procedure can be used for developing their own *PI*:

(1) Determining the significance of process parameters. A Taguchi array or a factorial design is needed to determine the significance of process parameters and those parameters that are insignificant will be excluded from the *PI* equation.

(2) Introducing a *PI* equation. The equation is suggested to be in a fraction form. Process parameters that have the inverse effects on the particle velocity and temperature are considered as denominators and the others are numerators. The range of the exponents for each parameter can be started with 0 to 3.

(3) Introducing a factorial design for the exponents.

(4) Calculating *PI* values. The *PI* values from each test in the Taguchi array are calculated, as shown in Table 4.16.

(5) Proposing model(s). A model for all microstructural features of the coatings or separate model for each coating feature can be proposed. The *PI* will be the only variable.

(6) Calculating  $R^2$  for each *PI* and each model. The *PI* values are substituted into the models to calculate  $R^2$  using MS excel software or statistical software.

(7) Calculating the geometrical mean factor(s) of  $R^2$ .

(8) Maximizing the factor. The factor is maximized using statistical software such as Minitab. This step can be repeated until the maximal value of the factor and the corresponding exponents are found. The model is finalized by substituting the exponents into the *PI* equation and *PI* into the model.

(9) Testing the validity of model(s). Another set of experiments should be carried out to verify the validity of the model(s).

#### 4.4 Summary of Process Optimization for NiCrAlY Coatings

The effects of the plasma spray process parameters on the percentages of cracks along coating/substrate interface, pores, unmelted particles and oxide content in NiCrAlY coatings have been investigated with the purpose of developing a process index (*PI*). The *PI* value, combining the plasma spray process parameters, is the only variable to the regression equations for coating microstructural features. Regression equations were verified with acceptable values of  $R^2$  which are more than 87.1%, and successfully predicted the coating microstructural features within 95% confidence level.

Among the parameters examined, the powder size and ratio of  $H_2 + N_2$  over total gas flow rate are the most significant parameters affecting the percentages of crack, porosity, the amount of unmelted particle and oxide. Within the range of the designed process parameters, lower powder size and higher ratio of  $H_2 + N_2$  over total gas flow rate result in fewer cracks, pores, and unmelted particles but more oxides. Increasing nozzle size marginally increases the occurrence of oxides. Gas flow rate has no influence on any coating feature evaluated. Further study is underway to generate process index combining all process parameters into single value and relate this value to coating microstructure. In terms of the regression equations developed, a procedure for optimizing the spray process can be summarized as below:

- (1) estimate the coating properties, such as cracks, porosity and etc
- (2) determine the *PI* value
- (3) select process parameters according to equation (4-8) using an iterative process
- (4) conduct coating spray and fine tune the process parameters

In selecting spray parameters, the following rules are recommended:

(1) The maximum powder size should be as small as possible; however the minimum size must be larger than 5  $\mu\text{m}$ .

(2) Nozzle size is around 0.44 in (7/16).

(3) Spray distance is in the vicinity of 150 mm.

(4) Gas flow is between 200 and 300 SL/min.

(5) For metallic powder, the proportion of hydrogen should exceed that of nitrogen.

(6) Current is between 200 and 250 A.

## **Chapter 5: Process Optimization for Diffusion Coatings**

### **5.1 Process Optimization for the Aluminide Coatings**

The objective of process optimization for the aluminized top layer is to achieve a quantitative relation between the coating features and the process parameters, and this relation can be used to produce a desirable multilayered coating with pre-determined compositions. Similarly the method of design of experiment (DOE) was used for the process optimization. Compared the screening function of other DOE statistical methods, response surface methodology emphasizes the optimization of a process and it has been extensively utilized to determine the influence of key process parameters on the coating features and predict the coating microstructure features [110]. The reasons for producing an response surface model for the aluminizing process are to [110]:

- achieve a quantitative understanding of the behavior of the coating over the testing region
- predict the coating properties throughout the region
- determine the optimum conditions for the aluminizing process
- find the conditions for aluminizing process stability

For this study, three process parameters, Al and Ni concentrations in the pack and process temperature, and their effects on the coating microstructural features were investigated. As outward-diffusion process produces coatings with reduced alloying contents (such as Ti) from the substrate, the process temperatures were kept within the “high temperature (HT)” region. The experimental procedure is further outlined in the following section.

### 5.1.1 Experimental Procedure

The coating specimens used in this study were 304L austenitic stainless steel (SS304L) plates coated with NiCrAlY by the plasma spray process. The dimensions of the specimens, NiCrAlY powder, and powders for aluminized coatings are given in Table 5.1. The compositions of SS304L and IN738 are listed in Table 5.2. IN738 is the substrate for the Cr-Si coating, and SiO<sub>2</sub>, Cr, and Si powders were also used to produce the Cr-Si coating, which will be discussed in the next section.

**Table 5.1 Conditions of the specimens for the aluminizing process**

	Composition or material	Dimension or coating thickness	Designation
NiCrAlY	Ni-22Cr-10Al-1Y	200 $\mu\text{m}$	
Substrate	SS304L	25 × 25 × 1.6 mm	
Al powder	99.0 wt.% Al		AL-104
Ni powder	5.0 wt.% Al, 95.0 wt.% Ni		480 NS
NH <sub>4</sub> Cl	99.9 wt.%		A649-3
Al <sub>2</sub> O <sub>3</sub> powder	99.0 wt.%		ALO-101
SiO <sub>2</sub> powder	99.9 wt.%		SI 604
Cr powder	99.8 wt.%		CR 105
Si powder	99.0 wt.%		SI 101

**Table 5.2 Compositions of SS304L and IN738**

	Composition, wt.%										
	Cr	Co	Mo	Ta	C	Ti	Al	Nb	W	Ni	Fe
SS304L	19.0				0.03					10.0	Bal.
IN738	16.0	8.5	1.8	1.8	0.2	3.4	3.4	0.9	2.6	61.0	

The specimens were ultrasonically cleaned in acetone and buried in the powder mixtures listed in Table 5.3, respectively, with alumina crucibles. The crucibles were placed in the center region of the heating zone of a laboratory tube furnace. The tube furnace consisted of an alumina tube (100 mm ID and 1000 mm length) and was heated by an 8 kw radio frequency generator. The temperature at the center of the heating zone

was measured by a B-type thermocouple, and the temperature variation along the axial direction of the heating zone during these experiments was measured to be within  $\pm 5^{\circ}\text{C}$ . The heating and cooling rate of the furnace was kept at  $3^{\circ}\text{C}/\text{min}$ , and all specimens were held at the aluminizing temperature for 4 hr. An argon atmosphere was maintained during the heating, aluminizing and subsequent cooling processes. The Ar flow rate was kept between 400 and 500 Std. ml/min.

The cross sections of the coatings were characterized using the TESCAN scanning electron microscopy (SEM). The percentages of key alloying elements in the aluminide coatings were measured by EDS in an increment of  $10\ \mu\text{m}$  from the coating surface toward the substrate.

A Box–Behnken experimental design was used to evaluate three process parameters of the aluminizing processes over three levels. All process parameters are summarized in Table 5.3. This design requires 15 experiments to produce a response surface model for the process.

**Table 5.3 Box–Behnken design for the aluminizing process**

Parameter	<i>A</i>	<i>N</i>	<i>T</i>	Activator	Filler	Duration
Level	Al, wt.%	Ni, wt.%	Temp., $^{\circ}\text{C}$	$\text{NH}_4\text{Cl}$ , wt.%	$\text{Al}_2\text{O}_3$ , wt.%	hr
0	5	5	1000			
1	10	10	1050	2	balance	4
2	15	15	1100			

The 15 experiments, which were designated as the coating numbers, are given in Table 5.4 along with corresponding process parameters. The process parameters selected lie on the mid-points of all cubic edges as illustrated in Figure 5.1. In addition, a center point was also selected to run in three independent trials to quantify

experimental variance. The coating thickness and the maximum ratio of Al content to Ni content in the coatings were measured and acted as responses for creating response surface models and plots.

**Table 5.4 Parameters for aluminizing process**

Coating	Al in pack, wt. %	Ni in pack, wt. %	Al in Al source, at. %	Ni in Al source, at. %	Temp., °C
4-1	5	5	69	32	1050
4-2	15	5	87	13	1050
4-3	5	15	42	58	1050
4-4	15	15	69	31	1050
4-5	5	10	52	48	1000
4-6	15	10	77	23	1000
4-7	5	10	52	48	1100
4-8	15	10	77	23	1100
4-9	10	5	81	19	1000
4-10	10	15	59	41	1000
4-11	10	5	81	19	1100
4-12	10	15	59	41	1100
4-13	10	10	68	32	1050
4-14	10	10	68	32	1050
4-15	10	10	68	32	1050

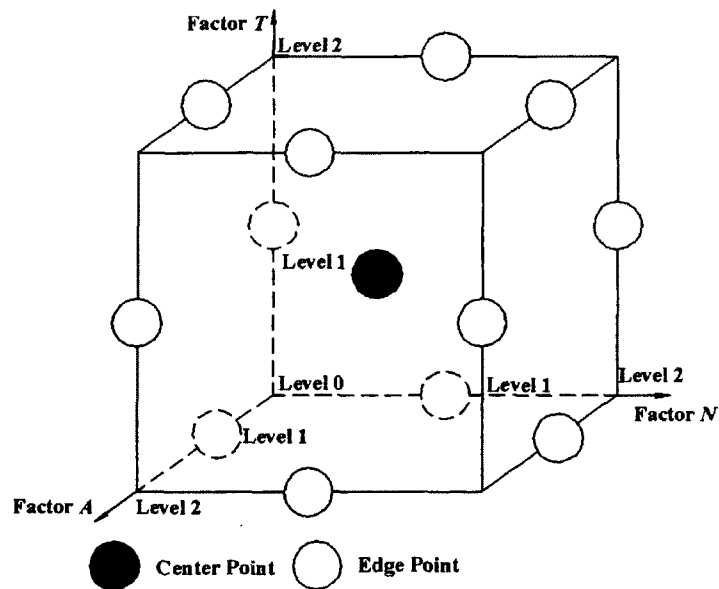


**Figure 5.1 Pictorial representation of a three-level Box-Behnken response surface design for the aluminizing process.**

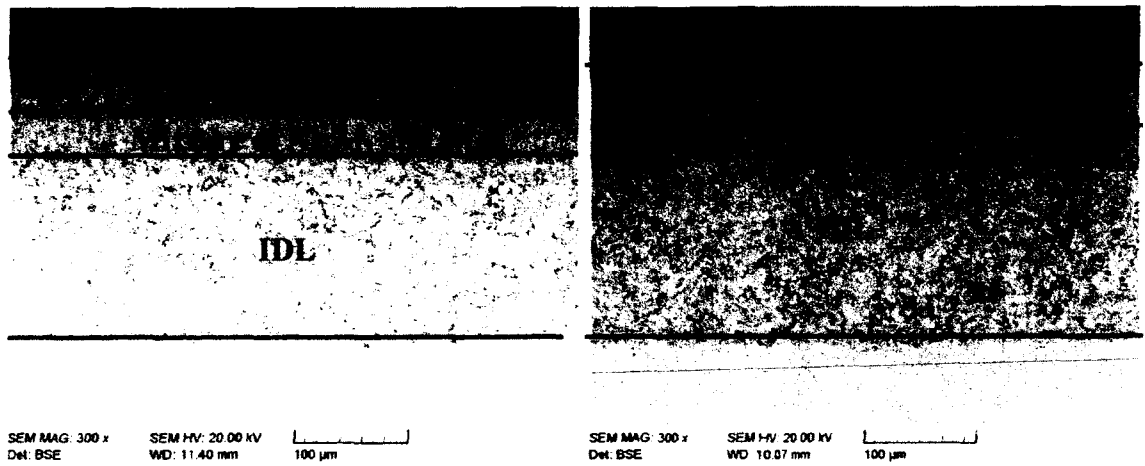
### 5.1.2 Elemental Distribution and Microstructure

The specimens for these experiments were designated as coating 4-1 to specimen 4-15. The microstructures of the aluminized layers were on the basis of elemental distributions and XRD results of the aluminized layers. The ratio of aluminum to nickel (at.%) in a coating is used to estimate phases in the coating (Table A.). When the ratio is around one, the dominant phase is NiAl, whereas the dominant phase is Ni<sub>2</sub>Al<sub>3</sub> if the ratio is around 1.5.

Two coating specimens, 4-1 and 4-7 shown in Figure 5.2, were selected for microstructure analysis. Cross section images of coating 4-1 and 4-7 are illustrated in Figure 5.3. The concentration profiles of the two selected coating specimens are illustrated in Figure 5.4. The diagram of the Al/Ni ratio versus the distance from coating surface for specimen 4-1 and specimen 4-7 is illustrated in Figure 5.5.



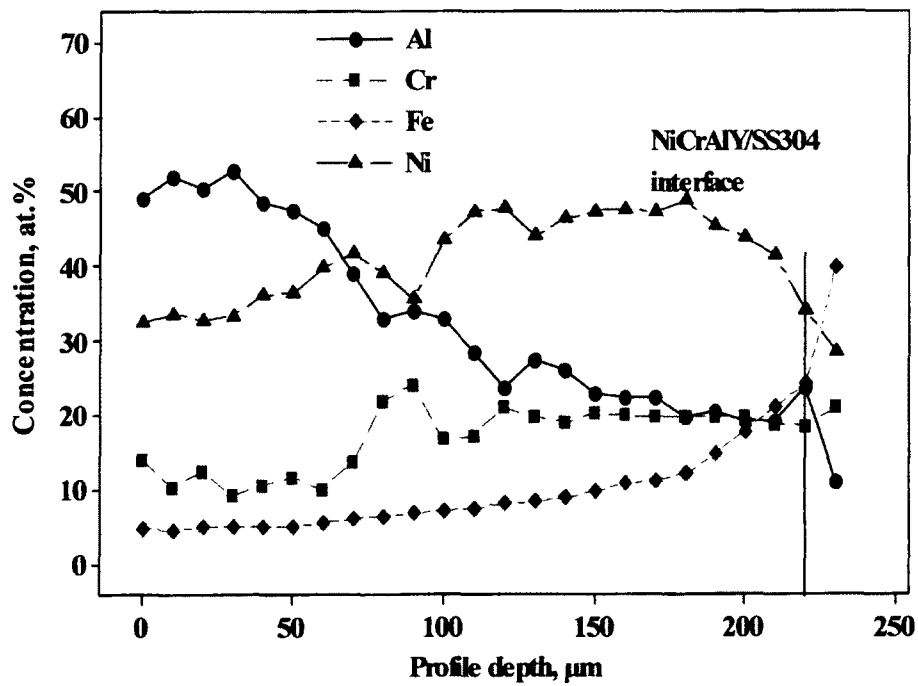
**Figure 5.2 Image of coating 4-1 and 4-7.**



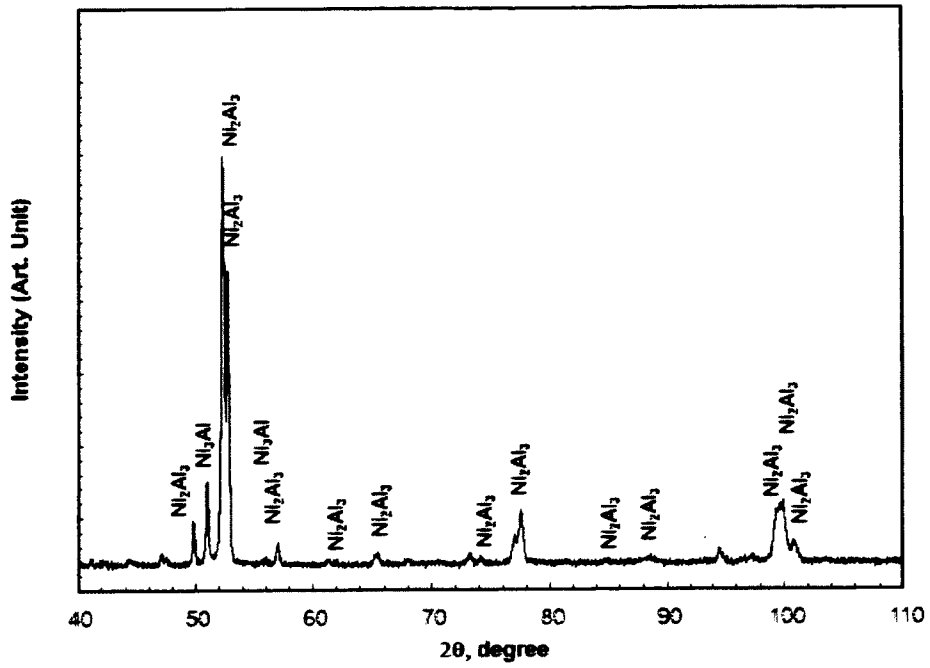
a) three-layer structure of coating 4-1

b) two-layer structure of coating 4-7

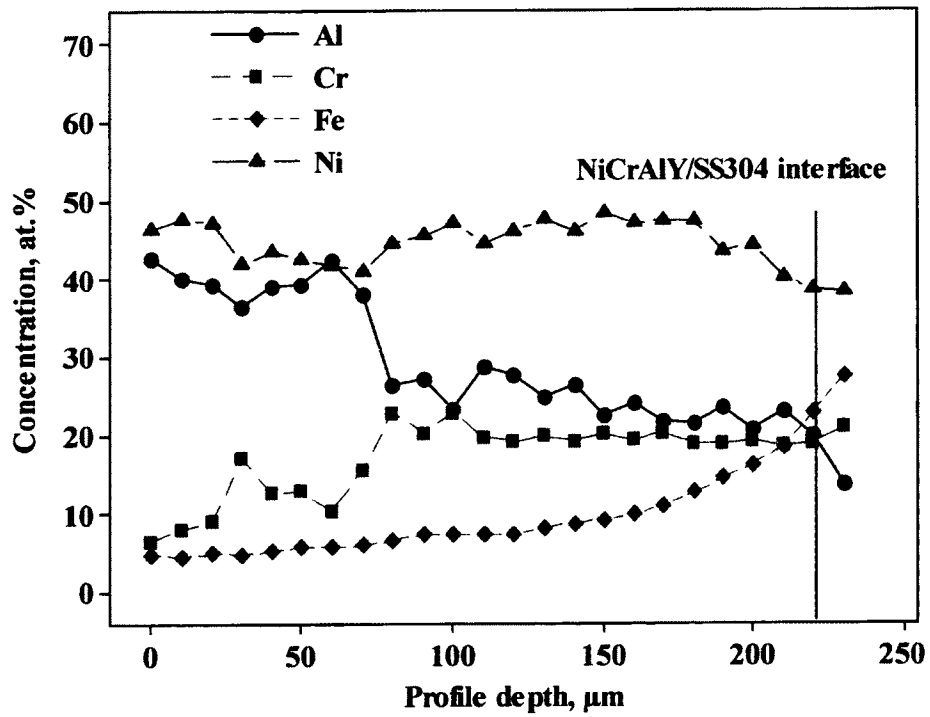
Figure 5.3 Cross section images of the coating 4-1 and 4-7.



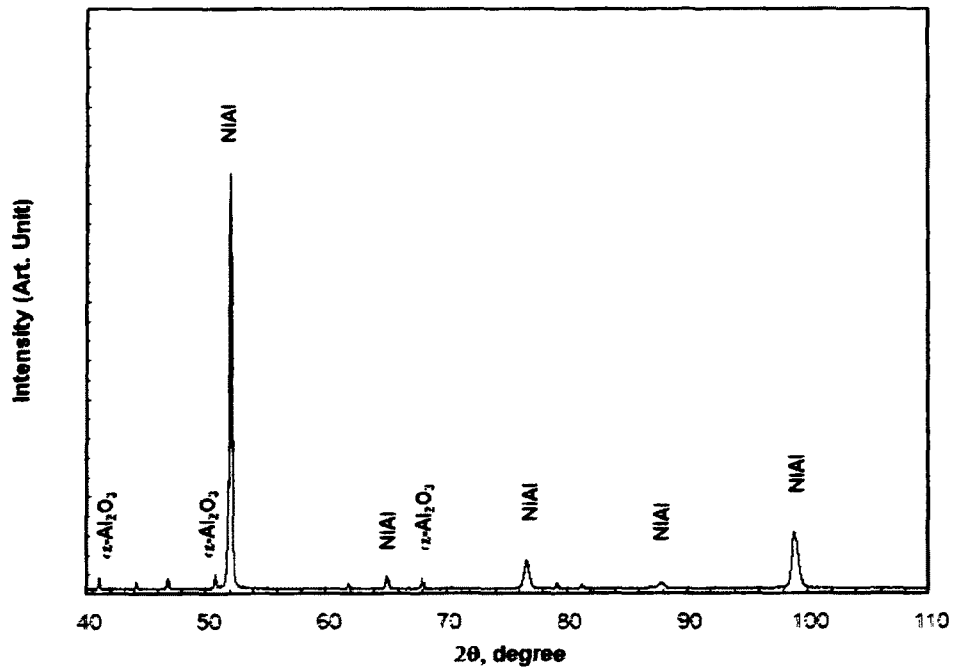
a) Concentration profiles of Al, Si, Cr, and Ni in coating 4-1



b) XRD spectrum of coating 4-1



c) Concentration profiles of Al, Si, Cr, and Ni in coating 4-7



d) XRD spectrum of coating 4-7

Figure 5.4 Concentration distribution and XRD spectra for coating 4-1 and 4-7.

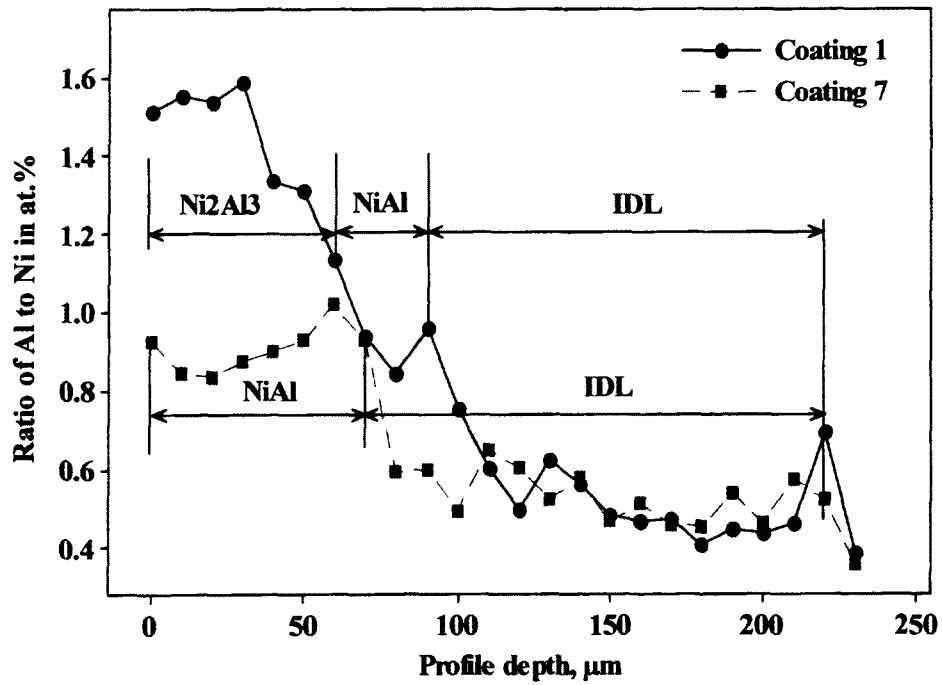


Figure 5.5 Ratio of Al at.% to Ni at.% versus the distance from coating surface for coating 4-1 and 4-7.

Based on the curve of Al/Ni ratio, specimen 4-1 has a three-layer structure that consists of an outer layer of Ni<sub>2</sub>Al<sub>3</sub> or a mixture of Ni<sub>2</sub>Al<sub>3</sub> and NiAl, an intermediate NiAl layer, and an inner diffusion layer (IDL), whereas specimen 4-7 has a two-layer structure that consists of an outer NiAl layer and an inner diffusion layer (IDL). The phases for top layers of specimen 4-1 and specimen 4-7 were verified as Ni<sub>2</sub>Al<sub>3</sub> and NiAl, respectively, based on the XRD spectra in Figure 5.4. The microstructures of other coating were estimated based on the Al/Ni ratios and are listed in Table 5.5. Beneath the diffusion layer, the microstructure is observed to be mainly  $\gamma$  (Ni) and  $\gamma'$  (Ni<sub>3</sub>Al), a typical NiCrAlY structure.

**Table 5.5 Coating thickness and the maximum ratio of aluminum to nickel content**

Coating	Coating thickness, $\mu\text{m}$	Al/Ni ratio	Coating microstructure
4-1	180	1.59	Three layer
4-2	280	2.55	Three layer
4-3	110	1.08	Two layer
4-4	200	1.98	Three layer
4-5	90	0.90	Two layer
4-6	140	2.10	Three layer
4-7	150	0.93	Two layer
4-8	210	1.83	Three layer
4-9	130	1.59	Three layer
4-10	130	1.39	Three layer
4-11	180	1.73	Three layer
4-12	120	1.47	Three layer
4-13	190	1.60	Three layer
4-14	170	1.64	Three layer
4-15	170	1.81	Three layer

### 5.1.3 Coating Thickness and Al/Ni Ratio

Also observed on the concentration profiles are minimum/maximum points of nickel (and chromium) contents in the coatings due to simultaneous aluminum inward (reduce nickel and chromium) and nickel outward diffusion (reducing nickel and increase

chromium). The coating thickness was defined as the distance from the surface to where the maximum nickel content was observed in the concentration profiles (Figure 5.4). The coating thickness and the maximum ratio of aluminum to nickel content (at.%) in the coatings were measured and the results were also included in Table 5.5. These results acted as the responses for creating response surface and plots.

#### 5.1.4 Analysis of Variance for Coating Thicknesses and Al/Ni Ratios

The two variations (coating thickness and maximum Al/Ni atomic ratio) for the aluminized coatings are summarized in two ANOVA tables (Table 5.6 and Table 5.7). In addition to the variations, these tables also contain the freedoms and mean squares of the coatings,  $F$  values and  $p$ -values. The assumption of the null hypothesis is valid when the  $p$ -value for a parameter is less than a significance level  $\alpha$ . The significance level in these tests was set to be 0.05. A parameter, however, cannot be eliminated if it appears in the higher order terms of the parameter even its  $p$ -value is greater than the significant level.

**Table 5.6 ANOVA table for coating thickness**

Source	Degree of freedom	Sum of squares	Mean square	$F$ value	$p$ -value
Model	4	35109.40	8777.35	13.75	0.000
Linear	3	26875.00	9938.43	15.57	0.000
$A$ , Al%	1				0.001
$N$ , Ni%	1				0.012
$T$ , Process temp. (°C)	1				0.005
Quadratic	1	8234.40	8234.40	12.90	0.004
$T \times T$		8234.40	8234.40		0.004
Residual	10	6383.90	638.39		
Lack of fit	8	4983.90	622.99	0.89	0.629
Pure error	2	1400.00	1400.00		
Total	14	41493.30			
$R^2$		84.61%			

After eliminating the insignificant terms, the significant terms for the coating thickness and Al/Ni ratio are given in Table 5.6 and Table 5.7 respectively. The  $p$ -values of lack-of-fit and  $R^2$  values show that the response surface model and experimental data have a very high degree of fitness.

**Table 5.7 ANOVA table for ratio of Al to Ni**

Source	Degree of freedom	Sum of squares	Mean square	$F$ value	$p$ -value
Model	5	2.5495	0.5099	35.03	0.000
Linear	3	2.2567	0.7522	51.68	0.000
$A$ , Al%	1				0.000
$N$ , Ni%	1				0.001
$T$ , Process temp. (°C)	1				0.955
Quadratic	2	0.2928	0.1464	10.06	0.005
$N \times N$	1				0.041
$T \times T$	1				0.003
Residual	9	0.1310	0.1310		
Lack of fit	7	0.1061	0.01516	1.22	0.521
Pure error	2	0.0249	0.00125		
Total	14	2.6805			
$R^2$	95.77%				

### 5.1.5 Regression Equation for Coating Thickness and Al/Ni Ratio

The regression equations for coating thickness ( $Y_T$ ) and the maximum Al/Ni ratio ( $Y_R$ ) in terms of the process parameters were developed using Minitab software and are given below:

$$Y_T = -18789.30 + 7.50 \times A - 5.25 \times N + 35.675 \times T - 16.79 \times 10^{-3} \times T^2 \quad (5-1)$$

$$Y_R = -108.504 + 0.099 \times A - 0.126 \times N + 0.209 \times T + 4.415 \times 10^{-3} \times N^2 - 99.846 \times 10^{-6} \times T^2 \quad (5-2)$$

As mentioned early, the analysis of a regression equation of response surface includes three aspects:

(1) Location of stationary points

The stationary points of the regression equations are determined by taking the partial derivative of  $Y_T$  and  $Y_R$  with respect to the factor terms. The values or formulas of the partial derivatives of the regression equations are summarized in Table 5.8.

**Table 5.8 Values or formulas of the partial derivatives**

Partial derivative	Value or formula	Stationary point
$\frac{\partial Y_T}{\partial A}$	7.505	
$\frac{\partial Y_T}{\partial B}$	-5.251	
$\frac{\partial Y_T}{\partial C}$	$35.675 - 33.580 \times 10^{-3} \times C$	1062°C, max
$\frac{\partial Y_R}{\partial A}$	0.099	
$\frac{\partial Y_R}{\partial B}$	$-126.808 \times 10^{-3} + 8.831 \times 10^{-3} \times B$	14.36, min
$\frac{\partial Y_R}{\partial C}$	$209.627 \times 10^{-3} - 199.692 \times 10^{-6} \times C$	1050°C, max

Based on the results in Table 5.8, the following conclusions are reached:

- Coating thickness increases with the Al content in the pack and decreases with the Ni content in the pack. The relation of coating thickness with Al and Ni contents is linear.
- The relation of coating thickness with the temperature is parabolic and the temperature at which the maximum coating thickness reaches is 1062°C.
- Al/Ni ratio increases linearly with Al content in the pack.

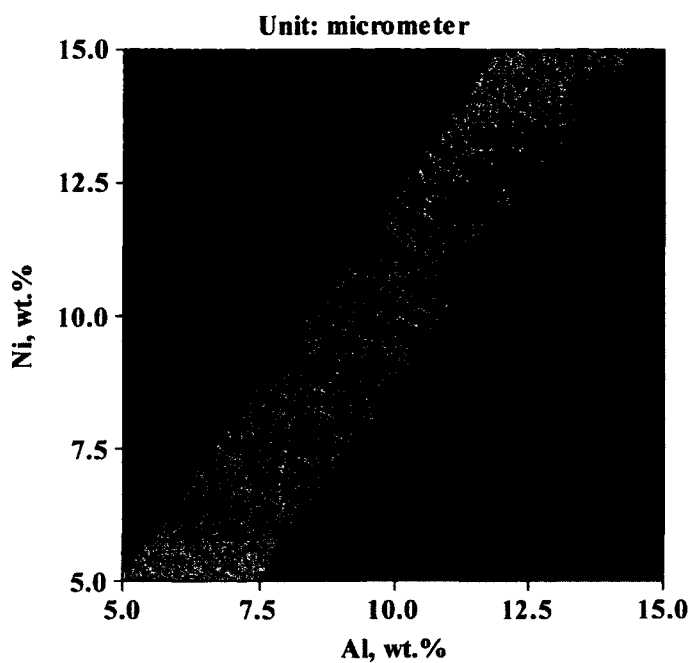
- The relation of Al/Ni ratio with the Ni content in the pack is parabolic. Al/Ni ratio decreases with the Ni content, and reaches the minimum point at 14.36 wt.% Ni.
- The relation of Al/Ni ratio with the temperature is parabolic as well. The temperature at which the maximum Al/Ni ratio reaches is 1050°C.
- A saddle point can be found at 14.36 wt.% Ni % and 1050°C.

Among the stationary points, the saddle point is most important since the variations of Al/Ni ratio are less intense with respect to the Ni content and temperature around the saddle point; such a phenomenon provides a chance for developing a robust process.

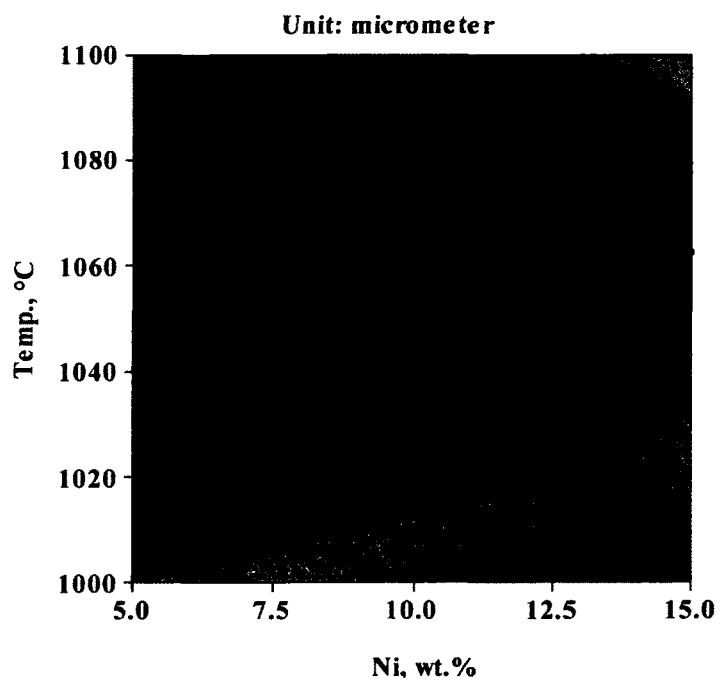
## (2) Evaluation of response surfaces and contour plots

As can be seen from equation (5-1), there are three linear terms and only one quadratic term of the temperature (C) in the regression equation of coating thickness. The quadratic temperature term suggests that the response surface of coating thickness with the fixed temperatures is a flat surface and the equivalent lines in the corresponding contour plot are straight lines (Figure 5.6a), whereas the response surface of coating thickness with the temperature is a curved surfaces and the equivalent lines in the corresponding contour plot are parabolic lines (Figure 5.6b), and coating thickness reaches the maximum at 1062°C.

Similarly there are three linear terms and two quadratic terms (temperature C and Ni content B) in the regression equation of the Al/Ni ratio. The response surfaces of Al/Ni ratio with the factors are all curved surfaces and the equivalent lines in the corresponding contour plots are parabolic lines (Figure 5.7).

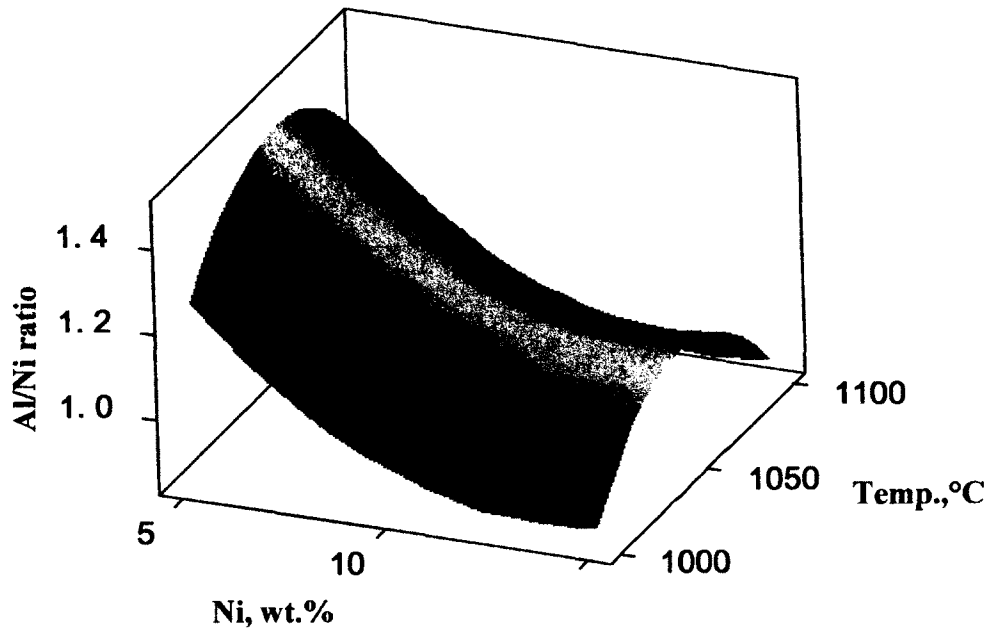


(a) Contour plot of coating thickness at 1000°C

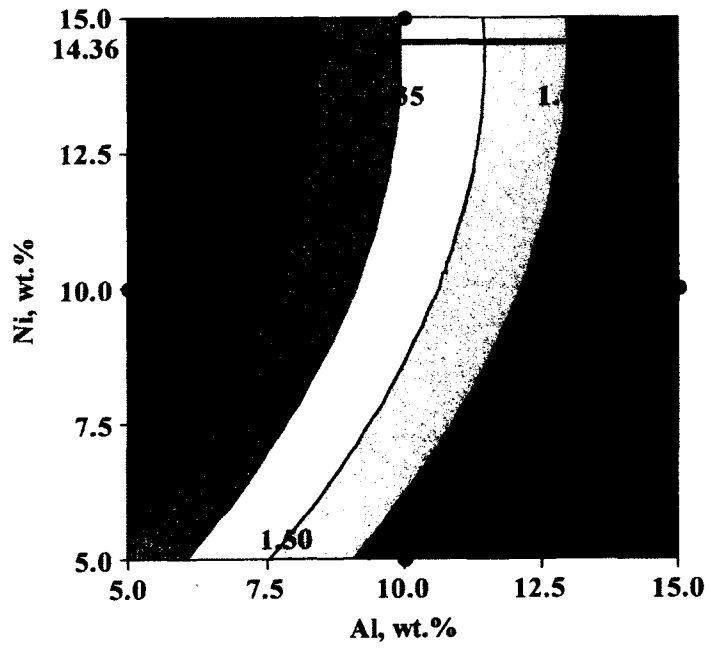


(b) Contour plot of coating thickness at 5 wt.% Al

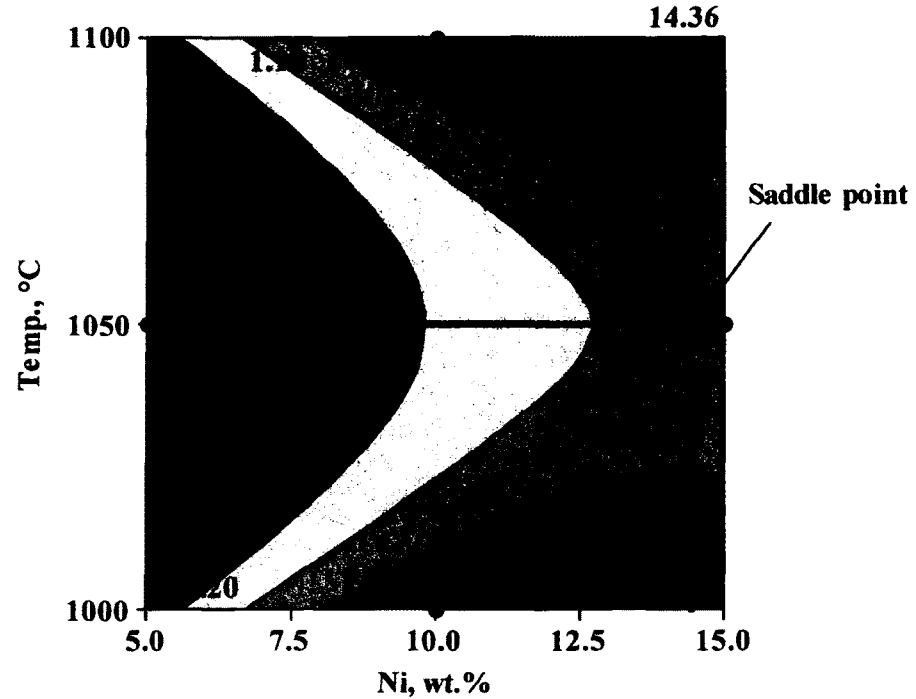
**Figure 5.6** Contour plots of the coating thickness.



(a) Response surface plot of Al/Ni ratio at 5 wt.% Al



(b) Contour plot of Al/Ni ratio at 1000°C



(c) Contour plot of Al/Ni ratio at 5 wt.% Al

**Figure 5.7 Response surface and contour plots of the Al/Ni ratio.**

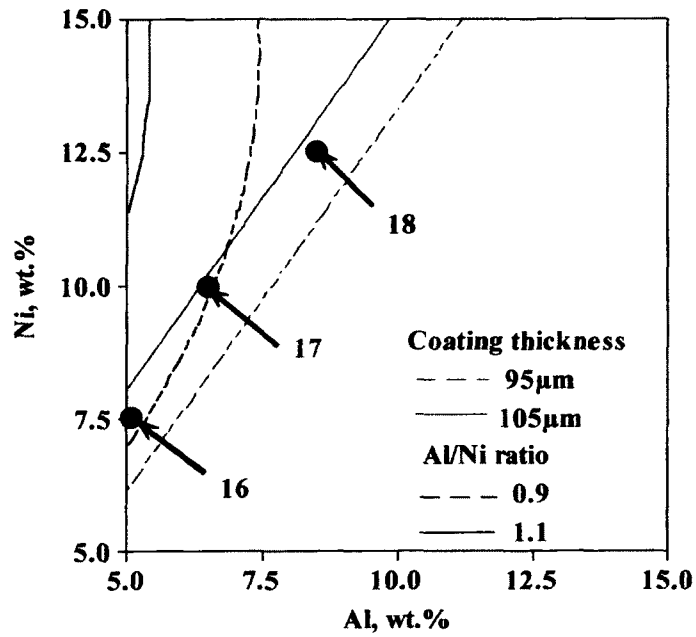
Coating thickness and the maximum Al/Ni ratio in the aluminized coatings depend on the activity of Al during the diffusion process. The Al content in the powder mixture increases Al activity (driving force) while the Ni content decreases Al activity; which are reflected in the regression equations. The experimental results clearly illustrates that the high Al activity resulted from the higher Al content in the pack led to an Al-rich  $\text{Ni}_2\text{Al}_3$  layer at higher Al/Ni ratio due to promoting Al-inward-diffusion and also increased coating thickness, whereas the low Al activity resulted from the higher Ni content in the pack led to a NiAl layer at lower Al/Ni ratio due to Ni outward-diffusion and coating thickness is thinner.

Temperature also plays an important role in the coating formation and composition. At a relatively low temperature the growth of a coating takes place primarily due to Al inward-diffusion. As the temperature increases, the thickness and Al/Ni ratio of the coating increase until the temperature is high enough for the Ni-outward-diffusion to dominate the coating growth, and then the coating thickness and Al/Ni ratio decrease with the temperature. Therefore there are maximum points for coating thickness and Al/Ni ratio with respect to the temperature in the response surface and contour plots (Figure 5.7).

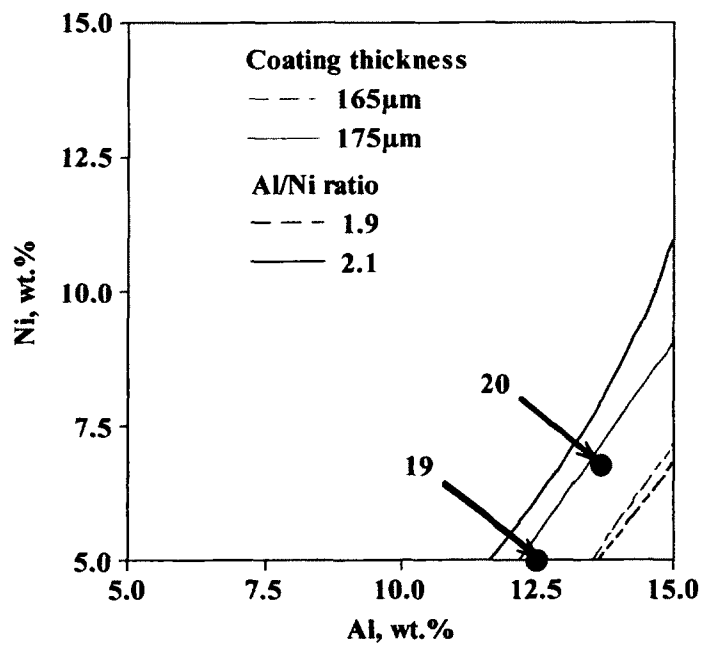
(3) Optimization of the coating thickness and the Al/Ni ratio by overlaying the contour plots

The optimization of both the coating thickness and the Al/Ni ratio was carried out by additional set of experiments. The aim of these experiments was to obtain (a) a coating with a targeted range of thickness between 95 to 105  $\mu\text{m}$  and an Al/Ni ratio between 0.9 to 1.1, and (b) a coating with a thickness between 165 to 175  $\mu\text{m}$  and an Al/Ni ratio from 1.9 to 2.1.

By observing the parameters from overlapped contour plots of the coating thickness and the Al/Ni ratio, five points were selected at 1000°C, as shown in Figure 5.8a and Figure 5.8b. The other four experiments were carried out at 1050°C and 1100°C to testify the validity of the regression equations at these temperatures. These additional experiments were assigned coating numbers 16 to 24. Table 5.9 provides parameters for each test.



(a) Coating thickness from 95 to 105 μm and Al/Ni ratio from 0.9 to 1.1



(b) Coating thickness from 165 to 175 μm and Al/Ni ratio from 1.9 to 2.1

**Figure 5.8 Overlapped contour plots for response surface models at 1000°C.**

**Table 5.9 Process parameters of additional tests for model verification**

Factor	Parameter								
	16	17	18	19	20	21	22	23	24
Al, wt.%	5.0	6.5	8.5	12.5	13.5	5.0	5.0	6.5	8.6
Ni, wt.%	7.5	10.0	12.5	5.0	7.0	10.0	12.0	10.0	12.5
Temp., °C	1000	1000	1000	1000	1000	1050	1050	1100	1100

The discrepancies between the predicted and experimental results are shown in Table 5.10. The differences between the experimental results and the predicted values are acceptable, which verifies the validity of the regression equations. The parameters for coating 17 and 20 were selected to fabricate the aluminized layer of multilayered coatings

**Table 5.10 Comparison between the predicted and experimental results**

Test	Coating thickness $\mu\text{m}$ ,			Al/Ni ratio		
	Experiment value	Predicted value	Relative Error, %	Experiment value	Predicted value	Relative Error, %
16	120	100	16.67	1.09	1.06	2.75
17	110	100	9.09	1.09	1.08	0.92
18	110	100	9.09	1.23	1.21	1.62
19	190	170	10.52	2.18	2.04	6.42
20	200	170	15.00	2.14	1.94	9.34
21	140	150	6.67	1.01	1.15	13.86
22	140	140	0.00	0.94	1.09	15.95
23	120	140	16.67	0.94	1.07	13.82
24	140	140	0.00	1.12	1.21	8.03

## 5.2 Process Development for Cr-Si Coatings

### 5.2.1 Experimental Procedure

The purpose of process development for a Cr-Si coating is to obtain a coating with 25-30% at.% Si and 25-30% at.% Cr on IN738. In order to achieve this goal, a Taguchi L4 array with two-levels and three factors was designed and is listed in Table 5.11. The

process parameters for each experiment are given in Table 5.12. The specimens for these experiments were designated as coating 5-1 to specimen 5-4. The experimental procedure was similar to the experimental procedure for aluminizing process that is described in section 5.1.1. A coating specimen is shown in Figure 5.9. Coating features, which include coating thickness, phases, and elemental distributions, were investigated after the coatings in Table 5.12 were produced.

**Table 5.11 Taguchi L4 array for the process development of Cr-Si coating**

Level	Metallic powder, wt. %	Si in metallic powder, wt. %	Cr in metallic powder, wt. %	Temp., °C
0	30	70	30	1100
1	40	60	40	1000

**Table 5.12 Parameters for the L4 array**

Coating	Si in powder, wt. %	Cr in powder, wt. %	NH <sub>4</sub> Cl in powder, wt. %	Al <sub>2</sub> O <sub>3</sub> in powder, wt. %	SiO <sub>2</sub> in powder, wt. %	Temp., °C	Time, hr
5-1	21	9		34	34	1100	
5-2	18	12	2	34	34	1000	4
5-3	28	12		29	29	1000	
5-4	24	16		29	29	1100	

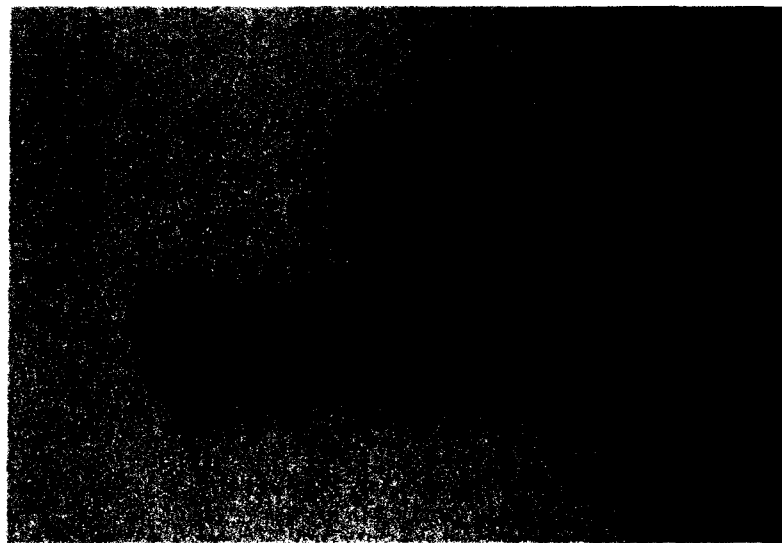


**Figure 5.9 Image of coating 5-4.**

### 5.3 Cr-Si Coating Thickness

The Cr-Si coating thickness was measured using image analysis software; the results are given in Table 5.13. A plot of the coating thicknesses against process parameters is provided in Figure 5.10. Examination of Figure 5.10 reveals two important aspects: one is that the thickness increases with an increase in the percentage of metallic powder in the powder mixture, silicon content in the metallic powder, and temperature; the other is that the effect of the percentage of metallic powder in powder mixture on coating thickness is larger than other two parameters, i.e., the coatings with more metallic powder in powder mixture are much thicker than those with less metallic powder. As the coating thickness is not the target to be optimized, there is no need to analyze the SNRs for process parameters.

**Table 5.13 Coating thickness for Cr-Si coating**

Specimen	5-1	5-2	5-3	5-4
Coating thickness, $\mu\text{m}$	50	40	70	70

#### 5.3.1 Optimization of Cr-Si Coating Process

To select the optimal process, the ideal values for silicon and chromium contents in a coating were set at 30 at.% and 25 at.%, respectively, and then the differences between measured data and ideal values are expected to be as small as possible. The differences between measured data and ideal values for silicon and chromium contents were defined as  $\Delta\text{Si}$  and  $\Delta\text{Cr}$ , as shown in Table 5.14. The process was optimized based on the Taguchi's smaller-the-better function for SNRs of  $\Delta\text{Si}$  and  $\Delta\text{Cr}$ .

The optimal parameters for minimizing the differences are summarized in Table 5.15 based on the plot of the SNRs versus process parameters (Figure 5.11b and Figure

5.12b). The process parameters for generating optimized silicon and chromium content are identical; they happened to be the process parameters used for coating 5-4. These parameters will be used to fabricate the final multilayered coating.

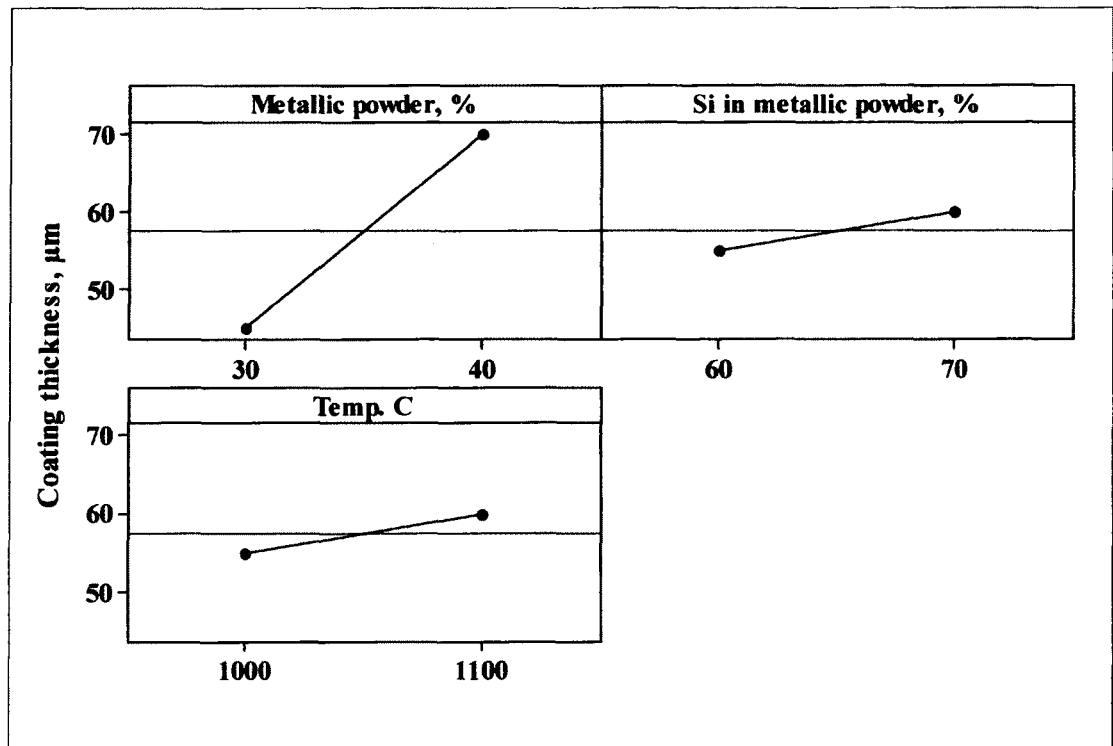


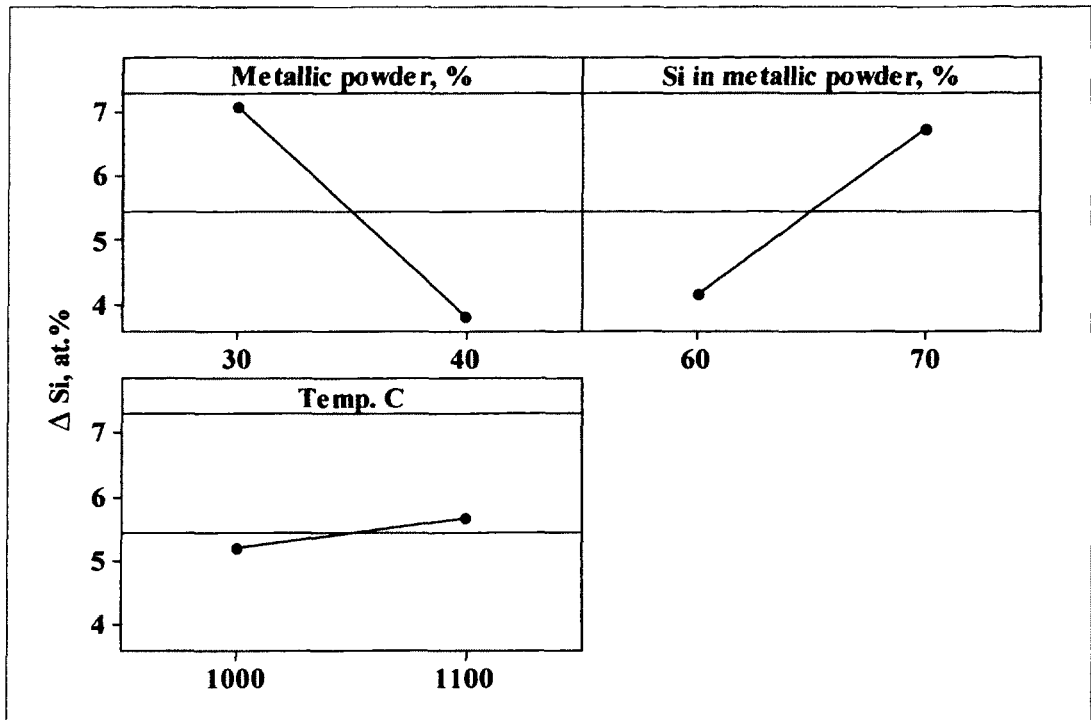
**Figure 5.10 Coating thickness versus process parameters.**

**Table 5.14 Concentrations of Si and Cr and the differences between measured data and ideal values in Cr-Si coatings**

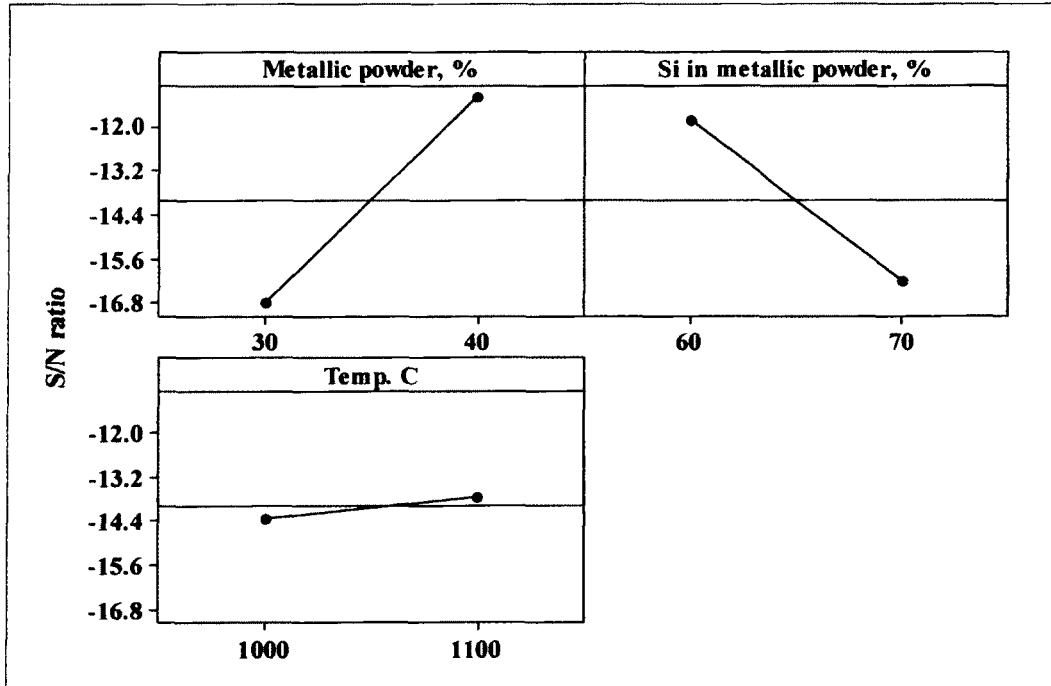
Specimen	Distance from coating surface, $\mu\text{m}$	Composition, at.%			
		Si	$\Delta\text{Si}$ (Si - 30)	Cr	$\Delta\text{Cr}$ (Cr - 25)
5-1	0	21.38	-8.62	13.51	-11.49
	10	18.31	-11.69	20.08	-4.92
	20	13.67	-16.33	18.52	-6.48
	30	13.53	-16.47	17.94	-7.06
	40	17.94	-12.06	12.97	-12.03
	50	15.07	-14.93	15.58	-9.42
5-2	0	24.44	-5.56	15.14	-9.86
	10	23.24	-6.76	22.22	-2.78
	20	17.26	-12.74	15.82	-9.18
	30	13.65	-16.35	18.68	-6.32
	40	6.39	-23.61	17.74	-7.26
5-3	0	34.83	4.83	13.41	-11.59
	10	34.35	4.35	12.95	-12.05
	20	34.02	4.02	12.22	-12.78
	30	33.41	3.41	14.20	-10.80
	40	32.01	2.01	14.02	-10.98
	50	27.50	-2.50	15.98	-9.02
	60	22.15	-7.85	19.63	-5.37
5-4	0	27.26	-2.74	14.07	-10.93
	10	24.70	-5.30	25.86	0.86
	20	23.47	-6.53	18.74	-6.26
	30	20.42	-9.58	17.69	-7.31
	40	16.13	-13.87	18.11	-6.89
	50	14.60	-15.40	17.40	-7.60
	60	11.77	-18.23	20.60	-4.40
	70	9.57	-20.43	18.58	-6.42

**Table 5.15 Parameters for optimizing both silicon and chromium contents**

Process parameter	Optimal parameter for $\Delta\text{Si}$	Optimal parameter for $\Delta\text{Cr}$
Metallic powder, wt.%	40	40
Si in metallic powder, wt.%	60	60
Temp., °C	1100	1100

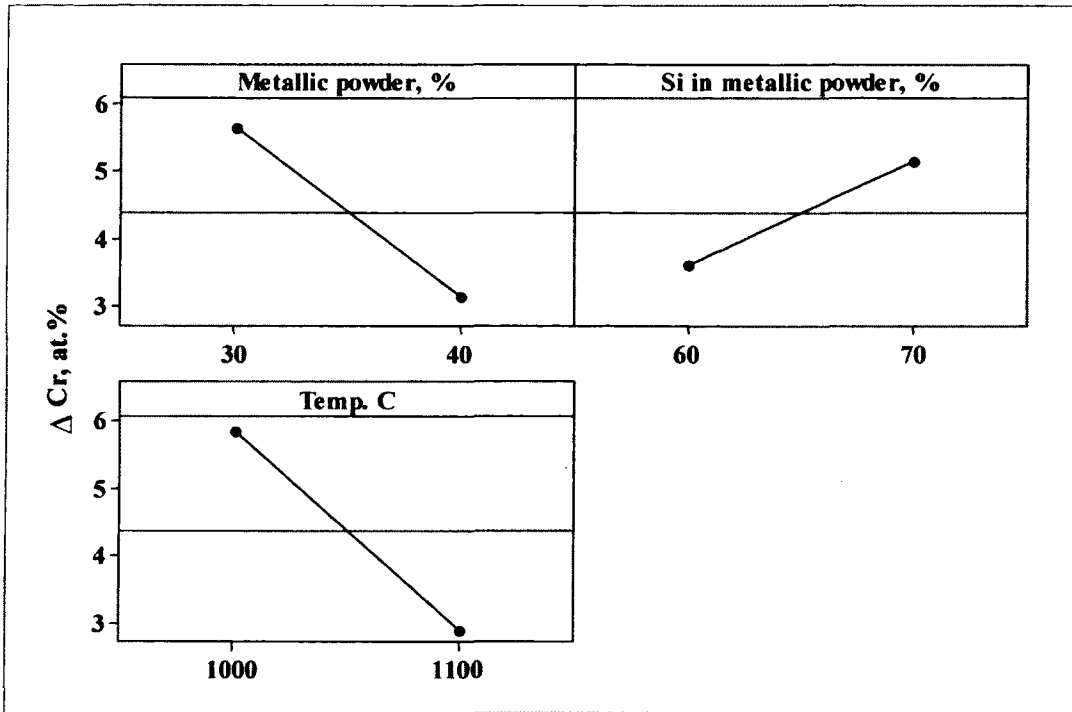


a) Si content versus process parameters

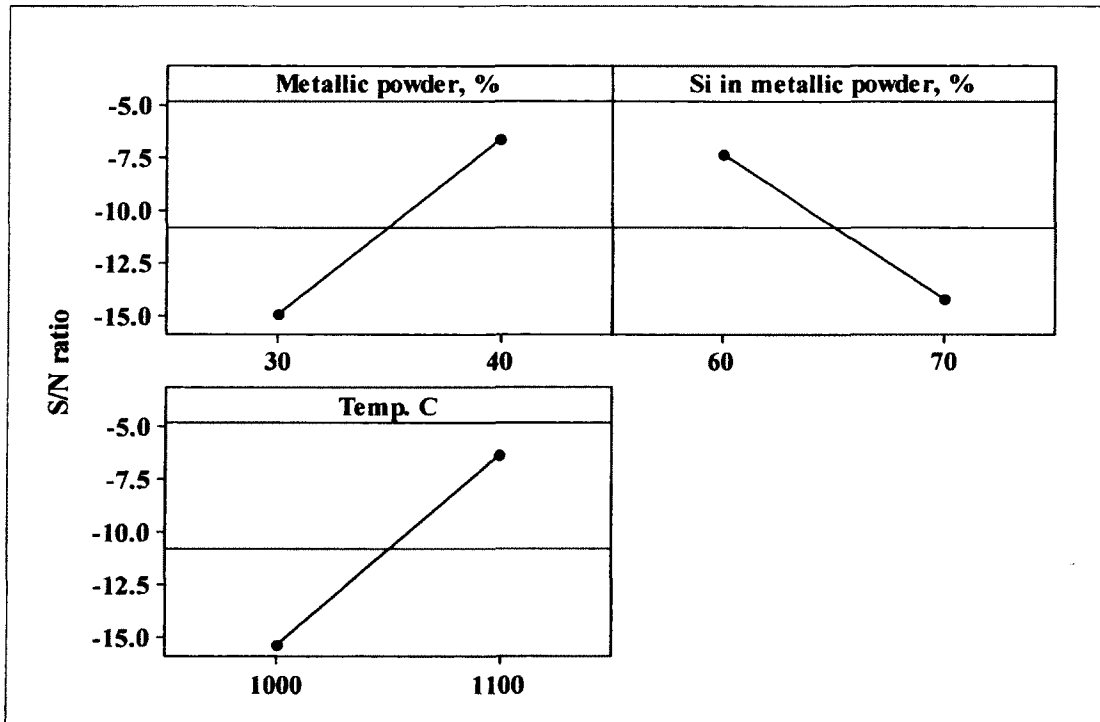


b) SNR versus process parameters

**Figure 5.11 Effects of process parameters on Si content and SNRs.**



a) Cr content versus process parameters



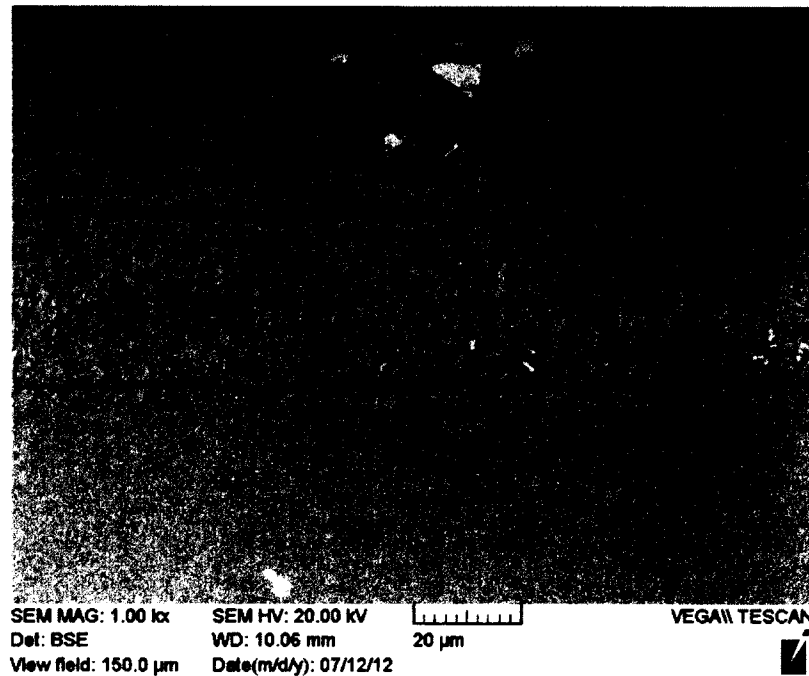
b) SNR versus process parameters

Figure 5.12 Effects of process parameters on Cr content and SNRs.

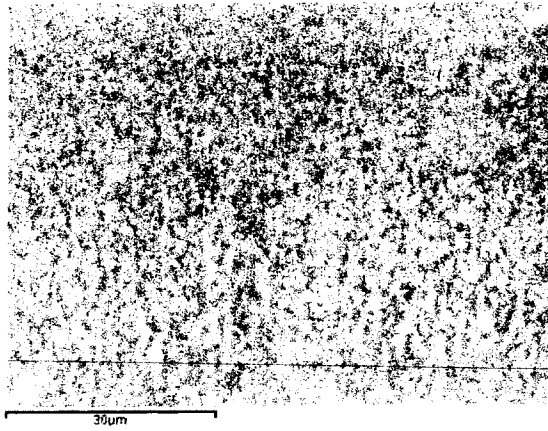
### 5.3.2 Microstructures of Cr-Si Coatings

The microstructure of coating specimen 5-4 is presented in Figure 5.13a. The X-ray mappings and concentration profiles (Figure 5.13d, 5.13e and 5.13f) show a two-layered structure: high-silicon layer (Si > 20 at.%) and chromium-rich layer (Cr > 20 at.%). Based on the XRD spectrum in Figure 5.13f, the phases in the coating are Z ( $\text{Cr}_3\text{Ni}_2\text{Si}$ ) phase,  $\delta$  ( $\text{Ni}_2\text{Si}$ ) phase (B), and  $\beta$  ( $\text{Cr}_3\text{Si}$ ) phase in addition to NiAl. The high-silicon layer may mainly consist of  $\delta$  ( $\text{Ni}_2\text{Si}$ ) and  $\text{Cr}_3\text{Si}$  phase while the chromium-rich layer consists of more Z phase ( $\text{Cr}_3\text{Ni}_2\text{Si}$ ) and some  $\beta$  ( $\text{Cr}_3\text{Si}$ ) phase. EDS results for some phases in Figure 5.13a are illustrated in Table 5.16.

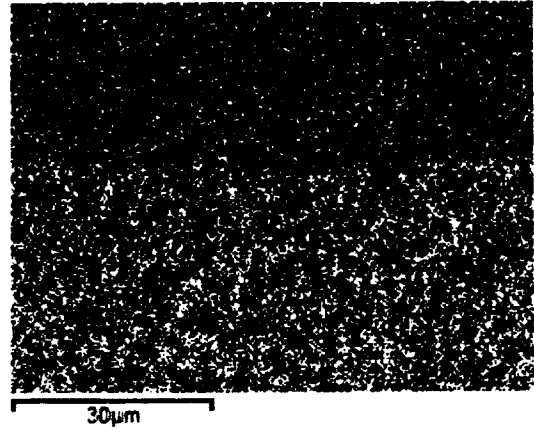
Similarly, for other Cr-Si coatings, the Si content reduces from the surface to the coating/substrate interface while Cr content increases in most of the specimens as shown in Table 5.14.



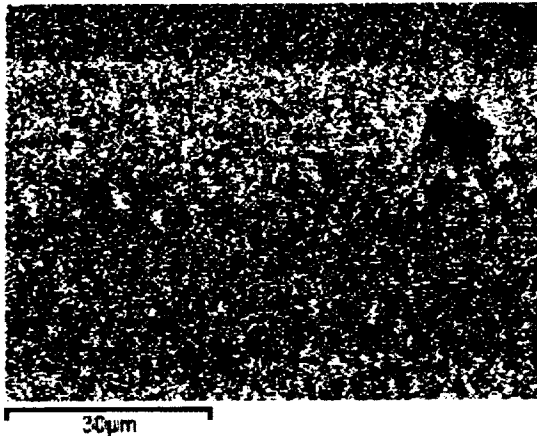
a) SEM image of microstructure



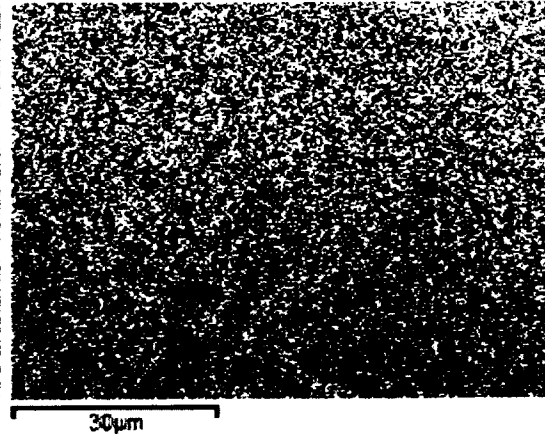
b) SEM image for mapping



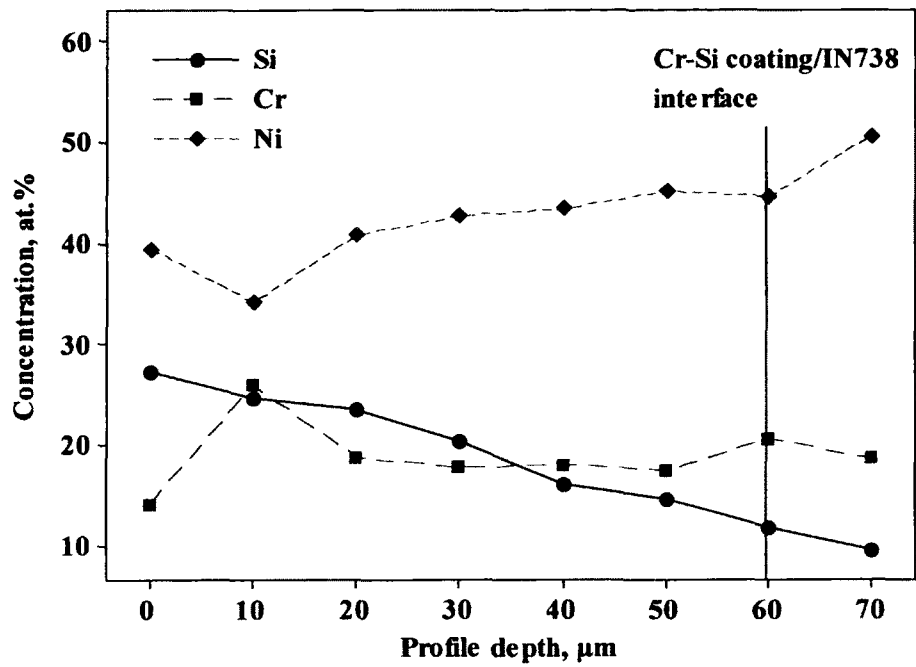
c) EDS mapping image for Al



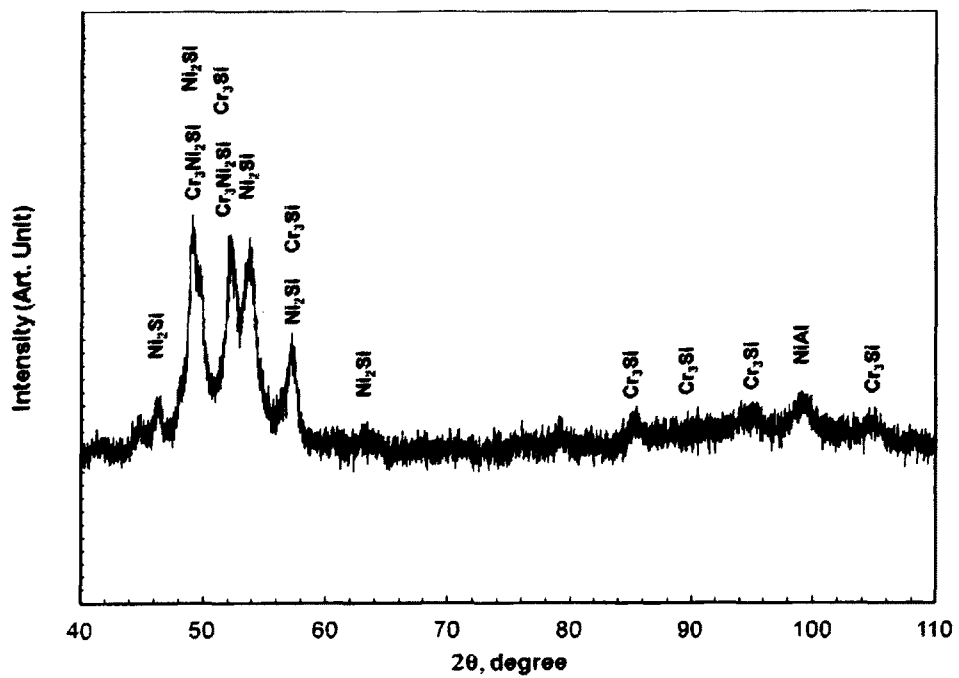
d) EDS mapping image for Cr



e) EDS mapping image for Si



f) Concentration profiles of Al, Si, Cr, and Ni



g) XRD spectrum for coating

**Figure 5.13 Microstructural analyses of coating 5-4.**

**Table 5.16 EDS results for the phases in the coating**

Phase	Concentration, at.%									
	Al	Si	Ti	Cr	Co	Ni	Mo	W	Nb	Ta
A	5.08	19.21	4.14	21.74	7.59	40.55		1.69		
B	4.15	24.52	7.68	11.87	6.40	45.37				
C	3.77	18.66	18.80	11.91	4.18	30.38			6.03	6.27
D	4.37	24.86	6.04	16.41	6.76	40.80	1.04			

#### **5.4 Summary of Process Optimization for Diffusion Coatings**

Surface response methodology is an invaluable tool for modeling and optimizing diffusion process. The results from aluminizing process are highly predictable based on the process parameters selected and regression equations. Similarly the coating composition from a Cr and Si co-deposition process can also be predicted. Both processes were used to produce multilayered coatings, which will be further discussed in Chapter 6.

## Chapter 6: Fabrication of Coatings

### 6.1 Coatings for Oxidation Tests

In order to compare the oxidation behavior of the developed multilayered coatings with other coatings, a control group of coatings, named as baseline coatings, was introduced. The baseline coatings were selected based on a two-level full factorial design, in which each coating layer acted as a factor, as shown Table 6.1. Three factors, the Cr-Si layer, NiCrAlY layer and aluminized layer, were assigned with  $U$ ,  $V$  and  $W$ .

There were two levels in the factorial design. The high level of these factors represented the coating layer design with the Cr-Si layer, NiCrAlY layer, and aluminide II layer, whereas the low level of these factors represented the coating layer design without the Cr-Si layer, NiCrAlY layer, and with the aluminide I layer. The advantage of using the two-level full factorial design is that two models can be developed to examine the effects of each layer and the interactions of each layer on the oxidation resistance of the multilayered coatings. One model was to examine the effects of each layer and the interactions of each layer on the area of oxide scales on the surface of coatings, which reflects the oxidation kinetics of metallic elements in coatings, especially Al. Another model was to examine the effects of each layer and the interactions of each layer on the mass change of coatings, which reflects the cohesion between oxide scales and coatings.

The bare IN738 and the NiCrAlY coating on IN738 were selected as reference specimens. All specimens are summarized in Table 6.2 and designated from O1 to O10. The processes for the baseline coatings were same as the processes for each coating layer.

**Table 6.1 Two-level full factorial design for determining coating layers for oxidation tests**

Level	Coating layer		
	Cr-Si coating, <i>U</i>	NiCrAlY, <i>V</i>	Aluminized coating, <i>W</i>
1	With a Cr-Si coating	With a NiCrAlY coating	Aluminide II: 2.0 Al/Ni ratio
0	Without a Cr-Si coating	Without a NiCrAlY coating	Aluminide I: 1.0 Al/Ni ratio

**Table 6.2 Design matrix for oxidation test coatings**

Coating	Design matrix			Coating combination
O1	1	0	0	Cr-Si coating/aluminide I
O2	1	1	1	Cr-Si coating/NiCrAlY/aluminide II
O3	0	0	0	aluminide I
O4	0	1	1	NiCrAlY/aluminide II
O5	1	1	0	Cr-Si coating/NiCrAlY/aluminide I
O6	0	1	0	NiCrAlY/aluminide I
O7	0	0	1	aluminide II
O8	1	0	1	Cr-Si coating/aluminide II
O9	Reference I			Bare IN738
O10	Reference II			NiCrAlY

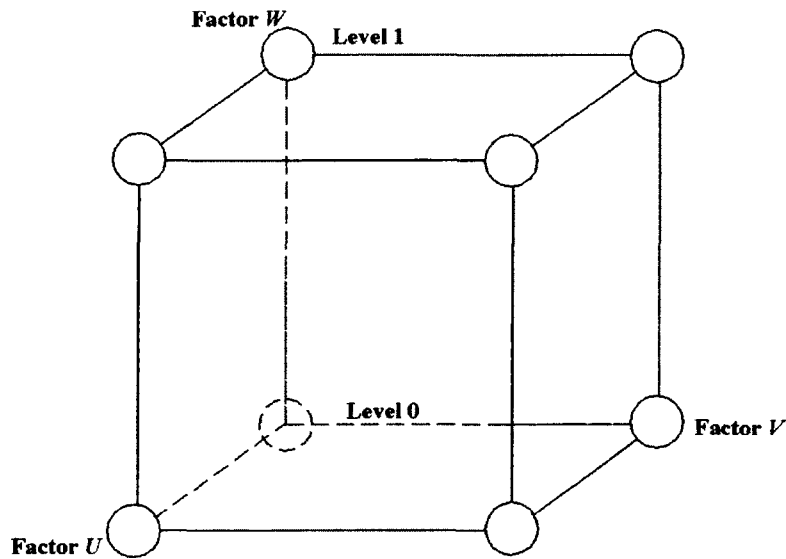


**Figure 6.1 Pictorial representation of a two-level full factorial design for the aluminizing process.**

## 6.2 Fabrication of Multilayered Coatings

### 6.2.1 Fabrication Procedures

The multilayered coatings designed in this research have a three-layer architecture, which consists of a Cr-Si coating on the IN738 substrate, a NiCrAlY overlay coating as the middle layer, and finally an aluminide layer on top. The multilayered coatings was fabricated through a combination of plasma spray and pack cementation processes. Each process was carried out using the optimal process parameters developed in the previous chapters.

The procedure for producing the multilayered coatings involved three steps. The first step was to co-diffuse chromium and silicon into the IN738 substrate using pack cementation process. The second step was to deposit a NiCrAlY coating on the Cr-Si coating using plasma spray process. The final step was an aluminizing treatment on the NiCrAlY coating to develop an aluminum-rich layer.

Two aluminizing processes were chosen to obtain the coatings with the range of the Al/Ni ratio varying from 0.8 to 1.2, and from 1.8 to 2.2, respectively. The coatings using these two processes were designated as aluminide I and aluminide II. Therefore, there were two types of multilayered coatings in which the first and second layers were identical but aluminizing treatment differed. The parameters for all processes are listed in Table 6.3 and Table 6.4. Two multilayered coatings are presented in Figure 6.2.

**Table 6.3 Pack cementation parameters for multilayered coatings**

Coating	Al, %	Ni, %	Si, %	Cr, %	NH <sub>4</sub> Cl, %	Al <sub>2</sub> O <sub>3</sub> , %	SiO <sub>2</sub> , %	Temp., ° C	Time, hr
Cr-Si barrier	-	-	24.0	16.0		29.0	29.0	1100	
aluminide I	6.5	10.0	-	-	2.0	81.5	-	1000	4
aluminide II	13.5	7.0	-	-		77.5	-	1000	

**Table 6.4 Plasma spray parameters for multilayered coatings**

Powder	Powder size, $\mu\text{m}$	Nozzle size, in	Total flow rate, sl/min	H <sub>2</sub> , %	N <sub>2</sub> , %	Current, A	Dist., mm	Powder feed setting	Time, sec
Ni 343	-45/+10	6/16	230	25	10	250	150	4	30

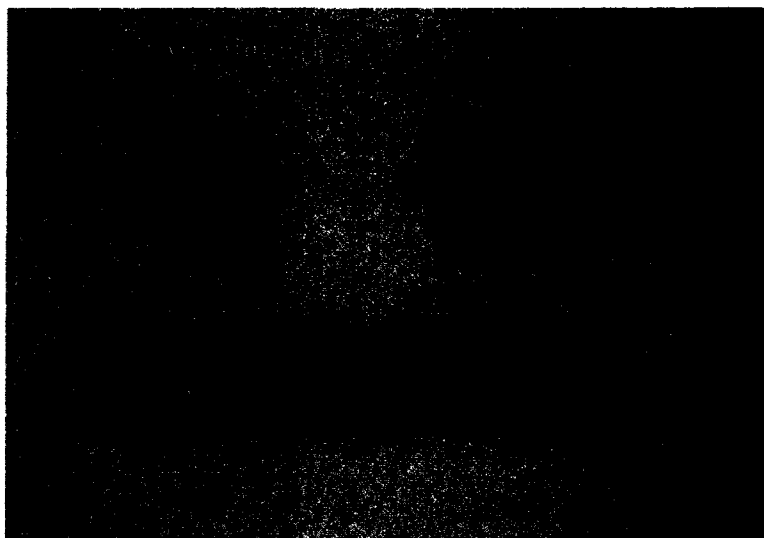


**Figure 6.2 Two multilayered coatings**

### **6.2.2 Elemental Distributions in Multilayered Coatings**

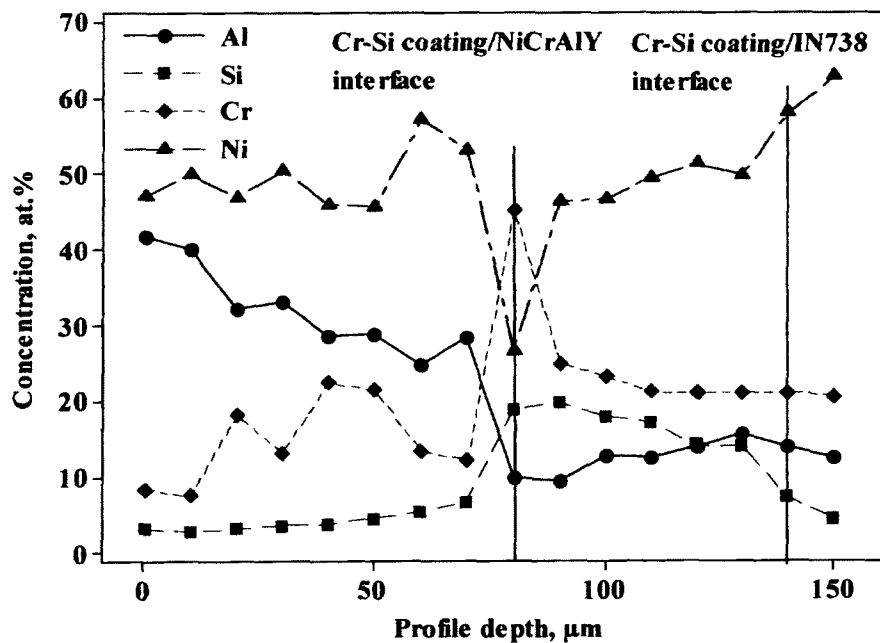
The main elements in two multilayered coatings were measured from the coating surface to the substrate using EDS. Based on the EDS results, the concentration profiles of the major elements in the multilayered coatings were plotted and shown in Figure 6.3. The interfaces between the NiCrAlY layer and the Cr-Si layer were measured at 80  $\mu\text{m}$  from the surface of the aluminide I layer and at 150  $\mu\text{m}$  from the surface of aluminide II layer, respectively.

Examination of Figure 6.3 reveals three important facts:

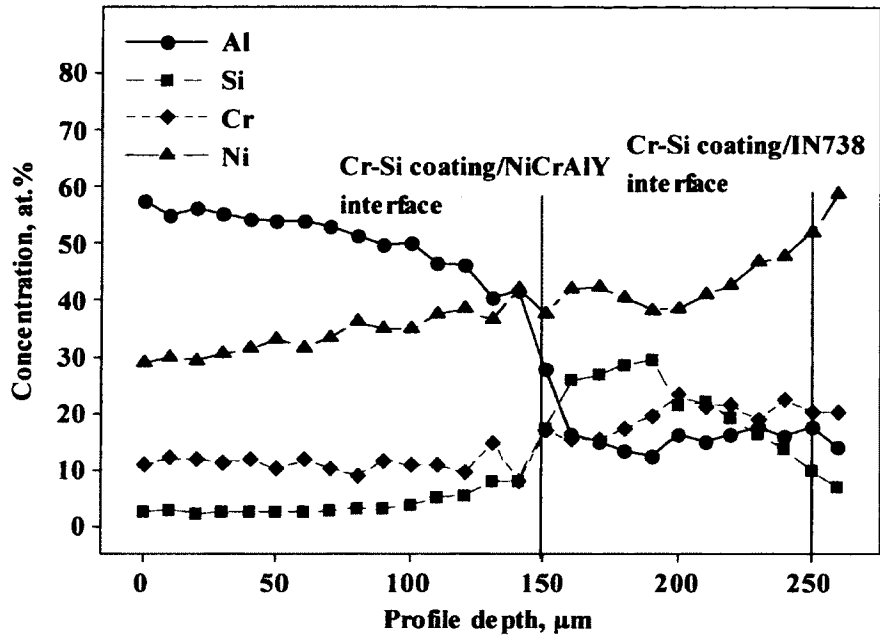
(1) The chromium content at the interface between the NiCrAlY layer and Cr-Si layer in MC I is around 45 at. %, which suggests a Cr layer formed between the NiCrAlY layer and Cr-Si layer in MC I during aluminizing process.

(2) The chromium content at the interface between the NiCrAlY layer and Cr-Si layer in MC II is around 16 at. %, which suggests no Cr layer formed in MC II during aluminizing process.

(3) The aluminum content (9-10 at.%) at the interface between the NiCrAlY layer and Cr-Si layer in MC I is much lower than the aluminum content (16-28 at.%) at the interface between the NiCrAlY layer and Cr-Si layer in MC II, which suggests the Cr layer in MC I effectively impeded aluminum diffusion while aluminum atoms in the NiCrAlY layer of MC II diffused into the substrate without the Cr layer.



a) Concentration profiles of Al, Si, Cr, and Ni in the multilayered coating with aluminide I top coat

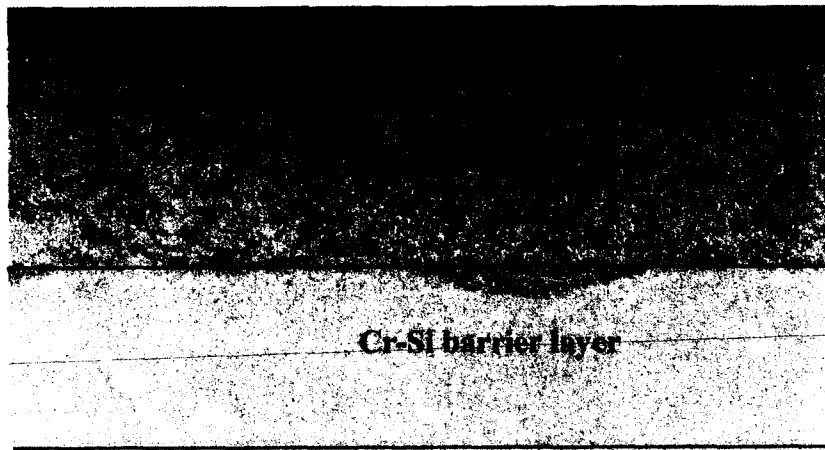


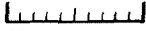
b) Concentration profiles of Al, Si, Cr, and Ni in the multilayered coating with aluminide II top coat

**Figure 6.3 Concentration profiles of major elements in multilayer coatings.**

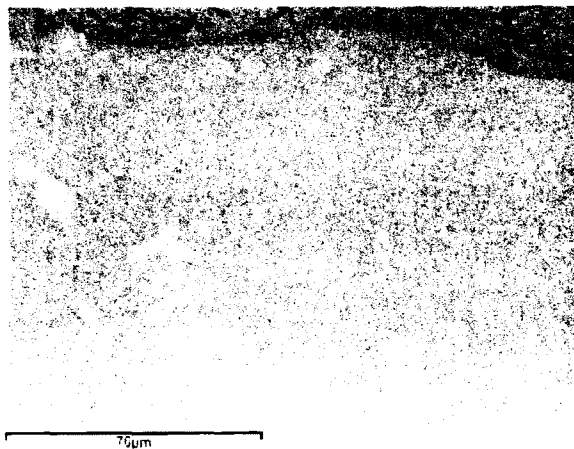
### 6.2.3 Microstructures of Multilayered Coatings

A typical microstructure of the multilayered coating with aluminide I top coat is presented in Figure 6.4. From the SEM image and elemental maps, the multilayered coating consists of three layers: an aluminum-rich top layer, a NiCrAlY middle layer, and Cr-Si rich layer. Based on the EDS and XRD analyses, the main phase in the top layer is NiAl. The middle layer is similarly NiCrAlY with NiAl phase. Mapping of the Cr-Si barrier layer indicates that the Cr-Si barrier layer was changed from a three-layer structure to a two-layer structure during the final diffusion process (to apply aluminide top coat), which consists of a Cr layer and Si-rich layer (Figure 6.4d and Figure 6.4e).

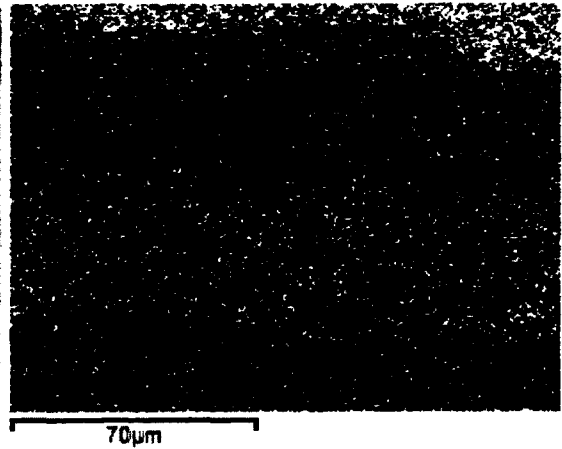


SEM MAG: 500 x      SEM HV: 20.00 kV            VEGAII TESCAN  
Det: BSE      WD: 9.971 mm      50 µm  
View field: 300.0 µm      Date(m/d/y): 07/12/12

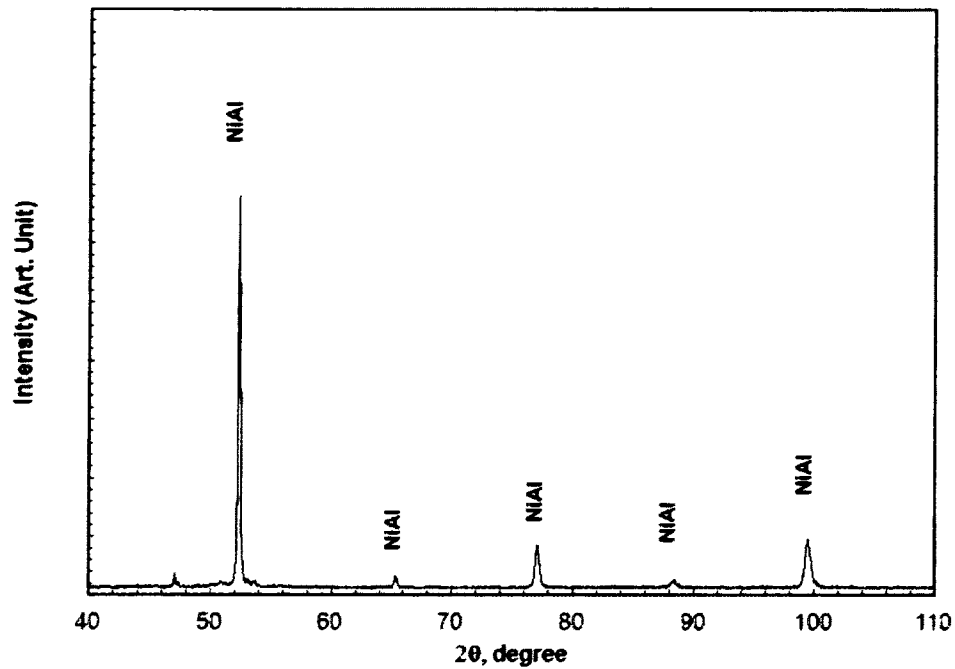
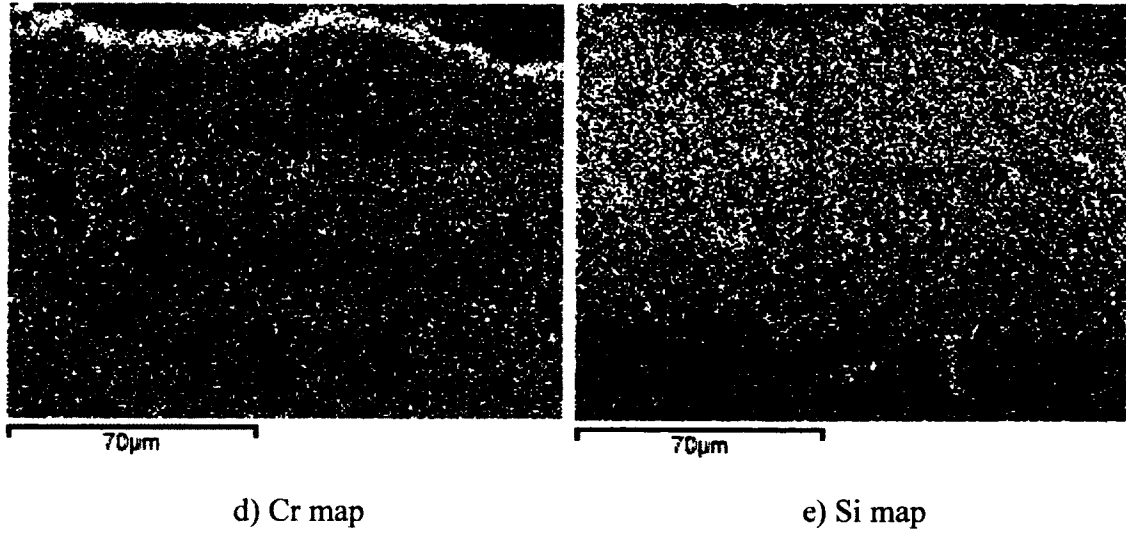
a) SEM image for the multilayered coating aluminide I top coat



b) SEM image for mapping



c) Al map

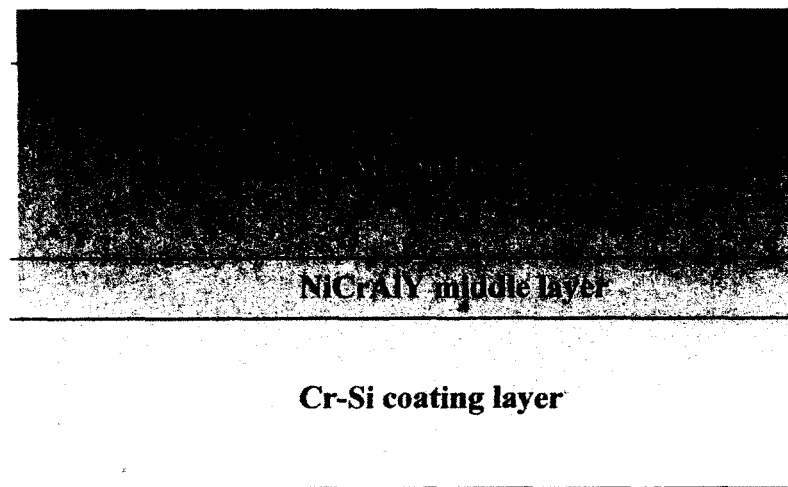


f) XRD spectrum of the multilayered coating with aluminide I coating

**Figure 6.4 Structure and phase analyses of the multilayered coating with aluminide I top coat.**

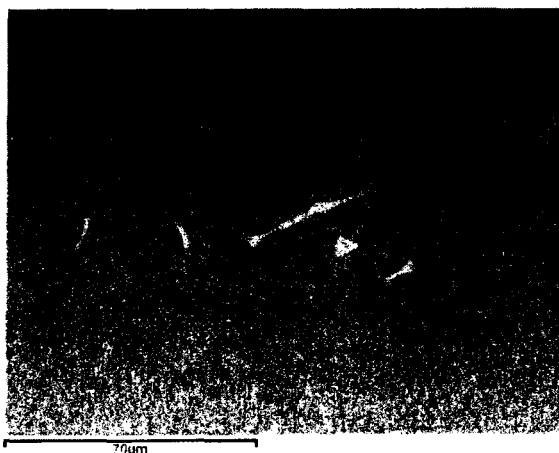
A typical microstructure for the multilayered coating with aluminide II top coat is presented in Figure 6.5. The multilayered coating also consists of three layers: an aluminum-rich top layer, a middle layer, and a Cr-Si coating. On the basis of an

analysis of Figure 6.5b, the major phase of the top layer is the  $Ni_2Al_3$  phase with minor the NiAl phase; the major phase of the middle layer is the NiAl phase. Mapping images of the Cr-Si barrier layer indicates that there are some Cr-rich phase instead of a Cr layer formed at the interface between the NiCrAlY layer and Cr-Si layer (Figure 6.5 6.5d and 5e).

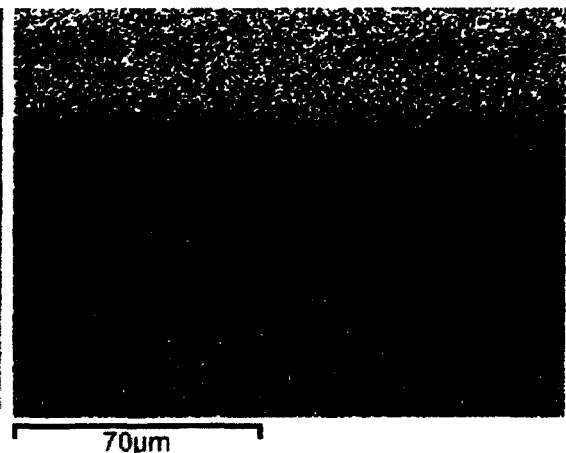


SEM MAG: 300 x      SEM HV: 20.00 kV      100 μm      VEGA\\ TESCAN  
 Det: BSE      WD: 9.985 mm  
 View field: 500.0 μm      Date(m/d/y): 02/16/12

a) SEM image for the multilayered coating with aluminide II top coat



b) SEM image for mapping



c) Al map

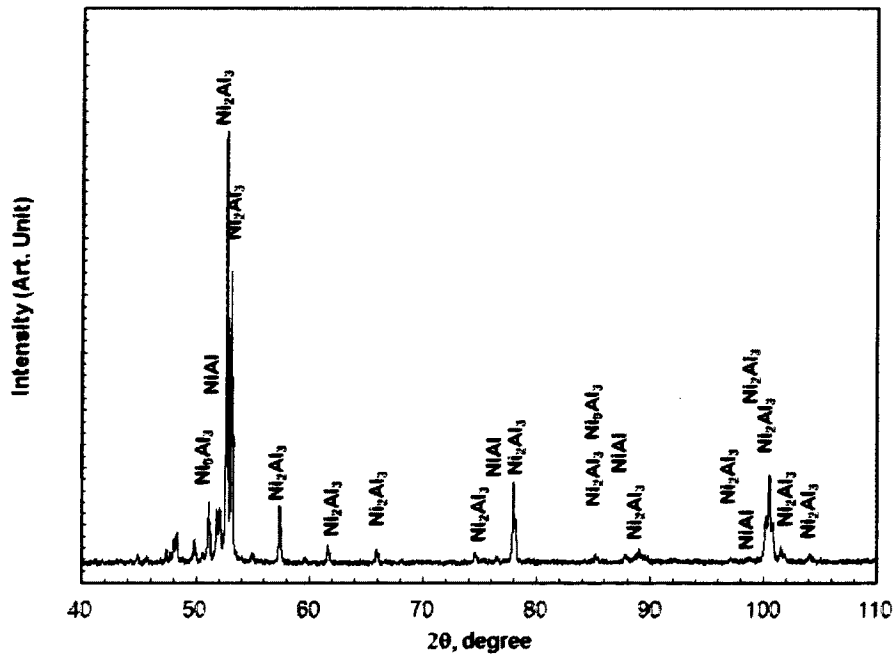
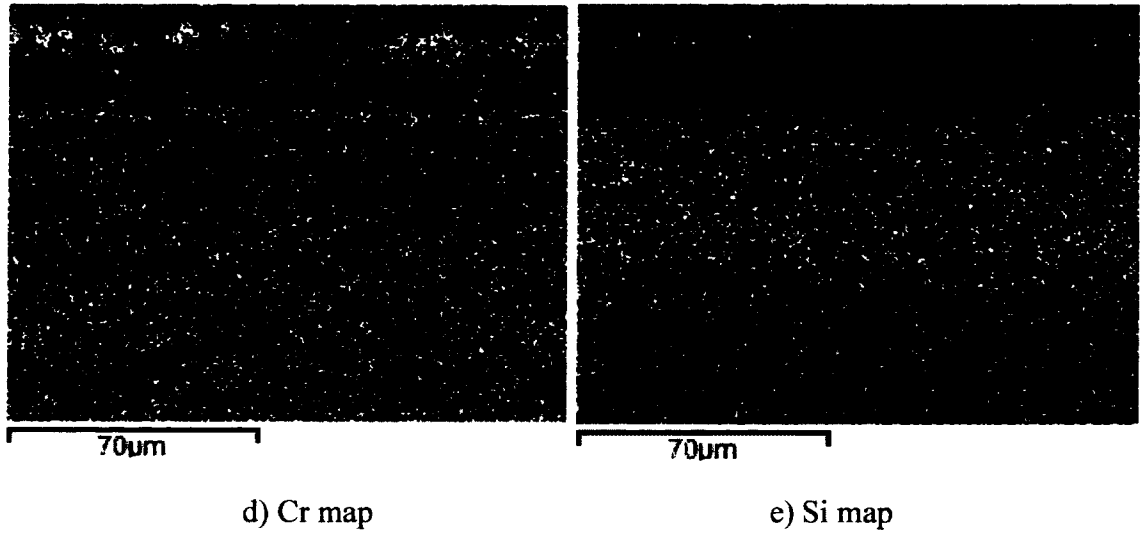


**Figure 6.5 Structure and phase analyses of the multilayered coating with aluminide II top coat.**

### 6.3 Fabrication of Baseline Coatings

The diffusion processes were simplified as CS (Cr-Si coating), AI (aluminide II) and AII (aluminide II); the details of the processes are given in Table 6.5. The process

durations were 4 hr; the plasma spray process was simplified as PS (plasma spray). The processes for the other baseline coatings are summarized in Table 6.6 along with two previously discussed multiple layered coatings. The microstructures and major elemental distributions for some baseline coatings and references are presented in Figure 6.6 to Figure 6.13. The phases in the coatings were estimated based on the distributions of the major elements, especially based on the distribution of Cr. When Cr content in a coating is around 8 at.%, the major phase in the coating is  $\beta$  phase.  $Ni_2Al_3$  and  $\gamma'/\gamma$  phase can dissolve more Cr. The estimated phases on coatings are presented in Table 6.6.

**Table 6.5 Parameters of diffusion processes**

Process	Coating	Al, wt.%	Ni, wt.%	Si, wt.%	Cr, wt.%	NH <sub>4</sub> Cl, wt.%	Al <sub>2</sub> O <sub>3</sub> , wt.%	SiO <sub>2</sub> , wt.%	Temp, °C
CS	Cr-Si coating	-	-	24.0	16.0	-	29.0	29.0	1100
AI	aluminide I	6.5	10.0	-	-	2.0	81.5	-	1000
AII	aluminide II	13.5	7.0	-	-	-	77.5	-	1000

**Table 6.6 Summary of coating processes**

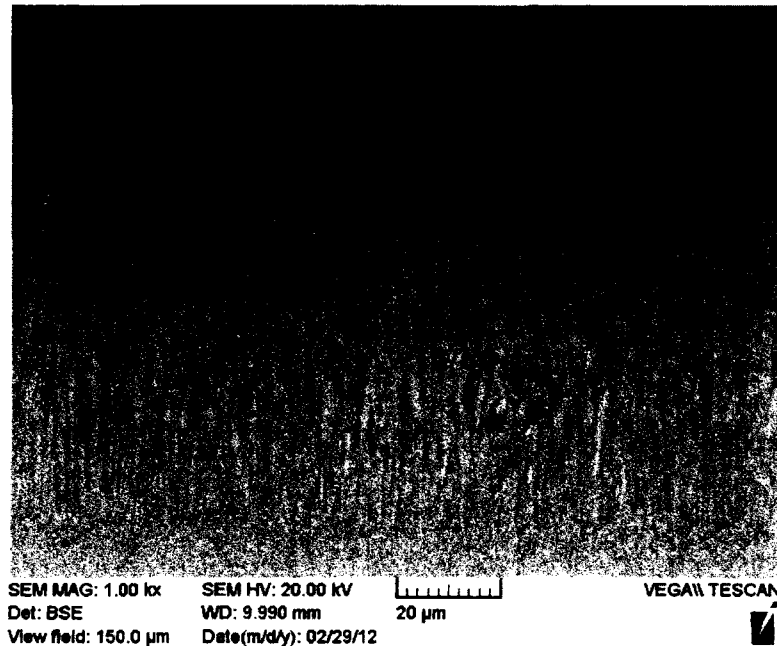
Coating	Coating combination	Process	Phase
O1	Cr-Si coating/aluminide I	CS + AI	( $\beta$ + silicon-rich) + ( $\gamma'$ + $\gamma$ )
O2	Cr-Si coating/ NiCrAlY/aluminide II	CS + PS + AII	$Ni_2Al_3$ + $\beta$ + $\gamma'$ + $\gamma$ + silicon-rich
O3	aluminide I	AI	$\beta$
O4	NiCrAlY/aluminide II	PS + AII	$Ni_2Al_3$
O5	Cr-Si coating/ NiCrAlY/aluminide I	CS + PS + AI	$\beta$ + $\gamma'$ + $\gamma$ + silicon-rich
O6	NiCrAlY/aluminide I	PS + AI	$\beta$ + $\gamma'$
O7	aluminide II	AII	$Ni_2Al_3$
O8	Cr-Si coating/aluminide II	CS + AII	( $\beta$ + silicon-rich) + ( $\gamma'$ + $\gamma$ )
O9	Bare IN738	-	$\gamma$
O10	NiCrAlY	PS	$\gamma/\gamma'$

Coating O1 and coating O8 are two-layer coatings without NiCrAlY middle layer.

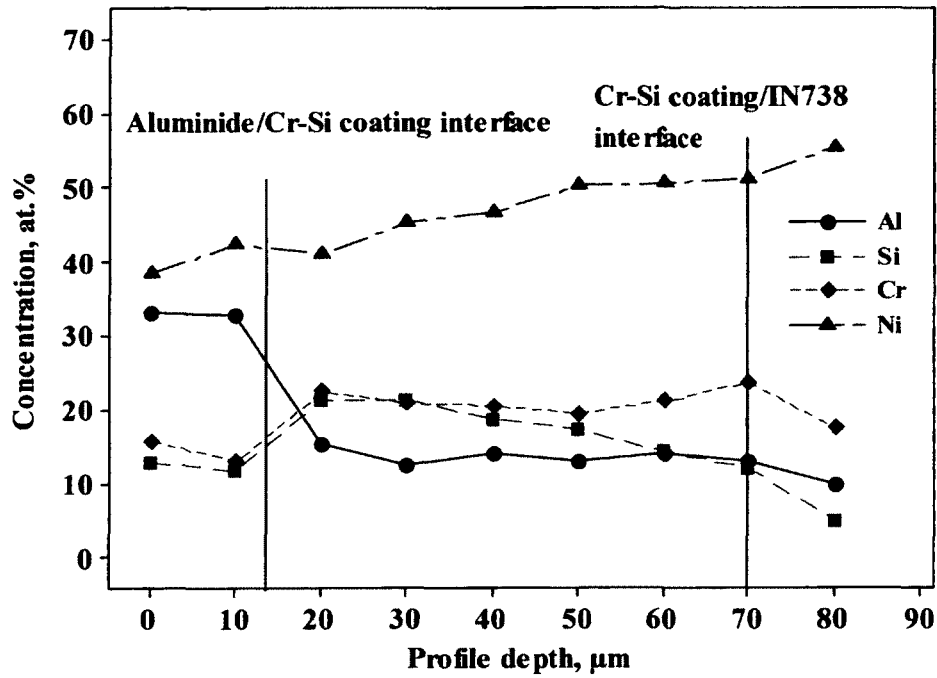
Examination of the aluminum profiles of coating O1 in Figure 6.6 and coating O8 in

Figure 6.7 reveals that the aluminum solubility is very low in the Cr-Si coating and Ni outward-diffusion dominated the growth of the aluminide coating. The averaged Al/Ni ratio for coating O1 is close to 1 within the aluminide layer (Figure 6.8), and NiAl phase constitutes the main phase in this layer. This was verified with XRD as shown in Figure 6.9a.

The Al/Ni ratios in aluminide top layer of coating O8 is larger than 1 within the aluminide coating (Figure 6.8), and the major phase in this layer is the  $\text{Ni}_2\text{Al}_3$  phase, which can be verified from the XRD spectrum of O8 coating in Figure 6.9b.

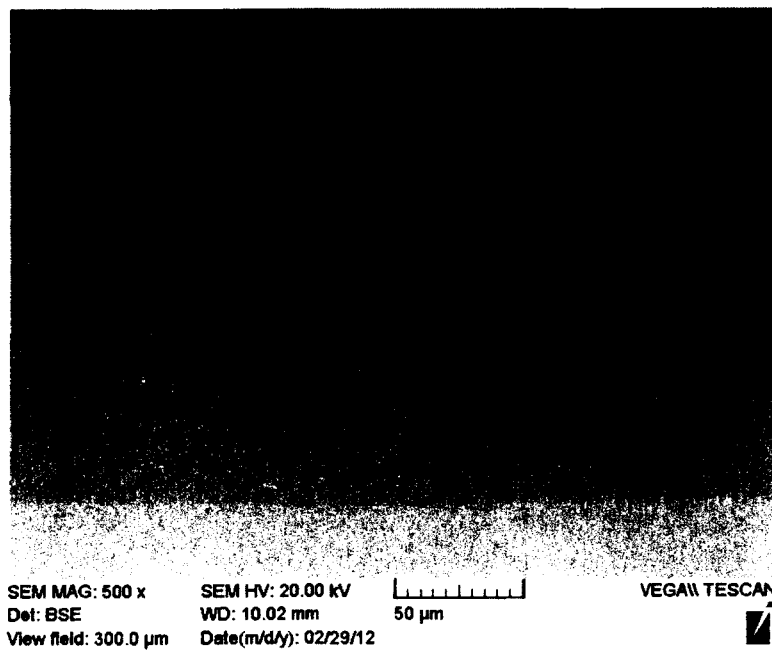


a) SEM image

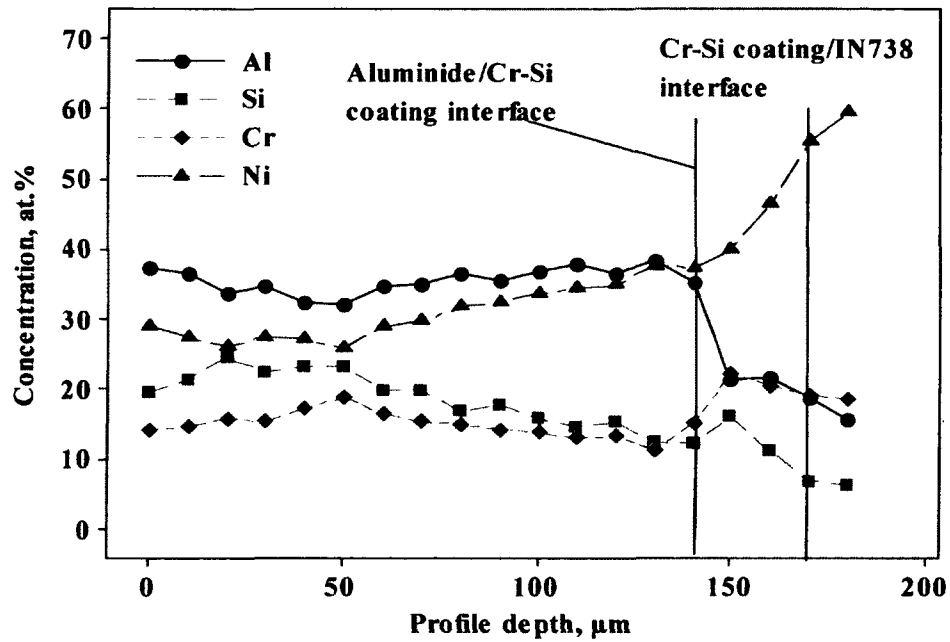


b) Concentration profiles of Al, Cr, Si and Ni

Figure 6.6 SEM image and concentration profiles of major elements for coating O1 (Cr-Si coating/aluminide I) before oxidation tests.



a) SEM image



b) Concentration profiles Al, Cr, Si and Ni

**Figure 6.7 SEM image and concentration profiles of major elements for coating O8 (Cr-Si coating/aluminide II) before oxidation tests.**

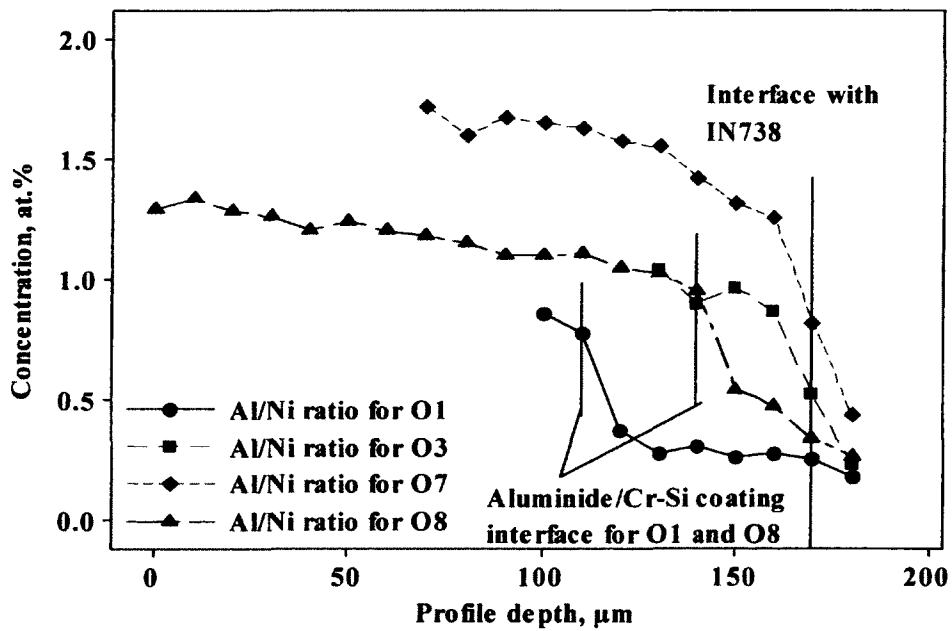
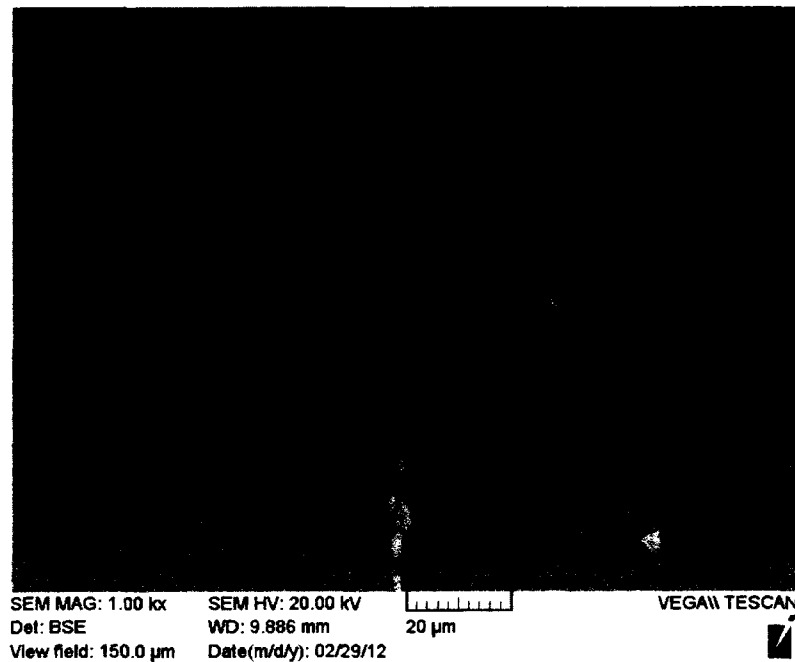


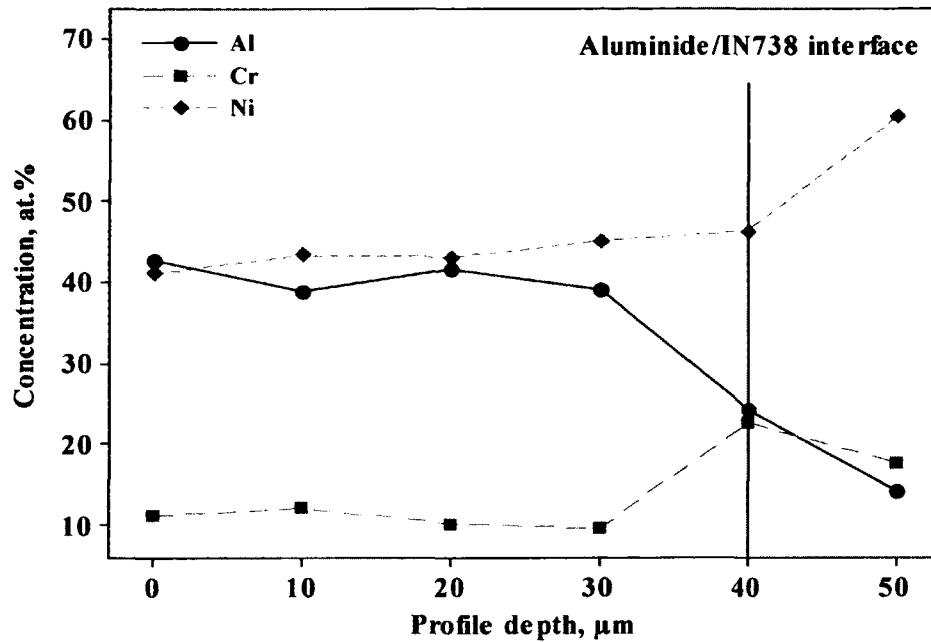
**Figure 6.8 Al/Ni ratio in coating O1, O3, O7 and O8.**



Coating O3 and O7 are one-layer coatings without NiCrAlY middle layer and Cr-Si barrier layer. The Al/Ni ratios for coating O3 and O7 are much higher than those for coating O1 and O8 (Figure 6.8), although the aluminizing process for coating O3 is the same as that for coating O1, and the aluminizing process for coating O7 is the same as that for coating O8. This phenomenon indicates that Al inward-diffusion dominated the coating growth of in coating O3 and O7. Based on the concentration profiles of O3 and O7 in Figure 6.10b and 6.11b, the major phase in coating O3 is  $\beta$  phase (Figure, and the major phase in coating O7 is  $\text{Ni}_2\text{Al}_3$  phase.

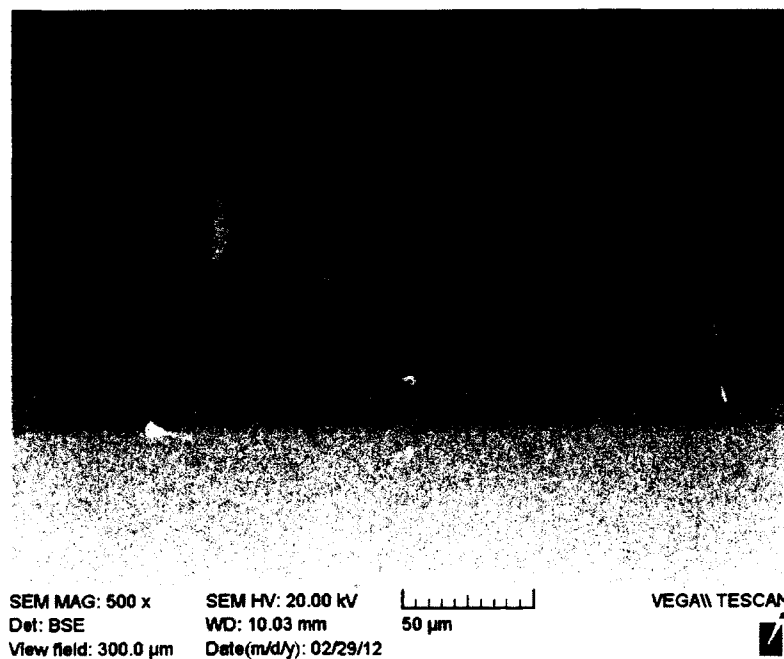


a) SEM image

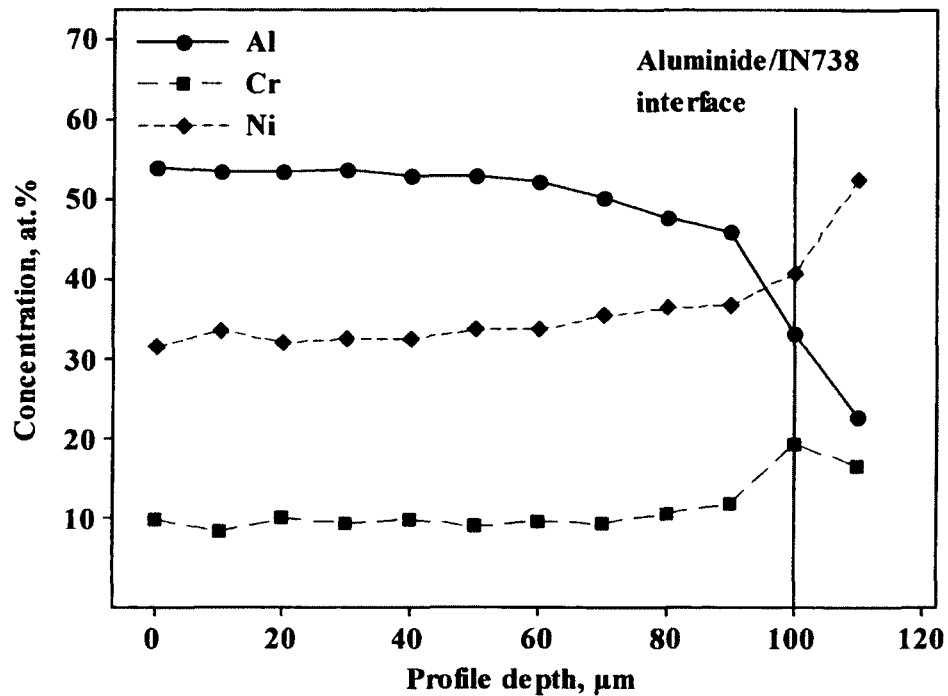


b) Concentration profiles of Al, Cr and Ni

Figure 6.10 SEM image and concentration profiles of major elements for coating O3 (aluminide I) before oxidation tests.



a) SEM image



b) Concentration profiles Al, Cr and Ni

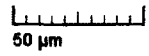
**Figure 6.11 SEM image and concentration profiles of major elements for coating O7 (aluminide II) before oxidation tests.**

Coating O4 and coating O6 are two-layer coatings without Cr-Si barrier layer. The Cr concentration in coating O4 steadily increased without the maximum point of Cr content that are observed in the Cr concentration profile of the multilayered coating with aluminide II top coat coating. The reasons for the maximum point of Cr content is that barrier layer blocked Cr diffusion into the substrate and Cr atoms accumulated on barrier layer.

Based on the concentration profiles of O4 and O6 in Figure 6.12b and 6.13b, the major phase in coating O4 is  $Ni_2Al_3$  phase, and the major phase in coating O6 is  $\beta$  phase and  $\gamma/\gamma'$  phase.

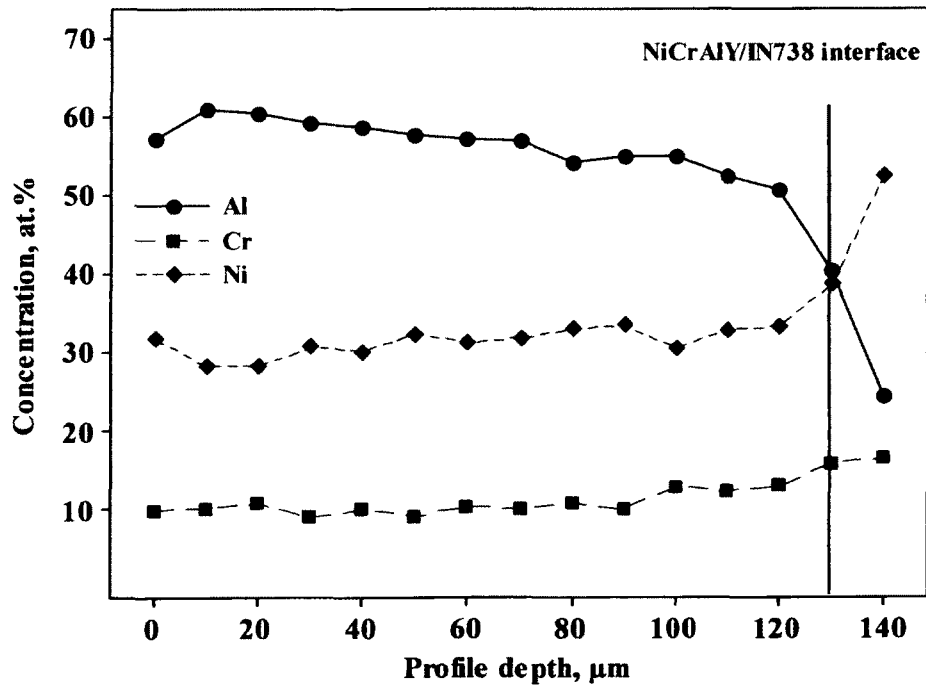


SEM MAG: 500 x SEM HV: 20.00 kV  
 Det: BSE WD: 9.950 mm  
 View field: 300.0  $\mu\text{m}$  Date(m/d/y): 02/29/12



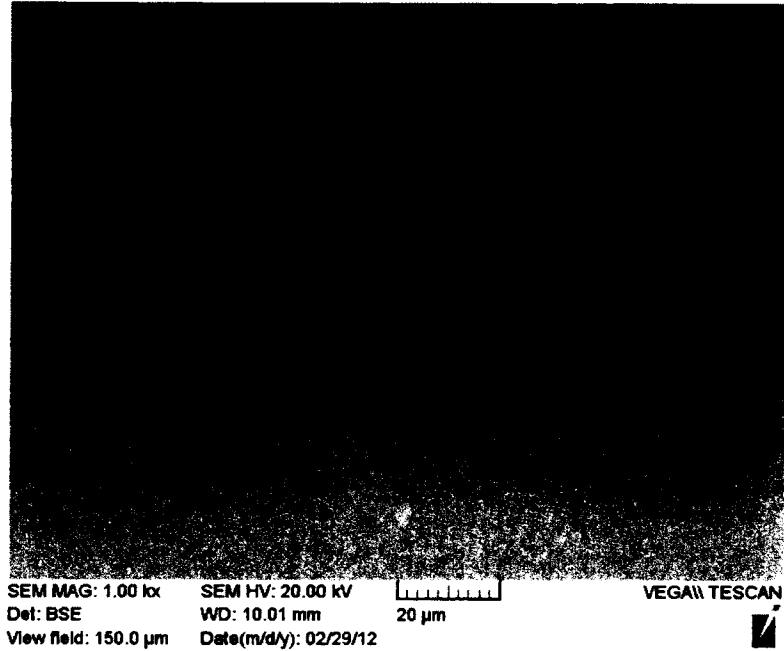
VEGAII TESCAN

a) SEM image

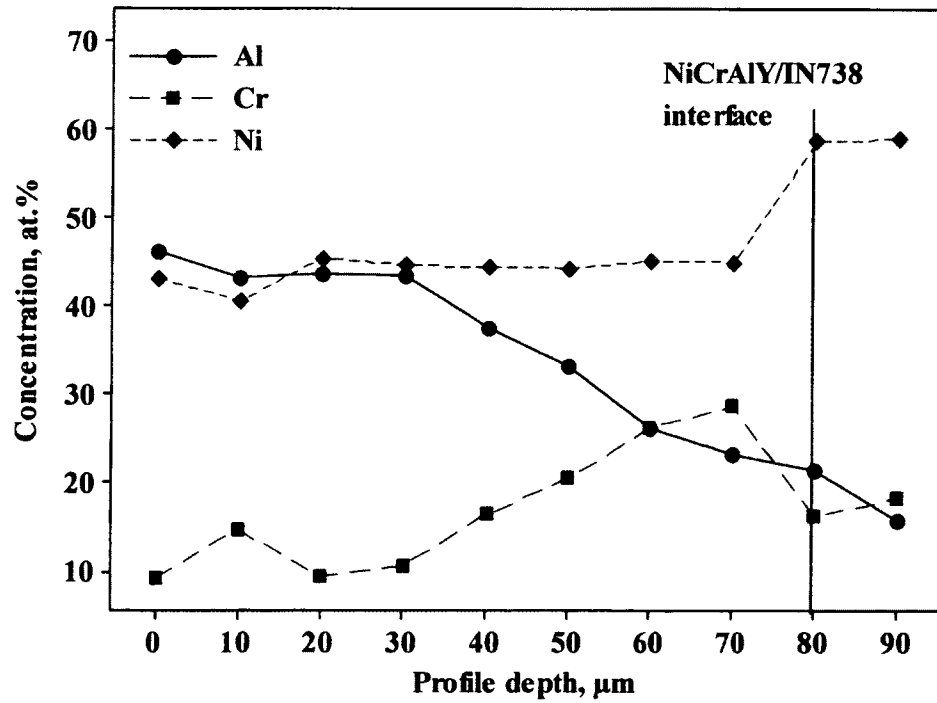


b) Concentration profiles Al, Cr and Ni

Figure 6.12 SEM image and concentration profiles of major elements for coating O4 (NiCrAlY/aluminide II) before oxidation tests.



a) SEM image



b) Concentration profiles of Al, Cr and Ni

**Figure 6.13 SEM image and concentration profiles of major elements for coating**

**O6 (NiCrAlY/aluminide I) before oxidation tests.**

#### **6.4 Summary of Coating Fabrication**

The optimal processes developed in this research and described in previous chapters were used to fabricate two multilayered coatings. The difference between the two multilayered coatings is that the aluminum content in the top layer of one coating was twice as much as that in the top layer of another coating. The multilayered coatings were fabricated through a combination of plasma spray process and pack cementation process. The entire fabrication procedure for the multilayered coatings was divided into three steps. The first step was to co-diffuse chromium and silicon into the IN738 substrate using pack cementation process. The second step was to deposit a NiCrAlY coating on the Cr-Si coating using plasma spray process. The final step was an aluminizing treatment on the NiCrAlY coating in order to create an aluminum-rich layer. To compare the oxidation behavior of the multilayered coatings with other coatings, the baseline coatings were also fabricated using the same process parameters for producing individual layers of the multilayered coatings. The baseline coatings were selected based on a two-level full factorial design, in which the coatings or coating layers were factors. Two reference specimens were also selected. All coatings and reference specimens were analyzed for elemental distributions across the coating layers and the results confirmed that the coatings and reference specimens all met design requirements.

## **Chapter 7: Oxidation Tests and Results Discussion**

### **7.1 Procedure of Oxidation Tests**

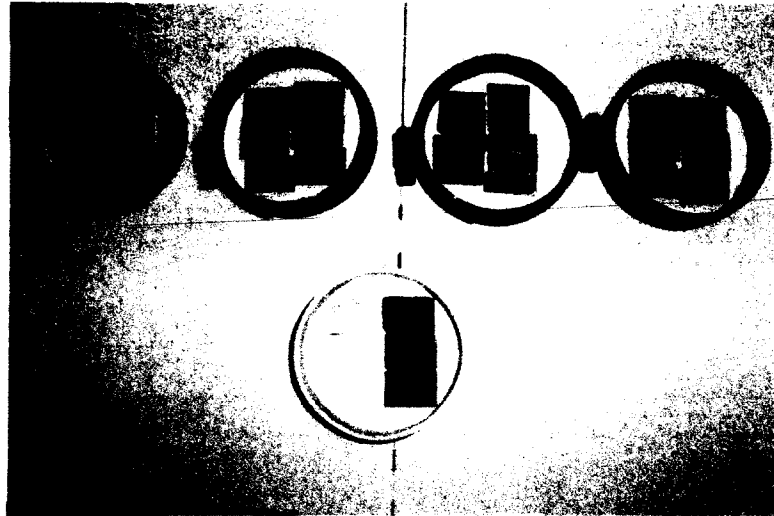
Three specimens for of each coating type were placed in an alumina crucible. Each crucible contained six specimens and all crucibles were placed in an air furnace at a constant temperature of 1050°C. The oxidized coating specimens were removed from the furnace, ultrasonically cleaned, and weighed after drying after 1000 hr exposure. The selection of exposure temperature and duration is based on the fact that the most simple aluminide coatings, for examples PWA73, spall catastrophically after 1000 hr at 1050°C [111]. Four coatings that are without NiCrAlY coating are simple aluminide coatings, which could spall after 1000 hr at 1050°C. The other coatings might maintain the integrity of the oxides. Therefore the exposure temperature and duration that are selected are supposed to be able to distinguish the oxidation behavior of all coatings. The coating specimens for the oxidation test at 1050°C are illustrated in Figure 7.1.

After the oxidation test, one specimen from each group was cut, mounted and polished for microstructural examination. The other two specimens were placed in the furnace for a further treatment at a constant temperature of 1150°C for another 1000 hr. This further oxidation test is to examine the oxidation behavior of multilayered coatings at the higher temperature. After the oxidation test, the coating specimens were removed from the furnace after the further treatment. Again one specimen from each group was cut, mounted and polished for microstructure examination.

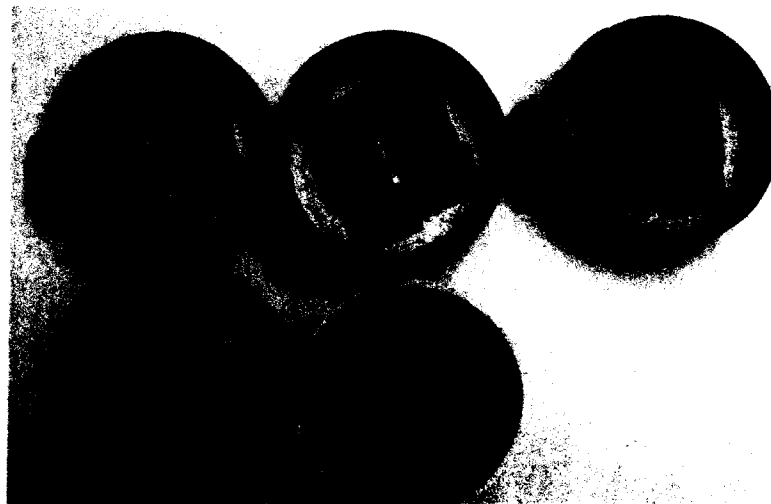
### **7.2 Mass Change of Coatings**

Most of the coating specimens that were exposed at 1150°C exhibited considerably high mass change due to spallation of oxide scales not only from the surfaces of the

coatings but also from the surfaces of the substrates. As such the mass changes for the coatings exposed to 1150°C will not be further discussed.



a) Specimens before the oxidation test



b) Specimens after the oxidation test

**Figure 7.1 Specimens for the oxidation test at 1050°C.**

The mass changes for the coating specimens exposed to 1050°C are given in Table 7.1. The coating specimens are further divided into three groups: mass lose group (O1,

O8, O9 and O10), mass gain group (O2, O4 and O7) and relatively constant mass group (O3, O5, and O6), according to the mass changes of each specimen.

**Table 7.1 Mass change for individual coating specimen**

Coating specimen	Mass change, mg/cm <sup>2</sup>	Coating
O1-1	-5.09	Cr-Si coating/aluminide I
O1-2	-6.37	
O1-3	-5.31	
O2-1	8.66	Cr-Si coating/NiCrAlY/aluminide II
O2-2	9.50	
O2-3	13.81	
O3-1	1.85	aluminide I
O3-2	1.81	
O3-3	0.52	
O4-1	8.46	NiCrAlY/aluminide II
O4-2	9.15	
O4-3	8.05	
O5-1	2.15	Cr-Si coating/NiCrAlY/aluminide I
O5-2	2.91	
O5-3	1.41	
O6-1	-0.85	NiCrAlY/aluminide I
O6-2	0.80	
O6-3	0.58	
O7-1	3.55	aluminide II
O7-2	2.53	
O7-3	3.38	
O8-1	-4.00	Cr-Si coating/aluminide II
O8-2	-3.72	
O8-3	-7.97	
O9-1	-20.62	IN738
O9-2	-38.74	
O9-3	-32.32	
O10-1	-34.71	NiCrAlY
O10-2	-46.30	
O10-3	-40.99	

The mass losses of all the coated specimens are much lower than those of the two references (IN 738 and NiCrAlY/IN 738). For the mass lose group, the coatings lost

weight due to the spallation of oxide scales. For the other groups, the coatings gained weight due to the formation and adherence of oxide scales on the surface of the coatings. However, coatings with weight gain may still suffer from spallation of the oxide scales as long as the mass of oxygen that the coating absorbed through oxidation is greater than the mass of the spalled scales.

The mass changes given in Table 7.1 were then used as a response for the analysis of variance and the development of a model associated with the coating layers. The  $p$ -values for the main factors and the two interactions of two factors are close to zero, but the  $p$ -values for the interaction of the Cr-Si layer ( $U$ ) and the aluminized layer ( $W$ ) and for the interaction of three factors are 0.35 and 0.30, respectively, which indicates that all factors and their interactions except the interaction of the Cr-Si layer ( $U$ ) and the aluminized layer ( $W$ ) and the interaction of three factors are significant in the model of mass change. The ANOVA results for the mass change are given in Table 7.2 after insignificant terms were eliminated. The  $R^2$  value obtained shows that the model and experimental data have a very high degree of fitness.

**Table 7.2 ANOVA table for mass change**

Source	Degree of freedom	Sum of squares	Mean square	$F$ value	$p$ -value
Main effect, $U, V, W$	3	506.87	168.96	70.17	0.000
Interaction between two factors, $UV, VW$	3	193.57	96.78	40.20	0.000
Residual	18	43.34	2.41		
Lack of fit	2	5.06	2.53	1.06	0.371
Pure error	16	38.28	38.28	2.39	
Total	23	743.77			
$R^2$		94.17%			

Some important concepts were introduced for evaluating the importance of factors and their interactions, which included the effect, sequential sums of squares, and percent contribution. The effect of a factor or an interaction of factors is defined to be the change in response produced by a change in the level of the factor or the interaction. In this case, that means increasing a factor from the low level to the high level causes an average response change. As mentioned above, the sequential sums of squares (SS) measure the reduction in the residual sums of squares (RSS) provided by each factor in a regression equation. If the sequential SS of a factor substantially reduces the residual sums of squares in a regression equation, this factor becomes significant in the regression equation. The percentage of the sequential sums of squares over the total sums of squares for is the percent contribution. The percent contribution represents the relative importance of each term in the regression equation.

Some results of effect, sequential SS, and percent contribution for mass change are presented in Table 7.3. Judging from the results, it is concluded that:

- The NiCrAlY layer dominated the mass change of coatings and the presence of the NiCrAlY layer increased mass gain.
- Higher Al/Ni ratio increased mass gain.
- The interaction between the Cr-Si layer and the NiCrAlY layer increased mass gain.

The factor that increased mass gain promoted the cohesion between oxide scales and coatings.

**Table 7.3 Effect, sequential SS, and percent contribution of factors and interactions for mass change**

Factor	Effect estimate	Seq SS	Percent contribution
<i>U</i>	-2.516	37.98	5.11
<i>V</i>	7.257	316.03	42.49
<i>W</i>	5.048	152.86	20.55
<i>UV</i>	4.554	124.44	16.73
<i>VW</i>	3.394	69.12	9.29

The model of mass change ( $Y_M$ ) with respect to the coating layers was developed and is expressed in the following regression equation:

$$Y_M = 0.84 - 7.07 \times U - 0.69 \times V + 1.65 \times W + 9.11 \times U \times V + 6.79 \times V \times W \quad (7-1)$$

where  $U$  represents the Cr-Si coating;  $V$  represents the NiCrAlY coating;  $W$  represents the aluminized coating.

The variables in regression equation (7-1) are uncoded qualitative variables and can only be zero or one. When variable  $W$  is set to be zero (aluminide I) or one (aluminide II), two regression equations,  $Y_{MI}$  and  $Y_{MII}$ , can be obtained as follows:

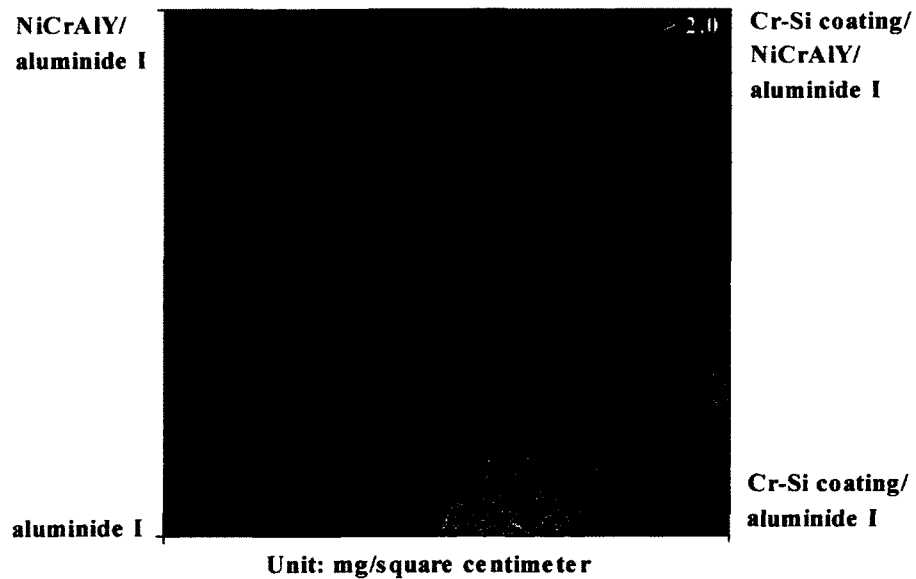
$$Y_{MI} = 0.84 - 7.07 \times U - 0.69 \times V + 9.11 \times U \times V \quad (7-2)$$

$$Y_{MII} = 2.39 - 7.07 \times U + 6.10 \times V + 9.11 \times U \times V \quad (7-3)$$

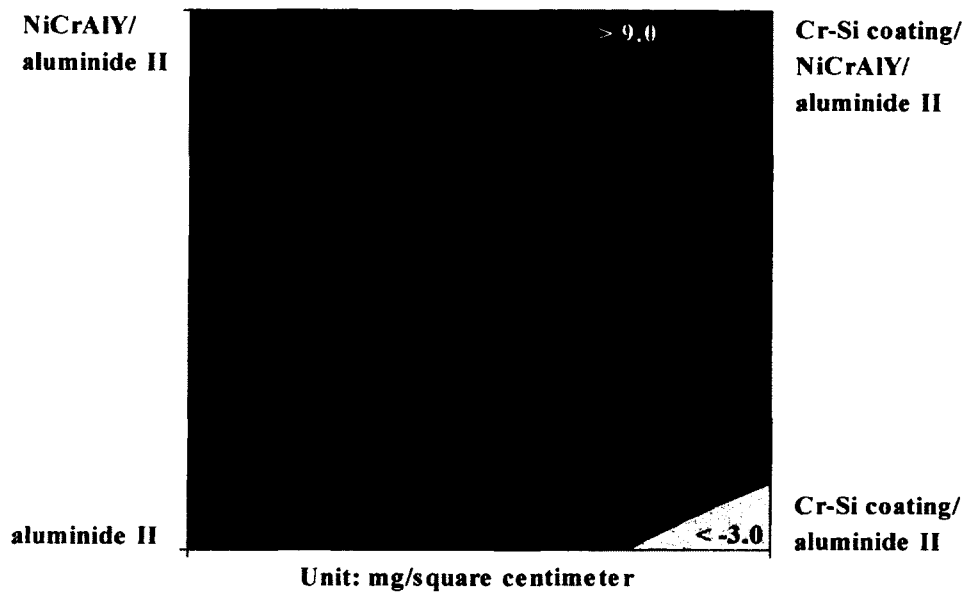
For equation (7-2), when variable  $U$  is zero,  $Y_{MI}$  is almost not affected by variable  $V$  since the coefficient for variable  $V$  is very small; when variables  $U$  and  $V$  are equal to one,  $Y_{MI}$  reaches the maximum. Such phenomena indicate that when the top layer of a coating was the aluminide I and no Cr-Si layer was applied, the mass change of the coating varied insignificantly whether a NiCrAlY layer was present or not; whereas

when the top layer of a coating is the aluminide I and a Cr-Si layer was present, the mass change of the coating varied significantly with the presence of a NiCrAlY layer. This observation suggested that the interaction between the Cr-Si layer and the NiCrAlY layer in a multilayered coating substantially affected the mass change of coatings. These phenomena can also be visually observed in the contour plot of equation (7-2) (Figure 7.2).

The mass changes for the coatings with or without a NiCrAlY layer were in the same range ( $-1.0 - 0.5 \text{ mg/cm}^2$ ) when a barrier Cr-Si layer was not applied; whereas when the coatings had the Cr-Si layer, the presence of the NiCrAlY layer resulted in mass gain while mass loss was observed without the NiCrAlY layer. Therefore, when a multilayered coating consisted of the aluminide I layer and a NiCrAlY layer, a Cr-Si layer was critical in ensuring mass gain and preventing oxide scales from spallation.



a) Coatings with the top layer of aluminide I coating



b) Coatings with the top layer of aluminide II coating

**Figure 7.2 Contour plots of mass changes for multilayered coatings.**

In equation (7-3), when variable  $V$  equals to one  $Y_{MII}$  is slightly higher when  $U = 1$  (than when  $U = 0$ ) as shown in Figure 7.2b. When variables  $U$  and  $V$  are both set to zero,  $Y_{MII}$  values are still positive since the higher aluminum content of the aluminide II layer definitely promoted mass gain; whereas  $Y_{MII}$  becomes negative and reaches the minimum value of  $-2.5 - -5.0 \text{ mg/cm}^2$  when  $V = 0$  and  $U = 1$ . Such findings indicate that when a multilayered coating consisted of a top layer of aluminide II and a middle layer of NiCrAlY, a Cr-Si barrier layer promoted mass gain; and when a coating only consisted of a top layer of aluminide II without the NiCrAlY layer, the presence of a Cr-Si layer caused significant amounts of mass loss due to the interaction between the Cr-Si layer and the aluminide II layer. Therefore, when a multilayered coating consisted of the aluminide II layer and a NiCrAlY layer, a Cr-Si layer in the multilayered coating could promote mass gain and prevent the coating from spallation.

### 7.3 Microstructure and Morphology of Oxidized Coating Surfaces

As mentioned in Chapter 2, the oxidation behavior of diffusion coatings and MCrAlY coatings follows a four-stage process: transient, steady-state, aluminum depletion and nickel outward diffusion, and internal Cr<sub>2</sub>O<sub>3</sub> oxide formation. The formation of Al<sub>2</sub>O<sub>3</sub>, Cr<sub>2</sub>O<sub>3</sub>, NiO, or Ni(Al,Cr)<sub>2</sub>O<sub>4</sub> is affected by the aluminum content in the coatings and exposure temperatures. When aluminum contents in coatings are above 21 at.%, the oxides on the surface of the coating are dominantly Al<sub>2</sub>O<sub>3</sub>, whereas a mixture of Cr<sub>2</sub>O<sub>3</sub>, NiO, and Ni(Al,Cr)<sub>2</sub>O<sub>4</sub> begins to form when the aluminum contents in the coatings drop below 21 at.% [112]. The aluminum contents for all coatings that were exposed to 1050°C were close or over 21 at.% except for coatings O1, O10 and specimen O9 (Table 7.4). Therefore most of the coatings examined in this study reached the steady-state, and aluminum depletion and nickel outward diffusion stages. However, the aluminum contents for the coatings exposed at 1150°C fell below 21 at.%, except for coating O2 (Table 7.4). For these coatings (except O2) the formation of internal Cr<sub>2</sub>O<sub>3</sub> oxide and other oxides such as Al<sub>2</sub>O<sub>3</sub>, Cr<sub>2</sub>O<sub>3</sub>, NiO, and Ni(Al,Cr)<sub>2</sub>O<sub>4</sub> would occur. Coating O2 was still in aluminum depletion and nickel outward diffusion stage after the oxidation test at 1150°C.

**Table 7.4 Maximum and surface aluminum contents after the oxidation tests**

Temp., °C	Scenario	Aluminum content, at.%									
		O1	O2	O3	O4	O5	O6	O7	O8	O9	O10
1050	Surface	11.1	36.1	21.4	37.7	19.1	19.7	28.0	25.3	10.3	17.5
	Max	11.5	36.1	21.4	39.9	21.6	24.0	29.9	26.0	11.9	17.4
1150	Surface	9.3	22.7	7.6	16.1	13.7	19.7	13.8	8.3	8.4	8.8
	Max	9.3	22.7	8.0	16.1	17.7	19.7	24.3	8.3	8.9	8.8

Three different contrasts are observed in the SEM images (Figure 7.3 to Figure 7.6) of the coatings: dark regions, grey regions and bright regions, which represent

indicating different oxides. The EDS results (Table 7.5) suggest that dark regions consist of Al<sub>2</sub>O<sub>3</sub> (points A, B, F, H, N, P, T and W in the figures), grey regions are mixtures of Al<sub>2</sub>O<sub>3</sub>, Cr<sub>2</sub>O<sub>3</sub>, NiO (points I and U in the figures) and Ni(Al,Cr)<sub>2</sub>O<sub>4</sub> (points D, G, R, and V in the figures), and bright regions represent the exposed coating after the spallation of oxide scales (points C, E, J, K, L, and S in the figures).

**Table 7.5 EDS results of various phases on the surface of coatings**

Loca -tion	Concentration, at.%						Oxide	
	O	Al	Cr	Ni	Ti	Si		Co
A	65.73	33.04	0.61	0.33				Al <sub>2</sub> O <sub>3</sub>
B	67.50	32.50						Al <sub>2</sub> O <sub>3</sub>
C	31.29	6.48	2.76	41.07	2.48	1.06	4.86	
D	66.99	20.16	3.87	7.54	0.31		1.13	Ni(Al,Cr) <sub>2</sub> O <sub>4</sub>
E	13.98	6.27	19.75	48.60	1.22	3.39	6.31	
F	62.66	31.96	1.40	3.37	0.60			Al <sub>2</sub> O <sub>3</sub>
G	63.55	25.03	0.63	9.48			1.31	NiAl <sub>2</sub> O <sub>4</sub>
H	60.68	34.23	0.87	3.62	0.14		0.46	Al <sub>2</sub> O <sub>3</sub>
I	48.42	1.75	0.78	46.87			2.19	NiO
J		16.14	14.42	59.62	3.76		6.06	
K		19.74	15.04	55.40	3.85		5.97	
L	13.98	6.64	16.22	52.52	2.35		7.91	
M	43.41	6.73	11.09	32.50	1.46		4.44	NiO
N	63.62	36.00	0.16	0.22				Al <sub>2</sub> O <sub>3</sub>
O	67.50	8.69	1.88	4.41	14.80	0.80	0.68	Al <sub>2</sub> O <sub>3</sub> , TiO <sub>2</sub>
P	64.52	34.55	0.16	0.23	0.53			Al <sub>2</sub> O <sub>3</sub>
Q	40.63	5.37	13.90	32.15	2.32	1.19	4.44	NiO
R	60.01	19.62	2.77	9.45	4.69	0.87	1.96	Ni(Al,Cr) <sub>2</sub> O <sub>4</sub>
S	16.33	10.00	18.01	48.87	0.78			
T	70.00	21.14	1.70	6.92				Al <sub>2</sub> O <sub>3</sub>
U	46.56	1.95	1.61	49.88				NiO
V	46.14	5.59	35.33	9.00	3.35		0.58	Cr <sub>2</sub> O <sub>3</sub> , Ni(Al,Cr) <sub>2</sub> O <sub>4</sub>
W	61.39	36.82	0.53	1.26				Al <sub>2</sub> O <sub>3</sub>



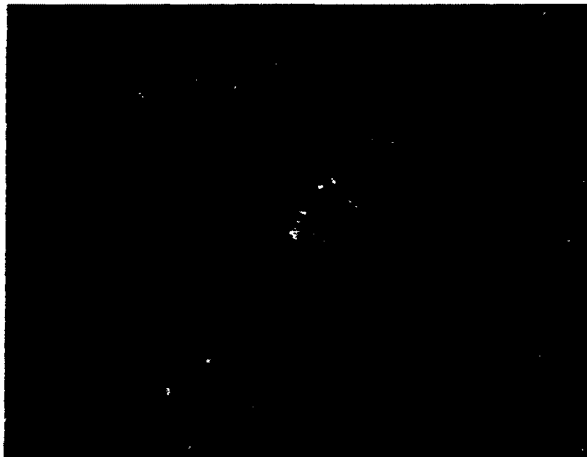
SEM MAG: 100 x SEM HV: 20.00 kV  
Det: BSE WD: 10.22 mm 200 μm  
View field: 1.50 mm Date(m/d/y): 06/07/12



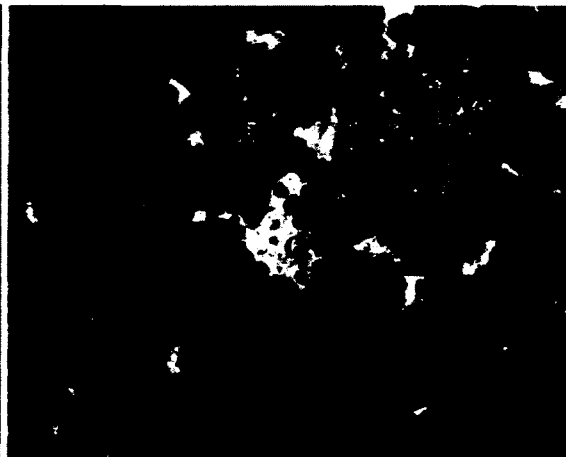
SEM MAG: 500 x SEM HV: 20.00 kV  
Det: BSE WD: 10.22 mm 50 μm  
View field: 300.0 μm Date(m/d/y): 06/07/12

a) Surface morphology of coating O<sub>2</sub>  
after 1000 hr exposure at 1050°C at low  
magnitude

b) Surface morphology of coating O<sub>2</sub>  
after 1000 hr exposure at 1050°C at high  
magnitude



SEM MAG: 100 x SEM HV: 20.00 kV  
Det: BSE WD: 10.31 mm 200 μm  
View field: 1.50 mm Date(m/d/y): 06/12/12

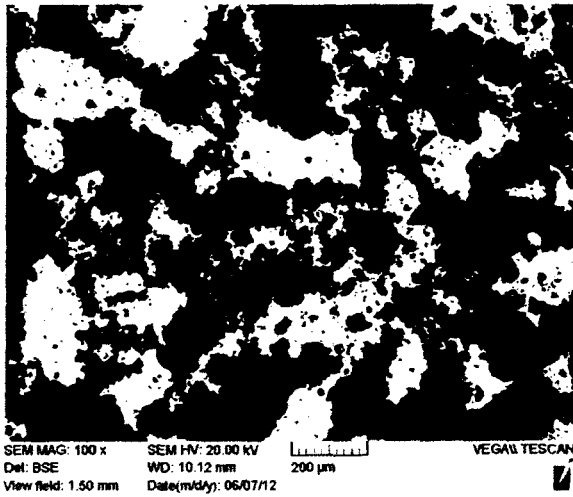


SEM MAG: 500 x SEM HV: 20.00 kV  
Det: BSE WD: 10.31 mm 50 μm  
View field: 300.0 μm Date(m/d/y): 06/12/12

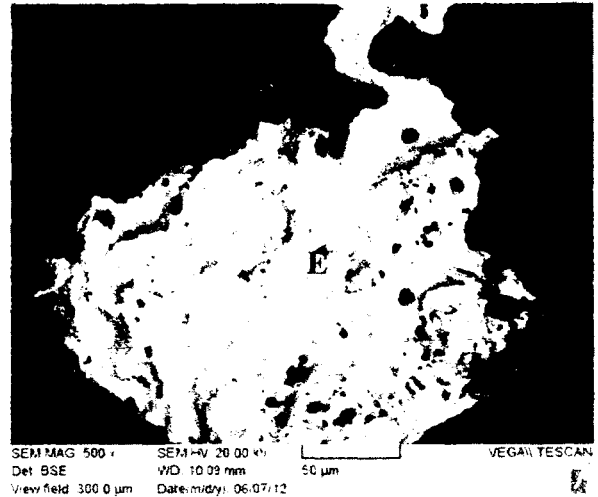
c) Surface morphology of coating O<sub>2</sub>  
after 1000 hr exposure at 1150°C at low  
magnitude

d) Surface morphology of coating O<sub>2</sub>  
after 1000 hr exposure at 1150°C at  
high magnitude

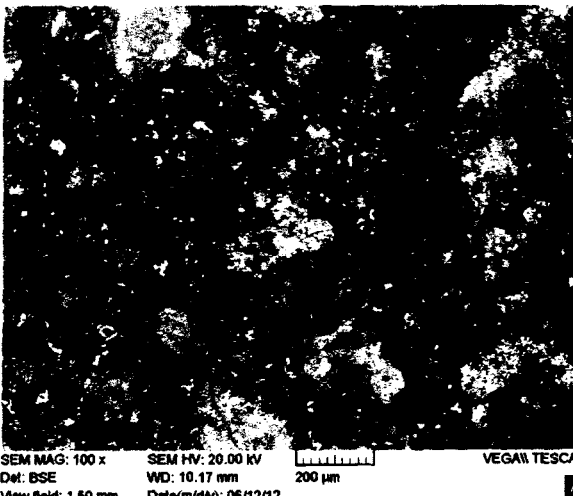




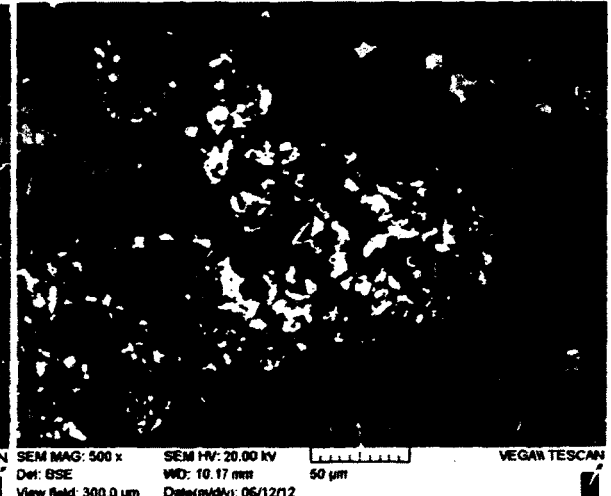
a) Surface morphology of coating O5 after 1000 hr exposure at 1050°C at low magnitude



b) surface morphology of coating O5 after 1000 hr exposure at 1050°C at high magnitude



c) Surface morphology of coating O5 after 1000 hr exposure at 1150°C at low magnitude



d) Surface morphology of coating O5 after 1000 hr exposure at 1150°C at high magnitude



the XRD spectra of coatings O2 and O5, respectively, after 1000 hr exposure at 1050°C. Only Al<sub>2</sub>O<sub>3</sub> was found on the surface of O2 and O5 specimens. Also, the top layer of O2 specimen changed from Ni<sub>2</sub>Al<sub>3</sub> into NiAl during 1000hr exposure at 1050°C, and the top layer of O5 coating transformed from NiAl into  $\gamma'/\gamma$  during the same exposure.

After 1000 hr exposure at 1150°C, the mixed oxides (grey region) on the surface of coating O2 are much less than that on the surface of coating O5 (Figure 7.3d and Figure 7.4d). Figure 7.3f and Figure 7.4f show the XRD spectra of coatings O2 and O5, respectively; a large amount of Al<sub>2</sub>O<sub>3</sub> and small amount of Ni(Al,Cr)<sub>2</sub>O<sub>4</sub> formed on the surface of coating O2, whereas the amount of Ni(Al,Cr)<sub>2</sub>O<sub>4</sub> on the surface of coating O5 is more than that on the surface of coating O2. The phases in the top layer changed from  $\beta$  (NiAl) phase into  $\gamma'/\gamma$  phase with certain NiAl phase remained during the exposure at 1150°C for coating O2. The  $\gamma'/\gamma$  phase structure in the top layer of O5 remained unchanged, although with lower aluminum content, during the exposure at 1150°C for 1000 hr. Figure 7.5 to Figure 7.12 illustrate the surface morphologies of other specimens. After 1000 hr exposure at 1050°C, dark regions and bright regions are observed on the surface of most other coatings; however, the grey regions are also found on specimen O9 and O10, which suggests that mixed oxides (Cr<sub>2</sub>O<sub>3</sub>, NiO and Ni(Al,Cr)<sub>2</sub>O<sub>4</sub> formed on the surfaces of specimens O9 and O10.

The cross section micrographs of specimens O1, O3, O4, O8, and O10 after 1000 hr exposure at 1150°C show that the top coating layers have disappeared. The surface morphologies of O1, O3, O9, and O10 are similar and grey regions become dominant. The surface morphologies of coatings O4 and O6 are similar and there are considerable

amounts of dark regions due to the high aluminum contents in the coatings (about 16 at.% and 20 at.%, respectively, based on spot analysis of spots J and K shown in Table 7.5). For coatings O7 and O8, both with the aluminide II coating and without a NiCrAlY coating, the oxides found in the surfaces are a mixtures of  $Al_2O_3$  (N and P in Table 7.4) and NiO (M and Q in Table 7.5), after 1000 hr exposure at 1150°C.

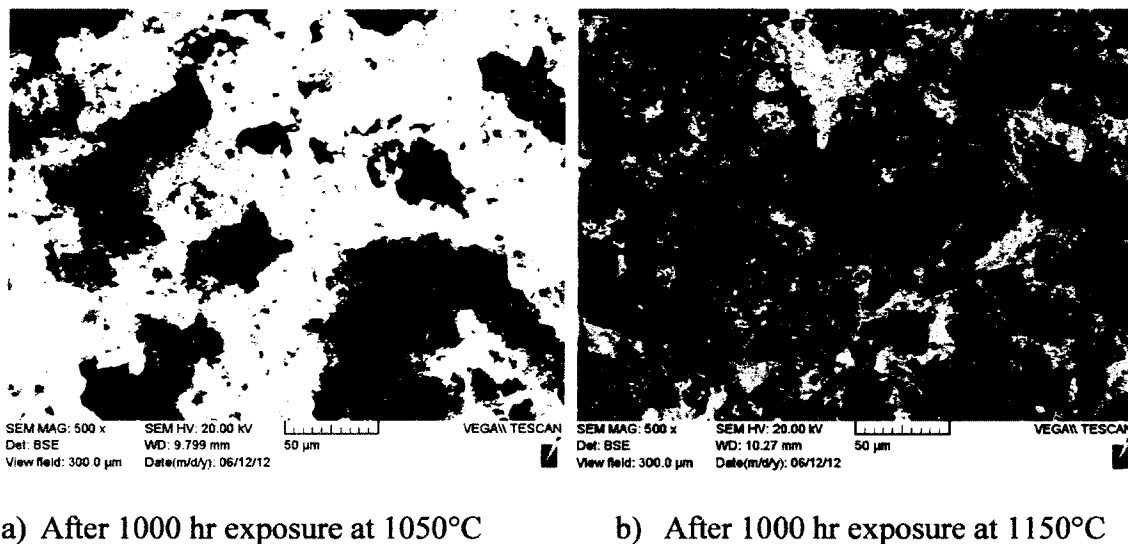


**Figure 7.5 Morphology on the top surface of the coating O1.**

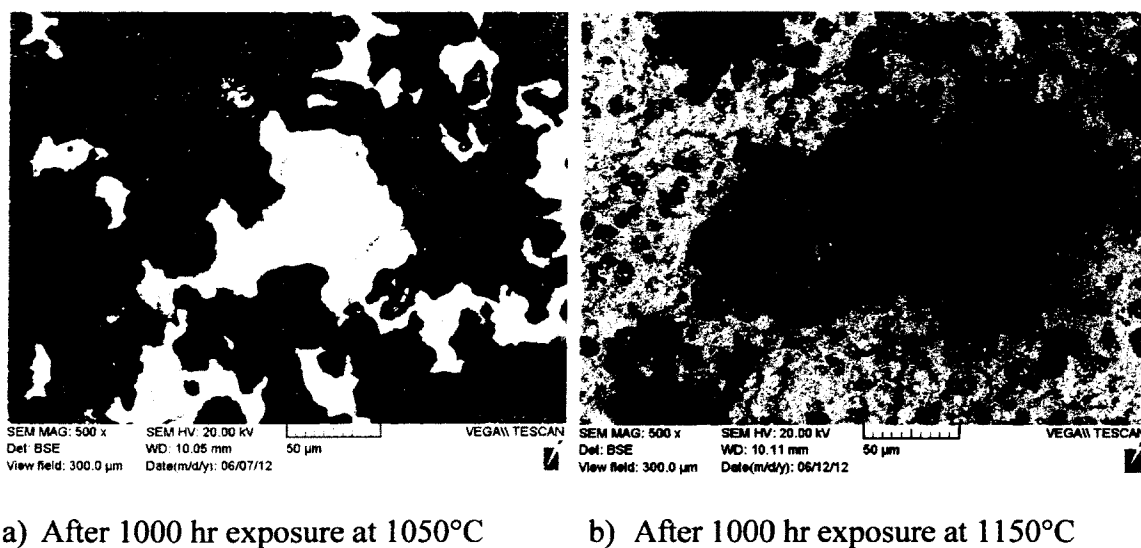
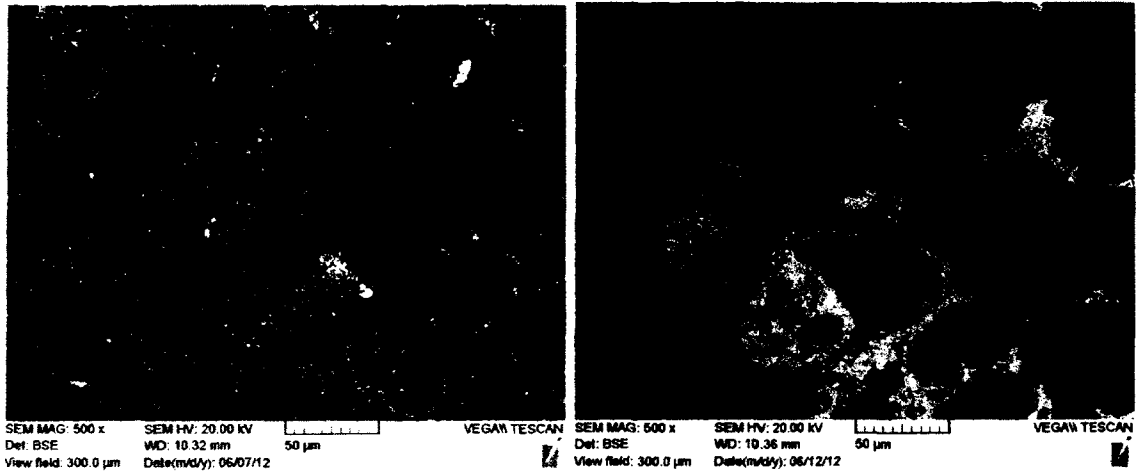


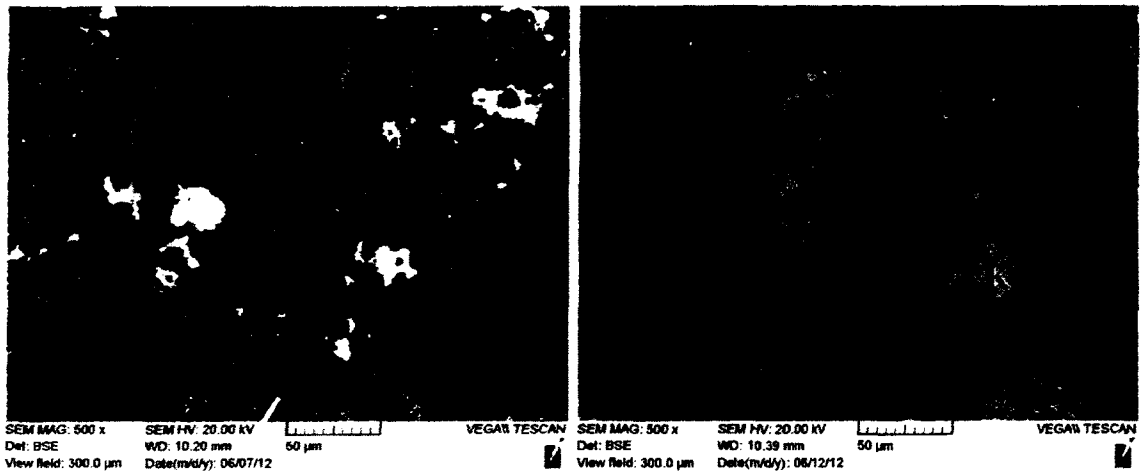
**Figure 7.6 Morphology of coating O3 surface.**



a) After 1000 hr exposure at 1050°C

b) After 1000 hr exposure at 1150°C

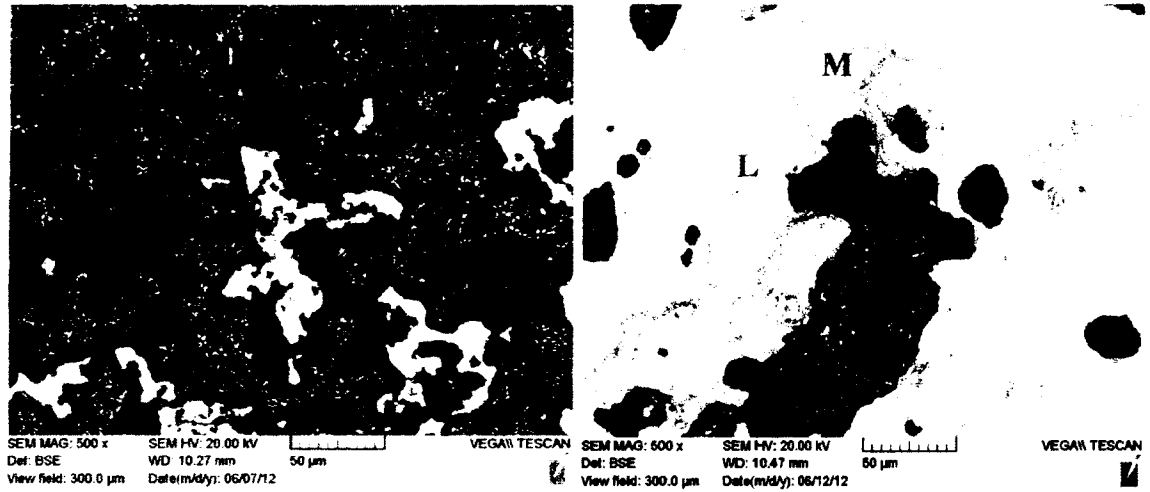
**Figure 7.7 Morphology the coating O4 surface.**



a) After 1000 hr exposure at 1050°C

b) After 1000 hr exposure at 1150°C

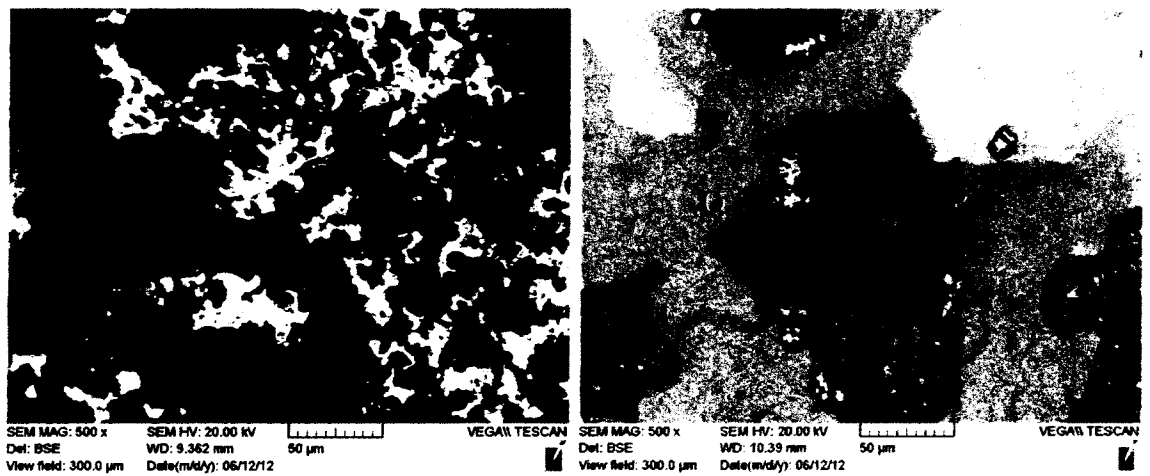
**Figure 7.8 Morphology of coating O6 surface.**



a) After 1000 hr exposure at 1050°C

b) After 1000 hr exposure at 1150°C

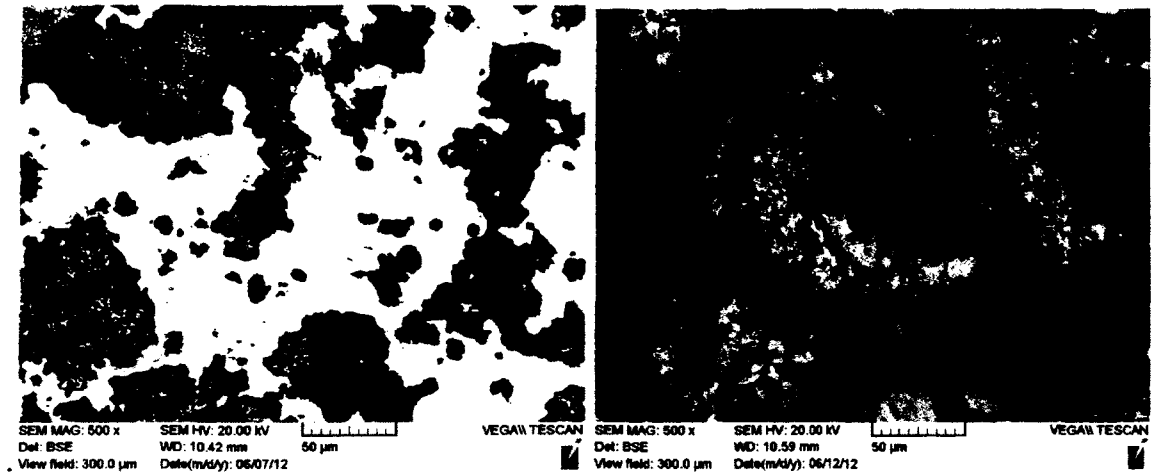
**Figure 7.9 Morphology of coating O7 surface.**



a) After 1000 hr exposure at 1050°C

b) After 1000 hr exposure at 1150°C

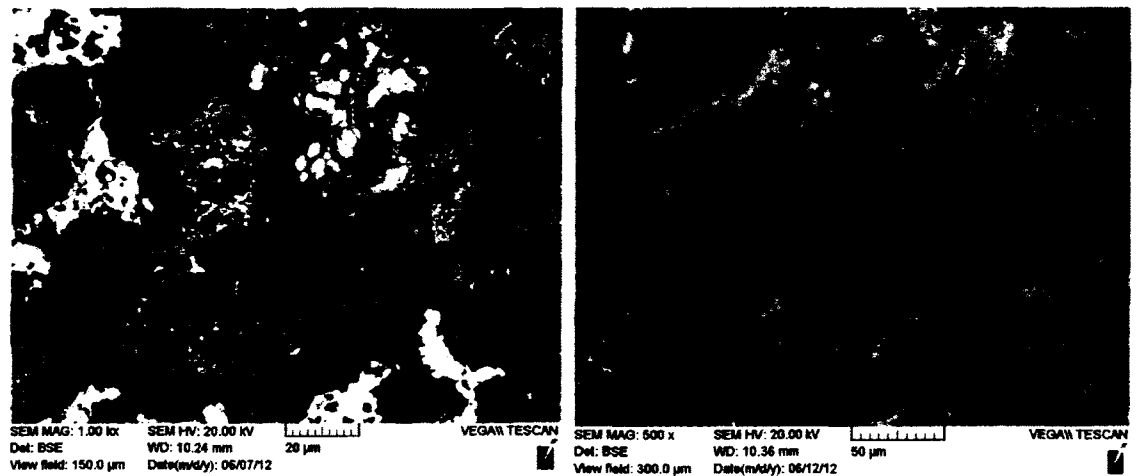
**Figure 7.10 Morphology of coating O8 surface.**



a) After 1000 hr exposure at 1050°C

b) After 1000 hr exposure at 1150°C

**Figure 7.11 Morphology specimen O9 surface.**



a) After 1000 hr exposure at 1050°C

b) After 1000 hr exposure at 1150°C

**Figure 7.12 Morphology of coating O10 surface.**

#### 7.4 Effects of Coating Layer on Area of Oxide Scales

To evaluate the effects of coating layers on the area of oxide scales, the areas of oxide scales of all coatings were measured and characterized. Oxide characterization was started with the measurement of the area of oxide scales on each coating after the oxidation tests. Twenty one (21) cross-sectional micrographs for each coating were taken along the surface of the coating at the same magnification and they were then

divided into three groups because three data points for each coating were needed for developing the model of the area of oxide scales (More replicates make the model more accurate). Every micrograph was processed using the image analysis software, and the area of oxide scales, the blue region in Figure 7.13, was measured from each micrograph. To obtain exact area of oxides scales, the first micrograph imported to the image analysis software was calibrated according to the scale on the micrograph, and this calibration was saved as a default mode for processing the rest of the micrographs.

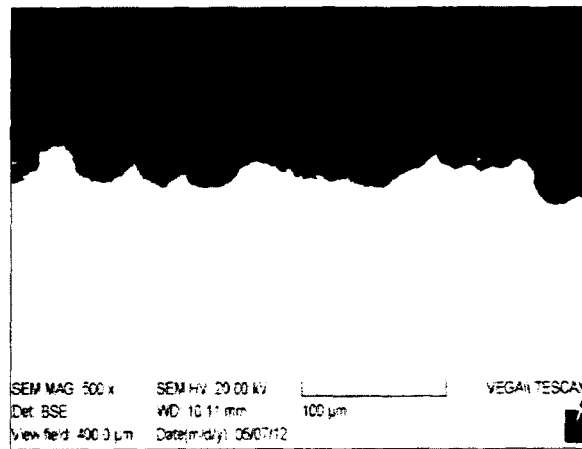


**Figure 7.13 Binarized cross sectional image for coating O1.**

The average values of the area representing oxide scales for each of the seven micrographs are given in Table 7.6 and named as the area of oxide scales. Spallation of oxide scales occurred to some of these coatings. If spallation did occur, determination of the actual oxide level before spallation would become necessary; the procedure was developed and is presented in Table 7.7. The purpose of the calculation was to compare the oxygen gain and mass change of the coating. If the oxygen gain of the coating was close to the mass change of the coating, then there was no spallation occurring in this coating; otherwise spallation occurred.

**Table 7.6 Average areas of oxide scales for the seven micrographs in each group**

Coating	Micrograph No.	Area of oxide scales after spallation, $\mu\text{m}^2$	Total area of oxide scales, $\mu\text{m}^2$	Coating type
O1-1	1-7	5896.5	16711.4	Cr-Si coating/ aluminide I
	8-15	5237.9	16052.8	
	16-21	5085.6	15900.5	
O2-1	1-7	17845.7	17845.7*	Cr-Si coating/ NiCrAlY/ aluminide II
	8-15	17481.6	17481.6*	
	16-21	18597.7	18597.7*	
O3-1	1-7	4601.1	6506.9	aluminide I
	8-15	4350.6	6256.4	
	16-21	4816.2	6722.0	
O4-1	1-7	10741.3	10741.3*	NiCrAlY/ aluminide II
	8-15	11136.1	11136.1*	
	16-21	12274.3	12274.3*	
O5-1	1-7	6052.8	8894.8	Cr-Si coating/ NiCrAlY/ aluminide I
	8-15	6085.4	8927.4	
	16-21	5565.3	8407.3	
O6-1	1-7	6401.3	13094.8	NiCrAlY/ aluminide I
	8-15	6939.2	13632.7	
	16-21	6534.1	13227.6	
O7-1	1-7	4468.2	4468.2*	aluminide II
	8-15	4547.3	4547.3*	
	16-21	4384.5	4384.5*	
O8-1	1-7	3188.7	11015.7	Cr-Si coating/ aluminide II
	8-15	3445.8	11272.8	
	16-21	3834.1	11661.1	

\*Spallation might not occur.

The mass of oxygen gain per square centimeter was used as a criterion to determine the spallation of oxide scales. Based on the difference between the measured mass change and the oxygen gain, spallation of oxide scales did occur in most of the coatings, except for O2, O4 and O7. The area of the spalled oxide scales (before spallation) was calculated following the reversed steps in Table 7.7. The total area of oxide scales in a coating was then obtained by summing up the area of the remaining

oxide scales and the area of the spalled oxide scales. The final results are given in Table 7.6.

**Table 7.7 Area calculation of oxide scale in a coating specimen**

Procedure	Calculation	Note
Calculating the average area of oxide scales per image field	$\frac{(17845.7 + 17481.6 + 18597.7) \times 2}{3 \times 10^6}$ $= 35.95 \times 10^{-3} \text{mm}^2$	Both sides of the coating are considered.
Calculating the volume of oxide per image field	$35.95 \times 0.001 \times 1 \text{ mm (depth)}$ $= 35.95 \times 10^{-3} \text{mm}^3$	Assuming 1 cm depth of the scale
Calculating the volume of oxide scales per square cm	$\frac{35.95 \times 10^{-3}}{400 \times 10^{-3}} \times 100$ $= 8.99 \text{mm}^3/\text{cm}^2$	The horizontal length for the field of each micrograph is 400 $\mu\text{m}$ .
Calculating the mass of oxide scales per square centimeter	$8.99 \times 4.0 = 35.95 \text{mg}$	The density of $\text{Al}_2\text{O}_3$ is $4 \text{mg}/\text{mm}^3$
Calculating the mass of oxygen per square centimeter	$35.95 \times \frac{16 \times 3}{16 \times 3 + 27 \times 2}$ $= 16.92 \text{mg}$	The atomic mass for O and Al is 16 and 27
Calculating the mass of oxygen per square centimeter due to porosity of oxide	$16.92 \times 0.8 = 13.44$	The porosity of $\text{Al}_2\text{O}_3$ is assumed to be 20%.
Determining the spallation of oxide scales	$\Delta w = O_g - Al_l$ $Al_l = O_g - \Delta w$ <i>If <math>O_g \geq \Delta w</math>, spallation occurs</i> $13.44(O_g) < 13.81(Al_l)$ , therefore no spallation	The mass of oxygen per square centimeter is used as a criterion to determine if spallation has occurred

The total areas of oxide scales in Table 7.6 were used for the analysis of variance and development of a model that is related to the coating types. The ANOVA results for the total area of oxide scales are given in Table 7.8. The  $R^2$  value shows that the model and the experimental data have a very high degree of fitness. The  $p$ -values for

the factors and the interactions of all factors are close to zero, which indicates all factors and their interactions are significant.

**Table 7.8 ANOVA results for oxide scales**

Source	DOF	Sum of squares	Mean square	F value	p-value
Main effect, <i>U, V, W</i>	3	192278620	64092873	348.06	0.000
Interaction between two factors, <i>UV, UW, VW</i>	3	181212283	60404094	328.03	0.000
Interaction between three factors, <i>UVE</i>	1	73950360	7395036	401.59	0.000
Residual	16	2946306	184144		
Total	23	450387569			
$R^2$		99.35%			

Some effects, sequential SS, and percent contributions for the total areas of oxide scales are presented in Table 7.9. Judging from the results, it is concluded that:

- All main factors and their interactions increased the total area of oxide scales except that the interaction of Cr-Si layer and NiCrAlY reduced the total area of oxide scales.
- The interaction terms dominated the total area of oxide scales as the summation of the percent contributions of all the interaction terms were over 50%.
- The Cr-Si layer increased the total area of oxide scales.
- Higher Al/Ni ratio hardly increased the total area of oxide scales.

The total area of oxide scales ( $Y_o$ ) with respect to the coating types is illustrated in the following regression equation:

$$Y_o = 6495.17 + 9726.47 \times U + 6823.20 \times V - 2028.42 \times W - 14301.60 \times U \times V - 2876.61 \times U \times W + 93.94 \times V \times W + 14042.80 \times U \times V \times W \quad (7-4)$$

When the variable  $W$  is set to be zero (aluminide I) or one (aluminide II), two regression equations,  $Y_{OI}$  and  $Y_{OII}$ , can be obtained as the follows:

$$Y_{OI} = 6495.17 + 9726.47 \times U + 6823.20 \times V - 14301.60 \times U \times V \quad (7-5)$$

$$Y_{OII} = 4466.75 + 6849.86 \times U + 6728.26 \times V - 258.8 \times U \times V \quad (7-6)$$

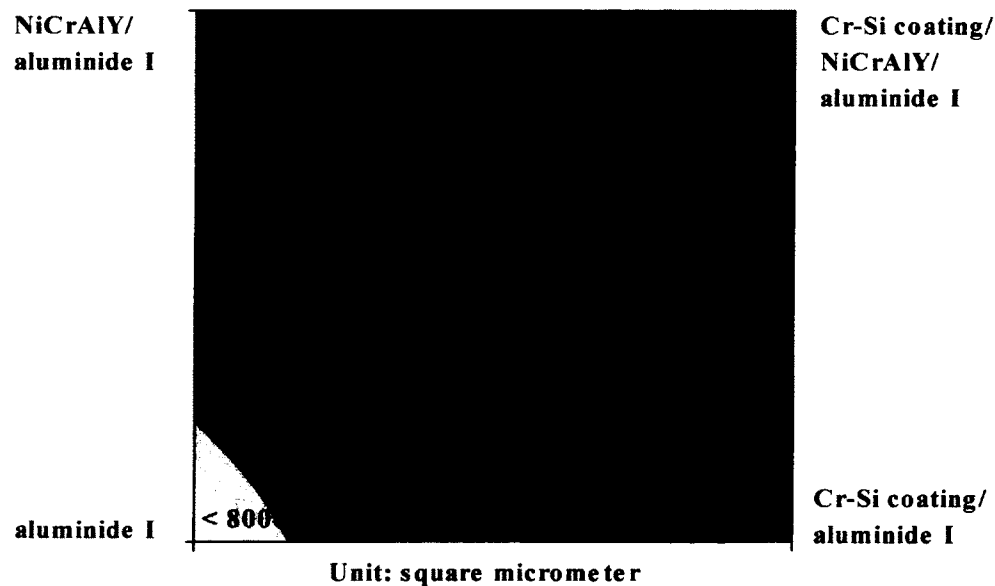
**Table 7.9 Effect, sequential SS, and percent contribution of factors and interactions for the total areas of oxide scales**

Factor	Effect	Sequential sums of squares	Percent contribution
$U$	4648	129628066	28.78
$V$	3230	62600926	13.90
$W$	91	49629	0.01
$UV$	-3640	79500957	17.65
$UW$	2072	25769048	5.72
$VW$	3558	75942278	16.86
$UVW$	3511	73950360	16.42

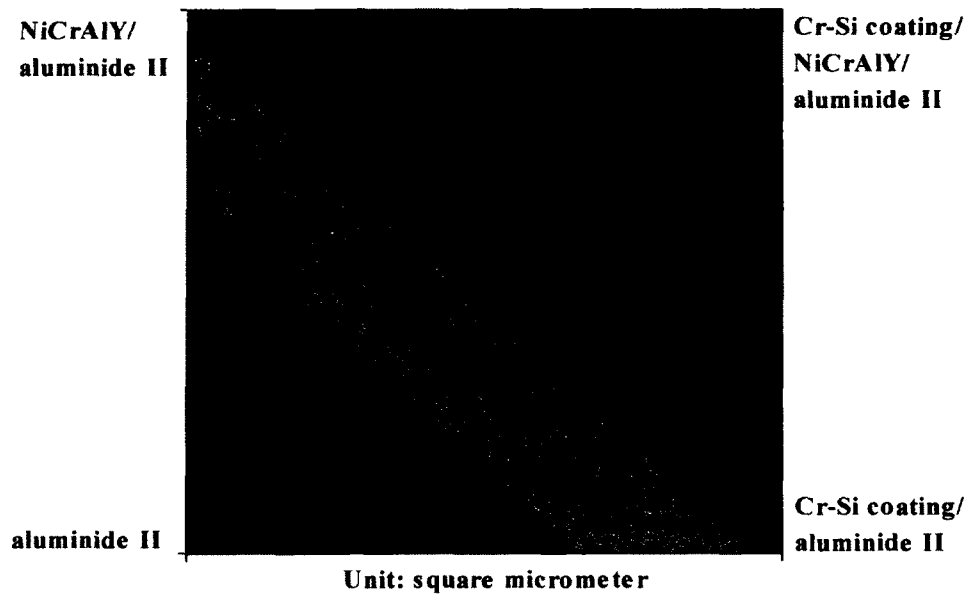
Based on two equations, both variables  $U$  and  $V$  increase the total area of oxide scales, whereas the interaction between  $U$  and  $V$  decreases the total area of oxide scales. It is noted that the interaction term in equation (7-5) is the dominant term. This suggests that when a multilayered coating consists of a top layer of aluminide I and a NiCrAlY middle layer, the interaction between the Cr-Si layer and the NiCrAlY layer substantially decreases the total area of oxide scales. The reason for this occurrence is that the Cr layer and Si rich layer prevented aluminum from diffusing into IN738 as such the top layer remained the NiAl phase for extended period of time. The NiAl phase is known to have better oxidation resistance than the  $Ni_3Al_2$  phase as aluminum content is reduced during the phase transition from  $Ni_3Al_2$  to  $\beta$  (NiAl [113]). This can be further observed in the contour plot of equation (7-5) (Figure 7.14a). The total area of

oxide scales for the coating with a Cr-Si layer (O5) is less than that of the coating without the Cr-Si layer (O6).

When a multilayered coating consists of a top layer of aluminide II and a middle layer of NiCrAlY, the total area of oxide scales of the multilayered coating increases significantly in comparison to that with aluminide I as top layer (Figure 7.14b). The interaction between the Cr-Si layer and the NiCrAlY layer hardly decreases the total area of oxide scales since the coefficient for the interaction term in equation (7-6) is very small. This is because the Cr-Si layer prevented aluminum from diffusing into the IN738 substrate, thus the phase in the top layer of the multilayered coating was mainly the  $Ni_3Al_2$  phase at the beginning of the oxidation test, which was easier to be oxidized before it can be transformed into the NiAl phases. Therefore the effect of the interaction between the Cr-Si layer and the NiCrAlY layer on the total area of oxide scales of a multilayered coating become significant only when the top layer is an aluminide I layer.



a) Contour plot of oxide scale area for the coatings with aluminide I top coat



b) Contour plot of oxide scale area for the coatings with aluminide II top coat

**Figure 7.14 Contour plots of the oxide scale area.**

## 7.5 Characterization of Cr-Si Barrier Layer

### 7.5.1 Structure of Barrier Layer

As detailed in previous sections, the mass changes and total areas of oxide scale are significantly associated with the interaction between adjacent coatings and number of coating layers. Therefore it is crucial to understand the mechanism of the interaction between coating layers. The elemental distribution analysis can be an approach to studying the interaction of the coatings [114]. Using the elemental distribution analysis, the barrier function of a Cr-Si coating during diffusion process has been verified in Chapter 6.

During the oxidation test, the silicon contents decreased to about 15 at.% from the original 20-30 at.% due to diffusion. According to the Ni-Cr-Si ternary diagram, when the chromium content at the interface between the NiCrAlY coating and the Cr-Si

coating increased to over 40 at.%, silicon-rich phases ( $\text{Ni}_2\text{Si}$ ,  $\text{Cr}_3\text{Ni}_2\text{Si}$ , and  $\text{Cr}_3\text{Ni}$ ) will form. The boundary layer of IN738 substrate was found to have transformed into  $\psi$  ( $\text{C}_2\text{Ni}_3\text{Si}$ ) phase after Cr-Si co-deposition. This silicon-rich layer was stable and prevented chromium from diffusing into the substrate [12]. Therefore the barrier layer in fact consisted of a Cr layer and a silicon-rich layer. To maintain the barrier function of the barrier layer in a coating under oxidation environment, two aspects must be satisfied:

- (1) The chromium content in the coating should not significantly decrease.
- (2) The layer containing chromium and silicon-rich phases between Cr-Si barrier layer and NiCrAlY should be stable.

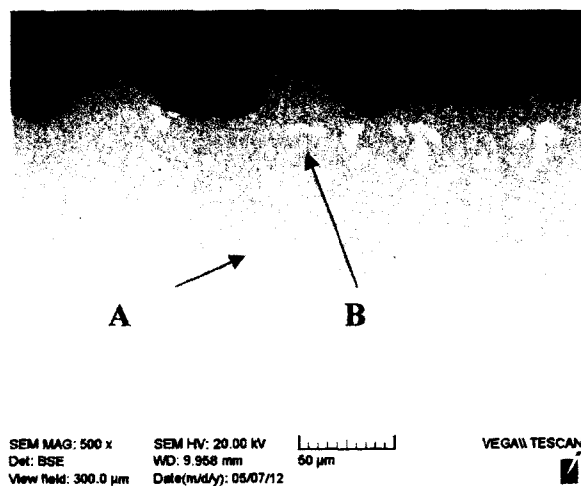
The chromium content in a coating significantly changes when internal  $\text{Cr}_2\text{O}_3$  oxide starts to form [115]. When the aluminum content in the coating falls below 21 at.%, internal  $\text{Cr}_2\text{O}_3$  oxide will form. Therefore, the aluminum content in a coating can be regarded as a governing factor for the stability of chromium and silicon-rich  $\gamma$  phase.

### **7.5.2 Elemental Distributions in Coatings without NiCrAlY Layer**

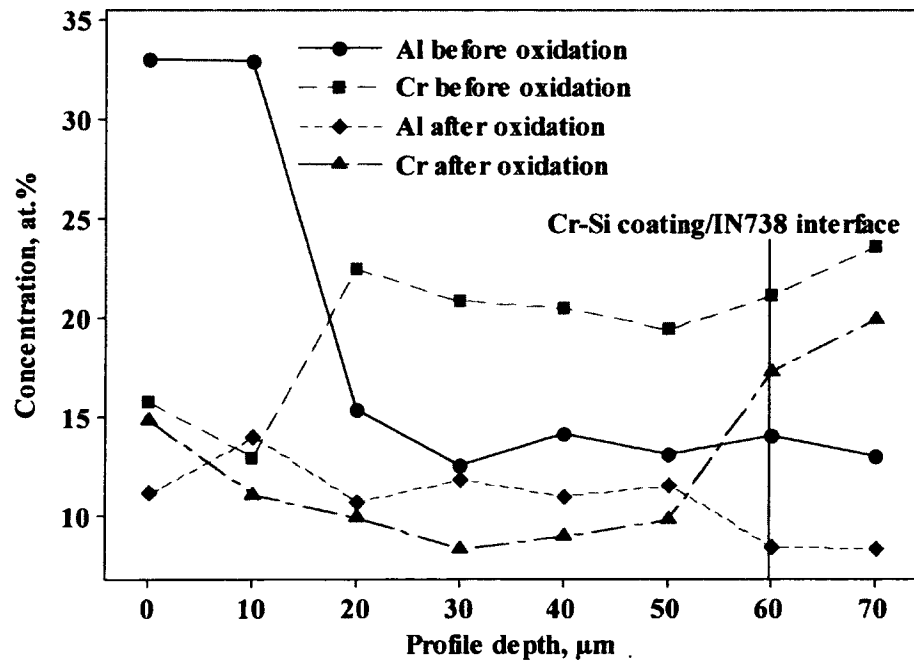
The aluminum contents in all coatings with a Cr-Si layer were all above 21 at.% except coating O1 after 1000 hr at 1050°C (Table 7.4). The examination of the aluminum and chromium contents in coating O1 indicated significant decreases of both elements after the oxidation test (Figure 7.15b). Compared with other coatings, the aluminum content in coating O1 before the oxidation test was lower and the thickness of the coating layer with high aluminum content (21 at.% Al) was also thinner (10  $\mu\text{m}$ ) due to the low aluminum solubility in the Cr-Si phase. As such the aluminum in coating O1 was quickly exhausted during the oxidation test causing internal chromium

oxidation. Moreover the formation of chromium-rich phases (phase A in Figure 7.15a with about 25 at.% Cr) further depleted the chromium content in the coating layer and deteriorated the oxidation resistance of coating O1. Instead of functioning as a barrier layer, chromium-rich phase (phase A in Figure 7.15a) and silicon-rich phase (phase B in Figure 7.15a) were separately precipitated in the coating matrix. Therefore without a middle layer of NiCrAlY, the Cr-Si coating quickly deteriorated and compromised the oxidation resistance of the coating.

The coating without a Cr-Si layer, coating O3, contained more aluminum before and after the oxidation test (Figure 7.16b). This was further supported by the changes of the chromium contents in coatings O1 and O3 after 1000 hr exposure at 1050°C, as shown in Figure 7.16c. The decrease in the chromium content in coating O1 after the exposure was more significant than that in coating O3, which indicated more chromium oxides formed and subsequently evaporated at the elevated temperatures.



a) SEM image



b) Concentration profiles of Cr and Al

**Figure 7.15 Al and Cr concentration analyses in coating O1 (Cr-Si coating/aluminide I) after 1000 hr exposure at 1050°C.**

Coating O8 had a similar microstructure to coating O1 except that the aluminum content in coating O8 was much higher before and after the oxidation test. In addition, more chromium-rich and silicon-rich phases formed on the top layer of coating O8 (Figure 7.17). This observation suggests internal chromium oxidation might not have occurred, although the formation of the chromium-rich phases further depleted the chromium content in the coating matrix.

Compared with coating O8, Figure 7.18 showed that coating O7 (without a Cr-Si barrier layer) had fewer chromium-rich precipitates (phase C and D in Figure 7.16a and phase F in Figure 7.17a) in and the aluminum content was higher before and after the oxidation test, resulting in less mass loss and lower area of oxide scales in coating O7.

**Table 7.10 EDS results of various phases in the coatings**

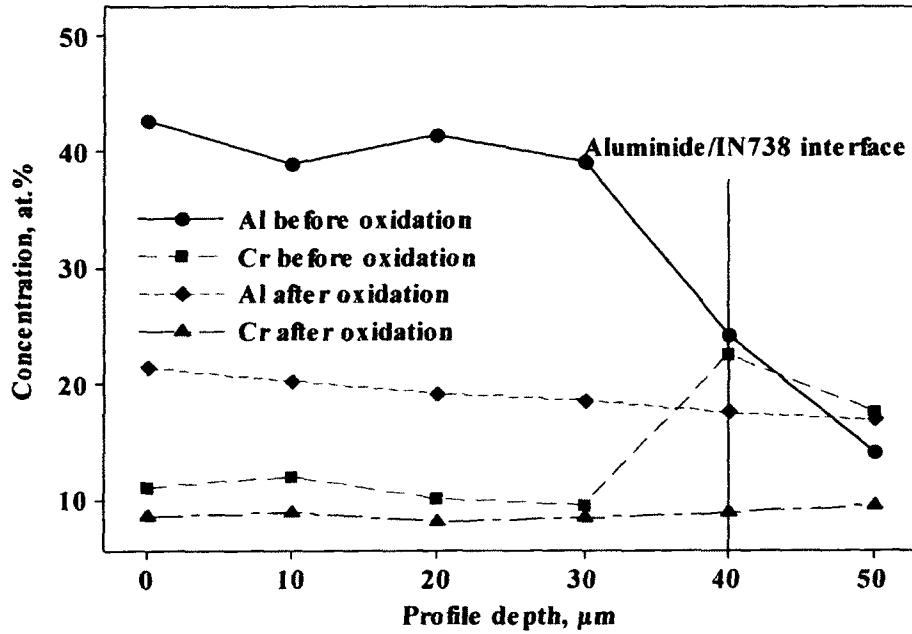
Phase	Concentration, at.%								
	O	Al	Cr	Ni	Ti	Si	Co	Mo	W
A			25.09	28.92	5.82	17.74	4.75	8.55	9.14
B		1.73	2.69	48.96	11.51	26.87	4.89	Nb 3.35	
C		1.41	43.65	26.12	2.34	9.93	10.27	3.70	2.59
D		1.54	21.61	27.65	6.28	18.00	5.45	10.12	9.36
E		1.73	22.19	27.27	6.34	17.35	5.71	9.67	9.71
F		1.52	52.93	20.47	0.54		13.10	6.43	5.00
G			86.53	4.69			1.56	3.24	3.97
H		25.79	6.47	58.80	2.46	2.27	4.20		
I			23.20	28.93	6.07	19.99	4.39	9.58	7.83
J		2.30	53.99	21.50			5.90	4.39	
K			85.37	4.38			1.82	4.17	
L		2.54	20.62	26.65	7.27	18.20	4.25	11.10	9.38
M			29.17	30.13	5.58	16.74		7.33	7.39
N		1.37	2.92	50.07	11.36	26.70	4.53	Nb 3.05	
Z	50.94	33.16	2.62	10.02	1.07	1.31	0.89		



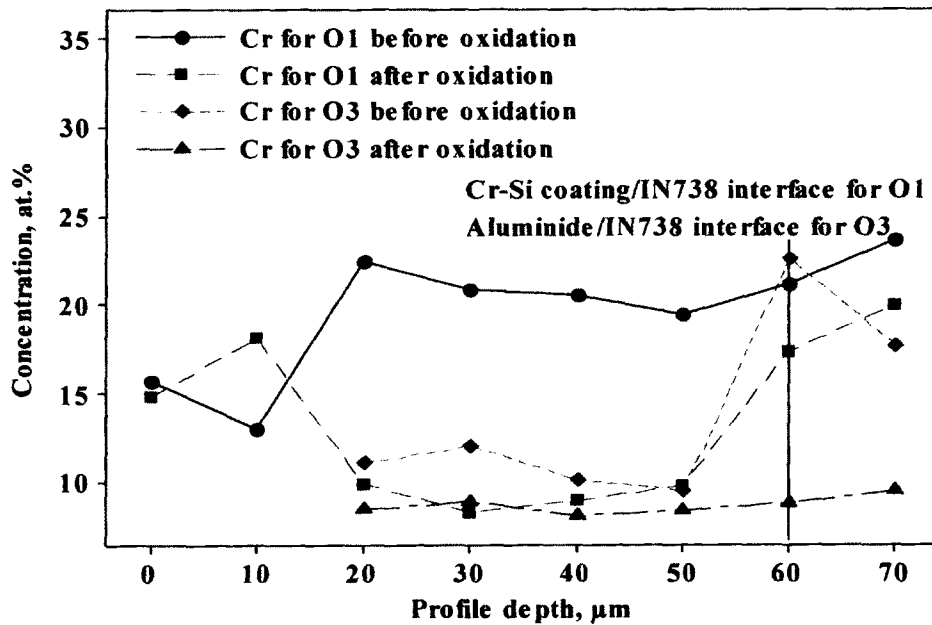
SEM MAG: 500 x SEM HV: 20.00 kV  
 Det: BSE WD: 9.849 mm  
 View field: 300.0 µm Date(m/d/y): 04/26/12

VEGA\\ TESCAN

a) SEM image of coating O3

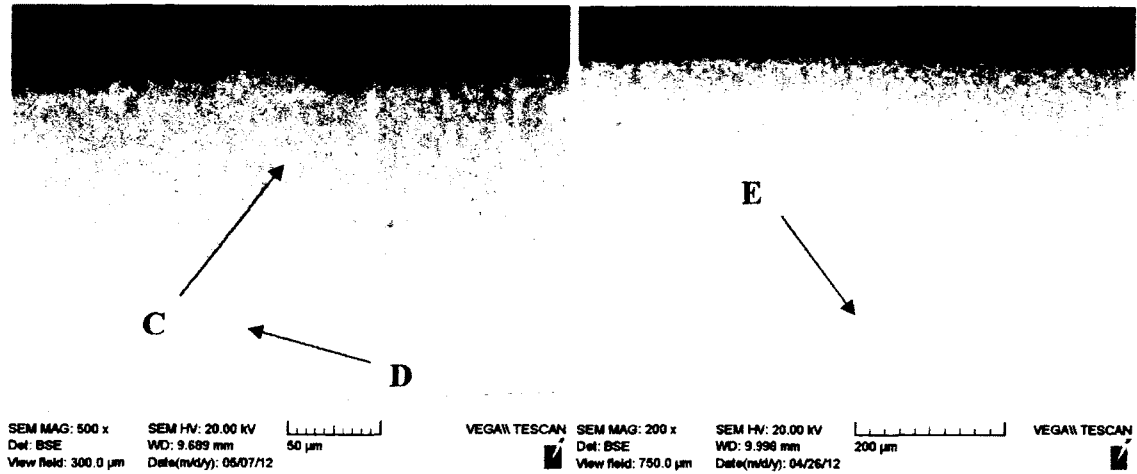


b) Concentration profiles of Al and Cr in coating O3



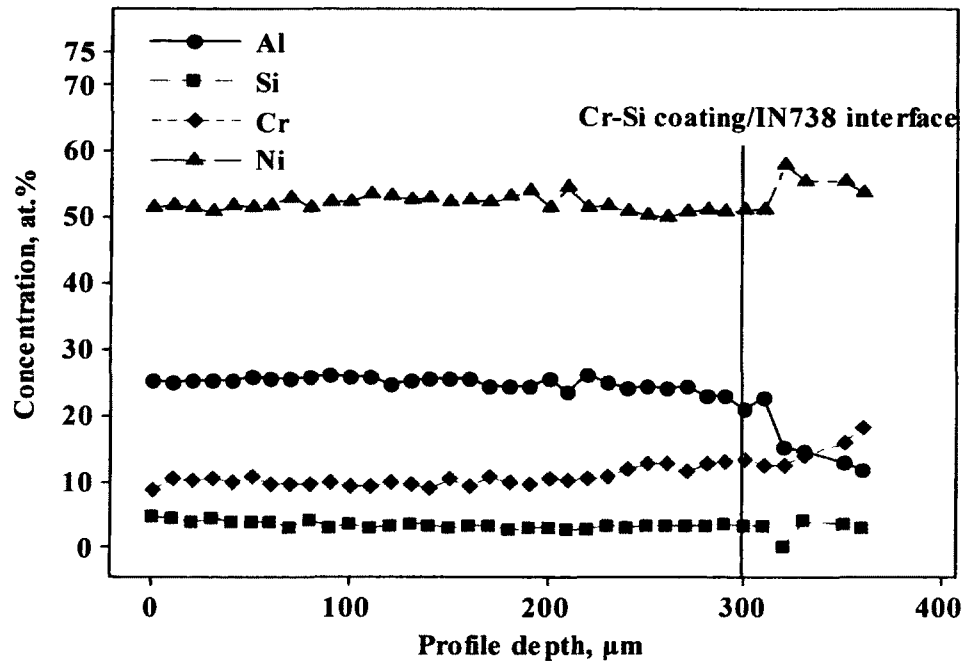
c) Cr profiles in coating O1 and O3 before and after 1000 hr exposure at 1050°C

**Figure 7.16 Concentration analyses in coating O3 (aluminide I) after 1000 hr exposure at 1050°C.**



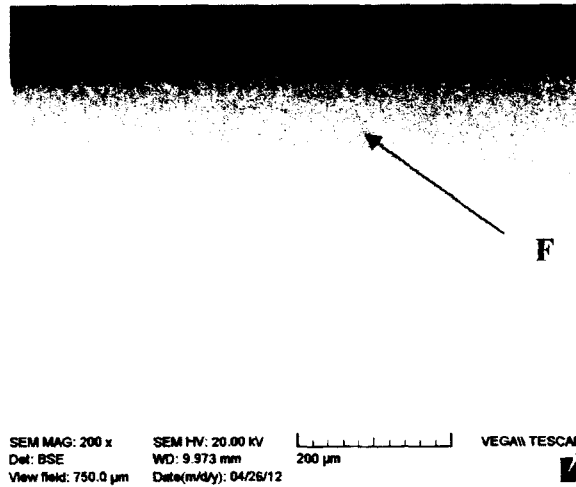
a) SEM image at high magnitude

b) SEM image at low magnitude

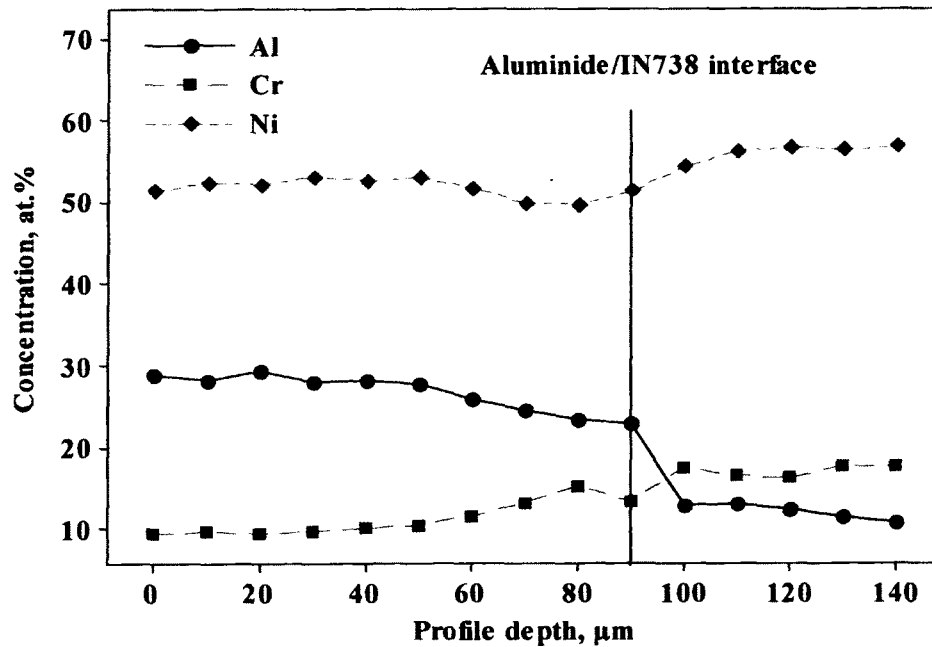


c) Concentration profiles of Al, Cr and Ni

**Figure 7.17 Concentration analyses in coating O8 (Cr-Si coating/aluminide II) after 1000 hr exposure at 1050°C.**



a) SEM image



b) Concentration profiles of Al, Cr and Ni

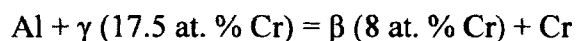
**Figure 7.18 Concentration analyses in coating O7 (aluminide II) after 1000 hr exposure at 1050°C.**

On the basis of the analysis of the concentration profiles and microstructures of the coatings without the NiCrAlY layer, the barrier layer was unable to form in these coatings during the oxidation test even there was a Cr-Si layer in coatings before the

oxidation test. The microstructure of the Cr-Si layer significantly changed from a columnar structure into a composite structure with a matrix and precipitates of Cr-rich, Si-rich phases instead of a Cr layer. Therefore the presence of the NiCrAlY layer is imperative to form the barrier layer.

### 7.5.3 Formation of Barrier Layer

With the NiCrAlY layer in coating O5, the Cr layer formed during the aluminizing process since the chromium content in coating O5 increased from 20 at.% (Figure 5.13d) to 45 at.% at the interface between the NiCrAlY layer and the Cr-Si layer after the aluminizing process (Figure 6.3). This increase in Cr was due to the inward diffusion of the chromium from the NiCrAlY layer [116,117], and the diffusion of chromium continued during 1000 hr exposure at 1050°C. Based on the Ni-Cr-Al ternary diagram (Figure 2.7), the solubility of Cr in the  $\beta$  phase is less than 8 at.% at 1000°C, which is below the chromium content in NiCrAlY (17.5 at.%) since  $\gamma$  phase in NiCrAlY contains more chromium. During aluminizing process, the following phase transition occurred:

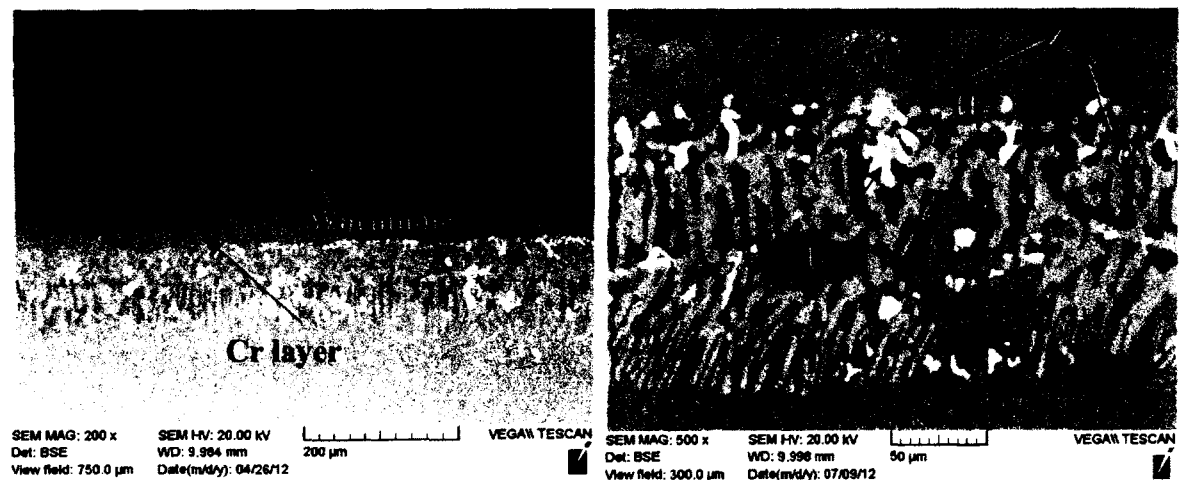


This phase transition produces  $\beta$  phases and excessive Cr atoms to form the Cr layer during coating process.

The Cr layer was believed to have formed during the oxidation test for coating O2 (Figure 7.19a). During 1000 hr exposure at 1050°C, the more  $\text{Ni}_2\text{Al}_3$  phases transformed into  $\beta$  phases due to the continuous diffusion of Al from the top layer into the NiCrAlY layer and a  $\beta$  phase layer at 160  $\mu\text{m}$  formed above the Cr layer (Figure 7.19c), and this  $\beta$  layer rejected the Cr atoms not only to the interface of the NiCrAlY

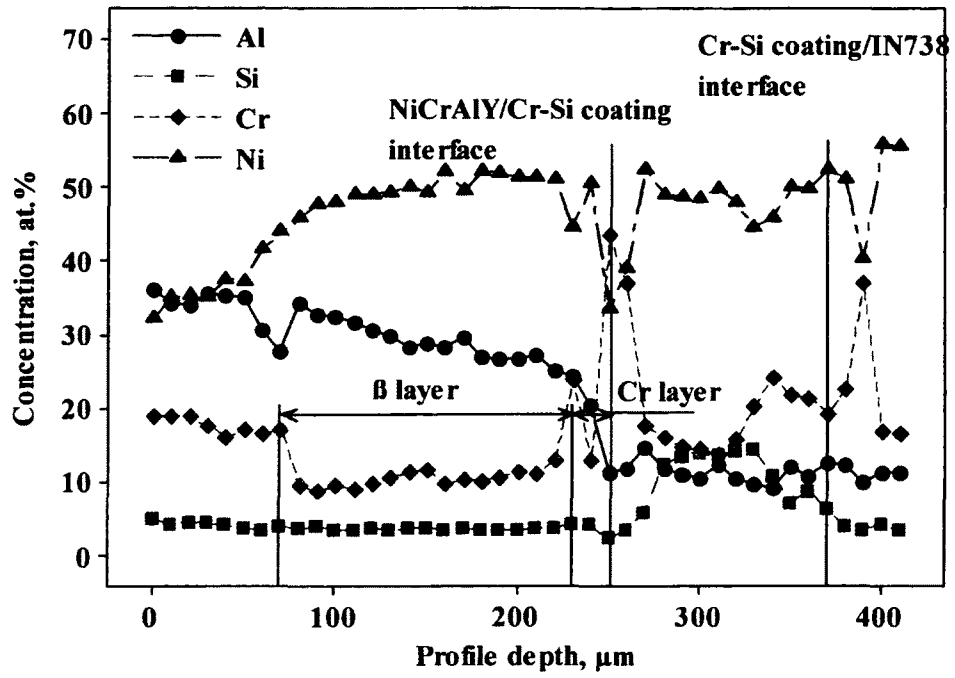
and Cr-Si layers to form the Cr layer but also to the coating surface to form a two-phase zone of the  $\beta$  phase and the Cr-rich phase. Therefore the chromium profile in coating O2 had a U shape with the longer right arm. The chromium content in the Cr layer could reach 86% (G at Table 7.5). According to previous studies [118], the phase of this layer became  $\alpha$ -Cr phase.

The formation of the Cr layer and the silicon-rich layer can be visualized by comparing the X-ray maps before and after the oxidation test. It was shown that silicon distributed uniformly across the Cr-Si layer in coating O2 before the oxidation test (Figure 6.5e) with a Cr-rich layer above it (Figure 6.5d). After the oxidation test, silicon and chromium concentrated on the boundary of the Cr-rich layer and Si-rich layer (Figure 7.19f and Figure 7.19g). Also observed was the impediment to aluminum diffusion by the barrier layer (Figure 7.19e).



a) SEM image of the coating

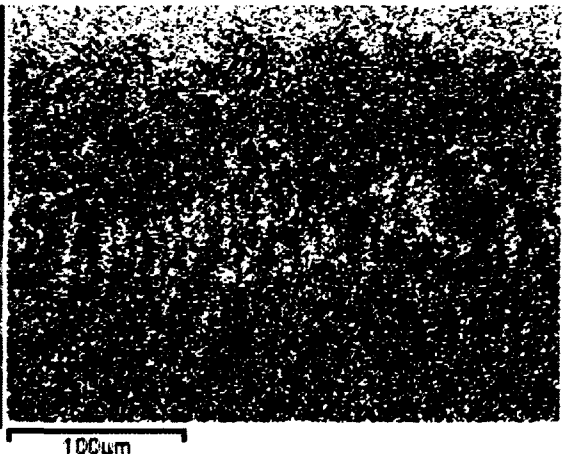
b) SEM image of the barrier layer



c) Concentration profiles of Al, Si, Cr and Ni



d) BSE image for mapping



e) Al map

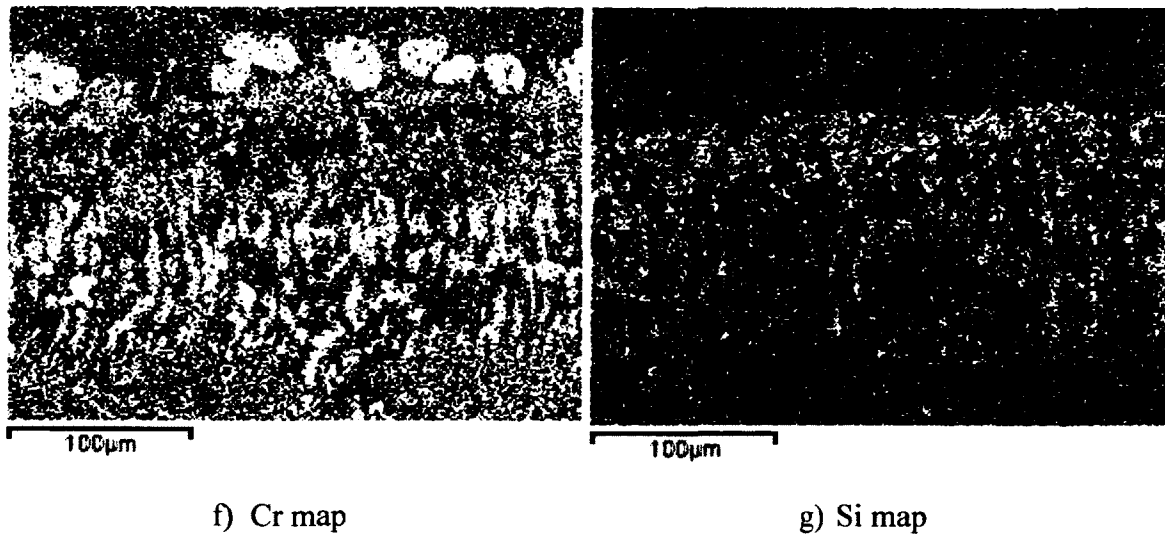
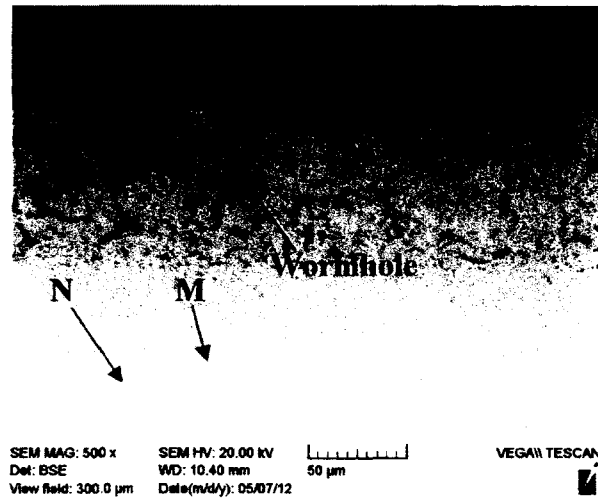


**Figure 7.19 Concentration analyses in coating O2 (aluminide II) after 1000 hr exposure at 1050°C.**

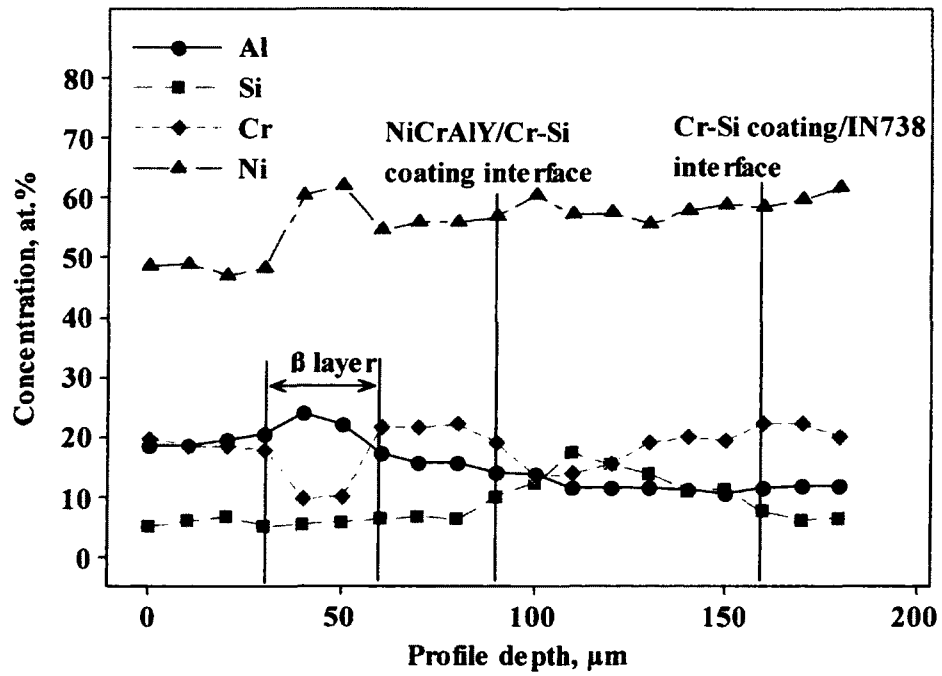
The Cr layer and Si-rich layer formed in coating O5 during the aluminizing process (Figure 6.4a and 6.4d) became less stable during 1000 hr exposure at 1050°C. Unlike that in coating O2, the microstructure below the barrier layer for coating O5 significantly changed from a columnar structure (Figure 6.4a) into a composite structure with a matrix and precipitates of Cr-rich, Si-rich (phase M in Figure 7.20a), and possible TCP (phase N in Figure 7.20a) during the exposure.

The aluminum content in the NiCrAlY layer significantly decreased after the oxidation test. However, Figure 7.20 shows that aluminum distributes evenly in the Cr-Si layer and in the interface region between the Cr-Si coating and IN738 substrate. Such sharply reduced aluminum content was unable to protect chromium from oxidizing and to keep the barrier layer stable. Therefore, to form and sustain a Cr layer and silicon-rich layer in a multilayered coating, three conditions must be met:

- silicon-containing phases form in a silicon-rich layer, preferably in a columnar form
- a chromium reservoir to build up a Cr layer above the silicon-rich layer
- a sufficient aluminum reservoir



a) SEM image



b) Concentration profiles of Al, Si, Cr and Ni

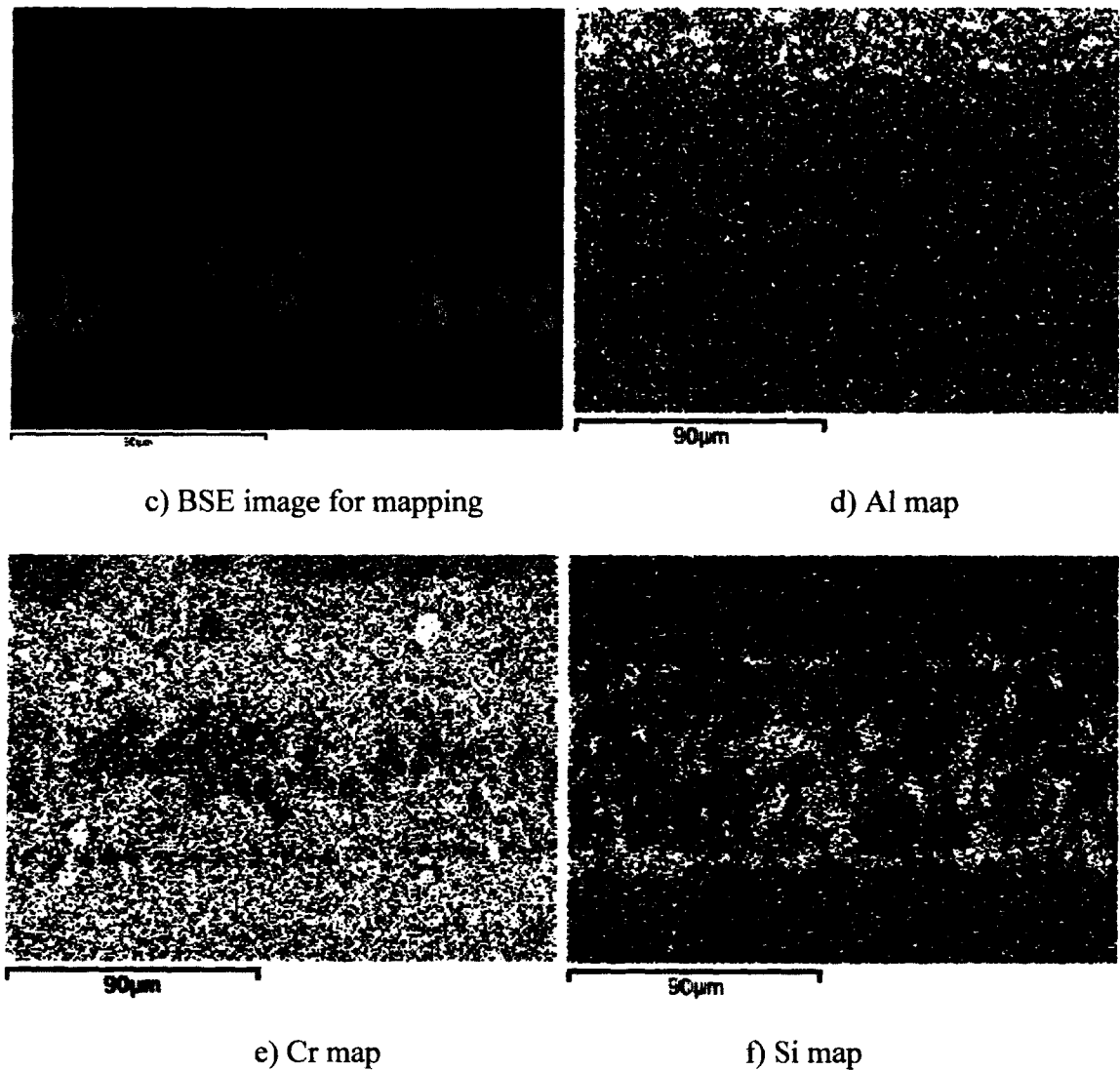


**Figure 7.20 Concentration analyses of coating O5 (Cr-Si coating/NiCrAlY/aluminide I) after 1000 hr exposure at 1050°C.**

The aluminum content in coating O5 (20 at.%) is much lower than that in coating O2 (> 30 at.%) and the  $\beta$  NiAl layer in coating O5 (about 50  $\mu\text{m}$ , Figure 7.20b) is much thinner than that in coating O2 (160  $\mu\text{m}$ ). Instead of a U shape, the shape of the chromium profile in coating O5 is more like a V. Therefore coating O2 is more resistant to oxidation than coating O5.

However, compared with the coating without the barrier layer (O6), the barrier layer in coating O5 did exhibit its positive effects on the oxidation resistance and enabled the top layer of NiAl to be evenly oxidized at relative low rate during the oxidation test at 1050°C. The barrier layer helped to sustain Al content in the top layer. Accordingly, coating O5 shows less area of oxide scales than coating O6 (Figure 7.21).

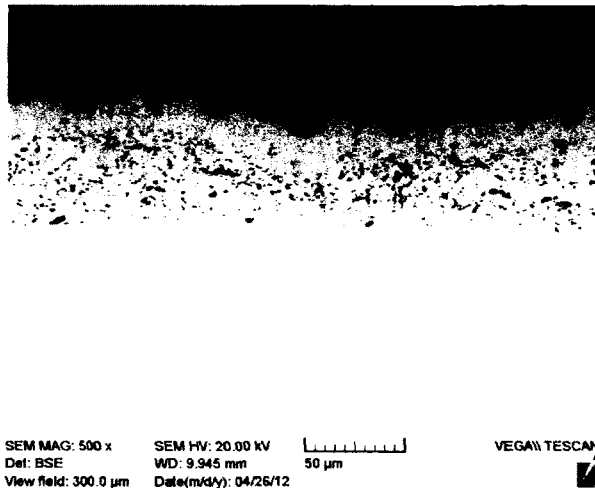


**Figure 7.21 SEM image of coating O6 (NiCrAlY/aluminide I) after 1000 hr exposure at 1050°C.**

#### **7.5.4 Function of Barrier Layer**

Evidently a Cr layer and silicon-rich barrier layer would not function as intended in the coatings without a middle layer of a NiCrAlY. With this layer, the barrier function was observed in the coating O2. The following evidence verified effects of the barrier layer:

- A grey Cr layer was observed at the interface between NiCrAlY and the Cr-Si layer (Figure 7.19a).

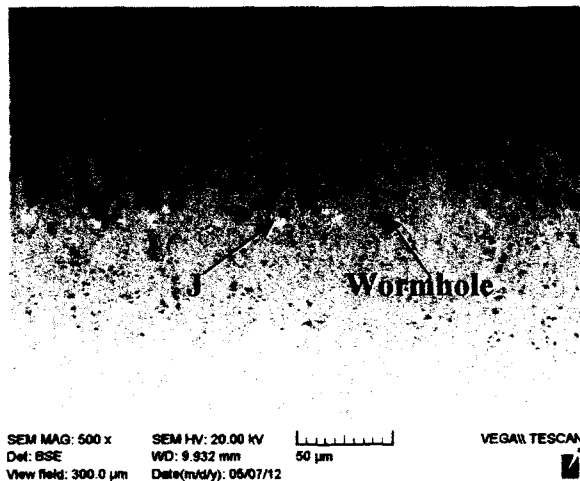
- This Cr layer contained over 80 at.% Cr (Figure 7.19c), and impeded Al diffusion .
- The aluminum and chromium contents across the interface between NiCrAlY layer and the barrier layer varied significantly (phase G and H at Figure 7.19b).
- The aluminum content steadily decreased from the coating surface to the substrate, but dropped sharply at the interface between the NiCrAlY layer and the barrier layer (Figure 7.19c).
- Some topologically closed packed (TCP) phases (phase I at Figure 7.19b), containing Mo and W, were observed under the Cr layer in coating O2, whereas TCP phases were observed in the NiCrAlY coating in coating O4 (phase J at Figure 7.22), which has no Cr-Si barrier layer. This finding suggests that the barrier layer not only prevented aluminum diffusing into the substrate, but also enable impeding the diffusion of other elements in the substrate diffusing into the coating.

Most of TCP phases were deleterious to the mechanical properties of the coating and the substrate because of the reasons below [119, 120]:

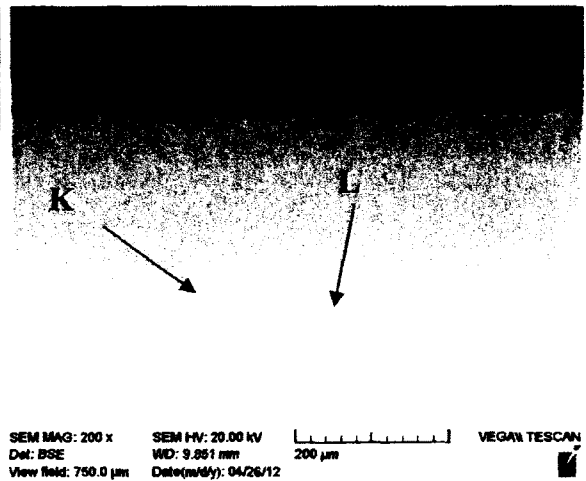
- All TCP phases have different lattice structures from the lattice structure of  $\gamma/\gamma'$  phase. For example, one of TCP phases,  $\sigma$  phase, has the tetragonal lattice structure, whereas  $\gamma/\gamma'$  phase has the fcc lattice structure. The difference in lattice structure induces shear strains and internal stresses in the surrounding  $\gamma/\gamma'$  phase. The internal stresses concentrates near the TCP-phases, and cause fracture of the TCP-phase or de-cohesion between the TCP-phase and the surrounding  $\gamma/\gamma'$  phase. The fracture of the brittle TCP-phase under these stresses could degrade the fatigue properties of the the

coating and the substrate, because the broken TCP-phases could act as initiation points for cracks.

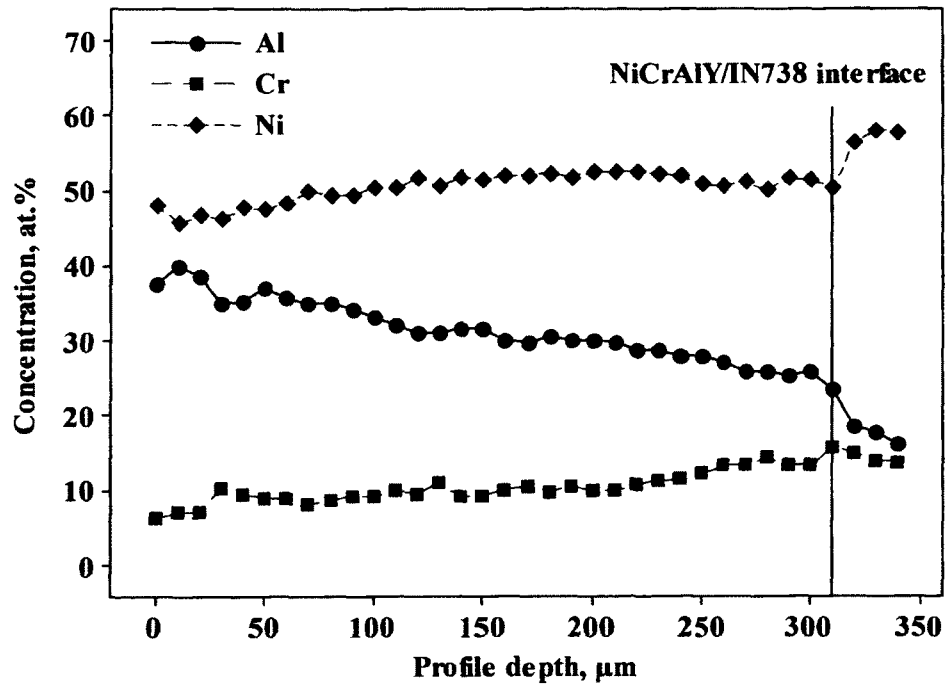
- The differences in thermal expansion coefficients between the TCP-phase and the surrounding  $\gamma'/\gamma$  phase can also affect the properties of the coating and the substrate in service. During temperatures changes, the differences in thermal expansion coefficients cause thermally induced internal strains in the TCP-phases and in the surrounding  $\gamma'/\gamma$  phase. These internal strains could cause the fracture of the TCP-phase and degrade the fatigue properties of the coating and the substrate.



a) SEM image at low magnitude



b) SEM image at high magnitude



c) Concentration profiles of Al, Cr and Ni

**Figure 7.22 Concentration analyses in coating O4 (aluminide II) after 1000 hr exposure at 1050°C.**

### 7.5.5 Effectiveness of Barrier Layer

The effectiveness of the barrier layer on the oxidation behavior of multilayered coatings has been observed to vary based on the aluminum content in the top layer [121,122]. The examination of the elemental profiles for coating O2 (Figure 7.19c) and coating O4 (Figure 7.22b) after 1000 hr exposure at 1050°C indicated that the originally formed  $Ni_2Al_3$  phases in the top layer of aluminized coatings transformed to  $\beta$  (NiAl) phases during the exposure due to Al consumption.

The consumption of the aluminum in coating O2 was mainly attributed to the oxidation of the aluminum in the top layer, whereas the reduction of the aluminum in

coating O4 was caused by both the oxidation of the aluminum in the top layer and the diffusion of aluminum into the substrate. In the cases where the  $\text{Ni}_2\text{Al}_3$  phase was the dominant phase in the top layer, the diffusion of aluminum into the substrate was favorable for achieving the  $\beta$  phase during the exposure and beneficial for oxidation resistance, at least during 1000 hr exposure at  $1050^\circ\text{C}$ .

Observed from Figure 7.19a and Figure 7.22a, the oxide scales in coating O2 (with barrier) was much thicker than that for coating O4 (without barrier). The reason for the heavier scale formation is that the phase transition from the  $\text{Ni}_2\text{Al}_3$  phase to the  $\beta$  (NiAl) phase released surplus aluminum atoms on the surface to create the thick  $\text{Al}_2\text{O}_3$  scales.

Also some wormholes were observed in coating O2, O4, and O5. The formation of wormholes was related to Kirkendall voids and locally accelerated metal vaporization [123]. During the oxidation test, the oxidation of Al caused Al depletion in the vicinity of the interface between oxide scales and the coatings. Al depletion forced Ni to diffuse away from the interface. Since the diffusivity of Ni is higher than that of Al in Al-rich phase at  $1050^\circ\text{C}$ , Kirkendall voids formed under the oxide-coating interface. After formation, the voids continued to grow by vapor-phase transport, where Al evaporation is accompanied by Ni diffusion away from the interface. Thus, the diffusion of voids was strong, and became concentrated to some region in the coatings so that the voids condense here, and a wormhole formed. The phase transformation during the oxidation test was also accompanied by a change in the molar volume of phases, which might contribute to the formation of wormholes in coatings as well [87].

### 7.5.6 Effects of Barrier Layer on the Formation of Interdiffusion Zone

A 120  $\mu\text{m}$  thick interdiffusion zone (IDZ) formed between NiCrAlY and IN 738 substrate in coating O4 (with no Cr-Si barrier layer). The IDZ consisted of a  $\beta$  phase matrix and some grey precipitates rich in Cr (K at Figure 7.22b) and bright granular TCP precipitates (L at Figure 7.22b). The formation of the IDZ was caused by the aluminum diffusion into the substrate, which made the initial  $\gamma'/\gamma$  microstructure of the substrate transform into the  $\beta/\gamma'$  microstructure. The solubility of strengthening elements such as Cr, W, and Mo in the initial  $\gamma'/\gamma$  microstructure was much higher than that in the  $\beta/\gamma'$  microstructure; therefore these elements were observed to precipitate from the  $\gamma'/\gamma$  phases and form the Cr-rich phases and TCP phases in the  $\beta/\gamma'$  matrix [124]. There are three types of TCP phases: namely tetragonal ( $\sigma$ ), rhombohedral ( $\mu$ ) and orthorhombic (P) phases [125]. At 1050°C, the rhombohedral ( $\mu$ ) phase is more stable because more refractory elements such as W, Mo are concentrated in the  $\mu$  phase [126]. The formation of the Cr-rich phases and TCP phases may deteriorates the mechanical properties of the substrate by altering the regularity of the  $\gamma'/\gamma$  rafted microstructure [127].

Interdiffusion zones were also observed in coatings O7 (Figure 7.18a) and O8 (Figure 7.17b). The common layers existing in coatings O4, O7, and O8 were the aluminide II top layer, which sustained sufficient aluminum to transform the initial  $\gamma'/\gamma$  microstructure of the substrate into the  $\beta/\gamma'$  microstructure by aluminum diffusion due to the absence of a barrier layer. With a barriers layer in coating O2, an interdiffusion zone (IDZ) was not observed in the coating, which indicated that the barriers layer in multilayered coatings effectively suppressed inward-aluminum diffusion. The

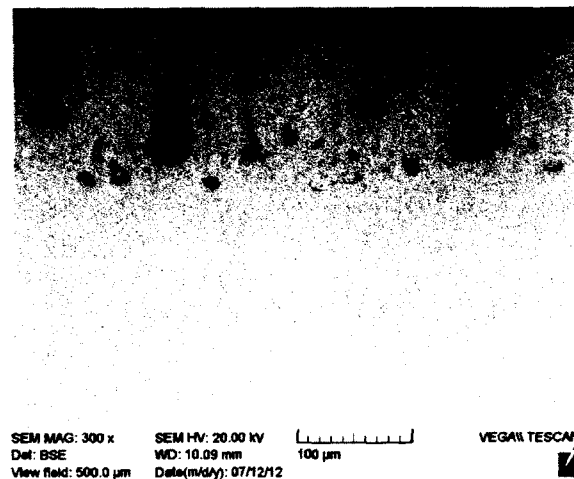
interdiffusion zone was not observed in coatings with aluminide I top layer because of the insufficient aluminum content and continuous aluminum consumption in the coatings during 1000 hr exposure at 1050°C. The microstructures of the substrates in these coatings remained  $\gamma'$  phase in  $\gamma$  matrix with occasional precipitates of Cr-Si-rich, and TCP phases.

### **7.5.7 Effects of Barrier Layer at Different Exposure Temperatures**

The Cr layer and Si-rich layer were stable when the exposure temperatures were only below 1100°C, since the chromium in the coatings could be oxidized and  $\text{CrO}_3$  would form.  $\text{CrO}_3$  is volatile and becomes gas at temperatures above 1100°C. The barrier layers in coating O2 and O5 disappeared after 1000 hr exposure at 1150°C (Figure 7.23a and Figure 7.24a). As demonstrated by the X-ray mapping images for the regions below the coating surfaces of coatings O2 and O5, chromium and silicon uniformly distributed within the regions after 1150°C exposure (Figure 7.23d, Figure 7.23e, Figure 7.24d, and Figure 7.24e). However, the barrier layer in coating O2 postponed aluminum exhaust and kept the aluminum content around 20 at.% before the barrier layer disappeared. A  $\beta$  layer still existed in the coating, which suggests coating O2 still kept its oxidation resistance after 1150°C exposure. However, coating O4, without the barrier layer in the coating, totally disappeared due to rapid aluminum exhaust (Figure 7.25).

When exposed at 1150°C, the barrier layer in coating O5 was unable to prevent aluminum exhaustion because the aluminum content in coating O5 was already around 20 at.% after the first stage of exposure at 1050°C (Figure 7.20b). During 1000 hr exposure at 1150°C, the aluminum content in coating O5 further decreased leading to

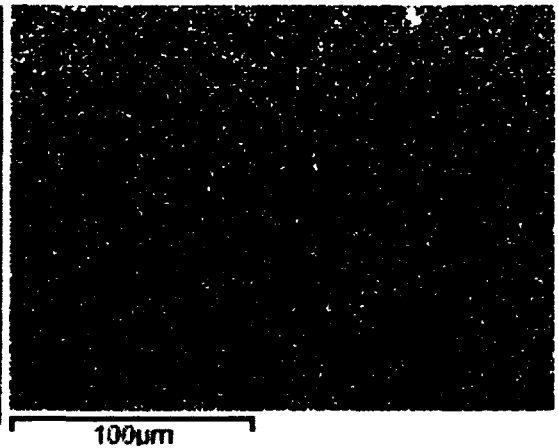
non-protective scale formation. In this case, the chromium in the barrier layer was easily oxidized and eventually evaporated. The evaporation of the chromium oxide ( $\text{CrO}_3$ ) destroyed the continuity of the oxide scales and further accelerated the consumption of Al. Therefore a chromium-rich barrier layer in a coating is harmful to the oxidation resistance of the coating if the aluminum content in the top layer of the coating falls below 21 at.%. This is the reason for the low aluminum content in coating O5 than that in coating O6 after 1000 hr exposure at  $1150^\circ\text{C}$  (Figure 7.26b). Other research found similar results that chromium vaporization from pure  $\text{Cr}_2\text{O}_3$  (transfers to  $\text{CrO}_3$ ) was three orders of magnitude higher than that from  $\text{Cr}_2\text{O}_3$  dispersed with  $\text{Al}_2\text{O}_3$  [128].



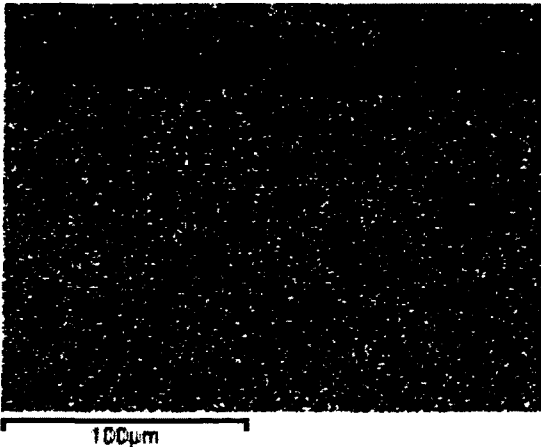
a) SEM image



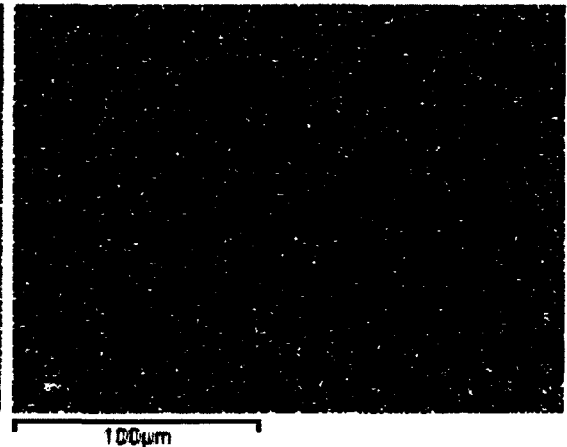
b) SEM image for mapping



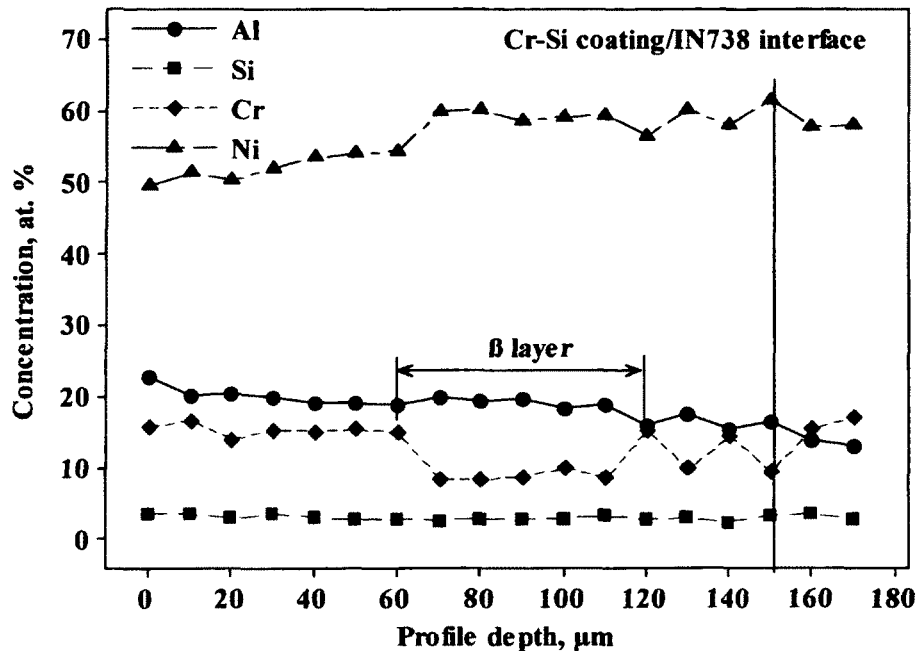
c) Al map



d) Cr map



e) Si map



f) Concentration profiles of Al, Si, Cr and Ni

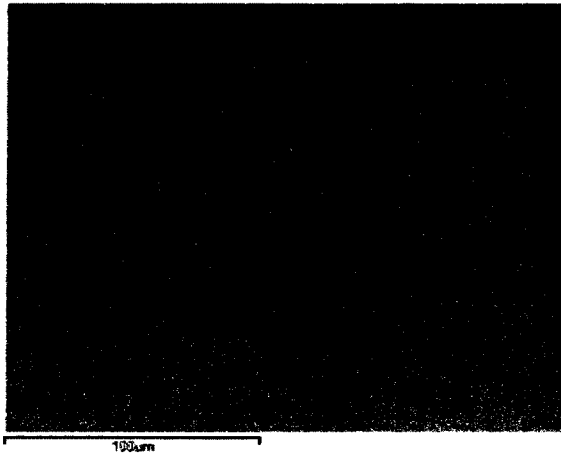
**Figure 7.23 Concentration analyses in coating O2 (Cr-Si coating/  
NiCrAlY/aluminide II) after 1000 hr exposure at 1150°C.**

Similarly, without a Cr-Si layer, coating O7 (aluminide II) still contained around 20 at.% Al after exposure at 1150°C (Figure 7.18b), whereas the oxide scale in coating O8 (Cr-Si coating/aluminide II) completely spalled. Spallation was found to be one of major oxidation characteristics for the coatings after the 1000 hr exposure at 1150°C; this has occurred to coatings O1, O3, O4 and O8. Another characteristic for the coatings after 1150°C exposure was the formation of mixed-oxide protrusions on surface of the coatings due to insufficient aluminum in the coatings [129], which were observed in coatings O5, O6 and O7 (Figure 7.26a and Figure 7.27a). Only coating O2 still kept certain thickness without major damage, which means coating O2 had the best oxidation resistance at 1150°C.

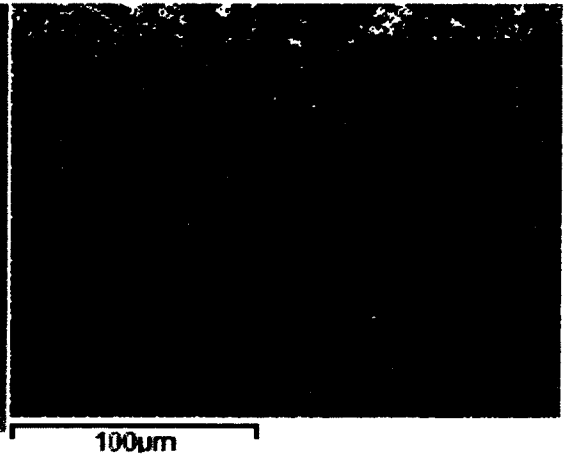


SEM MAG: 500 x SEM HV: 20.00 kV  
Det: BSE WD: 9.733 mm  
View field: 300.0  $\mu$ m Date(m/d/y): 07/12/12 VEGA1 TESCAN

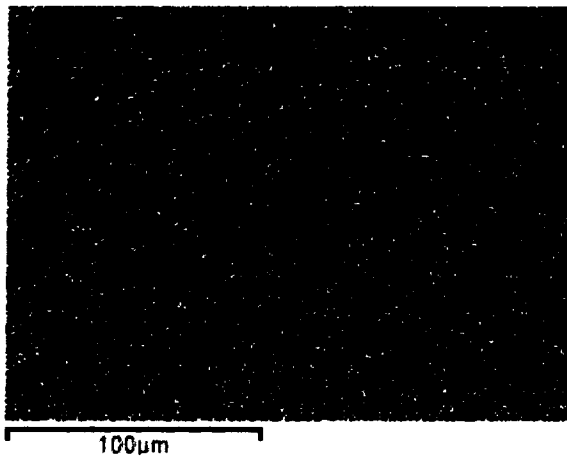
a) SEM image



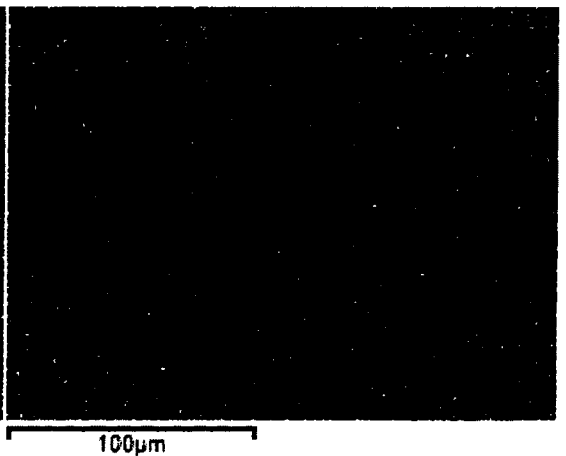
b) SEM image for mapping



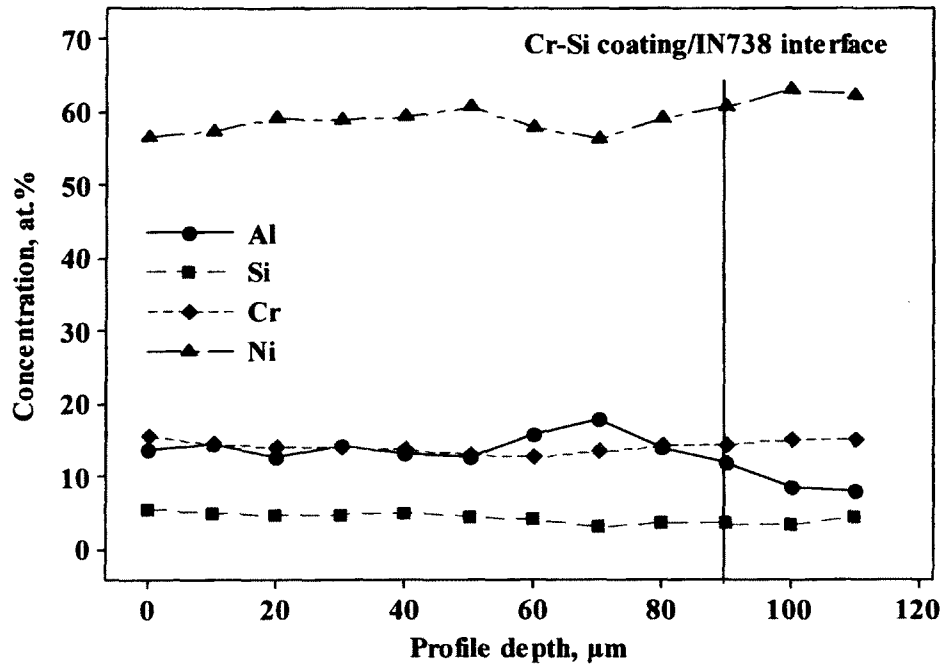
c) Al map



d) Cr map



e) Si map



f) Concentration profiles of Al, Cr and Ni

**Figure 7.24 Concentration analyses in coating O5 (Cr-Si coating/NiCrAlY/aluminide I) after 1000 hr exposure at 1150°C.**

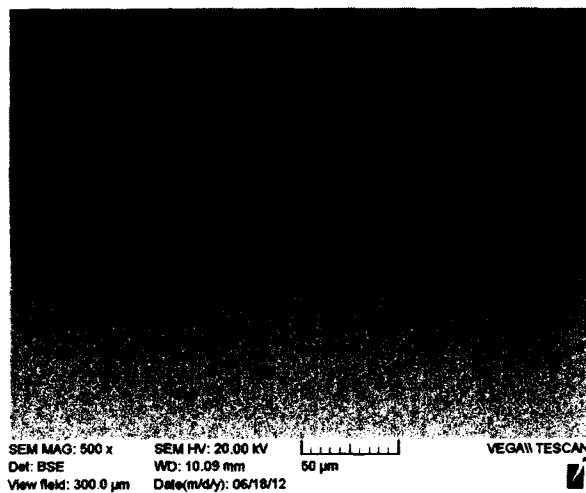
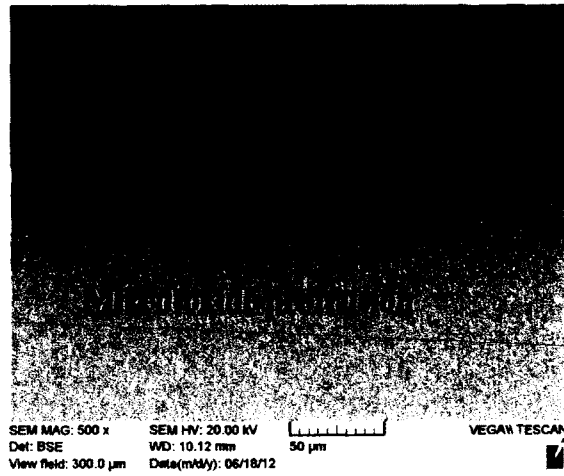
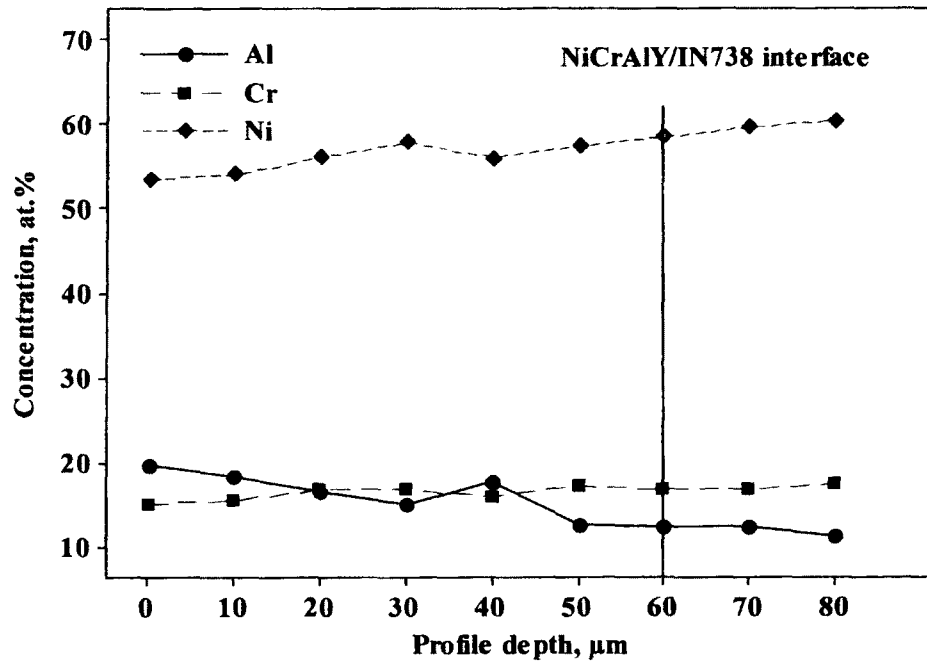


**Figure 7.25 SEM image of coating O4 (NiCrAlY/aluminide II) after 1000 hr exposure at 1150°C.**

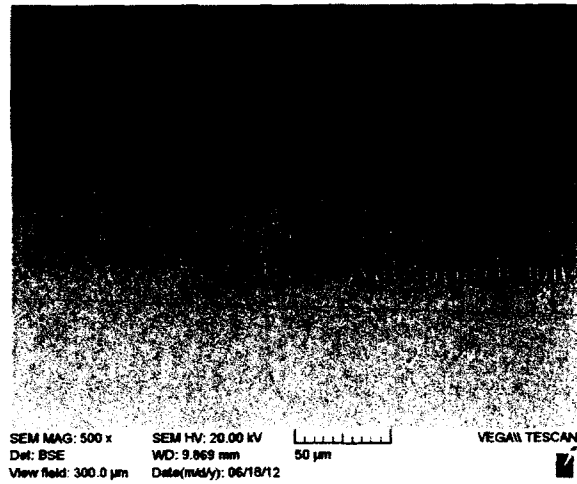


a) SEM image of coating O6

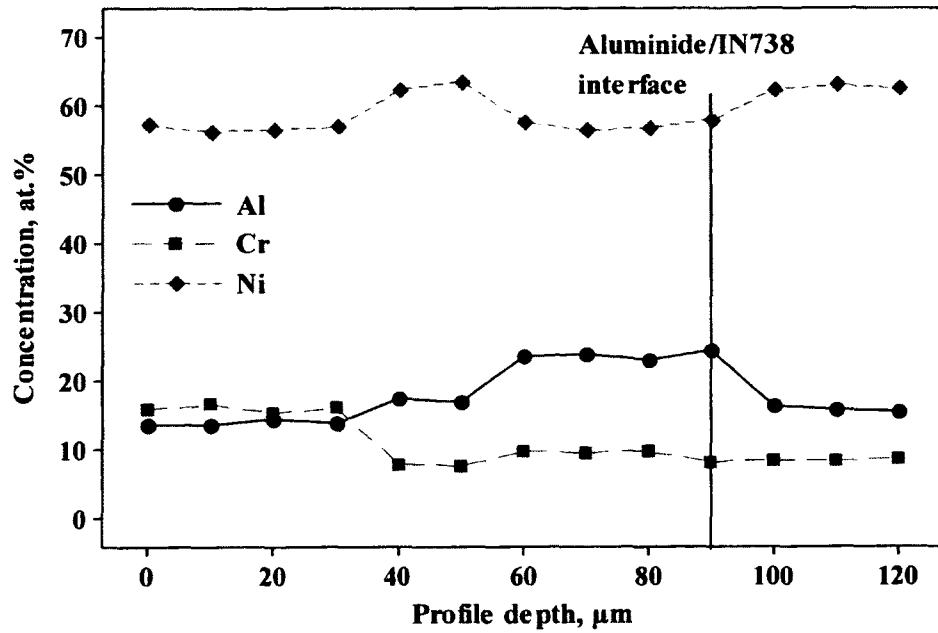


b) Concentration profiles of Al, Cr and Ni

**Figure 7.26 Concentration analyses in coating O6 (NiCrAlY/aluminide I) after 1000 hr exposure at 1150°C.**



a) SEM image of coating O7



b) Concentration profiles of Al, Cr and Ni

**Figure 7.27 Concentration analyses in coating O7 (aluminide II) after 1000 hr exposure at 1150°C.**

After 1000 hr exposure at 1050°C and 1150°C, the microstructures of the coatings significantly changed. A comparison of the microstructures before and after the

exposures is summarized in Table 7.11. More specifically, the microstructures of the coatings changed from the high aluminum content phases ( $\text{Ni}_2\text{Al}_3$  and  $\beta$ ) to low aluminum content phases ( $\gamma'$  and  $\gamma$ ) [129, 130]. A coating loses its protective ability when  $\gamma$  phase starts to form in the top and middle layers since protective  $\text{Al}_2\text{O}_3$  forms on top of  $\beta$  rich phases [131]. Based on the remained phases in Table 7.11, most of coatings except coating O1 sustained their protective function after 1000 hr exposure at 1050°C. Only O2 sustained its protective nature after 1000 hr exposure at 1150°C.

**Table 7.11 Phases in the coatings after exposure at 1050°C and 1150°C**

Coating	Coating layer	Phase before oxidation	Exposure temperature, °C	
			1050	1150
O1	Cr-Si coating/ aluminide I	$\beta + \gamma'/\gamma + (\text{Cr-Si-}$ columnar phases)	$\gamma'/\gamma + (\text{Cr-Si-rich}$ precipitate)	No coating
O2	Cr-Si coating/ NiCrAlY/ aluminide II	$\text{Ni}_2\text{Al}_3 + \beta + \gamma'/\gamma + (\text{Cr-}$ Si-columnar phases)	$\beta + \gamma'/\gamma + (\text{Cr layer}$ + Si-rich columnar phases)	$\beta + \gamma'/\gamma$
O3	aluminide I	$\beta$	$\beta + \gamma'/\gamma$	No coating
O4	NiCrAlY/ aluminide II	$\text{Ni}_2\text{Al}_3$	$\beta + \gamma'/\gamma$	No coating
O5	Cr-Si coating/ NiCrAlY/ aluminide I	$\beta + \gamma'/\gamma + (\text{Cr-Si-}$ columnar phases)	$\beta + \gamma'/\gamma + (\text{Cr-Si-}$ rich precipitates)	$\gamma'/\gamma$
O6	NiCrAlY/ aluminide I	$\beta + \gamma'/\gamma$	$\beta + \gamma'/\gamma$	$\gamma'/\gamma$
O7	aluminide II	$\text{Ni}_2\text{Al}_3$	$\beta + \gamma'/\gamma + \text{Cr-rich}$ precipitate	$\gamma'/\gamma$
O8	Cr-Si coating/ aluminide II	$\text{Ni}_2\text{Al}_3 + \beta + \gamma'/\gamma + (\text{Cr-}$ Si-columnar phases)	$\beta + \gamma'/\gamma + \text{Cr-rich}$ precipitate	No coating
O9	Bare IN738	$\gamma'/\gamma$	$\gamma'/\gamma$	$\gamma'/\gamma$
O10	NiCrAlY	$\gamma'/\gamma$	$\gamma'/\gamma$	No coating

## 7.6 Summary of Oxidation Tests

The barrier layer, which consisted of a Cr layer and a Si-rich layer, was found to have significant effects on the oxidation behavior of multilayered coatings in terms of mass change and total area of oxide scales. During oxidation test at 1050°C, the barrier layer improved the oxidation resistance for the multilayered coatings as the Cr layer that formed during coating process kept aluminum within the coating and sustained NiAl microstructure in the top coating layer. However, with aluminide I top coat the sustainability of the barrier layer became questionable with a decrease in aluminum content in the coating after a long period of exposure at a high temperature (in coating O5, for example).

The Cr layer in the multilayered coating where the Al/Ni ratio was around two formed during the oxidation test as the  $\text{Ni}_2\text{Al}_3$  phase transformed into the  $\beta$  phase to release Cr atoms. The barrier layer promoted the formation of stable oxides (primarily  $\text{Al}_2\text{O}_3$ ) at the surface of aluminized layer when the Al/Ni ratio of the multilayered coating was around two (aluminide II top coat) because the barrier layer kept aluminum within the coating and sustained the  $\beta$  phase microstructure. The higher aluminum content (> 50 at.%) in aluminide II top coat kept the barrier layer stable during the oxidation tests. A stable coating structure was characterized as the combination of a layer of columnar silicon-rich phase, a Cr layer, and a  $\beta$  layer. At 1150°C, the multilayered coating with the high Al/Ni ratio (aluminide II top coat) exhibited the best oxidation resistance.

Furthermore, the methodology of Design of Experiments has been effectively implemented to interpret the results from the oxidation tests. This method enhanced the

understanding of the effects of each coating layer and composition on the oxidation behavior of the multilayered coatings.

## **Chapter 8: Conclusions and Future Work**

### **8.1 Conclusions**

In the first phase of this research, two coating processes, plasma spraying and pack cementation, were developed and optimized using statistical method. This development provided semi-quantitative means to generate coatings based on microstructure and composition requirements. As the plasma spray equipment installed at Carleton University was based a new state-of-the-art three-axial system, there was no prior knowledge in the open literature on how process parameters would affect the resulting coatings. Therefore, the generation of semi-quantitative means relating process parameters and microstructure from this study has provided guidelines for researchers working in the field.

Additionally, although pack-cementation is a half-century old process, the process parameters have mostly kept as proprietary information. Process development in the past was primarily based on repeated experimental trials. The development and quantification of in-house pack cementation processes for applying Al, Cr, Al-Ni and Cr-Si coatings is by far one of the most comprehensive ones. The resulting semi-empirical relationships are currently used to select coating process parameters based on the design requirement.

With both coating processes fully developed in this research, a series of novel multilayered coating structures were designed with the objective to overcome the most commonly seen gas turbine hot section coating failure mode – interdiffusion and Al depletion. Nine coating systems were designed and produced using plasma spraying and pack cementation processes.

The nine multilayered coatings were then exposed at 1050°C and 1150°C for 1000 hr. From this research, the following conclusions can be drawn:

(1) Plasma spraying process with 3-Axial system was developed and optimized using statistical method and regression equations.

(2) Process index (*PI*) for 3-Axial plasma spraying process was for the first time introduced.

(3) The ratio of Al to Ni (at.%) in a pack aluminized coating determines the microstructure of the coating ( $\text{Ni}_2\text{Al}_3$ ,  $\beta$ ,  $\gamma$  or  $\gamma/\gamma'$ ). The required ratio can be produced using process parameters predicted by the response surface methodology.

(4) Chromium and silicon co-deposition process was developed and proven to be an effective method to produce a chromium-rich and silicon-rich barrier layer on IN738.

(5) A Cr layer formed during coating process for the multilayered coating with low Al/Ni (approximately = 1) as top coat; whereas the Cr layer formed during the oxidation test for the multilayered coating with the high Al/Ni (close to 2).

(6) The presence of a middle NiCrAlY layer is crucial in providing Cr atoms to form the Cr layer and in preventing interaction between diffusion barrier and aluminide top coat.

(7) The barrier layer, which consisted of the Cr layer and silicon-rich layer, not only prevented aluminum and chromium from diffusing into the substrate, but also prohibited other elements in the substrate from diffusing into the coating during oxidation tests.

(8) After 1000 hr exposure at 1050°C, both multilayered coatings exhibited better oxidation resistance; whereas the multilayered coating with the high Al/Ni as a top coat provided the best oxidation resistance at 1150°C.

(9) DOE (Design of Experiments) is not only the great tool for coating process optimization, but also helpful to gain a more precise insight into the effects of each layer and composition on the diffusion and oxidation behavior. Furthermore, the effects of coating layer interactions on the oxidation performance of the multilayered coatings were also better understood with the use of this statistical tool.

(10) The following multiple coating structures are recommended for service at 1050°C and 1150°C, respectively:

- a. For oxidation resistance at 1050°C: Cr-Si coating/NiCrAlY/aluminide I (Al/Ni ratio from 1.0 to 1.5)
- b. For oxidation resistance at 1150°C: Cr-Si coating/NiCrAlY/aluminide II (Al/Ni ratio from 2.0 to 2.5)

## **8.2 Future Work**

This work was focused on the oxidation behavior of multilayered coatings, especially isothermal oxidation behavior. However gas turbine engines hardly work at constant temperatures during operation. Therefore a cycle oxidation test will be conducted to evaluate the oxidation behavior under cyclic thermal stress. Cyclic oxidation is the test that coated specimens are exposed at certain temperature in static air for a period of time and withdrawn from the furnace at set intervals. Forced air can be added to increase the severity of the thermal shock on the test specimens. The

evaluation of coatings is based on thermal cycling to the spallation and weight gain at test temperature.

In Addition, a Cr layer and silicon-rich layer combined with an over aluminized top coat also has the potential to promote the resistance to hot corrosion due to the following reasons:

(1) Chromium reservoir in the multilayered coatings can promote chromium oxide scale to form at low to intermediate temperatures. The chromium oxide scale is particularly resistant to salt fluxing, one of the hot corrosion conditions. Another positive effect of chromium on hot corrosion resistance is the stabilizing effect on  $\text{Na}_2\text{CrO}_4$  salt.

(2) Silicon-rich layers are very resistant to both high-temperature hot corrosion and low-temperature hot corrosion. Chromium silicide phases are particularly resistant to acidic hot corrosion, and can also act as a physical barrier to sulfate corrosion. Therefore further investigation should be undertaken to determine the hot corrosion resistance of the multilayered coatings.

## REFERENCES

- [1] I. Gokalp, E. Lebas, Alternative fuels for industrial gas turbines, *Appl. Therm. Eng.*, 24 (2004) 1655-1663
- [2] N. Eliaz, G. Shemesh, R. M. Latanision, Hot corrosion in gas turbine components, *Engineering Failure Analysis*, 9 (2002) 31-43
- [3] I. G. Wright, T. B. Gibbons, Recent developments in gas turbine materials and technology and implications for syngas firing, *Int. J. Hydrogen Energy*, 32 (2007) 3610-3621
- [4] B. Gleeson, High-Temperature Corrosion of Metallic Alloys and Coatings, in *Corrosion and Environmental Degradation, Vol II, Materials Science and Technology*, M. Schutze, Ed., Wiley-VCH, Weinheim, (2000) 173-174
- [5] George Y. Lai, *High-Temperature Corrosion and Materials Applications*, ASM International, (2007) 5-66
- [6] F. Gao, Master thesis, Carleton University, (2003) 58
- [7] J. Cermak, V. Rotova, Influence of composition on diffusion in binary nickel aluminides, *Def Diff Forum.*, 237-240 (2005) 390-395
- [8] E. Perez, T. Patterson, Y. Sohn, Interdiffusion analysis for NiAl versus superalloys diffusion couples, *J. Phase Equilib.*, 27 (2006) 659-664
- [9] G. W. Goward, Progress in coatings for gas turbine airfoils, *Surf. Coat. Technol.*, 109 (1998) 73-79
- [10] J. Ma, S. Jiang, J. Gong, C. Sun, Composite coatings with and without an in situ forming Cr-based interlayer: Preparation and oxidation behavior, *Corros. Sci.*, 53 (2011) 2894-2901

- [11] D. Yoshida, Y. Shibata, S. Hayashi, T. Narita, Changes of an Outer  $\beta$ -NiAl and Inner  $\alpha$ -Cr Coating on Ni-40 wt.% Cr Alloy during Oxidation at 1373K in Air, *Oxid. Met.*, 64( 2005) 119-130
- [12] K. P. Gupta, The Cr-Ni-Si (Chromium-Nickel-Silicon) System, *J. Phase Equilib.*, 27 (2000) 523-528
- [13] W. S. Walston, Coating and surface technologies for turbine airfoils, *Superalloys* (2004) 579-588
- [14] C. F. McDonald, Helium turbomachinery operating experience from gas turbine power plants and test facilities, *Appl. Therm. Eng.*, 44 (2012) 108-142
- [15] C. F. McDonald, Low-cost compact primary surface recuperator concept for micro-turbines, *Appl. Therm. Eng.*, 20 (2000) 471-497
- [16] R. Sivakumar, B. L. Mordike, High temperature coatings for gas turbine blades: a review, *Surf. Coat. Technol.*, 37 (1989) 136-160
- [17] S. Bose, *High Temperature Coatings*, Elsevier Inc (2007) 33-47
- [18] T. A. Kircher, Oxidation, sulfidation, and hot corrosion: Mechanisms and interrelationship, *Advisory Group for Aerospace Research and Development Conference Proceedings*, 461 (1989) 4-8
- [19] N. Mott, Mechanisms for the oxidation of silicon and the formation of charged defects, *Proceedings of the Royal Society of London Series A, Mathematical and Physical Sciences*, 376 (1981) 207-215
- [20] M. H. Li, Z. Y. Zhang, X.F. Sun, Oxidation and degradation of EB-PVD thermal barrier coating, *Oxid. Met.*, 58 (2002) 499-512

- [21] K. Izdinsky, J. Ivan, M. Zemankova, Microstructure of plasma sprayed NiCrAlY coating isothermally exposed at 850°C for 1, 10 and 100 hours, *Kovove Mater.*, 39 (2001) 316-330
- [22] H. Choi, B. Yoon, H. Kim, C. Lee, Isothermal oxidation of air plasma spray NiCrAlY bond coatings, *Surf. Coat. Technol.*, 150 (2002) 297-308
- [23] G. Fisher a, P. K. Datta, J. S. Burnell-Gray, W. Y. Chan, J.C. Soares, The effects of active element additions on the oxidation performance of a platinum aluminide coating at 1100 °C, *Surf. Coat. Technol.*, 110 (1998) 24-30
- [24] R. Anton, J. Birkner, N. Czech and W. Stamm, Degradation of advanced MCrAlY coatings by oxidation and interdiffusion, *Mater. Sci. Forum*, 369 (2001) 719-726
- [25] M. Schütze, Proc. Res. *Topical Symp. 2005 Corrosion Resistant Materials for Extreme Conditions*, NACE Int., Houston, (2005) 1-6
- [26] J. R. Nicholls, N. J. Simms, W.Y. Chan, H. E. Evans, Smart overlay coatings – concepts and practice, *Surf. Coat. Technol.*, 149 (2002) 236-244
- [27] T. Jeanine. D. Marcin, K. Dinesh. Gupta, Protective coatings in the gas turbine engine, *Surf. Coat. Technol.*, 68/69 (1994) 1-9
- [28] R. Sivakumar, B. L. Mordile, High temperature coating for gas turbine blades: a review, *Surf. Coat. Technol.*, 37 (1989) 139-160
- [29] M. Qiao, C. Zhou, Codeposition of Co and Al on nickel base superalloys by pack cementation process, *Surf. Coat. Technol.*, 206 (2012) 2899-2904

- [30] Y. Q. Wang, Y. Zhang, D. A. Wilson, Formation of aluminide coatings on ferritic–martensitic steels by a low-temperature pack cementation process, *Surf. Coat. Technol.*, 204 (2010) 2737–2744
- [31] J. Kalivodova, D. Baxter, M. Schutze, V. Rohr, Gaseous corrosion of alloys and novel coatings in simulated environments for coal, waste and biomass boilers, *Mater. Corros.*, 56 (2005) 882–889
- [32] C. Y. Bai, Y. J. Luo, C. H. Koo, Improvement of high temperature oxidation and corrosion resistance of superalloy IN738LC by pack cementation, *Surf. Coat. Technol.*, 183 (2004) 74–88
- [33] D. K. Das, V. Singh, S. V. Joshi, Evolution of aluminide coating microstructure on nickel-base cast superalloy CM-247 in a single-step high-activity aluminizing process, *Metall. Mater. Trans. A*, 29A (1998) 2173–2188.
- [34] G. Ottovianni, Review of binary alloy formation by thin film interactions, *J. Vac. Sci Technol.*, 16 (1979) 1112–1119
- [35] S. Shankar, L. L. Seigle, Interdiffusion and intrinsic diffusion in the Ni Al ( $\delta$ ) phase of the Al-Ni system, *Metall. Trans.* 9A (1978) 1467–1476
- [36] A. R. Castle, D. R. Gabe, Chromium diffusion coatings, *Int. Mater. Rev.*, 44 (1999) 37–58.
- [37] L. Swadzba, A. Maciejny, B. Formanek, J. Biedron, Diffusion coatings on nickel-base superalloys, *Surf. Coat. Technol.*, 54/55 (1992) 84–90

- [38] G. W. Goward, D. H. Boone, S. Giggins, Formation and degradation mechanisms of aluminide coating on nickel-base superalloys, *ASM Transactions*, 196760 (1967) 228-241
- [39] S. RASTEGARI, H. ARABI, M.R. ABOUTALEBI and A. ESLAMI, A study of the microstructure change of Cr-modified aluminide coatings on a nickel-based superalloy during hot corrosion, *Can. Metall. Q.*, 47 (2008) 223-232
- [40] H. L. Du, J. Kipemoi, D. N. Tsipas, P. K. Datta, The high temperature corrosion behavior of Hf modified chromo-aluminized coatings produced by a single step process, *Surf. Coat. Technol.*, 85-86 (1996) 1-8
- [41] Z. D. Xiang, P. K. Datta, Deposition of silicon modified aluminide coatings on nickel base superalloys by pack cementation process, *Mater. Sci. Technol.*, 19 (2003) 935-942
- [42] R. Bianco, M. A. Harper, R. A. Rapp, Co-depositing elements by halide-activated pack cementation, *JOM*, 43 (1991) 68-73
- [43] B. Grushko, W. Kowalski, D. Pavlyuchkov, B. Przepiorzynski M. Surowiec, A contribution to the Al-Ni-Cr phase diagram, *J. Alloys Compd.*, 460 (2008) 299-304
- [44] T. Nishimotoa, T. Izumia, S. Hayashib, T. Narita, Two-step Cr and Al diffusion coating on TiAl at high temperatures, *Intermetallics*, 11 (2003) 225-235
- [45] G. Joaquim, C. Neto, S. Gama, C. A. Ribeiro, Experimental study of the Al-Cr equilibrium diagram, *J. Alloys Compd.*, 182 (1992) 271-280
- [46] J. Kohlscheen, H. R. Stock, Deposition of silicon enriched nickel aluminide coatings on internally cooled airfoils, *Surf. Coat. Technol.*, 203 (2008) 476-479

- [47] R. C. Pennefather, D.H. Boone, Mechanical degradation of coating systems in high temperature cyclic oxidation, *INT J PRES VES PIP*, 66 (1996) 351-358
- [48] K. Shirvani, M. Saremi, A. Nishikata, T. Tsuru, The role of silicon on microstructure and high temperature performance of aluminide coating on superalloy In 738LC, *Mater. Trans.*, 43 (2002) 2622-2628
- [49] Mark A. Harper, Robert A. Rapp, Codeposited Chromium and Silicon Diffusion Coatings for Fe-Base Alloys via Pack Cementation, *Oxid Met.*, 42 (1994) 303-333
- [50] P. Wei, X.R. Wan, The effect of a coating heat-treatment on Cr-Si and heat-treatment on the mechanical properties of Cr17Ni2 stainless steel, *Surf. Coat. Technol.*, 132 (2000) 137-142
- [51] B. M. Warnes, D. C. Punola, Clean diffusion coatings by chemical vapor deposition, *Surf. Coat. Technol.*, 94/95 (1997) 1-6
- [52] T. S. Sidhu, S. Prakash, R. D. Agrawal, Characterizations of HVOF sprayed NiCrBSi coatings on Ni- and Fe-based superalloys and evaluation of cyclic oxidation behavior of some Ni-based superalloys in molten salt environment, *Thin Solid Films*, 515 (2006) 95-105
- [53] H. W. W. Wong, Heat Transfer Analysis of the Plasma Spray Deposition Process, PhD thesis at UBC
- [54] <http://www.mettech.com/company/corporate/technical-papers-presentations.html>
- [55] G. W. Goward, Low-temperature hot corrosion in gas turbine: a review of causes and coatings, *ASME*, 85-GT-60 (1985) 1-5

- [56] J. R. Nicholls, S. R. J. Saunders, High temperature materials for power engineering, *Kluwer Academic Publishers, Dordrecht*, (1990) 865-875
- [57] D. Toma, W. Brandl, G. Marginean, Wear and corrosion behavior of thermally sprayed cement coatings, *Surf. Coat. Technol.*, 138 (2001) 149-158
- [58] K. Izdinsky, J. Ivan, M. Zemankova, V. Kolenciak, Microstructure of the as-plasma sprayed NiCrAlY coating, *Kovove Mater.*, 36 (1998) 367-377
- [59] A. S. Radcliff, Factors influencing gas turbine use and performance, *Mater. Sci. Technol.*, 3 (1987) 554-561
- [60] R. Anton, J. Birkner, N. Czech, W. Stamm, Degradation of advanced MCrAlY coatings by oxidation and interdiffusion, *Mater. Sci. Forum*, 369-372 (2001) 719-726
- [61] R. Lowrie, D. H. Boone, Composite coatings of CoCrAlY plus platinum, *Thin Solid Films*, 45 (1977) 491-498
- [62] S. Mercier, F. Lozzelli, M. P. Bacos, P. Josso, Formation of a rhenium-base diffusion-barrier-coating system on Ni-base single crystal superalloy and its stability at 1,423 K, *Mater. Sci. Forum.*, 461/464 (2004) 949-956
- [63] A. Strawbridge, H. E. Evans, C. B. Ponon, Spallation of oxide scales from NiCrAlY overlay coatings, *Mater. Sci. Forum.*, 251/254 (1997) 365-372
- [64] S. Saeidi, K. T. Voisey, D. G. McCartney, The Effect of heat treatment on the oxidation behavior of HVOF and VPS CoNiCrAlY coatings, *J. Therm. Spray Technol.*, 18 (2009) 209-215

- [65] V. K. Tolpygo, D. R. Clarke, The effect of oxidation pre-treatment on the cyclic life of EB-PVD thermal barrier coatings with platinum aluminide bond coats, *Surf. Coat. Technol.*, 200 (2005) 1276-1286
- [66] H. Lau, C. Leyens, U. Schulz, C. Friedrich, Influence of bond coat pre-treatment and surface topology on the lifetime of EB-PVD TBCs, *Surf. Coat. Technol.*, 165 (2003) 217-223
- [67] B. Baufeld, U. Schulz, Life time dependency on the pre-coating treatment of a thermal barrier coating under thermal cycling, *Surf. Coat. Technol.*, 201 (2006) 2667-2675
- [68] F. Tang, L. Ajdelsztajn, J.M. Schoenung, Characterization of oxide scales formed on HVOF NiCrAlY coatings with various oxygen contents introduced during thermal spraying, *Scripta Mater.*, 51 (2004) 25-29
- [69] E.Y. Lee, D.M. Charter, R. R. Biederman, R. D. Sisson Jr., Interdiffusion analysis for NiAl versus superalloys diffusion couples, *Surf. Coat. Technol.*, 32 (1987) 19-39
- [70] B. Wang, J. Gong, C. Sun, R. F. Huang, L. S. Wen, Oxidation behavior of NiCrAlY coatings on Ni-based superalloy, *Surf. Coat. Technol.*, 149 (2002) 70-75
- [71] O. Knotek, F. Löffler, W. Beele, Diffusion barrier design against rapid interdiffusion of MCrAlY and Ni-base material, *Surf. Coat. Technol.*, 61 (1993) 6-13
- [72] M. Schütze, M. Malessa, V. Rohr, T. Weber, Development of coatings for protection in specific high temperature environments, *Surf. Coat. Technol.*, 201 (2006) 3872-3879

- [73] T. Narita, K. Z. Thosin, L. F. Qun, S. Hayashi, H. Murakami, B. Gleeson, D. Young, Development of Re-based diffusion barrier coatings on nickel based superalloys, *Mater. Corros.*, 56 (2005) 923-929
- [74] C. P. Lungu, I. Mustata, G. Musa, A. M. Lungu, V. Zeroschi, K. Iwasaki, R. Tanaka, Y. Matsumurab, I. Iwanaga, H. Tanaka, T. Oi, K. Fujita, Formation of nanostructured Re–Cr–Ni diffusion barrier coatings on Nb superalloys by TVA method, *Surf. Coat. Technol.*, 200 (2005) 399-402
- [75] W. Z. Li, Y. Yao, Q. M. Wang, Z. B. Bao, J. Gong, C. Sun, X. Jiang, Improvement of oxidation-resistance of NiCrAlY coatings by application of CrN or CrON interlayer, *J. Mater. Res.*, 23 (2008) 341-352.
- [76] Y. Wu, Y. M. Wang, G. M. Song, X. W. Li, The Improvement of Oxidation Resistance of a Re-Based Diffusion Barrier/Ni–Al Coating on the Single-Crystal Ni-Based TMS-82+ Superalloy, *Oxid Met.*, 76 (2011) 419-431
- [77] D. Sumoyama, K. Z. Thosin, T. Nishimoto, T. Yoshioka, Formation of a Rhenium-base Diffusion-barrier-coating System on Ni-base Single Crystal Superalloy and its Stability at 1,423 K, *Oxid Met.*, 68 (2007) 313-329
- [78] J. A. Haynes, Y. Zhang, K. M. Cooley, L. Walker, K. S. Reeves, B. A. Pint, High-temperature diffusion barriers for protective coatings, *Surf. Coat. Technol.*, 188–189 (2004) 153-157
- [79] R. Cremer, M. Witthaut, K. Reichert, M. Schierling, D. Neuschütz, Thermal stability of Al–O–N PVD diffusion barriers, *Surf. Coat. Technol.*, 108–109 (1998) 48-58

- [80] Q. M. Wang, Y. N. Wu, M. H. Guo, P. L. Ke, J. Gong, C. Sun, L. S. Wen, Ion-plated Al–O–N and Cr–O–N films on Ni-base superalloys as diffusion barriers, *Surf. Coat. Technol.*, 197 (2005) 68-76
- [81] J. Muller, D. Neuschütz, Efficiency of  $\alpha$ -alumina as diffusion barrier between bond coat and bulk material of gas turbine blades, *Vacuum*, 71 (2003) 247-251
- [82] E. Cavaletti, S. Naveos, S. Mercier, P. Josso, M.P. Bacos, D. Monceau, Ni–W diffusion barrier: Its influence on the oxidation behavior of a  $\beta$ -(Ni,Pt)Al coated fourth generation nickel-base superalloy, *Surf. Coat. Technol.*, 204 (2009) 761-765
- [83] J. Kameda, T. E. Bloomer, Y. Sugita, A. Ito, S. Sakurai, Mechanical properties of aluminized CoCrAlY coatings in advanced gas turbine blades, *Mater. Sci. Eng., A*, A234-236 (1997) 489-492
- [84] N. S. Cheruve, K. S. Chan, G. R. Leverant, In-service degradation and life prediction of coatings for advanced land-base gas turbine buckets, *JSME Int J., Ser. A*, 64 (2003) 635-641
- [85] B. M. Warnes, Improved aluminide/MCrAlX coating systems for super alloys using CVD low activity aluminizing, *Surf. Coat. Technol.*, 163–164 (2003) 106-111
- [86] X. Li, C. Zhuo, Development and oxidation resistance of Si- modified MCrAlY coatings on Nb-base alloy, *Mater. Sci. Forum.*, 546-549 (2007) 1721-1724
- [87] D. K. Das, V. Singh, S. V. Joshi, Effect of prealuminizing diffusion treatment on microstructural evolution of high-activity Pt-aluminide coatings, *Metall. Mater. Trans. A*, 31A (2000) 2037-2047

- [88] C. Pierlot, L. Pawlowski, M. Bigan, and P. Chagnon, Design of Experiments in Thermal Spraying: A Review, *Surf. Coat. Technol.*, 202 (2008) 4483-4490
- [89] P. Saravanan, V. Selvarajan, M.P. Srivastava, D.S. Rao, S.V. Joshi, and G. Sundararajan, Study of Plasma- and Detonation Gun-Sprayed Alumina Coatings Using Taguchi Experimental Design, *J. Therm. Spray Technol.*, 9 (2000) 505-512
- [90] T. Goyal, R. Singh Walia, T. S. Sidhu, Study of Coating Thickness of Cold Spray Process Using Taguchi Method, *Mater. Manuf. Processes*, 27 (2012) 193–200
- [91] C. D. Montgomery, *Design and Analysis of Experiments*, Seventh Edition, John Wiley & Sons, Inc (2009).
- [92] R. H. Myers, C. D. Montgomery, C. M. Anderson-Cook, *Response Surface Methodology: Process and Product Optimization Using Designed Experiments*, 3rd Edition, John Wiley & Sons, Inc (2009).
- [93] R. J. Del Vecchio, *Understanding Design of Experiments: A Primer for Technology*, Hanser Publishers, Munich, New York, 1997 91
- [94] [http://www.ee.iitb.ac.in/~apte/CV\\_PRA\\_TAGUCHI\\_INTRO.htm](http://www.ee.iitb.ac.in/~apte/CV_PRA_TAGUCHI_INTRO.htm)
- [95] [https://controls.engin.umich.edu/wiki/index.php/Design\\_of\\_experiments\\_via\\_taguchi\\_methods:\\_orthogonal\\_arrays](https://controls.engin.umich.edu/wiki/index.php/Design_of_experiments_via_taguchi_methods:_orthogonal_arrays)
- [96] Y. Wang, and T. W. Coyle, Optimization of Solution Precursor Plasma Spray Process by Statistical Design of Experiment, *J. Therm. Spray Technol.*, 17 (2008) 692-699
- [97] J. Neter, W. Wasserman, G. A. Whitmore, *Applied Statistics*, Allyn and Bacon, Inc., (1979)

- [98] J. F. Li, H. L. Liao, C. X. Ding, and C. Coddet, Optimizing the plasma spray process parameters of yttria stabilized zirconia coatings using a uniform design of experiments, *J. Mater. Process. Technol.*, 160 (2005) 34-42
- [99] M. Friis, C. Persson, and J. Wigren, Influence of particle in-flight characteristics on the microstructure of atmospheric plasma sprayed yttria stabilized ZrO<sub>2</sub>, *Surf. Coat. Technol.*, 141 (2001) 115-127
- [100] S. R. J. Saunders, M. Monteiro, F. Rizzo, Oxidation behavior of metals and alloys at high temperatures in atmospheres containing water vapor, *Prog. Mater Sci.*, 53 (2008) 775-837
- [101] R. Subramanian, A. Burns, W. Stamm, Advanced multi-functional coatings for land-based industrial gas turbines, *Proceeding of ASME Turbo Expo 2008*
- [102] K. P. Gupta, Cr-Ni-Si (Chromium-Nickel-Silicon) System, *J. Phase Equilib.*, 27 (2006) 523-528
- [103] Y.A. Tamarin, Protective Coatings for Turbine Blades, Technological Processes for Deposition of Protective Coatings to Turbine Blades, ASM International, (2002) 37
- [104] F. Azarmi, T. W. Coyle, and J. Mostaghimi, Optimization of Atmospheric Plasma Spray Process Parameters using a Design of Experiment for Alloy 625 coatings, *J. Therm. Spray Technol.*, 17 (2008) 144-156
- [105] H. J. Bajaria, Vital few, trivial many– Challenged, 52nd AQC 98 Transactions, Philadelphia, May 5, 98 1-7

- [106] C. Moreau, P. Burgess, and D. Ross, Characterization of Particle Flow in an Axial Injection Plasma Torch, Thermal Spray Science and Technology, *ASM International, Materials Park, OH, USA, 1995, Proceeding of the 8th National Thermal Spray Conference*, Houston, 11-15 September, 1995 141-147
- [107] S. Sampath, X. Y. Jiang, J. Matejicek, L. Prchlik, A. Kulkarni, and A. Vaidya, Role of thermal spray processing method on the microstructure, residual stress and properties of coatings: an integrated study for Ni-5 wt.% Al bond coats, *Mater. Sci. Eng.*, A364 (2008) 216-231
- [108] J. Day, X. Huang and N. L. Richards, Examination of Grit Blasting Process for Thermal Spraying Using Statistical Methods, *J. Therm. Spray Technol.*, 14 (2004) 471-479
- [109] J. F. Bisson, C. Moreau, M. Dorfman, C. Dambra, and J. Mallon, Influence of Hydrogen on the Microstructure of Plasma-Sprayed Yttria-Stabilized Zirconia Coatings, *J. Therm. Spray Technol.*, 14 (2005) 85-90
- [110] T. A. Kircher, B.G. McMordie, K. Richards, Use of experimental designs to evaluate formation of aluminide and platinum aluminide coatings, *Surf. Coat. Technol.*, 201 (2006) 2054-2060
- [111] J. Angenete, K. Stiller, V. Langer, Oxidation of Simple and Pt-Modified Aluminide Diffusion Coatings on Ni-Base Superalloys— I. Oxide Scale Microstructure, *Oxid Met.*, 60 (2003) 47-82

- [112] A. S. Demirkıran, E. C. Elik, M. Yargan, E. Avcı, Oxidation behavior of functionally gradient coatings including different composition of cermets, *Surf. Coat. Technol.*, 142-144 (2001) 551-556
- [113] Z. Surek<sup>1</sup>, A. Stawiarski, M. Faryna, A. Jaroń, The formation and oxidation behavior of diffusion barrier coating system on  $\gamma$ -TiAl, *Acta Microscopica*, 18 (2009) 221-222
- [114] D. Seo, K. Ogawa, Y. Suzuki, K. Ichimura, T. Shoji, S. Murata, Comparative study on oxidation behavior of selected MCrAlY coatings by elemental concentration profile analysis, *Appl. Surf. Sci.*, 255 (2008) 2581-2590
- [115] M. Stanislawski, E. Wessel, T. Markus, L. Singheiser, W. J. Quadackers, Chromium vaporization from alumina-forming and aluminized alloys, *Solid State Ionics*, 179 (2008) 2406-2415
- [116] J. Ma, S. Jiang, J. Gong, C. Sun, Composite coatings with and without an in situ forming Cr-based interlayer: Preparation and oxidation behavior, *Corros. Sci.*, 53 (2011) 2894-2901
- [117] C. Z. Xu, S. M. Jiang, Z. B. Bao, J. Gong, C. Sun, Isothermal oxidation behavior of a gradient NiCoCrAlSiY coating deposited by arc ion plating on a Ni-based single crystal superalloy, *Corros. Sci.*, 51 (2009) 1467-1474
- [118] M. A. Bestor, J. P. Alfano, M. L. Weaver, Influences of chromium and hafnium additions on the microstructures of  $\beta$ -NiAl coatings on superalloy substrates, *Intermetallics*, 19 (2011) 1693-1704

- [119] B. Bai, H. Guo, H. Peng, et al., Cyclic oxidation and interdiffusion behavior of a NiAlDy/RuNiAl coating on a Ni-based single crystal superalloy, *Corros. Sci.*, 53 (2011) 2721-2727
- [120] F. Pyczak, H. Biermann, H. Mughrabi, A. Volek, R. E. Singer, CBED-measurement of residual internal strains in the neighbourhood of TCP phase in Ni-based superalloys, *Superalloys* (2000) 367-376
- [121] Z. Bai, D. Li, H. Peng, J. Wang, H. Guon, S. Gong, Suppressing the formation of SRZ in a Ni-based single crystal superalloy by RuNiAl diffusion barrier, *Progress in Natural Science: Materials International*, 22 (2012) 146-152
- [122] E. Cavaletti, S. Naveos, S. Mercier, P. Josso, M.P. Bacos, D. Monceau, *Surf. Coat. Technol.*, 204 (2009) 761-765
- [123] J. Angenete, K. Stiller, V. Langer, Oxidation of Simple and Pt-Modified Aluminide Diffusion Coatings on Ni-Base Superalloys— I. Oxide Scale Failure, *Oxid Met.*, 60 (2003) 83-101
- [124] T. Liang, H. Guo, H. Peng, S. Gong, Precipitation phases in the nickel-based superalloy DZ 125 with YSZ/CoCrAlY thermal barrier coating, *J. Alloys Compd.*, 509 (2011) 8542-8548
- [125] R. Darolia, D. F. Lahrman, R. D. Field, R. Sisson, Formation of topologically closed packed phases in nickel base single crystal superalloys, *Superalloys*, TMS, Warrendale, PA, (1988) 255-264

- [126] J. X. Yang , Q. Zheng, X. F. Sun, H. R. Guan, Z. Q. Hu, Topologically close-packed phase precipitation in a nickel-base superalloy during thermal exposure, *Mater. Sci. Eng* , A 465 (2007) 100-108
- [127] M. Simonetti, P. Caron, Role and behavior of m phase during deformation of a nickel-based single crystal superalloy, *Mater. Sci. Eng.*, A254 (1998) 1-12
- [128] M. Stanislawski, E. Wessel, T. Markus, L. Singheiser, W. J. Quadakkers, Chromium vaporization from alumina-forming and aluminized alloys, *Solid State Ionics*, 179 (2008) 2406-2415
- [129] M. J. Li, X. F. Sun, H. R. Guan, X. X. Jiang, Z. Q. Hu, The degradation of (Ni,Pd)Al coatings on superalloy IN738 during isothermal oxidation, *Surf. Coat. Technol.*, 185 (2004) 172-177
- [130] C. T. Liu, J. Ma, X. F. Sun, P. C. Zhao, Mechanism of the oxidation and degradation of the aluminide coating on the nickel–base single-crystal superalloy DD32M, *Surf. Coat. Technol.*, 204 (2010) 3641-3646
- [131] P. Saltykov, O. Fabrichnaya, J. Golczewski, F. Aldinger, Thermodynamic modeling of oxidation of Al–Cr–Ni alloys, *J. Alloys Compd.*, 381 (2004) 99-113

**APPENDIX**

**Table A.1 Concentrations of coating 4-1 and coating 4-7**

Distance from coating surface, $\mu\text{m}$	Composition, at. %							
	Coating 4-1				Coating 4-7			
	Al	Cr	Fe	Ni	Al	Cr	Fe	Ni
0	49.05	13.90	4.66	32.39	42.75	6.46	4.60	46.19
10	52.04	10.20	4.29	33.47	40.09	7.94	4.42	47.55
20	50.36	12.17	4.75	32.71	39.29	8.93	4.76	47.03
30	52.78	9.02	4.93	33.26	36.50	16.93	4.72	41.85
40	48.41	10.49	4.93	36.17	38.99	12.57	5.15	43.29
50	47.48	11.45	4.86	36.21	39.25	12.78	5.62	42.34
60	44.98	9.95	5.42	39.65	42.47	10.30	5.56	41.67
70	39.08	13.42	5.88	41.62	37.97	15.34	5.79	40.90
80	32.98	21.82	6.20	39.00	26.34	22.73	6.51	44.43
90	34.03	23.88	6.62	35.47	27.21	20.24	7.15	45.40
100	32.80	16.61	7.00	43.59	23.11	22.76	7.19	46.94
110	28.49	17.10	7.21	47.2	28.73	19.58	7.17	44.52
120	23.55	20.84	7.96	47.65	27.66	19.11	7.31	45.91
130	27.38	19.56	8.18	43.88	24.76	19.77	8.05	47.42
140	26.03	18.87	8.72	46.38	26.43	19.09	8.58	45.91
150	22.87	20.20	9.63	47.3	22.47	20.01	9.10	48.43
160	22.17	19.78	10.54	47.5	23.97	19.31	9.68	47.04
170	22.19	19.65	10.96	47.2	21.55	20.17	10.93	47.35
180	19.64	19.75	11.95	48.67	21.41	18.87	12.49	47.23
190	20.35	19.67	14.60	45.38	23.38	18.73	14.37	43.53
200	19.07	19.57	17.64	43.72	20.52	19.10	16.10	44.28
210	19.09	18.58	20.91	41.42	23.02	18.58	18.27	40.13
220	23.57	18.43	24.07	33.93	19.99	18.95	22.63	38.44
230	11.00	20.83	39.78	28.39	13.55	20.83	27.45	38.18

**Table A.2 Concentration of IN738 before oxidation tests**

Concentration, at. %					
Al	Ti	Cr	Co	Ni	W
10.65	3.50	18.44	6.74	59.84	0.83

**Table A.3 Concentrations of the major elements in Cr-Si coatings**

Specimen	Distance from coating surface, $\mu\text{m}$	Composition, at. %					
		Al	Si	Ti	Cr	Co	Ni
5-1	0	5.78	21.38	10.54	13.51	5.62	43.17
	10	5.43	18.31	4.18	20.08	7.70	42.20
	20	7.99	13.67	3.19	18.52	7.40	47.91
	30	7.28	13.53	3.66	17.94	7.90	48.23
	40	6.17	17.94	5.46	12.97	6.75	50.72
	50	6.63	15.07	3.96	15.58	8.03	50.73
5-2	0	3.13	24.44	6.52	15.14	7.99	40.77
	10	4.07	23.24	6.32	22.22	6.46	37.69
	20	10.45	17.26	5.10	15.82	6.54	44.84
	30	10.56	13.65	5.10	18.68	6.83	45.18
	40	7.54	6.39	5.58	17.74	7.26	55.48
5-3	0	3.69	34.83	3.52	13.41	5.54	39.00
	10	2.44	34.35	3.02	12.95	6.13	41.11
	20	2.42	34.02	3.02	12.22	5.94	42.38
	30	2.93	33.41	3.72	14.20	7.23	38.51
	40	3.52	32.01	3.94	14.02	7.06	39.45
	50	6.99	27.50	5.40	15.98	7.09	37.05
	60	9.18	22.15	4.91	19.63	6.08	38.05
5-4	70	8.10	10.49	5.18	17.83	7.22	51.19
	0	4.67	27.26	5.67	14.07	7.05	39.40
	10	4.56	24.70	4.66	25.86	6.10	34.12
	20	5.19	23.47	5.25	18.74	6.53	40.82
	30	7.58	20.42	4.57	17.69	7.08	42.66
	40	9.89	16.13	4.14	18.11	7.08	43.40
	50	10.20	14.60	4.08	17.40	7.12	45.11
	60	12.01	11.77	3.80	20.60	7.20	44.61
70	9.31	9.57	4.04	18.58	7.88	50.62	

**Table A.4 Concentrations of the major elements in multilayered coatings**

Coating thickness, $\mu\text{m}$	Composition, at.%									
	Multilayered coating with aluminide I					Multilayered coating with aluminide II				
	Al	Si	Cr	Ni	Al/Ni Ratio	Al	Si	Cr	Ni	Al/Ni Ratio
0	44.21	4.17	11.12	40.50	1.09	56.94	2.89	12.00	28.17	2.02
10	42.44	2.84	10.17	44.55	0.95	55.86	2.57	9.68	31.88	1.75
20	42.71	2.43	8.22	46.64	0.92	56.54	2.26	11.81	29.39	1.92
30	37.64	2.42	13.87	46.07	0.82	58.11	2.50	9.39	30.00	1.94
40	32.52	2.47	25.60	39.41	0.83	59.15	2.10	8.97	29.77	1.99
50	36.13	2.63	20.07	41.18	0.88	55.23	2.65	13.28	28.84	1.92
60	27.57	2.89	25.63	43.91	0.63	56.28	2.78	10.67	30.28	1.86
70	22.29	3.57	15.35	58.79	0.38	54.31	2.86	9.37	33.45	1.62
80	20.96	3.70	20.24	55.11	0.38	54.09	3.02	7.98	34.91	1.55
90	22.51	4.48	13.53	59.47	0.38	53.16	3.27	10.60	32.96	1.61
100	21.11	5.71	20.81	52.38	0.40	52.98	4.03	9.54	33.45	1.58
110	18.38	7.89	19.22	54.52	0.34	50.26	5.14	9.16	35.44	1.42
120	9.25	17.90	26.66	46.18	0.20	50.37	5.46	7.26	36.91	1.36
130	11.54	16.81	23.52	48.13	0.24	39.07	9.94	17.14	33.86	1.15
140	10.73	22.13	13.95	53.19	0.20	46.40	7.48	8.57	37.55	1.24
150	13.62	17.89	15.23	53.26	0.26	40.03	13.88	11.75	34.34	1.17
160	13.93	14.88	21.83	49.36	0.28	35.07	18.36	14.27	32.30	1.09
170	14.14	13.61	20.76	51.50	0.27	19.21	28.50	18.10	34.18	0.56
180	14.46	12.00	21.93	51.61	0.28	15.30	30.78	19.17	34.76	0.44
190						13.70	29.30	24.33	32.67	0.42
200						15.06	24.64	25.49	34.81	0.43
210						16.51	23.88	19.32	40.29	0.41
220						16.94	22.69	20.12	40.24	0.42
230						16.02	21.96	20.95	41.06	0.39
240						18.28	18.87	17.71	45.14	0.40
250						18.48	16.84	17.78	46.90	0.39
260						18.21	15.29	18.40	48.10	0.38
270						19.29	12.78	19.31	48.62	0.40